Storage, Stability, and Activity of ctDNA, tRNA, Hemoglobin and Cytochrome c in Choline-based Ionic Liquids

By

KIRAN DEVI TULSIYAN

CHEM11201704016

National Institute of Science Education and Research

Bhubaneswar, Odisha - 752050

A thesis submitted to the
Board of Studies in Chemical Sciences
In partial fulfilment of requirements
for the degree of

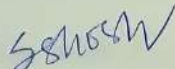## DOCTOR OF PHILOSOPHY
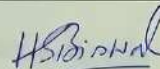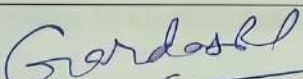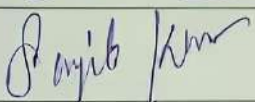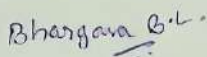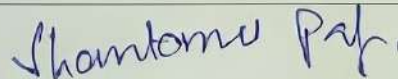
Of

HOMI BHABHA NATIONAL INSTITUTE

July, 2023

Homi Bhabha National Institute

Recommendations of the Viva Voce Committee

As members of the Viva Voce Committee, we certify that we have read the dissertation prepared by **Ms. Kiran Devi Tulsiyan** entitled "**Storage, Stability, and Activity of ctDNA, tRNA, Hemoglobin and Cytochrome c in Choline-based Ionic Liquids**" and recommend that it may be accepted as fulfilling the thesis requirement for the award of Degree of Doctor of Philosophy.
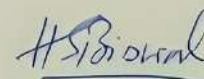
Chairman – Dr. Subhadip Ghosh	*Sghosh*	Date: 13/12/2023
Guide / Convener – Prof. Himansu Sekhar Biswal	*HSBiswal*	Date: 13/12/2023
Co-guide - (if any)		Date:
Examiner – Prof. Ramesh L. Gardas	*Gardas*	Date: 13/12/2023
Member 1- Dr. Sanjib Kar	*Sanjib Kar*	Date: 13/12/2023
Member 2- Dr. B. L. Bhargava	*Bhargava B.L.*	Date: 13/12/2023
Member 3- Dr. Santanu pal	*Shantomu Pal.*	Date: 13/12/23

Final approval and acceptance of this thesis is contingent upon the candidate's submission of the final copies of the thesis to HBNI.

I/We hereby certify that I/we have read this thesis prepared under my/our direction and recommend that it may be accepted as fulfilling the thesis requirement.
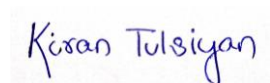
Date: 13/12/2023

Place: NISER

HSBiswal

Prof. Himansu Sekhar Biswal

Guide

II

STATEMENT BY AUTHOR

This dissertation has been submitted in partial fulfillment of requirements for an advanced degree at Homi Bhabha National Institute (HBNI) and is deposited in the library to be made available to borrowers under rules of the HBNI.

Brief quotations from this dissertation are allowable without special permission, provided that accurate acknowledgement of source is made. Requests for permission for extended quotation from or reproduction of this manuscript in whole or in part may be granted by the Competent Authority of HBNI when in his or her judgment the proposed use of the material is in the interests of scholarship. In all other instances, however, permission must be obtained from the author.
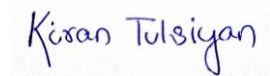
Kiran Devi Tulsiyan

DECLARATION

I, hereby declare that the investigation presented in the thesis has been carried out by me. The work is original and has not been submitted earlier as a whole or in part for a degree / diploma at this or any other Institution / University.

Kiran Tulsiyan

Kiran Devi Tulsiyan

List of Publications

Published

1. #**K. D. Tulsiyan**, S. Jena, M. González-Viegas, R. K. Kar, H. S. Biswal*; "Structural Dynamics of RNA in the Presence of Choline Amino Acid Based Ionic Liquid: A Spectroscopic and Computational Outlook." ACS Cent. Sci. (2021), 7, 1688-1697.

2. #**K. D. Tulsiyan**, A. Mahalik, B. R. Dandekar, J. Mondal, and H. S. Biswal*; "Enhancement of Peroxidase Activity in Magnetic Ionic Liquids" ACS Sustainable Chem. Eng. (2023), *11, 8487–8494*

3. #**K. D. Tulsiyan**, M. R. Prusty, and H. S. Biswal*; "Effect of Choline Amino Acid-Based Ionic Liquids on Stability and Structure of Haemoglobin" Chemphyschem (2023), *e202300201*

4. #**K. D. Tulsiyan**, S. K. Panda, M. K. Rana, and H. S. Biswal*; "Critical Assessment of the Compaction and Decompaction of DNA in Magnetic Ionic Liquids" (Manuscript under preparation)

5. **K. D. Tulsiyan**, S. Jena, J. Dutta H. S. Biswal*; "Hydrogen bonding with polonium" Phys. Chem. Chem. Phys. (2022), 24, 17185-17194

6. S. Jena, J. Dutta, **K. D. Tulsiyan**, A. K. Sahu, S. S. Choudhury, H. S. Biswal*, "Noncovalent Interactions in Proteins and Nucleic Acids: Beyond Hydrogen Bonding and π-Stacking." Chem. Soc. Rev. (2022), 51, 4261-4286

7. S. Jena, **K. D. Tulsiyan**, A. Rana, S. S. Choudhury, H. S. Biswal*; "Non-Conventional Hydrogen Bonding and Aromaticity: A Systematic Study on Model Nucleobases and Their Solvated Clusters." ChemPhysChem (2020), 21, 1826-1835.

8. S. Jena, **K. D. Tulsiyan**, R. K. Kar, H. K. Kisan, H. S. Biswal*; "Doubling Förster Resonance Energy Transfer Efficiency in Proteins with Extrinsic Thioamide Probes: Implications for Thiomodified Nucleobases." Chem. Eur. J. (2021), 27, 4373-4383.

9. S. Jena, **K. D. Tulsiyan**, A. Kumari. R. Das, H. S. Biswal*; "Thiolumazines as Heavy-Atom-Free Photosensitizers for Applications in Daylight Photodynamic Therapy: Insights from Ultrafast Excited-State Dynamics." J. Phys. Chem. B (2022), 126, 32, 6083–6094

10. D. K. Sahoo, S. Jena, **K. D. Tulsiyan**, J. Dutta, S. Chakrabarty*, and Himansu S. Biswal*, "Amino-Acid-Based Ionic Liquids for the Improvement in Stability and Activity of Cytochrome-c: A Combined Experimental and Molecular Dynamics Study" J. Phys. Chem. B, (2019), 123, 10100–10109

11. D. K. Sahoo, **K. D. Tulsiyan**, S. Jena, H. S. Biswal, "Implication of Threonine-Based Ionic Liquids on the Structural Stability, Binding and Activity of Cytochrome c." ChemPhysChem (2020), 21, 2525.

12. J. Dutta, D. K. Sahoo, S. Jena, **K. D. Tulsiyan**, H. S. Biswal, "Non-covalent interactions with inverted carbon: a carbo-hydrogen bond or a new type of hydrogen bond?" Phys. Chem. Chem. Phys., (2020), 22, 8988-8997.

13. R. R. Samal, K. Sundaray, **K. D. Tulsiyan**, S. Saha, G. B.N. Chainy , U. Subudhi, "Compromised conformation and kinetics of catalase in the presence of propylthiouracil: A biophysical study and alleviation by curcumin" Int. J. Biol. Macromol., (2022), 226, 1547-1559.

14. T. S. Dash, Sheetal, **K. D. Tulsiyan**, A. Mishra, D. Sama, C. S. Yadav, S. L. Samal, "Mn2− xHOxSnS4: A mixed quaternary metal chalcogenide system with an antiferromagnetic ordering." J. Solid State Chem., (2022), 314, 123350.

15. B. Baral, B. Panigrahi, A. Kar, **K. D. Tulsiyan**, U. Suryakant, D. Mandal, U. Subudhi, Peptide nanostructures-based delivery of DNA nanomaterial therapeutics for regulating gene expression, Molecular Therapy: Nucleic Acid (2023), doi: https://doi.org/10.1016/j.omtn.2023.07.017.
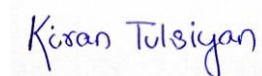
 # Pertaining to the thesis.

Conference/Symposium

1. **Participated** in the "National Workshop on Fluorescence and Raman Spectroscopy" (FCS 2020) held between 7-12th of December 2020, organized virtually by the Indian Institute of Technology Bombay, Mumbai, India; under the umbrella of "fluorescence Society."

2. **Participated** in the 1st international conference on "Emerging Porous Materials (ePorMat-2021)", a virtual conference held during 29-30th July 2021.

3. **Presented a poster** at the "12th National Workshop on Fluorescence and Raman Spectroscopy" (FCS 2021) held between 29th November to 4th December of 2021, organized virtually by the Indian Institute of Science Education and Research Thiruvananthapuram, Kerala, India.

4. **Delivered a flash talk** at the "Trombay Symposium on Radiation & Photochemistry" (TSRP-2022) held between 12-15th of January 2022, virtually organized by Training School Hostel, Anushaktinagar, Mumbai, India.

5. **Participated** in all deliberations in Birth Centenary Celebration Summit of Late Prof Dr Gokulananda Mahapatra, held during 22-24th May 2022 at Cuttack, Odisha.

6. **Participated** in all deliberations in Birth Centenary Celebration Summit of Late Prof Dr Gokulananda Mahapatra, held during 16-18th Dec 2022 at NISER,

Bhubaneswar.

7. **Presented a poster** at the "1st HBNI Interaction meeting in Chemical Sciences" held between 18th -20th January of 2023, organized by the School of Chemical Sciences, NISER Bhubaneswar, Odisha.

8. **Presented a poster** at the "National Conference on Recent Advances in Chemical Sciences (NCRACS 2023)" held between 19-20th March of 2023, organized by P. G. Department of Chemistry, Berhampur University, Odisha.

Kiran Tulsiyan

Kiran Devi Tulsiyan

Dedicated to

My Parents, and Brother

ACKNOWLEDGEMENTS

While this thesis may appear to result from one individual's dedication and perseverance, it represents the culmination of a collective endeavor involving numerous unsung heroes, irrespective of their awareness of the role played. The day I decided to pursue chemistry as my field of study remains vivid in my memory, accompanied by the dream of achieving a distinguished title associated with my name. With this thesis, I aim to seize the opportunity soon. I wholeheartedly acknowledge and extend my deepest gratitude to all those who have played a pivotal role in supporting me throughout the past six years, providing unwavering assistance not only in my academic pursuits but also in navigating the emotional challenges that accompanied them.

Firstly, I would like to express my sincere gratitude to my supervisor, Prof. Himansu Sekhar Biswal, for his relentless support and guidance throughout the process. With his valuable assistance, I was able to design my project and work on it independently. This freedom helped me analyze my data effectively and facilitated a deep understanding of my chosen topic. I will forever be grateful for his feedback, encouragement, and criticism alike, which are crucial for a successful research experience.

I would like to extend my heartfelt gratitude to Prof. A. Srinivasan, Director, and Prof. T. Chandrashekhar, the Founder Director, for providing exceptional research opportunities and facilities at NISER Bhubaneswar. I would also like to express my appreciation to Prof. A. Srinivasan, Dr. U Lourderaj, Dr. Moloy Sarkar, Dr. Arindam Ghosh, Dr. Prasanjit Mal, Prof. C. Gunanathan, and Dr. Sudip Barman for their invaluable teaching during my coursework. Furthermore, I acknowledge my doctoral committee members Dr. Subhadip Ghosh (Chairman), Dr. Sanjib Kar, Dr. B. L. Bhargava, and Dr. Shantanu Pal (IIT-BBS) for their valuable suggestions and guidance. I also thank Prof. C. Gunanathan, Convener

who have been the pillars of strength in my life. Your friendship has been invaluable. I am also deeply thankful to Mr. Kiran Mishra for being my constant and motivating me during my difficult times.

Lastly, I would like to sincerely thank my parents, Mr. Manoj Kumar Tulsiyan and Mrs. Durgi Devi Tulsiyan, for their boundless love, patience, blessings, support, and numerous sacrifices. Their presence has been a constant source of motivation throughout my journey. I would also like to express my heartfelt appreciation to my brother, Pankaj, and my sister-in-law, Nirja, for their continuous moral support. They have been my pillars of strength, offering guidance, motivation and encouragement during frustration, failure, and the lows.

Above all, I am grateful to the Almighty for granting me the courage and fortitude to pursue and achieve this remarkable milestone.

"The most important thing is to never stop questioning." - Albert Einstein

Kiran Devi Tulsiyan

CONTENTS

SYNOPSIS

Chapter-1: Introduction

Over the past two decades, ionic liquids (ILs) have garnered significant attention as a novel class of materials with diverse applications across various fields. These ILs have captured the interest of researchers due to their unique and adjustable properties, making them a promising option as environmentally friendly solvents.[1-5] Typically composed of molten or fused salts consisting of organic cations and inorganic anions, often asymmetric in nature, ILs are often referred to as designer green solvents. Their physical properties, such as viscosity, density, miscibility, and polarity, can be tailored by selecting specific combinations of cations and anions.

Despite their potential, the adoption of ILs in medical applications has been hindered by concerns regarding their toxicity and biodegradability. However, the development of third-generation ILs has sparked considerable interest in their utilization for storing and stabilizing biomolecules.[6-11] The advent of third-generation ILs has demonstrated their significance in drug delivery by improving administration methods, reducing toxicity, and enhancing absorption rates. Their relevance in various biological processes stems from their ability to interact through multiple forces, including hydrogen bonding, electrostatic interactions, and dispersion.[12-20]

These factors have motivated extensive research into the biomolecular interactions with ILs, which have the potential to yield exciting applications. This thesis aims to explore the storage, stability, and activity of proteins and nucleic acids in choline-based ILs. We have also attempted to provide insight into these interactions and shed light on the binding modes between ILs and biomolecules, combining experimental and theoretical approaches. The thesis is divided into six chapters, focusing on the role of biocompatible

choline-based ILs in protein folding/unfolding studies and their impact on the structure, stability, and activity of biomolecules. Ultimately, this thesis seeks to contribute to the understanding of IL behavior, structures, and underlying mechanisms, providing valuable insights for future research endeavors.

Chapter-2: Adopted Methodologies and Instrumentation

This chapter discusses the experimental and computational techniques used in the thesis.

Experimental techniques

Nuclear Magnetic Resonance (NMR) Spectroscopy

- ✎ ^{1}H and ^{13}C NMR spectroscopy

Spectroscopic Techniques

- ❖ Steady-state UV-vis absorption spectroscopy
- ❖ Steady-state emission spectroscopy
- ❖ Time-correlated single photon counting (TCSPC) technique
- ❖ Circular Dichroism (CD) Spectroscopy
- ❖ Florescence Correlation Spectroscopy

Other Techniques

- ✎ Isothermal Titration Calorimetry
- ✎ Field-emission Scanning Electron Microscopy

Computational techniques

Optimization, Frequency and Binding Energy Calculation

- ❖ Density functional theory (DFT) method using Gaussian 16 Software

Molecular Docking Methods

- ❖ Auto-dock Vina Software

Molecular Dynamics Simulations

- ❖ Gromacs Software

Chapter-3: Choline amino acid ionic liquids (CAAILs) for the long-term storage and stability of RNA

RNA has demonstrated immense potential in medical applications, molecular and cellular biology research, and nano/biotechnology advancements. However, one of the primary challenges of studying RNA in both in-vivo and in-vitro settings is maintaining its structural integrity in solution samples. Traditionally, cold storage has been the most commonly employed method for RNA storage. Samples are stored at sub-zero temperatures ranging from -20 °C to -80 °C or in liquid nitrogen, slowing down degradation processes.[21] However, these storage methods often require specialized equipment and infrastructure, making them expensive and cumbersome. Lately, choline-based ILs have demonstrated their suitability for long-term storage and extraction of macromolecules, such as
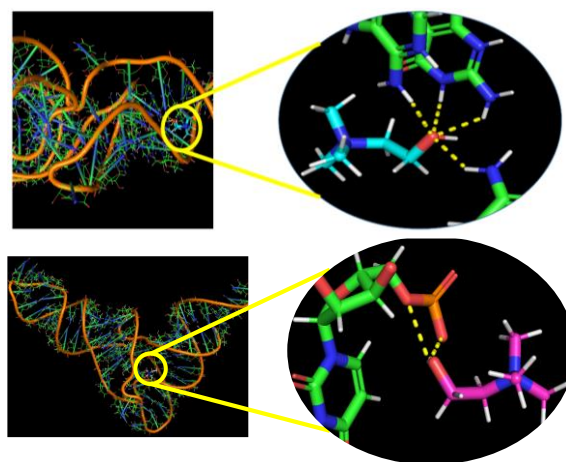
Figure 1: Molecular docking structure of RNA complex with ChAAILs and EB: zoomed section of IL bound to macromolecule

proteins and DNA, as these biomolecules can maintain their functionality in IL environments. To gain insights into the interaction between ChAAILs and RNA, we have developed an initial hypothesis and employed theoretical modeling techniques, complemented by classical simulations up to microsecond timescales. To confirm the RNA-IL interaction, a range of spectroscopic techniques was utilized, including steady-state absorption (UV-Vis) and emission measurements, time-correlated single-photon counting (TCSPC) integrated with femtosecond-fluorescence up-conversion, and fluorescence correlation spectroscopy (FCS). Additionally, isothermal titration

calorimetry experiments were conducted to provide thermodynamic information on the binding between RNA and ILs.

Our findings revealed that the presence of ILs did not lead to any changes in the hydrodynamic radius of RNA, indicating the preservation of its structural integrity in the IL environment. This result was further supported by CD analysis. UV-vis spectra analysis demonstrated that CAAILs exhibited multimodal binding with RNA, and fluorescence emission studies confirmed IL molecules' intrusion into the minor RNA groove through dye displacement experiments.

We observed that increasing IL concentration resulted in the structural stability of RNA. Isothermal titration calorimetry and molecular docking revealed weak binding energy ($\sim$-4 kcal·mol^{-1}) between ILs and RNA. This weak binding suggests that ILs can preserve the structural integrity of RNA while also allowing for its extraction from the IL medium. Moreover, ILs were found to be non-toxic, biocompatible solvents, making them suitable for the safe storage and extraction of RNA.

This study holds significance as it provides spectroscopic and theoretical evidence supporting the use of non-toxic and environmentally friendly choline amino acid-based ILs for the extraction and storage of RNA. The molecular-level insights obtained from this research can guide the design of ILs for the in vivo application of RNA.

Chapter-4: Choline amino acid ionic liquids (CAAILs) effect on Haemoglobin

Choline amino acid-based ILs (ChAAILs) have emerged as promising biocompatible ILs, particularly for applications involving the storage and stability of proteins and biomolecules. ChAAILs are environmentally friendly, as their constituent ingredients are non-toxic.[7, 8, 11, 12, 14, 17, 19, 20] Recent studies have explored the cytotoxicity and skin permeation properties of ChAAILs for their potential application as drug delivery agents.

We aim to provide insights into the effect of ChAAILs on hemoglobin (Hb) protein, an iron-containing oxygen transporter found exclusively in red blood cells. The findings indicate that choline amino acid-based ILs induce alterations in the native structure of hemoglobin. Fluorescence and CD measurements suggest that ChAAILs cause partial unfolding of the protein. Although [Chl][Met] (choline-based IL with methionine) exhibits a binding to Hb with a binding energy of -4.7 kcal/mol, neither of the ChAAILs completely denatures the protein. The primary interactions between ILs and Hb are predominantly through hydrogen bonding. The potential use of ChAAILs as external ligands to explore the hemichrome intermediate
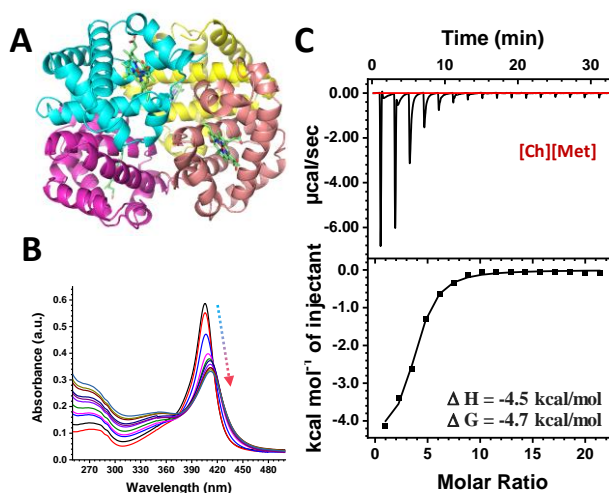
Figure 2: (A) Cartoon representation of Hemoglobin (PDB ID: 2b4z), (B) Absorbance spectra of Hb with the increasing concentration of [Chl][Gly] up to 5 M, (C) ITC isotherm of the Hb and [Chl][Met] binding interaction. The top panel shows heat flow for each injection (μcal/s) as a function of time (min). The lower panel shows integrated heats in each injection as a function of the molar ratio of the IL along with the thermodynamic parameters (ΔH, ΔG)

state of hemoglobin is quite promising. The implications of this study could be extended to various areas of chemistry and biology, as ILs have demonstrated a strong binding affinity with Hb. However, further comprehensive investigations are necessary to explore the broader applications of ILs in bioanalytical processes.

Chapter-5: Compaction of DNA in Magnetic Ionic Liquids

In biomedical applications, the compaction and decompaction of DNA at room temperature play a crucial role. Ionic liquids (ILs) have emerged as green solvents that shows diverse applications in storage, preservation and extraction of DNA. Magnetic ILs (MILs) have shown great promise due to their tunable physicochemical properties. Herein we have employed various spectroscopic techniques and molecular simulations to understand the binding and molecular interactions between MILs and DNA.

Scanning electron microscopy (SEM) and fluorescence correlation spectroscopy (FCS) analysis validated the compaction of ct-DNA. The molecular interactions between ILs and ct-DNA, including electrostatic, hydrogen bonding, and hydrophobic interactions, were elucidated through UV-Vis spectra, fluorescence dye displacement studies, zeta potential measurements, and molecular docking. These investigations revealed that ChMILs could bind to ct-DNA
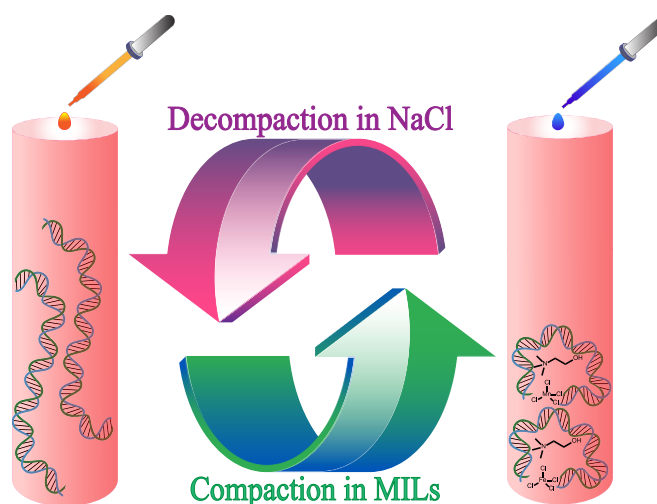
Figure 3: Schematic representation of compaction and decompaction of DNA in presence of magnetic ionic liquid and NaCl respectively

through the choline cation, irrespective of the specific anions used in this study. Molecular dynamics (MD) studies indicated a strong interaction between [Ch]$_2$[Mn] (choline-based magnetic ionic liquid with manganese) and DNA. Furthermore, in comparison to [Ch][Fe] (choline-based ionic liquid with iron), DNA exhibited a more significant conformational shift in the presence of [Ch]$_2$[Mn]. During the simulation, the exposed surface area of DNA gradually decreased for both complexes. The interaction with the two magnetic ionic liquids caused the structure of DNA to bend or become more spherical compared to

its initial form, indicating DNA compaction. Importantly, [Ch]2[Mn] demonstrated a more pronounced interaction, resulting in a more prominent DNA compaction compared to [Ch][Fe]. The estimated binding free energy, ΔG = -642 kcal/mol, confirmed the stronger affinity of DNA towards [Ch]2[Mn] compared to [Ch][Fe].

In summary, using MILs as compacting agents for DNA in biomedical applications holds great potential. Through spectroscopic techniques, molecular simulations, and post-MD analysis, we have gained valuable insights into the binding strength and mechanisms of MILs with DNA and the compaction and decompaction processes.

Chapter-6: Peroxidase Activity of Cytochrome-c in Magnetic Ionic Liquids

Cytochrome c (Cyt-c) is an important heme-containing protein that is an electron carrier in the mitochondrial respiratory chain. Despite having a six-coordinated heme iron, Cyt-c exhibits peroxidase-like activity in its native state. This study investigated the impact of magnetic ionic liquids (MILs) on the peroxidase activity of Cyt-c was investigated. Specifically, the effect of cholinium (Ch) based MILs, namely [Ch][Fe] and [Ch]2[Mn], on the guaiacol oxidation activity of Cyt-c was examined.

We conducted a comprehensive analysis of the kinetics and thermodynamics of Cyt-c activity in the presence of MILs using techniques such as
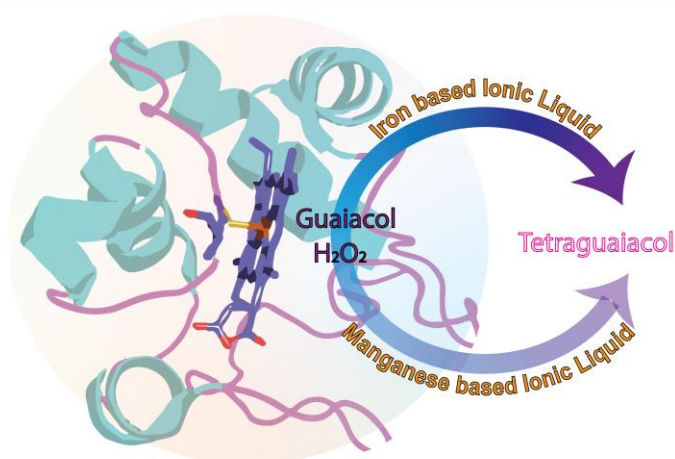
Figure 4: Schematic representation of enhancement of peroxidase activity of Cyt-c in presence of magnetic ionic liquid

isothermal titration calorimetry (ITC), UV-Vis spectroscopy, CD spectroscopy, and

fluorescence spectroscopy. The results indicated that the peroxidase activity of Cyt-c was enhanced twofold in the presence of [Ch][Fe], while only a 20% increase was observed with [Ch]$_2$[Mn]. This enhancement in activity correlated with the accessibility of the heme iron in Cyt-c. To gain further insights into the interaction mechanism, molecular docking and molecular dynamics simulations were employed.

The observed increase in Cyt-c peroxidase activity was attributed to the perturbation of the native sixth coordination bond of methionine-80, which is associated with the heme region of Cyt-c. The presence of MILs induced this perturbation. Notably, there has been limited research on enzymatic activity in the presence of MILs, and this study provides a foundation for utilizing MILs to modulate and control enzymatic activity and catalysis.

Overall, this investigation sheds light on the influence of MILs on the peroxidase activity of Cyt-c. By elucidating the underlying mechanism of interaction, this research paves the way for the future utilization of MILs to regulate and manipulate enzymatic activity, opening new possibilities in the field of enzymology and catalysis.

Summary and Future Perspective

Ionic liquids (ILs) have emerged as promising and environmentally friendly solvents with a wide range of potential applications in various fields, including energy, healthcare, and environmental sciences. Over the past decade, ILs have gained attention due to their advantageous properties, such as thermal stability, chemical resistance, excellent dissolving power, biocompatibility, and biodegradability. These characteristics make ILs attractive alternatives to conventional organic and inorganic solvents for biomolecule applications.

However, the use of ILs in biotechnological processes poses challenges due to the limited understanding of their biodegradability and potential toxicity, including ecotoxicity and

cytotoxicity. It is crucial to address these uncertainties by conducting extensive research on ILs specifically tailored for biomolecular applications. By obtaining quantitative and robust physicochemical data, researchers can design novel ILs that meet the requirements of various biomolecule-based processes.

Efforts are needed to assess the biodegradability and toxicity profiles of ILs to ensure their safe and sustainable use. This will involve investigating the fate of ILs in different environmental conditions and their potential impacts on ecosystems. Additionally, studies should focus on evaluating the cytotoxicity of ILs to ensure their compatibility with living systems and their potential for use in biomedical applications.

By expanding our knowledge of ILs in the context of biomolecules, we can unlock their full potential as designer solvents. This will enable the development of innovative IL-based approaches for various biotechnological processes, ranging from biomolecule extraction and purification to drug delivery systems and biofuel production. Continued research in this area will contribute to the design and optimisation of ILs tailored specifically for biomolecular applications, leading to more sustainable and efficient processes in energy, health, and the environment.

References:

1.   Choudhury, S.; Mahapatra, S.; Sahu, A.; Hembram, P.; Jena, S.; Biswal, H., Synthesis of α,β-Unsaturated Ketones in Water: The Claisen–Schmidt Condensation Revisited. ACS Sustainable Chem. Eng. 2022, 10.

2.   Choudhury, S. S.; Jena, S.; Sahoo, D. K.; Shekh, S.; Kar, R. K.; Dhakad, A.; Gowd, K. H.; Biswal, H. S., Gram-Scale Synthesis of 1,8-Naphthyridines in Water: The Friedlander Reaction Revisited. ACS Omega 2021, 6 (29), 19304-19313.

3.   Choudhury, S. S.;   Mahapatra, S.; Biswal, H. S., Hydrogen bond mediated conversion of benzenenitriles and arylacetonitriles to amides: an "on/in-water" reaction strategy. Green Chem. 2022, 24 (12), 4981-4990.

4.   Welton, T., Ionic liquids: a brief history. Biophysical Reviews 2018, 10 (3), 691-706.

5.   Zhigang Lei, B. C., Yoon-Mo Koo, and Douglas R. MacFarlane, Introduction: Ionic Liquids. Chem. Rev. 2017, 117 (10), 6633-6635.

6.   Flieger, J.; Flieger, M. Ionic Liquids Toxicity—Benefits and Threats Int. J. Mol. Sci., 2020.

7.   Sahoo, D. K.;   Chand, A.;   Jena, S.; Biswal, H. S., Hydrogen-bond-driven thiouracil dissolution in aqueous ionic liquid: A combined microscopic, spectroscopic and molecular dynamics study. J. Mol. Liq. 2020, 319, 114275.

8.   Sahoo, D. K.;   Jena, S.;   Dutta, J.;   Chakrabarty, S.; Biswal, H. S., Critical Assessment of the Interaction between DNA and Choline Amino Acid Ionic Liquids: Evidences of Multimodal Binding and Stability Enhancement. ACS Cent. Sci. 2018, 4 (12), 1642-1651.

9.   Sahoo, D. K.;   Jena, S.;   Tulsiyan, K. D.;   Dutta, J.;   Chakrabarty, S.; Biswal, H. S., Amino-Acid-Based Ionic Liquids for the Improvement in Stability and Activity of Cytochrome c: A Combined Experimental and Molecular Dynamics Study. J. Phys. Chem. B 2019, 123 (47), 10100-10109.

10.   Sahoo, D. K.;   Mundlapati, V. R.;   Gagrai, A. A.; Biswal, H. S., Efficient SO2 Capture through Multiple Chalcogen Bonds, Sulfur-Centered Hydrogen Bonds and S••π Interactions: A Computational Study. ChemistrySelect 2016, 1 (8), 1688-1694.

11.   Siopa, F.; Figueiredo, T.; Frade, R. F. M.; Neto, I.; Meirinhos, A.; Reis, C. P.; Sobral, R. G.; Afonso, C. A. M.; Rijo, P., Choline-Based Ionic Liquids: Improvement of Antimicrobial Activity. ChemistrySelect 2016, 1 (18), 5909-5916.

12.   Gadilohar, B. L.; Shankarling, G. S., Choline based ionic liquids and their applications in organic transformation. J. Mol. Liq. 2017, 227, 234-261.

13.   Greer, A. J.; Jacquemin, J.; Hardacre, C. Industrial Applications of Ionic Liquids Molecules, 2020.

14.   Kumar, P. K.; Bisht, M.; Venkatesu, P.; Bahadur, I.; Ebenso, E. E., Exploring the Effect of Choline-Based Ionic Liquids on the Stability and Activity of Stem Bromelain. J. Phys. Chem. B 2018, 122 (46), 10435-10444.

15.   Kumar Sahoo, D.; Devi Tulsiyan, K.; Jena, S.; Biswal, H. S., Implication of Threonine-Based Ionic Liquids on the Structural Stability, Binding and Activity of Cytochrome c. ChemPhysChem 2020, 21 (23), 2525-2535.

16.   Le Donne, A.; Bodo, E., Cholinium amino acid-based ionic liquids. Biophys. Rev. 2021, 13 (1), 147-160.

17.   Li, X.; Ma, N.; Zhang, L.; Ling, G.; Zhang, P., Applications of choline-based ionic liquids in drug delivery. Int. J. Pharm. 2022, 612, 121366.

18.   Md Moshikur, R.; Chowdhury, M. R.; Moniruzzaman, M.; Goto, M., Biocompatible ionic liquids and their applications in pharmaceutics. Green Chem. 2020, 22 (23), 8116-8139.

19.   Miao, S.; Atkin, R.; Warr, G., Design and applications of biocompatible choline amino acid ionic liquids. Green Chem. 2022, 24 (19), 7281-7304.

20.   Moosavi, M.; Banazadeh, N.; Torkzadeh, M., Structure and Dynamics in Amino Acid Choline-Based Ionic Liquids: A Combined QTAIM, NCI, DFT, and Molecular Dynamics Study. J. Phys. Chem. B 2019, 123 (18), 4070-4084.

21.   Fabre, A.-L.; Colotte, M.; Luis, A.; Tuffet, S.; Bonnet, J., An efficient method for long-term room temperature storage of RNA. Eur J Hum Genet 2014, 22 (3), 379-385.

Thesis Title: Storage, Stability, and Activity of ctDNA, tRNA, Hemoglobin and Cytochrome c in Choline-based Ionic Liquids

The combination of room-temperature ionic liquids (RTILs) and biomolecules represents an exciting opportunity for discoveries and applications in various fields, including biochemistry, biomedicine, pharmacology, food science, and nanotechnology. RTILs and biomolecules are significant classes of organic molecules, comprising numerous distinct chemical species and organized into extensive families of related compounds. This convergence of RTILs and biomolecules holds great potential to unlock new avenues of research and innovation, enabling advancements in diverse areas that impact our understanding of life sciences and offer practical solutions for various industries. Our primary objective in this thesis is to uncover and elucidate the fundamental principles that can effectively organize and rationalize the wide range of properties and phenomena exhibited by the combination of choline-based ionic liquids (ChILs) and biomolecules. With such a diverse array of characteristics and behaviors observed within these systems, it becomes essential to establish a solid foundation of understanding that can provide coherence and a logical framework to analyze and interpret their complexities comprehensively. By identifying these underlying principles, we can gain valuable insights into the nature of RTIL-biomolecule interactions and pave the way for a more systematic and informed exploration of their properties and potential applications. The thesis is structured into six chapters based on this motivation and idea. Each chapter addresses specific aspects and contributes to the overall goal of organizing and rationalizing the diverse properties and phenomena exhibited by the combination of

choline-based ionic liquids (RTILs) and biomolecules. The breakdown of the chapters is as follows:

Chapter 1 provides an overview of the research topic, including the significance of studying choline-based-biomolecule systems, current knowledge, and the research objectives and questions addressed in the thesis. Chapter 2 focuses on the experimental and computational methods implemented to achieve fundamental insights into these interactions. It provides an overview of spectroscopic methods, imaging techniques, and computational approaches used to probe and analyze the properties and phenomena observed in these systems. Chapter 3 delves into the storage and extraction of RNA in choline amino acid-based ILs. It explores various structural characteristics and functions governing their stability at room temperature. This is followed by chapter 4, which presents the main findings and observations related to the properties and phenomena exhibited by choline amino acid-based ILs -Hemoglobin systems. Experimental studies and computational simulations highlight the conversion of the native state to the hemichrome state and its underlying principles. Chapter 5 discusses the experimental techniques and methodologies employed to study choline-based magnetic ILs -DNA systems. It provides an overview of spectroscopic methods and computational approaches used to probe and analyze the compacted DNA observed in the presence of ILs. Thereafter, chapter 6 unravels the increase in peroxidase activity of cytochrome-c in the presence of choline-based magnetic ILs from the experimental studies and computational simulations.

Finally, we summarize the main conclusions drawn from the research and discuss their implications. It also outlines potential future directions for further investigation, including unresolved questions, challenges, and opportunities for advancing the understanding and applications of choline-based biomolecule systems.

By structuring the thesis in this manner, the aim is to provide a comprehensive and systematic exploration of the subject matter, laying the groundwork for a better understanding of the fundamental principles governing choline-based-biomolecule interactions and offering insights for future research and applications.

List of Figures

List of Tables

ABBREVIATIONS

ADC   Analog to digital converter

AIM   Atoms in molecules

BCP   Bond Critical Poinr

CD   Circular Dichroism

CFD   Constant function discriminator

DFT   Density Functional Theory

DLS   Dynamic light Scattering

DNA   Deoxyribonucleic Acid

FTIR   Fourier Transform Infrared

FWHM   Full Width Half Maxima

IL   Ionic Liquids

ITC   Isothrmal Titration Calorimetry

LED   Light emitting Diode

MD   Molecular Dynamics

NCI   Non-covalent Interactions

NMR   Nucleic Magneic Resonamce

PDB   Protein Data Bank

RDF   Radial Distribution Function

RMSD   Root mean square deviation

RNA   Ribonucleic Acid

RTIL   Room Temperature Ionic Liquids

TAC   Time to amplitude converter

TCSPC   Time Correlated Single Photon Counting

WD   Window Discriminator

Chapter 1

Introduction

The objective of the thesis is to unravel the origin and strength of intermolecular interactions between ionic liquids (ILs) and biomolecules. A growing number of biological applications using ILs are underway as a replacement solvent for synthesis, as a biological constituent, and for the preservation and enhancement of the functionality of biomolecular species. The storage and stability of biomolecules have always been a matter of concern for biochemists. The therapeutic biomolecules are usually stored at low temperatures ranging from -20 °C to -80 °C. Recently it was realized that ILs can be alternative solvents for biomolecules. With a brief introduction to ILs and biomolecules, this chapter discusses the about research progress in this direction already published in the literature, followed by the objective and structure of the thesis.

1.1. Ionic liquids at play

The ionic liquids (ILs) have gained much attention during the past two decades as a novel class of materials with many applications in various disciplines.[1] They have become an emerging field of research because of their tuneable and unique properties. Due to these characteristics, ILs have emerged as a promising green solvent, an alternative to conventional organic compounds, mainly because of their low vapor. ILs are a class of salts with a melting temperature lower than 100 °C. Most ILs are liquid at room temperature and are also referred to as room-temperature ionic liquids (RTILs). Nowadays, ILs are an essential part of academic research because of their diverse chemical and physical properties.[2] RTILs are usually molten salts of asymmetric cations and anions, which lowers the lattice energy while packing. They are also called designer green solvents owing to their physical properties, including viscosity, density, and polarity. They can be tuned according to the requirement by selecting appropriate cations and anions species. Furthermore, ILs have earned a wide range of attention in protein

folding/ unfolding because of their biological significance. ILs are also considerd as a novel solvent for its applications in biochemical and medicinal industries.

The first RTIL, namely, ethyl ammonium nitrate ([$C_2H_5NH_3$][NO_3]) with a melting point of 12 °C, was reported by Paul Walden early in 20th century.[4] Nearly 40 years later, in 1951, Hurley and Wier at Rice University discovered low-melting salts using chloroaluminate anions for low-temperature electrodeposition of aluminum chloride ($AlCl_3$).[5] During the 1970s and 1980s, these ILs were mainly used for electrochemical applications. However, the drawback of this ionic liquid is that it is liquid at room temperature for a particular composition.[6] This drives the group to seek a liquid system at room temperature over a broader range of compositions. In the early 1980s, alkyl imidazolium salts (CnMIm)$^+$ were also testified as ILs because of their high viscosity.[7-9] John S. Wilkes has skillfully outlined a concise history detailing the emergence of ionic liquids (ILs), capturing pivotal moments in the research field.[10] Subsequently, in the 1990s, molten or fused salts with a melting point below 100 °C became a groundbreaking and unique medium for biochemical reactions..[11] A key breakthrough in "Air and water stable 1-ethyl-3-methylimidazolium based ionic liquids" in 1992 by Wilkes led to a growth in the interest in ILs.[11] By the end of the twentieth century, ionic liquids were coming to the attention of a wider audience and several researchers from different areas for various applications.[12-14]

1.1.1. Synthesis of Ionic Liquids

The synthesis of ionic liquids involves a two-step process [15] (Figure 1.1):

1. Formation of the Desired Cation: The desired cation can be produced either through the acid-driven protonation of the amine or via quaternization reactions involving an amine and a haloalkane, followed by heating the mixture.

2. Anion Exchange: Anion exchange reactions can be conducted by treating halide salts with Lewis acids to create Lewis acid-based ionic liquids or by employing anion metathesis.

$$NR_3$$

Step 1: $R'X$

$$[R'R_3N]^+ X^-$$

Metal salt (M^+A^-)

Step 2a : Lewis acid (MX_y)   **Step 2b :** Ion exchange resin

Bronsted acid (H^+A^-)

$$[R'R_3N]^+[MX_{y+1}]^-$$ $$[R'R_3N]^+ A^-$$
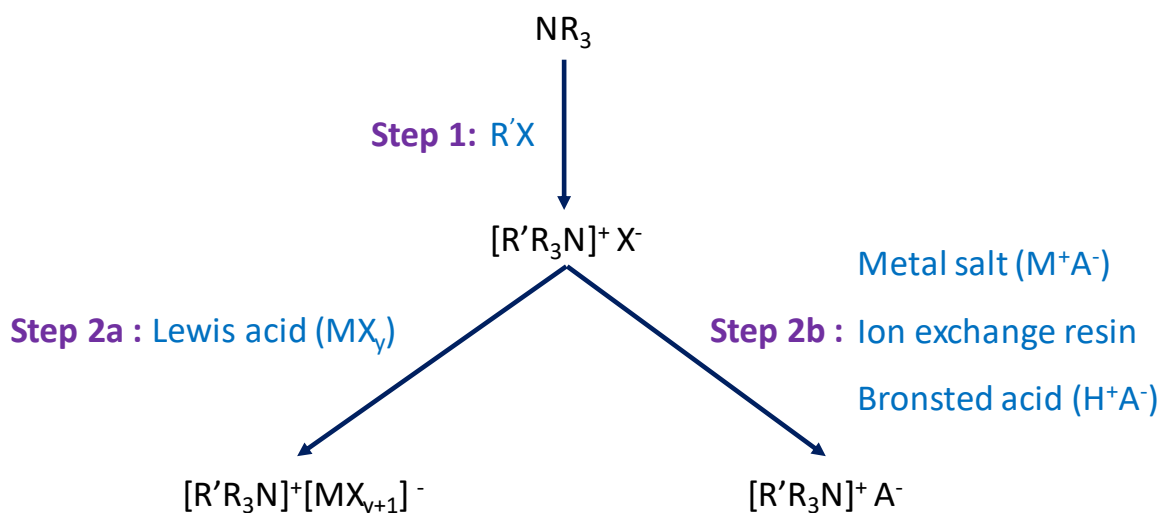
Figure 1.1 Synthesis paths for preparation of ionic liquids.

Ionic liquids can be categorized into protic ionic liquids (PILs) and aprotic ionic liquids (AILs), depending on whether the base is quaternized by a proton (H+) or an alkyl group (-R), respectively.[16-17] The Coulomb and hydrogen bonding (H-bonding) interactions are more robust in protic ionic liquids compared to aprotic ones, resembling water closely due to their extensive H-bonding network.[18] Additionally, ionic liquids are further classified into various categories based on combinations of cations and anions, each exhibiting unique biological, physical, chemical, and thermal properties.[19] However, Welton quoted it well: *"Room-temperature ionic liquid, non-aqueous ionic liquid, molten salt, liquid organic salt, and fused salt have all been used to describe salts in the liquid phase. With the increase in electronic databases, they are using keywords as search tools are becoming more important. While authors are free to choose any name that they wish for their systems, I would suggest that they at least include the term ionic liquid in*

keyword lists. In this paper, I allow the term ionic liquid to imply that the salt is low melting.''[12]

1.1.2. Properties of ionic liquids:

Interest in ionic liquids (ILs) has grown with its evolution now spanning three generations (Figure 1.2):

(1) Physical properties.

(2) Chemical properties; and

(3) Biological properties.
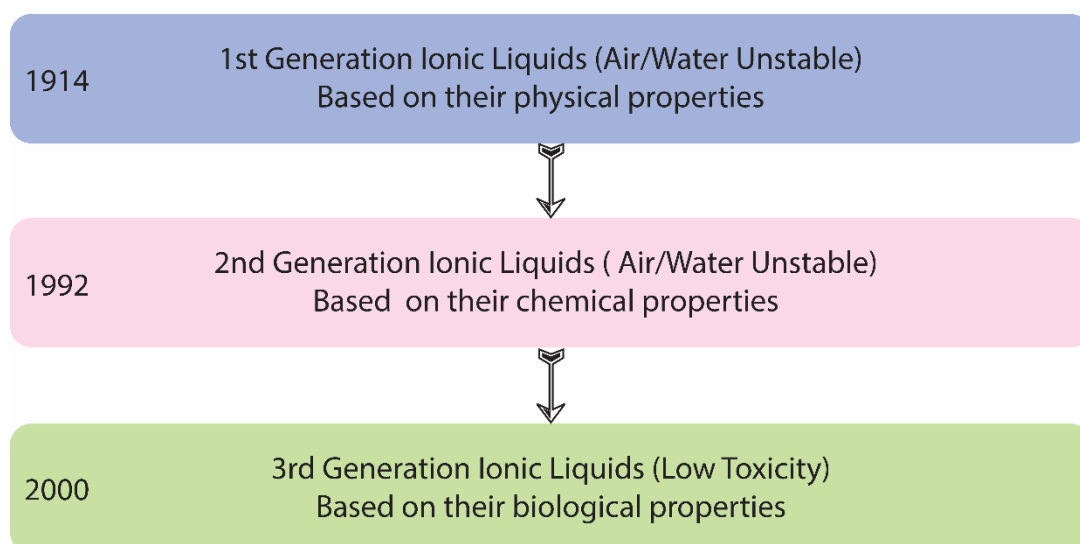
Figure 1.2. Evolution of properties of ionic liquids with timeline.

Ionic liquids exhibit a range of intriguing physicochemical properties, encompassing characteristics such as density, acidity, polarity, viscosity, and various other noteworthy attributes (Figure 1.3).[20] It is well known as a designer solvent since designing properties suitable ILs for specific requirements was feasible. Therefore, a clear understanding physical and chemical properties of ILs is crucial.
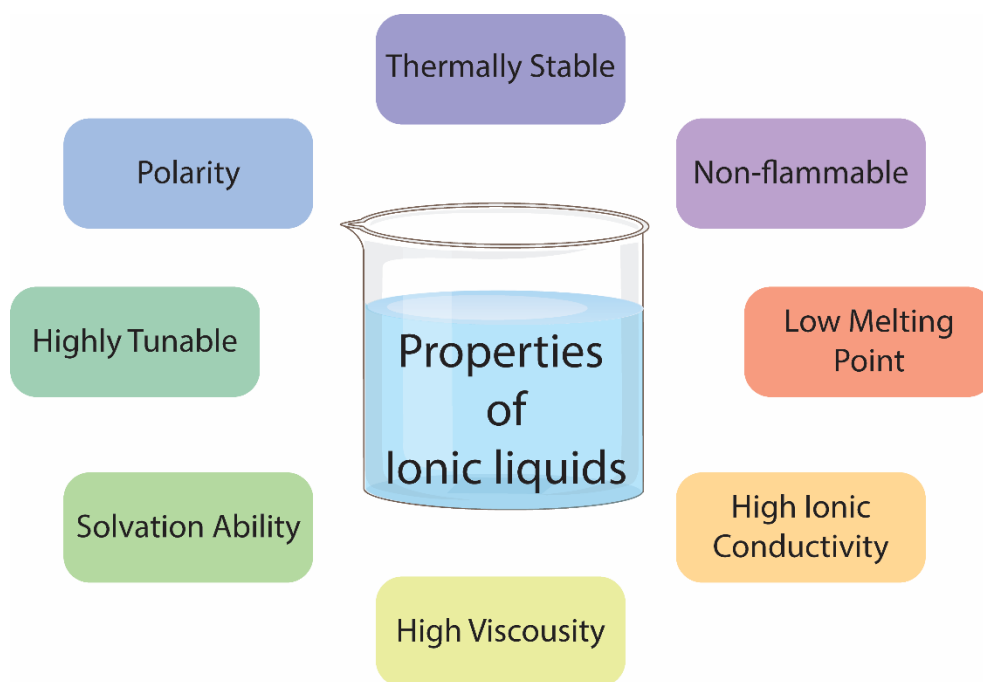
Figure 1.3. Physio-chemical properties of ionic liquids

1.1.2.1. Density

Ionic liquids typically possess higher density compared to other solvents, with typical values ranging from 0.9 to 1.7 g.cm^{-3}. The density values are often provided at standard conditions of 25 °C and 1 atm, though density is generally influenced by factors such as temperature, pressure, molecular mass, and the interactions between molecules and their structure. The density of ionic liquids is notably impacted by the molecular weight and design of both the anions and cations.[22] Specifically, density varies significantly based on the arrangement and conformation of the species involved.

Fisher provided a formula for density of dialkylimidazolium ILs at different temperatures:

$$\rho = a + b\,(T - 60)$$

where ρ is the density in kg.m^{-3}; T is the temperature in K.

1.1.2.2. Viscosity

Viscosity stands out as a critical factor influencing the application of ionic liquids (ILs), arising from the motion and molecular interactions among the constituent ions.[23] The viscosity coefficients of ILs typically represent their dynamic viscosity, with most ILs exhibiting higher viscosity compared to molecular solvents. These liquids are generally characterized by a viscosity range of around 1000 cP at room temperature. Unlike many molecular solvents, the temperature-dependent behavior of IL viscosity is more complex, as ILs often deviate from ordinary Arrhenius behavior. Additionally, the elongation of alkyl chains in the cation does not consistently lead to a straightforward increase in viscosity..

1.1.2.3. Melting point

The melting points of ionic liquid (IL) solvents establish the lower limit of the liquidus range. In comparison to molecular solvents, the two significant properties that enhance the appeal of ILs as solvents are their low vapor pressure and extensive liquid range. To qualify as a room-temperature ionic liquid (RTIL), the substance's melting point should be below 100 °C. The primary factors influencing the melting point include the charge distribution, Hydrogen bonding ability, asymmetry of ions, and vanderWaals interactions. The melting points of many ILs exhibit uncertainty due to considerable supercooling, rendering their freezing points unreliable and irreproducible. Katritzky et al. highlighted that critical parameters influencing the melting point of RTILs include the coordination ability of cations which can be determined from molecular shape and symmetry, the electrostatic intermolecular interactions between the ionic counterparts, and the number of degrees of freedom in both phases.[24]

1.1.2.4. Polarity

Solvents polarity is an important factor that influences ILs application in biomolecules. The polarity of ILs can give a positive insight for further application of ILs. ILs with long chain branching are generally hydrophobic because of the hydrophobicity of alkyl chains. In contrast, hydrophilic ILs always have no chain branching, or their chain branching is very short. Correspondingly, the longer the alkyl chain branching of the cationic counterpart of the ILs is, the stronger the polarity ILs have. Further, ILs can dissolve many compounds because they have strong polarity.

1.1.2.5. Cytotoxicity

For an extended period, there was a prevailing belief in the environmental safety of these chemicals due to their composition of charged units, high thermal stability, low vapor pressure at standard temperatures, and classification as non-volatile. This characteristic made them seemingly safe as they didn't contribute to atmospheric evaporation, which is associated with issues like smog formation, ozone depletion, and climate change. Additionally, their low volatility compared to traditional solvents reduced the risk of inhalation exposure or potential explosions, given their higher flashpoints. Consequently, from this perspective, ionic liquids (ILs) were viewed as less harmful compounds.

However, it became apparent that despite their non-volatile nature and reduced risk of immediate harm, ILs could persist in the environment for extended periods due to their high stability, leading to poor biodegradability. The emergence of the new generation of ILs in the early 21st century aimed to combine desired biological properties with specific physicochemical attributes. This involved using cations known for low toxicity and beneficial activity, along with carefully chosen anions with specific properties to achieve the desired biological characteristics of the ILs.

1.1.3. Applications of Ionic liquids:

The exciting properties of ionic liquids paved the way for their applications in many science and technology fields, including gas separation, metal extraction, organic catalytic synthesis, electrolytes, solar cells, and many more.[25-31] All these applications of ILs are summarized in Figure 1.3. With the advent of third generation ILs, there is considerable current interest in their utilization in their storage and stability of biomolecules. It has also received increased interest in enzymatic reaction because of its environmentally friendly aspects.[32] ILs have played a vital role in drug delivery to improve its administration, reduce toxicity and achieve better absorption. These studies motivated us to carefully investigate the biomolecular interactions with ILs which further can be responsible for several exciting applications. However, before the detailed analysis of the biological applications of ILs, it is essential to have a brief idea of biomolecules.
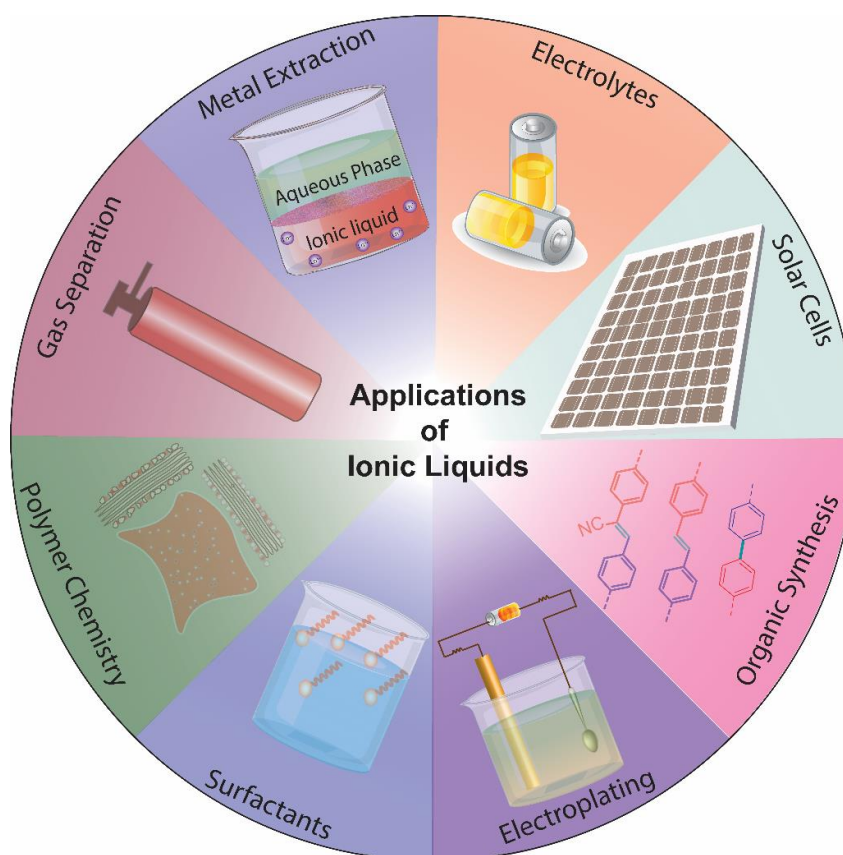
Figure 1.4. Graphical summary of applications of ILs

1.2. An introduction to biomolecules:

Biomolecules are molecules present in a cell that is responsible for the structural and functional activities of a cell. There are four major types of biomolecules: carbohydrates, lipids, nucleic acids, and proteins.[33-34] This thesis mainly focuses on nucleic acid and proteins.
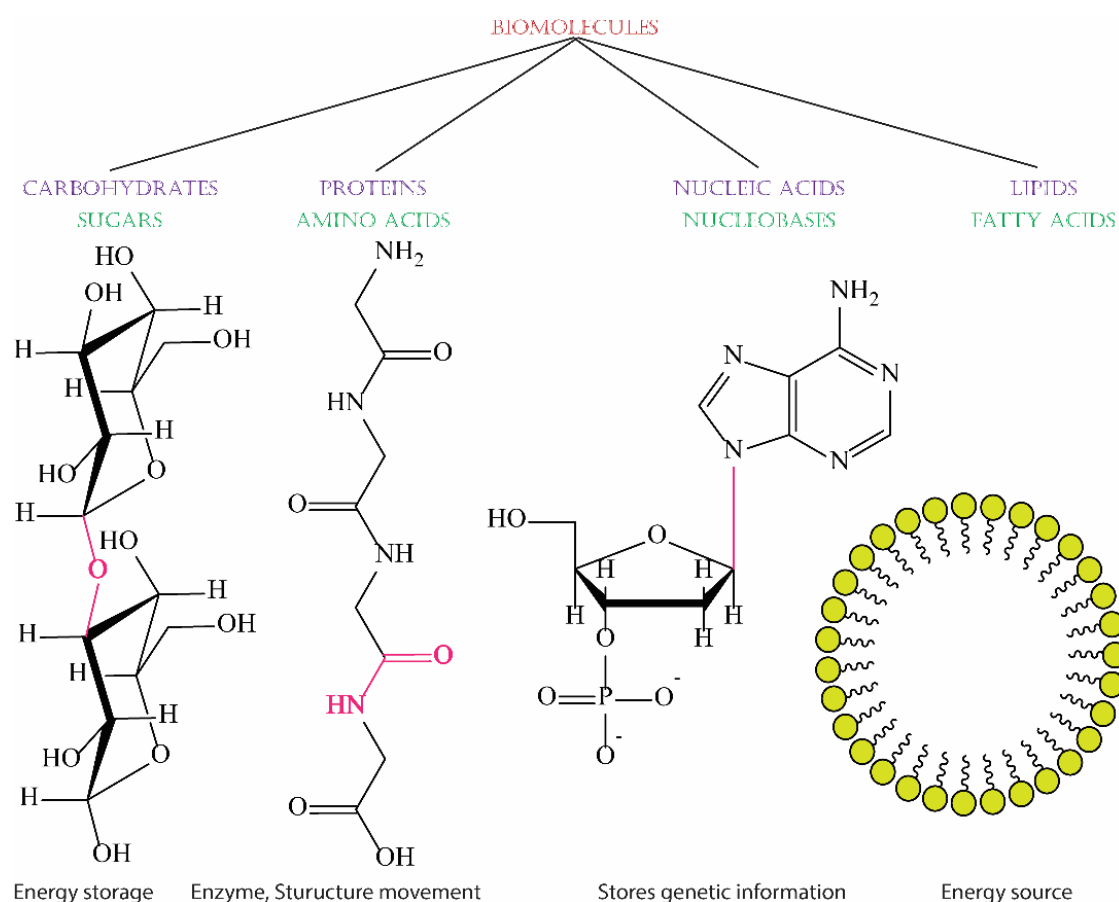
Figure 1.5. .Classifications of Biomolecules

1.2.1. Nucleic acids

Nucleic acids are large biomolecules that involve storing and expressing genomic information.[35-37] These are long polymeric chains of nucleotides. A nucleotide has three subunits: a nitrogenous base, pentose sugar, and phosphate. Five different nitrogenous bases are used in the construction of a nucleotide. Those are adenine, cytosine, guanine,

thymine, and uracil. Thymine is present in deoxyribonucleic acid (DNA), whereas uracil is in ribonucleic acid (RNA). DNA is of two types: single-stranded DNAs and double-stranded DNAs. Double-stranded DNA consists of two polynucleotide chains in which hydrogen bonds connect the nitrogenous bases. A-T and C-G are complementary base pairs. RNA is of two types: single-stranded RNAs and double-stranded RNAs. Single-strand RNAs are the most common. A-U and C-G are complementary base pairs. While DNA carries genetic information, RNA is responsible for synthesizing protein by translating that information. Denaturation is a process of separating double strands into single strands. It occurs at high temperatures or extreme pH when hydrogen bonds that hold the two strands together weaken and finally break.

1.2.1.1. Compaction and decompaction

DNA compaction is a process where the DNA molecule transforms from a coil to a compacted globule state accompanied by double helix bending.[38] The compaction of DNA in gene delivery plays a pivotal role for the success of gene therapy. DNA can go from the elongated coil to the compact state by following three pathways.

1. The initial form of compaction is an all-or-none compaction process, characterized by the absence of an intermediate state. Instead, there is a coexistence between the elongated coil and compact states. This phenomenon typically occurs when attraction is induced between DNA monomers throughout the chain, either by introducing small multivalent counter-ions or creating unfavorable contacts between DNA monomers and the solvent.[39]

2. The second type is a progressive transition from the elongated coil to the compact state. This usually occurs when there is a strong attraction between several

consecutive DNA monomers upon complexation with polycations longer than 10 monomers.[40]

3. The third potential pathway involves an assisted, hierarchical compaction facilitated by DNA adsorption and wrapping around nanoscale objects. This compaction mode is analogous to the process of DNA condensation into chromatin within eukaryotic cells. In vitro, this phenomenon is observed when DNA is compacted by cationic nanoparticles or dendrimers.[41]

Cationic species with $Z \geq 3$ are most used as compacting agents. Naturally occurring polyamines such as spermidine (3^+ at pH = 7) and spermine (4^+ at pH = 7), and the inorganic cation Co $(NH_3)_6^{3+}$ can also induce compaction in DNA.[42-43] For $Z > 10$, compaction agents can be considered long polycations, such as polyethyleneimine and polylysine.[44]
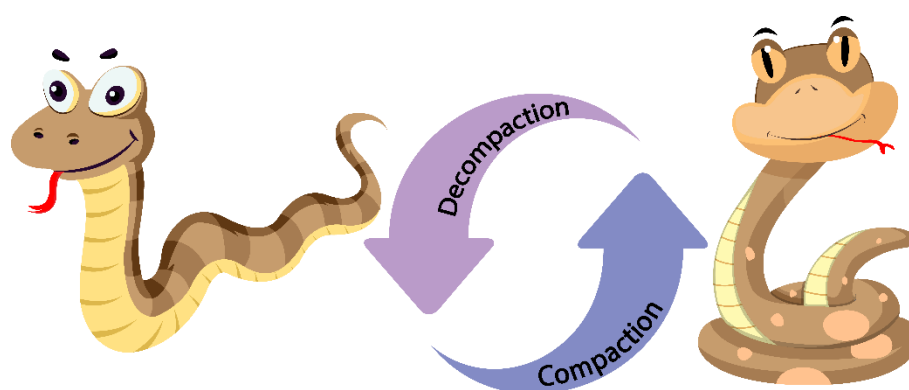
Figure 1.6. Cartoon diagram representing the process of compaction and decompaction in DNA

In contrast, DNA decompaction is the reverse process of compaction, i.e., DNA molecules are released from its single stranded from and regains its double stranded DNA form. In general, the decompaction of DNA molecules can be achieved by adding a new salts into the compacted DNA complex. Increasing mono- and divalent cation (Na^+, Mg^{2+})

concentration induces decompaction in the presence of multivalent cations such as spermine.[45-46]

1.2.2. Proteins

Proteins are the biological macromolecules in living organisms , made up of polypeptide chains of amino acid residues. Proteins gained significant importance in biological processes regarding stability, kinetics, and activity.[47] These processes are mainly influenced by various chemical and physical properties such as co-solvent, additives, environmental conditions etc. Proteins are the major structural fragments of the blood cells, enzymes, ligaments, and others which help in body growth and development. Moreover, they also exist in plants to provide structure and biological activity. Proteins are polypeptide chains of amino acids that can form a unique three-dimensional structure known to be their folded or native state.[48]

1.2.2.1. Classification of protein structures

Proteins adopt a stable three-dimensional conformation based on their amino acid sequence. The entire structure of a protein can be delineated at four distinct levels of complexity: primary, secondary, tertiary, and quaternary structure. Protein structures are generally determined by X-ray crystallography and by nuclear magnetic resonance (NMR). Several groups have attempted to classify protein structures into complexities of the folds without focusing on function. The structure of a protein can be classified into four different types based on the complexity of the folds and sequence of amino acids: primary, secondary, tertiary, and quaternary structure.

1.2.2.1.1. Primary structure

There are 20 different standard L-α-amino acids used by cells for protein construction. Peptide bonds are formed between the -NH$_2$ of one amino acid and the -COOH of another. A protein is made up of one or more polypeptide molecules.[49] The end of the peptide or protein sequence with a free carboxyl group is called the carboxy-terminus or C-terminus. In contrast, the end of the sequence with a free α-amino group is called the amino terminus and N-terminus. The amino acid sequence makes the protein's primary structure, and the chemical and biological properties depend on its three-dimensional or tertiary structure.

1.2.2.1.2. Secondary structure

Depending on the H-bonding, the sequence of peptides or proteins has distinct, characteristic local structural conformations or secondary structures. The two main types of secondary structures are the *α*-helix and the *ß*-sheet.[50]

The α-helix adopts a right-handed coiled structure, with the side-chain substituents of amino acid groups extending outward. Hydrogen bonds form within the α-helix between the oxygen of each C=O bond and the hydrogen of each N-H group. These hydrogen bonds contribute significantly to the α-helix's remarkable stability, with the side-chain substituents fitting in alongside the N-H groups.

In contrast, in a ß-sheet, the hydrogen bonding pattern occurs between strands (inter-strand). The ß-sheet configuration comprises pairs of strands lying side-by-side, where the amino hydrogens in one strand form bonds with the carbonyl oxygens of the adjacent strand. The two strands can be arranged either in a parallel or anti-parallel orientation, depending on whether the strand directions (N-terminus to C-terminus) are the same or

opposite. The anti-parallel ß-sheet is considered more stable due to the improved alignment of hydrogen bonds.

1.2.2.1.3. Tertiary structure

The tertiary structure of a protein refers to its overall three-dimensional shape, where the molecule undergoes bending and twisting to attain maximum stability or the lowest energy state. This stability is achieved through bonding interactions among the side-chain groups of amino acids. An essential aspect of stabilizing the tertiary structure involves the formation of disulfide bridges through the oxidation of sulfhydryl groups on cysteine. Additionally, hydrogen bonds may develop between different side-chain groups. In physiological conditions, the hydrophobic side chains of neutral, non-polar amino acids, such as phenylalanine or isoleucine, are typically sequestered within the interior of the protein molecule, protecting them from the surrounding aqueous environment.

1.2.2.1.4. Quaternary structure

Certain proteins consist of multiple polypeptide chains, which are referred to as protein subunits. These subunits can be identical, forming a homodimer, or diverse, resulting in a heterodimer. The quaternary structure pertains to the arrangement and interaction of these protein subunits, forming a larger complex protein aggregate. Various interactions, including hydrogen bonding, disulfide bridges, and salt bridges, stabilize the protein complex's final shape.

Heme proteins constitute a distinct class of intensely colored proteins, primarily owing to the presence of the heme moiety. The heme moiety comprises a substituted porphyrin ring containing a chelated iron atom. The chelated iron, whether in a ferrous or ferric state, tends to preferentially adopt six-coordinated structures. Within heme proteins, four of these ligands are associated with the nitrogen atoms of the four pyrroles in the

protoporphyrin ring. The fifth ligand, commonly referred to as the proximal ligand, is established by an amino acid residue within the protein. In oxygen-carrying proteins like myoglobin and hemoglobin, this is typically a histidine residue, with the bond to the oxygen molecule serving as the sixth or distal ligand. In electron-carrying cytochromes, both the fifth and sixth ligands are occupied by amino acid residues.

1.2.2.2. Protein folding and unfolding

Proteins rely on various molecular interactions for their structural integrity, encompassing factors such as thermodynamic stability, hydrophobic interactions, and the formation of disulfide bonds. Thermodynamic equilibrium influences the propensity for extended conformations, while residue-dependent long-range contact potentials and orientation-dependent hydrogen bonds contribute to the stability of the complex.[51] Short-range interactions govern the secondary structure through hydrophobic interactions, and long-range interactions impact the tertiary structure. Disulfide bonds, formed through an oxidative process between nonadjacent cysteines, further contribute to the molecular architecture of proteins.[52] The native state of a protein refers to its most stable, naturally occurring conformation in its native environment. However, the interactions defining the native state are inherently weak. Various external stressors, such as temperature fluctuations, pH changes, dehydration, exposure to hydrophobic surfaces, presence of metal ions, and high shear forces, can disrupt these interactions. This disruption, leading to the loss of secondary, tertiary, or quaternary structure, is termed denaturation.[53] Denaturation results in the unfolding of the protein, adopting a random or misfolded conformation.

In addition, there is an intermediate state between the folded and unfolded state of the protein. This state is known as the molten globule state. This state is described as a

intermediate in which the tertiary structural features of the protein is lost, however the secondary structural features remains intact.[54] This state can be considered like the partially folded state and is an intermediate state during the unfolding of a protein. It provides vital information about protein folding and unfolding.

1.2.2.3. Protein structure analysis

The complexities of protein structure make elucidating a complete protein structure difficult, even with the most advanced analytical equipment.[55] An amino acid analyzer is utilized to identify the presence of amino acids and determine their molar ratios. Subsequently, the protein's sequence can be examined through peptide mapping, employing techniques like Edman degradation or mass spectrometry. Mass spectrometry has become a crucial tool for analyzing enzyme-digested proteins, employing peptide fingerprinting methods and database searches. Edman degradation involves the stepwise cleavage, separation, and identification of individual amino acids from a short peptide, commencing from the N-terminus. Circular dichroism spectroscopy (CD) is a method employed to characterize the secondary structure of a protein. In the far-UV region of the spectrum, different secondary structures such as α-helix, ß-sheet, and random coil exhibit characteristic circular dichroism spectra. Tertiary structure manifests distinctive circular dichroism spectra in the near-UV region. Heme proteins feature a distinct Soret band in the Soret region of the spectrum (350-450 nm). For a more comprehensive and high-resolution analysis of a protein's three-dimensional structure, techniques like X-ray crystallography or nuclear magnetic resonance (NMR) analysis are employed.

1.3. A bridge between ionic liquids and proteins:

The past few decades have witnessed an upsurge of ILs pursuing "green" solvents. This has led to the development of three generations of ILs. The first generation focuses on

their intrinsic physicochemical properties. The second generation of ILs tailored some of these physicochemical properties, allowing its applications in lubricants, energetic materials, and "greener" reaction solvents. The primary reason behind the limited use of ILs in medical applications ows to the toxicity, biodegradability, and biocompatibility of these compounds. The third generation of ILs involves active pharmaceutical ingredients, which produce ILs with biological activity. The third-generation ILs mainly focus on overcoming the threat they pose to the environment by lowering their toxicity. With the advent of third generation ILs, a dramatic increase in their usage in pharmaceutical applications is observed.[56-59] Over the past decade, numerous studies in both chemical and physical domains have delved into comprehending the atomic-level mechanisms governing the interaction between ionic liquids and biomolecules.[60] A wide array of biological systems and ionic liquids has been explored, revealing that specific ionic liquids can (1) permeate biomembranes and induce disruption at elevated concentrations;[61-62]; (2) Stabilize proteins and enzymes, thereby preserving their biochemical functions.[63-65]; (3) Influence the aggregation of proteins in amyloids, either supporting or impeding the process.[66-67]; (4) Facilitate the extraction, purification, and preservation of DNA.[68-73]; and (5) Exhibit antibacterial and anticancer properties, selectively targeting bacteria and cancer cells while having minimal impact on healthy eukaryotic cells.[74-80]. Figure 1.6 summarizes the potential of ILs for their applications in biochemistry, biomedicine, and drug delivery.

Their relevance in various biological processes is due to their ability to interact through multiple forces such as H-bonding, electrostatic, and sometimes dispersion.[81-83] Table 1.1 lists the interactions between ionic liquids and protein and DNA molecules.
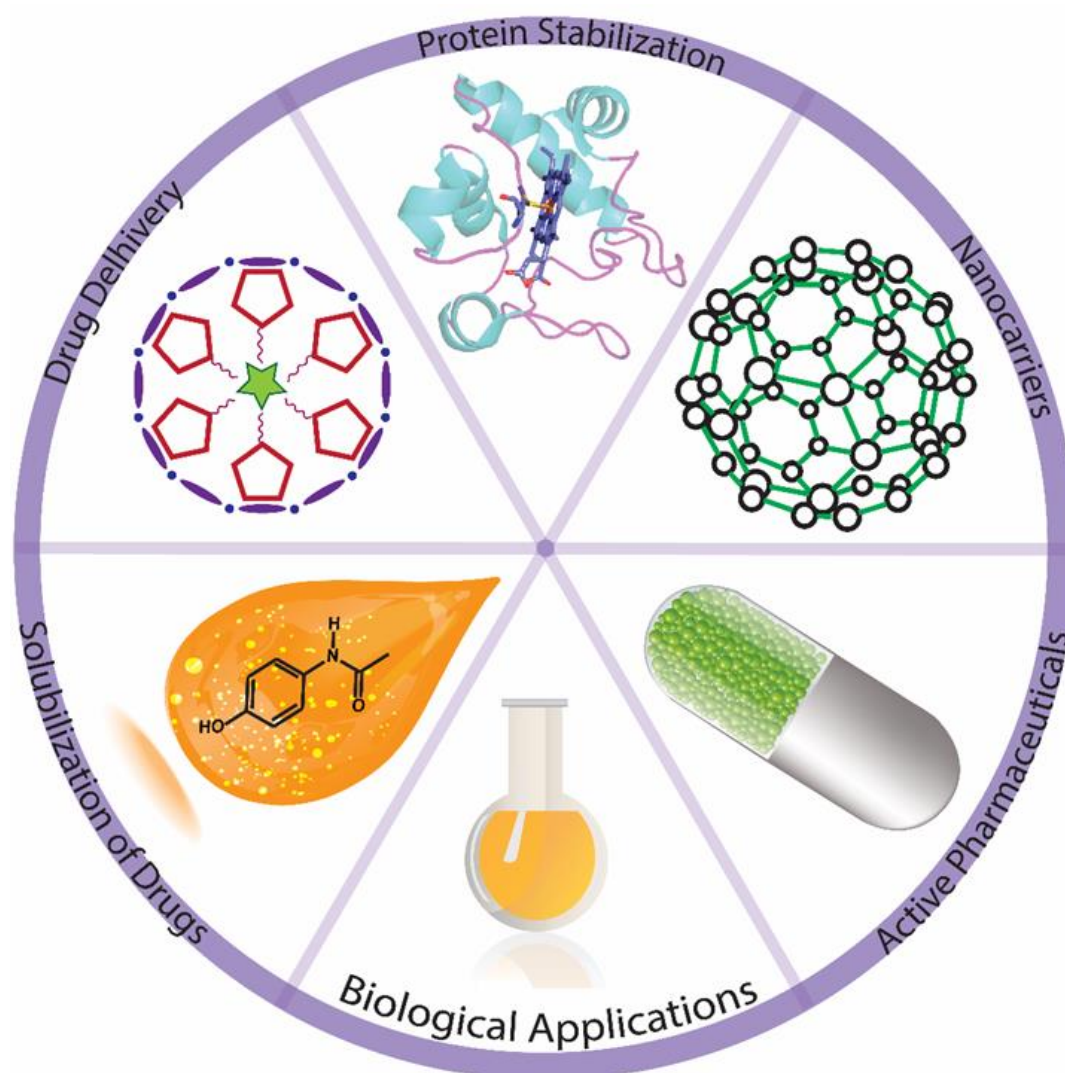
Figure 1.7. Potential Applications of ILs in Biochemistry

Rabideau and co-workers found a "patchwork" of cations and anions would form around the cellulose strand due to Hydroge bonding and other noncovalent interactions, during the dissolution of the cellulose in the IL, and an increasing chain length on the cations decreases in binding capability.[84] Further, drug dissolution in ILs involves forming hydrogen bonds between the IL anions and the drug molecules. Some excellent review articles are available on the use of ionic liquids in stabilizing and functioning proteins and DNA. The review article by Schindl et al. thoroughly discusses the use of various ionic liquids in the dissolution and processing of various types of biomolecules.[85]

Table 1.1. Interactions between ionic liquids and biomolecules

Type of interactions	Responsible group/moiety on ionic liquids
Hydrophobic interactions	Hydrophobic core of protein/DNA and alkyl chain on cation
Disulphide (S-S) interactions	Anion counterpart of IL and protein linkage
Hydrogen bonding interactions	Anion counterpart and electron component on biomolecules and nucleotide bases in nucleic acids
Electrostatic interactions	Cations with P=O bonds on DNA strands and anions with negatively charged surfaces on protein

Biocompatibility has been achieved for several ILs in recent decades by playing with their cationic and anionic counterparts. Moreover, the mechanisms of the Hofmeister anion series of choline-based and magnetic ILs' special effects on various biomolecules have been extensively studied. Bhattacharyya and co-workers focused on the atomic-level molecular interactions between ionic liquids and proteins.[86] They nicely highlighted how combining experimental techniques with computer simulation approaches is essential for the molecular-level study of the interactions. Various studies have been carried out by many research groups on proteins since a complete understanding of the protein folding will undoubtedly result in obvious biological and medical applications.

In recent years, cholinium-based ionic liquids (ILs) have gained significant importance due to their environmentally friendly properties, making them the preferred choice for studying protein stability. These cholinium-based ILs have demonstrated unmatched biocompatibility as stabilizers for proteins in various studies. For example, choline

chloride, an ionic liquid (IL) based on cholinium, has shown significant efficacy in influencing the stability and activity of enzymes such as horseradish peroxidase and bovine pancreatic trypsin inhibitor. In a study conducted by Bisht and Venkatesu, different cholinium ILs were investigated for their impact on the conformational and thermal stability of α-chymotrypsin, with choline acetate exhibiting the most substantial stabilizing effect. Notably, a series of cholinium-based ILs, were found to enhance the structural stability of α-chymotrypsin against thermal denaturation.

In these IL media, the transition temperature (Tm) of α-chymotrypsin increased from around 48.9 °C (in buffer) to 58 °C, showcasing the stabilizing influence of these ILs. Moreover, the enzymatic activity of α-chymotrypsin was preserved when using [Ch][Ac], [Ch][Cl], and [Ch][Dhp], indicating the suitability of these ILs as high-temperature bio-catalytic reactors. Choline-based ionic liquids, especially [Ch][Dhp], have demonstrated remarkable properties in stabilizing biomolecules, including proteins like lysozyme, DNA, and nuclease inhibitor. Among the choline-based ILs investigated, [Ch][Dhp] has emerged as the most effective medium for enhancing protein stability. It has been shown to be an exceptional stabilizing agent for various proteins, including lysozyme and cytochrome c, preserving their secondary structures even at elevated temperatures. Moreover, [Ch][Dhp] has been found to have lower cytotoxicity compared to other choline ILs and is considered a biocompatible medium for strong protein stabilization. It has been utilized in long-term storage and packaging of proteins, making it a promising candidate for various biotechnological applications. In drug solubility studies, choline-based ILs have proven advantageous over imidazole-based ILs. They exhibit higher impact on drug solubility and lower cytotoxicity in human keratinocytes (HaCat cells). As a result, choline-based ILs are more suitable as functional ingredients in topical formulations, as they can enhance drug solubility and facilitate the incorporation of higher

concentrations of active drugs, making them potentially valuable in pharmaceutical applications. Choline cation itself is a naturally occurring feedstock and is considered non-toxic. The cytotoxicity of cholinium-based ILs mainly depends on the anion they are paired with, and [Cho][Dhp] stands out with the lowest cytotoxicity among the tested choline ILs. This further supports the potential of cholinium-based ILs as biocompatible media for protein stabilization. Overall, ionic liquids show great promise in fulfilling the demands for stabilizing active peptides and protein drugs in various applications. Choline-based ILs, in particular, have proven effective in enhancing protein stability and can be designed in various combinations of cations and anions, making them potential green and sustainable solvents for diverse peptides and proteins in the future. Considering the significant progress and potential in the field of ionic liquids, they hold a promising future as a versatile platform for various biotechnological and pharmaceutical applications, offering greener and more sustainable alternatives for the stabilization of biomolecules.

Therefore, we have taken this opportunity to unravel the effect of the structure and stability of proteins in choline-based and magnetic ILs by combining experimental techniques with computer simulation approaches.

1.4. Aim and objectives of the thesis.

The present research aims to explore the role of biocompatible ILs on protein folding/unfolding studies and to enhance the structure, stability, and activity of biomolecules in the presence of different (cations and anions) biocompatible ILs. In addition,

1. To identify the anion effect of biocompatible ILs on protein structure

2. To see the concentration effect of biocompatible ILs on protein stability and

3. Identification of suitable co-solvent for a particular protein

The objectives below will be achieved in the following steps:

1. To explore protein folding/unfolding in the presence of different ILs.

2. To understand the molecular interactions between the ammonium group of ILs and biomolecules.

3. Various thermodynamic parameters are involved in the interactions between ILs and biomolecules.

4. To investigate the enhancement in the peroxidase activity of cytochrome c in the presence of ILs.

1.5. Structure of the thesis

During our research with ionic liquids due to their exciting applications, we sought a deeper understanding of their behaviors, structures, and how these arise.

The thesis is divided mainly into two parts:

1. The study of stability of protein and nucleic acids in choline amino acid-based ILs.

2. The study of protein folding and enhancement of activity in the presence of choline-based magnetic ILs

Chapter 1 introduces ionic liquids and proteins. It also explains the benefits and properties of ionic liquids. It provides a brief literature review of the revolutionized research on broad biological applications of ionic liquids.

Chapter 2 elaborates on detailed descriptions of the adopted computational methodology and experimental techniques to achieve the objectives. Steady-state absorption, fluorescence, time-correlated single photon counting, circular dichroism, and

fluorescence correlation spectroscopy techniques were used to study the binding interactions. Isothermal titration calorimetry was used to calculate the thermodynamic parameters between ionic liquids and biomolecules. Molecular docking and molecular dynamics provide insight into the atomic-level interactions among them.

Chapter 3 discusses the stability and extraction of RNA in choline amino acid-based ionic liquids.

Chapter 4 reports the unfolding of hemoglobin in choline amino acid-based ionic liquids.

Chapter 5 proposes the role of magnetic ionic liquids in the compaction and decompaction of calf thymus DNA.

Chapter 6 deals with enhancing the peroxidase activity of cytochrome c in an environment of magnetic ionic liquid.

Chapter 7 comprises concluding remarks and future prospective on this work.

1.6. REFERENCES

1.   Introduction: Ionic Liquids. *Chem. Rev.* **2017,** *117* (10), 6633-6635.

2.   Eyckens, D. J.; Henderson, L. C., A Review of Solvate Ionic Liquids: Physical Parameters and Synthetic Applications. *Front. Chem.* **2019,** *7*.

3.   Vekariya, R. L., A review of ionic liquids: Applications towards catalytic organic transformations. *J. Mol. Liq.* **2017,** *227*, 44-60.

4.   Walden, P. T., Molecular weights and electrical conductivity of several fused salts. *Bull. Acad. Imper. Sci.(St. Petersburg)* **1914**, 1800.

5.   Hurley, F. H.; Wier, T. P., Electrodeposition of Metals from Fused Quaternary Ammonium Salts. *J. Electrochem. Soc.* **1951,** *98* (5), 203.

6.   Robinson, J.; Osteryoung, R. A., An electrochemical and spectroscopic study of some aromatic hydrocarbons in the room temperature molten salt system aluminum chloride-n-butylpyridinium chloride. *J. Am. Chem. Soc.* **1979,** *101* (2), 323-327.

7.   Bühring, K. U.; Garbe, A., Determination of the new beta-blocker bisoprolol and of metoprolol, atenolol and propranolol in plasma and urine by high-performance liquid chromatography. *J. Chromatogr.* **1986,** *382*, 215-24.

8.   Pacholec, F.; Butler, H. T.; Poole, C. F., Molten organic salt phase for gas-liquid chromatography. *Anal. Chem.* **1982,** *54* (12), 1938-1941.

9.   Evans, D. F.; Chen, S.-H.; Schriver, G. W.; Arnett, E. M., Thermodynamics of solution of nonpolar gases in a fused salt. Hydrophobic bonding behavior in a nonaqueous system. *J. Am. Chem. Soc.* **1981,** *103* (2), 481-482.

10.   Wilkes, J. S.; Levisky, J. A.; Wilson, R. A.; Hussey, C. L., Dialkylimidazolium chloroaluminate melts: a new class of room-temperature ionic liquids for electrochemistry, spectroscopy and synthesis. *Inorg. Chem.* **1982,** *21* (3), 1263-1264.

11.   Wilkes, J. S.; Zaworotko, M. J., Air and water stable 1-ethyl-3-methylimidazolium based ionic liquids. *J. Chem. Soc., Chem. Commun.* **1992,** (13), 965-967.

12.   Welton, T., Ionic liquids: a brief history. *Biophys Rev.* **2018,** *10* (3), 691-706.

13.   H. Davis, J., James Task-specific ionic liquids. *Chem. Lett.* **2004,** *33* (9), 1072-1077.

14.   Kilpeläinen, I.; Xie, H.; King, A.; Granstrom, M.; Heikkinen, S.; Argyropoulos, D. S., Dissolution of wood in ionic liquids. *J. Agric. Food Chem.* **2007,** *55* (22), 9142-9148.

15.   Ratti, R., Ionic Liquids: Synthesis and Applications in Catalysis. *Advances in Chemistry* **2014,** *2014*, 729842.

16.   Greaves, T. L.; Drummond, C. J., Protic ionic liquids: properties and applications. *Chem. Rev.* **2008,** *108* (1), 206-237.

17.   M. S. S. Esperança, J.; Canongia Lopes, J. N.; Tariq, M.; Santos, L. M. N. B. F.; Magee, J. W.; Rebelo, L. P. N., Volatility of Aprotic Ionic Liquids — A Review. *J. Chem. Eng. Data* **2010,** *55* (1), 3-12.

18.   Tsuzuki, S.; Shinoda, W.; Miran, M. S.; Kinoshita, H.; Yasuda, T.; Watanabe, M., Interactions in ion pairs of protic ionic liquids: Comparison with aprotic ionic liquids. *J. Chem. Phys.* **2013,** *139* (17), 174504.

19.   Herrmann, S., Introduction. In *New Synthetic Routes to Polyoxometalate Containing Ionic Liquids: An Investigation of their Properties*, Herrmann, S., Ed. Springer Fachmedien Wiesbaden: Wiesbaden, 2015; pp 1-17.

20.   Zhang, S.; Sun, N.; He, X.; Lu, X.; Zhang, X., Physical Properties of Ionic Liquids: Database and Evaluation. *J Phys Chem Ref Data* **2006,** *35* (4), 1475-1517.

21.   Yu, Y.; Chen, Y., Density Prediction of Ionic Liquids at Different Temperatures Using the Average Free Volume Model. *ACS Omega* **2021,** *6* (23), 14869-14874.

22.   D. Holbrey, J.; R. Seddon, K., The phase behaviour of 1-alkyl-3-methylimidazolium tetrafluoroborates; ionic liquids and ionic liquid crystals. *J. Chem. Soc., Dalton Trans.* **1999,** (13), 2133-2140.

23.   Bonhôte, P.; Dias, A.-P.; Papageorgiou, N.; Kalyanasundaram, K.; Grätzel, M., Hydrophobic, Highly Conductive Ambient-Temperature Molten Salts. *Inorg. Chem.* **1996,** *35* (5), 1168-1178.

24.   Katritzky, A. R.; Jain, R.; Lomaka, A.; Petrukhin, R.; Karelson, M.; Visser, A. E.; Rogers, R. D., Correlation of the melting points of potential ionic liquids (imidazolium bromides and benzimidazolium bromides) using the CODESSA program. *J. Chem. Inf. Comput. Sci.* **2002,** *42* (2), 225-231.

25.   Patel, D. D.; Lee, J. M., Applications of ionic liquids. *Chem. Rec.* **2012,** *12* (3), 329-355.

26.   Plechkova, N. V.; Seddon, K. R., Applications of ionic liquids in the chemical industry. *Chem Soc Rev.* **2008,** *37* (1), 123-150.

27.   MacFarlane, D. R.; Tachikawa, N.; Forsyth, M.; Pringle, J. M.; Howlett, P. C.; Elliott, G. D.; Davis, J. H.; Watanabe, M.; Simon, P.; Angell, C. A., Energy applications of ionic liquids. *Energy Environ. Sci.* **2014,** *7* (1), 232-250.

28.   Lu, J.; Yan, F.; Texter, J., Advanced applications of ionic liquids in polymer science. *Prog. Polym. Sci.* **2009,** *34* (5), 431-448.

29.   Wei, D.; Ivaska, A., Applications of ionic liquids in electrochemical sensors. *Analytica Chimica Acta.* **2008,** *607* (2), 126-135.

30.   Kubota, F.; Goto, M., Application of ionic liquids to solvent extraction. *Solvent Extr. Res. Dev.* **2006,** *13*, 23-36.

31.   Zia ul Mustafa, M.; bin Mukhtar, H.; Md Nordin, N. A. H.; Mannan, H. A.; Nasir, R.; Fazil, N., Recent developments and applications of ionic liquids in gas separation membranes. *Chem Eng Technol.* **2019,** *42* (12), 2580-2593.

32.   Shukla, S. K.; Mikkola, J.-P., Use of Ionic Liquids in Protein and DNA Chemistry. *Front. Chem.* **2020,** *8*.

33.   Bukusoglu, E.; Koku, H.; Çulfaz-Emecen, P. Z., Addressing challenges in the ultrafiltration of biomolecules from complex aqueous environments. *Curr Opin Colloid Interface* **2020,** *46*, 52-64.

34.   Datta, L. P.; Manchineella, S.; Govindaraju, T., Biomolecules-derived biomaterials. *Biomaterials* **2020,** *230*, 119633.

35.   Chargaff, E., *The nucleic acids*. Elsevier: 2012.

36.   Adams, R. L., *The biochemistry of the nucleic acids*. Springer Science & Business Media: 2012.

37.   Levene, P. A.; Bass, L. W., *Nucleic acids*. Chemical Catalog Company New York: 1931.

38.   Estévez-Torres, A.; Baigl, D., DNA compaction: fundamentals and applications. *Soft Matter* **2011,** *7* (15), 6746-6756.

39.   Takahashi, M.; Yoshikawa, K.; Vasilevskaya, V.; Khokhlov, A., Discrete coil−globule transition of single duplex DNAs induced by polyamines. *J. Phys. Chem. B* **1997,** *101* (45), 9396-9401.

40.   Yoshikawa, K.; Takahashi, M.; Vasilevskaya, V. V.; Khokhlov, A. R., Large Discrete Transition in a Single DNA Molecule Appears Continuous in the Ensemble. *Phys. Rev. Lett.* **1996,** *76* (16), 3029-3031.

41.   Akitaya, T.; Seno, A.; Nakai, T.; Hazemoto, N.; Murata, S.; Yoshikawa, K., Weak interaction induces an ON/OFF switch, whereas strong interaction causes gradual change: Folding transition of a long duplex DNA chain by poly-L-lysine. *Biomacromolecules* **2007,** *8* (1), 273-278.

42.   Widom, J.; Baldwin, R. L., Cation-induced toroidal condensation of DNA studies with Co3+(NH3)6. *J Mol Biol.* **1980,** *144* (4), 431-53.

43.   Widom, J.; Baldwin, R. L., Monomolecular condensation of λ-DNA induced by cobalt hexammine. *Biopolymers* **1983,** *22* (6), 1595-1620.

44.   Laemmli, U. K.; Paulson, J. R.; Hitchins, V., Maturation of the head of bacteriophage T4. V. A possible DNA packaging mechanism: in vitro cleavage of the head proteins and the structure of the core of the polyhead. *J Supramol Struct.* **1974,** *2* (2-4), 276-301.

45.   Lerman, L. S., A transition to a compact form of DNA in polymer solutions. *Proceedings of the National Academy of Sciences of the United States of America* **1971,** *68* (8), 1886-90.

46.   Vasilevskaya, V. V.; Khokhlov, A. R.; Matsuzawa, Y.; Yoshikawa, K., Collapse of single DNA molecule in poly(ethylene glycol) solutions. *J. Chem. Phys.* **1995,** *102* (16), 6595-6602.

47.   Zhao, X.; Zhang, R.; Liu, Y.; He, M.; Su, Y.; Gao, C.; Jiang, Z., Antifouling membrane surface construction: Chemistry plays a critical role. *J. Membr. Sci.* **2018,** *551*, 145-171.

48.   Hadidi, M.; Zydney, A. L., Fouling behavior of zwitterionic membranes: Impact of electrostatic and hydrophobic interactions. *J. Membr. Sci.* **2014,** *452*, 97-103.

49.   Sun, P. D.; Foster, C. E.; Boyington, J. C., Overview of protein structural and functional folds. *Current protocols in protein science* **2004,** *Chapter 17* (1), Unit 17.1.

50.   Konno, S.; Namiki, T.; Ishimori, K., Quantitative description and classification of protein structures by a novel robust amino acid network: interaction selective network (ISN). *Sci Rep.* **2019** *9*,16654.

51.   Lapidus, L. J., Protein unfolding mechanisms and their effects on folding experiments. *F1000Research* **2017,** *6*, 1723.

52.   Jamin, M.; Baldwin, R. L., Refolding and unfolding kinetics of the equilibrium folding intermediate of apomyoglobin. *Nat Struct Mol Biol.* **1996,** *3* (7), 613-618.

53.   Fersht, A. R.; Daggett, V., Protein Folding and Unfolding at Atomic Resolution. *Cell* **2002,** *108* (4), 573-582.

54.   Judy, E.; Kishore, N., A look back at the molten globule state of proteins: thermodynamic aspects. *Biophys Rev* **2019,** *11* (3), 365-375.

55.   Kuhlman, B.; Bradley, P., Advances in protein structure prediction and design. *Nature reviews. Molecular cell biology* **2019,** *20* (11), 681-697.

56.   Faisal, M.; Saeed, A., 6 - The role of ionic liquid in medicinal chemistry. In *Green Approaches in Medicinal Chemistry for Sustainable Drug Design*, Banik, B. K., Ed. Elsevier: 2020; pp 143-180.

57.   Shukla, M. K.; Tiwari, H.; Verma, R.; Dong, W.-L.; Azizov, S.; Kumar, B.; Pandey, S.; Kumar, D., Role and Recent Advancements of Ionic Liquids in Drug Delivery Systems. *Pharmaceutics* **2023,** *15* (2), 702.

58.   Curreri, A. M.; Mitragotri, S.; Tanner, E. E. L., Recent Advances in Ionic Liquids in Biomedicine. *Adv. Sci.* **2021,** *8* (17), 2004819.

59.   Shamshina, J. L.; Kelley, S. P.; Gurau, G.; Rogers, R. D., Chemistry: Develop ionic liquid drugs. *Nature* **2015,** *528* (7581), 188-189.

60.   Benedetto, A.; Ballone, P., Room Temperature Ionic Liquids Meet Biomolecules: A Microscopic View of Structure and Dynamics. *ACS Sustainable Chem. Eng.* **2016,** *4* (2), 392-412.

61.   Yoo, B.; Shah, J. K.; Zhu, Y.; Maginn, E. J., Amphiphilic interactions of ionic liquids with lipid biomembranes: a molecular simulation study. *Soft Matter* **2014,** *10* (43), 8641-8651.

62.   Berkowitz, M. L.; Vácha, R. J. A. o. c. r., Aqueous solutions at the interface with phospholipid bilayers. *Acc. Chem. Res.* **2012,** *45* (1), 74-82.

63.   Bui-Le, L.; Clarke, C. J.; Bröhl, A.; Brogan, A. P. S.; Arpino, J. A. J.; Polizzi, K. M.; Hallett, J. P., Revealing the complexity of ionic liquid–protein interactions through a multi-technique investigation. *Commun Chem.* **2020,** *3* (1), 55.

64.   Nordwald, E. M.; Kaar, J. L. J. T. J. o. P. C. B., Mediating electrostatic binding of 1-butyl-3-methylimidazolium chloride to enzyme surfaces improves conformational stability. *J. Phys. Chem. B* **2013,** *117* (30), 8977-8986.

65.   Janati-Fard, F.; Housaindokht, M. R.; Monhemi, H.; Esmaeili, A. A.; Pour, A. N. J. I. j. o. b. m., The influence of two imidazolium-based ionic liquids on the structure and

activity of glucose oxidase: experimental and theoretical studies. *Int. J. Biol. Macromol.* **2018,** *114*, 656-665.

66.	Pillai, V. V. S.; Benedetto, A., Ionic liquids in protein amyloidogenesis: a brief screenshot of the state-of-the-art. *Biophys Rev* **2018,** *10* (3), 847-852.

67.	Takekiyo, T.; Yoshimura, Y., Suppression and dissolution of amyloid aggregates using ionic liquids. *Biophys Rev* **2018,** *10* (3), 853-860.

68.	Dinis, T. B. V.; Sousa, F.; Freire, M. G., Insights on the DNA Stability in Aqueous Solutions of Ionic Liquids. *Front. Bioeng. Biotechnol.* **2020,** *8*.

69.	Clark, K. D.; Nacham, O.; Yu, H.; Li, T.; Yamsek, M. M.; Ronning, D. R.; Anderson, J. L., Extraction of DNA by Magnetic Ionic Liquids: Tunable Solvents for Rapid and Selective DNA Analysis. *Anal. Chem.* **2015,** *87* (3), 1552-1559.

70.	Egorova, K. S.; Posvyatenko, A. V.; Larin, S. S.; Ananikov, Valentine P., Ionic liquids: prospects for nucleic acid handling and delivery. *Nucleic Acids Research* **2021,** *49* (3), 1201-1234.

71.	Jumbri, K.; Abdul Rahman, M. B.; Abdulmalek, E.; Ahmad, H.; Micaelo, N. M., An insight into structure and stability of DNA in ionic liquids from molecular dynamics simulation and experimental studies. *Phys. Chem. Chem. Phys.* **2014,** *16* (27), 14036-14046.

72.	Sarkar, S.; Rajdev, P.; Singh, P. C., Hydrogen bonding of ionic liquids in the groove region of DNA controls the extent of its stabilization: synthesis, spectroscopic and simulation studies. *Phys. Chem. Chem. Phys.* **2020,** *22* (27), 15582-15591.

73.	Haque, A.; Khan, I.; Hassan, S. I.; Khan, M. S., Interaction studies of cholinium-based ionic liquids with calf thymus DNA: Spectrophotometric and computational methods. *J. Mol. Liq.* **2017,** *237*, 201-207.

74.	Taokaew, S.; Kriangkrai, W., Recent Progress in Processing Cellulose Using Ionic Liquids as Solvents. *Polysaccharides* **2022,** *3* (4), 671-691.

75.	Isik, M.; Sardon, H.; Mecerreyes, D., Ionic liquids and cellulose: dissolution, chemical modification and preparation of new cellulosic materials. *International journal of molecular sciences* **2014,** *15* (7), 11922-40.

76.	Bodachivskyi, I.; Page, C. J.; Kuzhiumparambil, U.; Hinkley, S. F. R.; Sims, I. M.; Williams, D. B. G., Dissolution of Cellulose: Are Ionic Liquids Innocent or Noninnocent Solvents? *ACS Sustainable Chem. Eng.* **2020,** *8* (27), 10142-10150.

77.   Nasrollahzadeh, M.; Ghasemzadeh, M.; Gharoubi, H.; Nezafat, Z., Progresses in polysaccharide and lignin-based ionic liquids: Catalytic applications and environmental remediation. *J. Mol. Liq.* **2021,** *342*, 117559.

78.   Li, Y.; Wang, J.; Liu, X.; Zhang, S., Towards a molecular understanding of cellulose dissolution in ionic liquids: anion/cation effect, synergistic mechanism and physicochemical aspects. *Chem. Sci.* **2018,** *9* (17), 4027-4043.

79.   Shi, Y.; Zhao, Z.; Peng, K.; Gao, Y.; Wu, D.; Kim, J.; Mitragotri, S., Enhancement of Anticancer Efficacy and Tumor Penetration of Sorafenib by Ionic Liquids. *Adv. Healthcare Mater.* **2021,** *10* (2), 2001455.

80.   Chowdhury, M. R.; Moshikur, R. M.; Wakabayashi, R.; Tahara, Y.; Kamiya, N.; Moniruzzaman, M.; Goto, M., Ionic-Liquid-Based Paclitaxel Preparation: A New Potential Formulation for Cancer Treatment. *Mol. Pharmaceutics* **2018,** *15* (6), 2484-2488.

81.   Monti, D.; Egiziano, E.; Burgalassi, S.; Chetoni, P.; Chiappe, C.; Sanzone, A.; Tampucci, S., Ionic liquids as potential enhancers for transdermal drug delivery. *International journal of pharmaceutics* **2017,** *516* (1-2), 45-51.

82.   Rawat, K.; Bohidar, H. B., Heparin-like native protein aggregate dissociation by 1-alkyl-3-methyl imidazolium chloride ionic liquids. *International journal of biological macromolecules* **2015,** *73*, 23-30.

83.   Sivapragasam, M.; Moniruzzaman, M.; Goto, M., Recent advances in exploiting ionic liquids for biomolecules: Solubility, stability and applications. *Biotechnol. J.* **2016,** *11* (8), 1000-1013.

84.   Rabideau, B. D.; Ismail, A. E., Mechanisms of hydrogen bond formation between ionic liquids and cellulose and the influence of water content. *Phys. Chem. Chem. Phys.* **2015,** *17* (8), 5767-5775.

85.   Schindl, A.; Hagen, M. L.; Muzammal, S.; Gunasekera, H. A. D.; Croft, A. K., Proteins in Ionic Liquids: Reactions, Applications, and Futures. *Front. Chem.* **2019,** *7*.

86.   Bhattacharya, G.; Mitra, S.; Mandal, P.; Dutta, S.; Giri, R. P.; Ghosh, S. K., Thermodynamics of interaction of ionic liquids with lipid monolayer. *Biophys Rev.* **2018,** *10* (3), 709-719.

Chapter 2

Experimental and Computational

Methodologies

EXPERIMENTAL AND COMPUTATIONAL METHODS

A brief overview of the various characterization and analysis techniques employed in this thesis is provided in this chapter.

Experimental methodologies

The characterization consists of direct characterization and indirect characterization. Experimental tools such as nucleus magnetic resonance (NMR), Fourier transmission infrared (FTIR), and mass spectrometry were employed to characterize synthesized ionic liquids. We also used scanning electron microscopy, transmission electron microscopy, fluorescence correlation spectroscopy, isothermal titration calorimetry, dynamic light scattering, and zeta potential techniques to study biomolecule and ILs interaction. These techniques are discussed in detail later in this chapter.

Computational methodologies

This part covers the computational techniques used in this thesis to provide an atomic-level insight into the interactions between biomolecules and ionic liquids. Molecular docking and molecular dynamics simulations are employed to understand better the forces responsible for the interactions and the nature of the interactions. These techniques are discussed in detail later in this chapter.

2.1 Experimental methodologies

2.1.1 Fourier-transform infrared (FTIR) spectroscopy

FTIR spectroscopy is an analytical technique that helps to determine the functional groups in organic and inorganic compounds. It is a highly sensitive and non-destructive technique used for the structure identification and annotation of other compounds and their possible impurities. The chemical bonds in different functional groups have a particular frequency of vibration. When infrared light is shined on the sample, the functional groups of the

sample can absorb an appropriate resonating wavelength, which is also indicative of its local chemical environment. This can be achieved by plotting a graph of transmitted/absorbed light versus wavenumber (energy in cm^{-1}). A typical FTIR instrument uses a source, beam splitter, movable and fixed mirrors, sample cell, detector, and signal processor unit.[1,2] Briefly, the infrared light from the source passes through a beam splitter and falls upon the mirrors, one of which is fixed, and the other is movable up to a fixed distance. As the path traveled by the two light beams differs, an interference pattern is created when these beams meet at the beam splitter. Constructive interference occurs from the two emerging rays when the path lengths from the beam splitter to the two mirrors differ by an integer wavelength (including the condition where the path lengths are equal). This beam is then made to pass through the sample, which is exposed to all wavelengths simultaneously. A detector collects the transmitted light and contains the time domain signal. This time domain signal is converted into the frequency domain by Fourier transformation. A spectrum is thus obtained by plotting transmitted/ absorbed light versus wavenumber. A schematic representation of a basic FTIR instrument is shown in Figure 2.1.
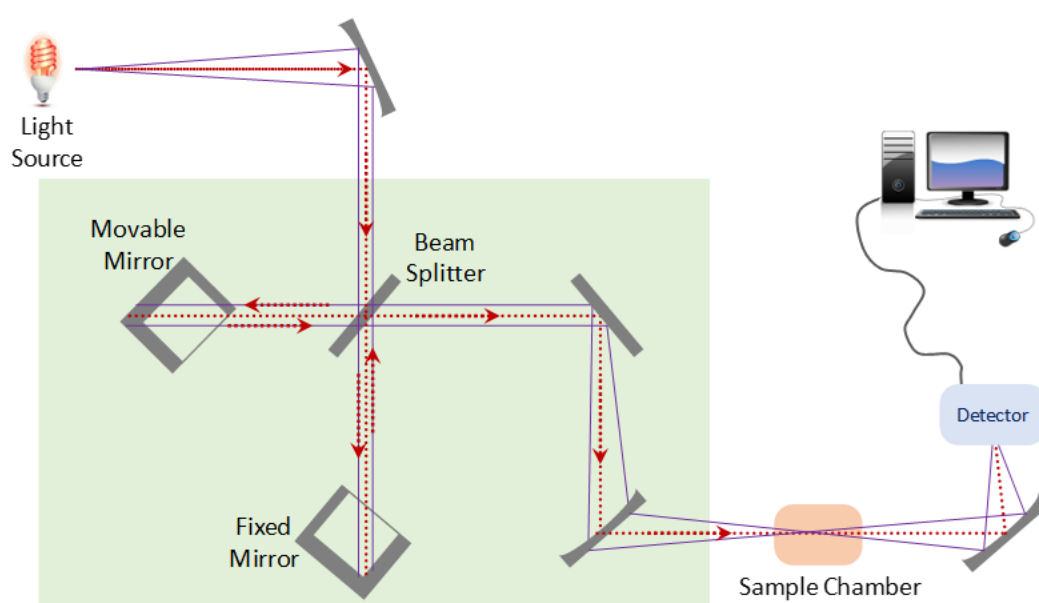
Figure 2.1 Schematic representation of FTIR.

2.1.2 Nuclear magnetic resonance spectroscopy

Nuclear magnetic resonance (NMR) spectroscopy is even more critical to the organic chemist than infrared spectroscopy. IR spectroscopy provides insight into the types of functional groups present in a molecule, while NMR reveals information about the number of magnetically distinct atoms in the molecule. Combining data from both IR and NMR is sufficient to determine the structure of an unknown molecule. Any atomic nucleus with odd mass, odd atomic number, or both possesses quantized spin angular momentum and a magnetic moment. [3]

An NMR spectrophotometer comprises a magnet, a radiofrequency source, a detector, and an amplifier. During the process, energy is transferred from the radiofrequency beam to the nucleus. The sample, housed in an NMR tube between the magnets, is exposed to the radiofrequency source, typically achieved by directing energy into a coil wound around the sample tube. A signal is detected when the nuclei in the sample resonate with the source, indicating that the energy required to flip the proton matches that of the source.

Increasing the current through the electromagnets enhances the total field strength. As the field strength rises, the processional frequency of each proton increases until radiofrequency resonance occurs. When a proton (or a set of equivalent protons) reaches resonance, the detector produces a peak on the chart paper. The NMR spectrum comprises peaks corresponding to different applied field strengths, with each peak representing a set of protons. Energy is transferred from the source through nuclei to the detector coil, and the output can be sent to a cathode ray oscillograph or a strip chart recorder after amplification. A schematic representation of a basic FTIR instrument is depicted in Figure 2.2.
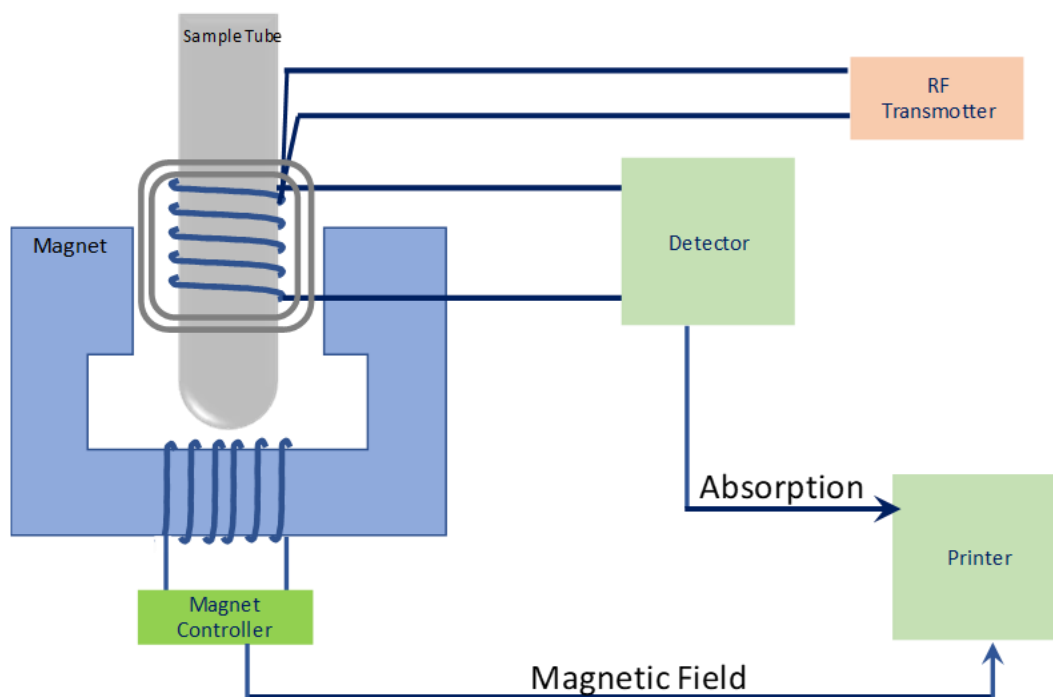
Figure 2.2 Schematic representation of NMR.

2.1.3 Mass Spectrometry

Mass spectrometry is an analytical technique that calculates the mass-to-charge ratio (m/z) of one or more molecules in a given sample. Utilizing Newton's second law of motion and momentum, a mass spectrometer leverages this property of matter to generate a mass spectrum, plotting ions with varying masses. According to this law, the relevance of mass to the inertia and acceleration of a body can be inferred, and this principle is applied to deflect ions with different mass-to-charge ratios at various angles in an electric or magnetic field.

A mass spectrometer comprises five fundamental components: a high vacuum system; a sample handling system for introducing the sample under investigation; an ion source capable of generating a beam of charged particles characteristic of the sample; an analyzer to separate the beam into its components; and a detector or receiver for observing or collecting the separated ion beams.[4]

2.1.4 Electron microscopy

The resolving power of an optical microscope is about $\lambda/2$ ($\lambda = 4000$-7000 Å). The optical microscope can not identify particle sizes less than 400 nm. Therefore, to have higher magnification and better resolution, the wavelength of the electron or electromagnetic wave must be close to 1 Å or less than it. The source of electrons can be a cathode tube, in which the applied potential difference is about a few kV. Such a microscope is known as an electron microscope. Here, two types of electron microscopes (scanning electron microscopy (SEM) and transmission electron microscopy (TEM) are discussed.

2.1.4.1 Scanning electron microscopy (SEM)

The scanning electron microscope generates the image by scanning the sample using a focused beam of electrons. The electrons are generated through thermionic or field emission and are accelerated by applying a few-kV potential (Figure 2.3). The electron beam is adjusted by magnetic lenses known as condenser lenses (for narrowing the beam diameter) and objective lenses (for focusing the beam over the sample). The scanning electron microscope images the sample after analyzing the electron beam and specimen interactions.[5] These interactions can be elastic or inelastic. Elastic scattering occurs when the nucleus or some outer shell electrons deflect the incident beam. If the incident electrons are scattered/reflected, these are called backscattered electrons (BSE), which provide information about the morphology of particles in the sample. Inelastic scattering occurs when incident energy is transferred to the sample generating secondary electrons. Apart from this, the electron beam-specimen interaction also results in the generation of characteristic X-rays (produced when an electron from the outer shell drops to the lower level to fill the vacancy in the inner K-shell), Auger electrons (produced as a result of knocking out of outmost shell electrons after receiving energy, which is released when an

electron from a higher level drops to the lower level to fill the vacancy) and cathodoluminescence (emission of photons when a material is bombarded with a high energy electron beam). The sample to be imaged through SEM must be conducted in nature to avoid any charging effect. As the high-energy electron beam falls upon a non-conducting sample, the electrons get trapped, creating an excess negative charge/local electrical potential that alters or modifies the electron beam-specimen interaction. This is called negative charging. Alternatively, positive charging occurs when the electron beam produces the secondary electrons. As a result, the image gets additional unwanted features such as featureless and irregular bright patches. As the conducting samples are electrically grounded, the excess charge passes through the sample, leaving no net charge. In contrast, to avoid this effect, the insulating samples are coated with a thin layer of metals such as Au, Pd, or W. SEM is particularly useful for studying the morphology of a system. It has a considerable depth of field which can see a large amount of sample at one time, and hence many times, SEM is preferred over TEM.
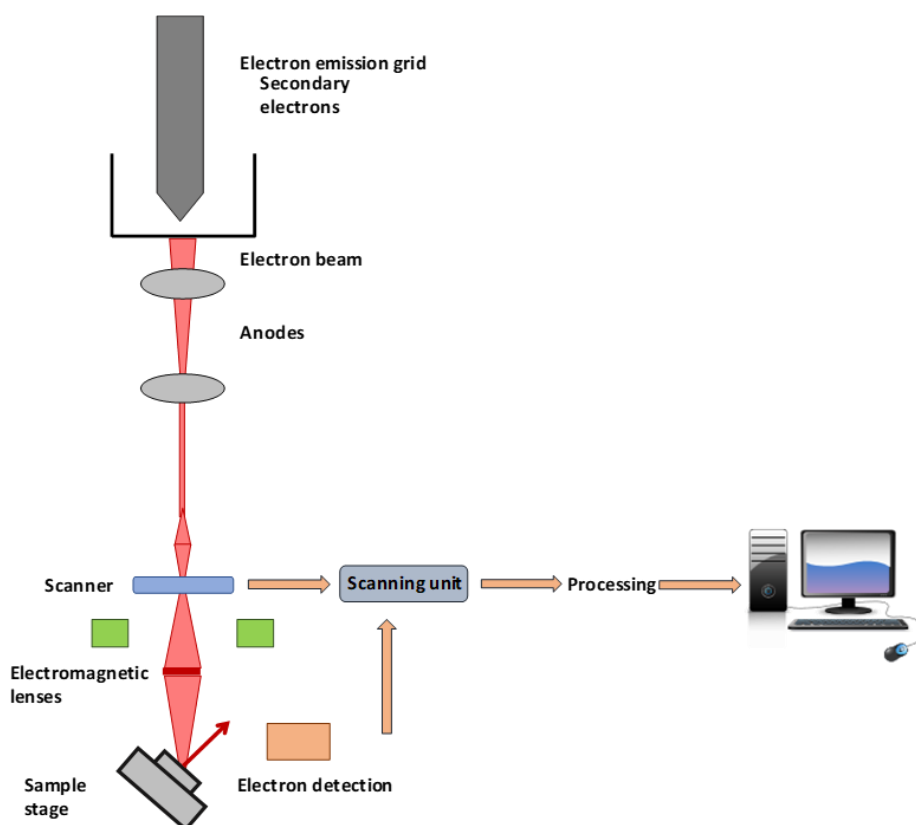
Figure 2.3 Schematic representation of SEM.

2.1.4.2 Transmission electron microscopy (TEM)

TEM, a form of microscopy, is exciting to biologists, chemists, physicists, and materials scientists because the small wavelength of the electron beam enables one to probe the morphological features at the nanometre to Angstrom level. It is an analytical technique that gives a clear picture of the shape of particles and crystallographic orientation via a selected area electron diffraction (SAED) pattern. It can also be used to calculate the particle size distribution. The resolution of a TEM image can further be enhanced by using HRTEM, which uses field emission (emission of electrons induced by an electrostatic field) as a source of electrons rather than thermionic emission (emission of electrons from a metal surface when heat energy is imparted to it) in case of TEM.[6] The acceleration of electrons by several kilovolts (30-200 kV) provides them a wavelength as small as 0.03 - 0.04 Å. It would have sufficient energy to pass through fragile sample

specimens, and diffraction can occur at a very small Bragg's angle at the focal plane of the lens if a sample is crystalline. These specimens can be imaged, and by changing the objective aperture of the TEM instrument, the selected area electron diffraction can be recorded. In several such kilovolts (V) used to accelerate electrons, the electron's velocity is a substantial fraction of the speed of light (c). According to relativistic effects, the wavelength (λ) of the emitted electron is given by:

$$\lambda = \frac{h}{\sqrt{(2m_0 eV)}} \; x \; \frac{1}{\sqrt{(1+(\frac{eV}{2m_0 e^2}))}}$$

where h is the Planck's constant, and m_0 is the rest mass of the electron. Applying an enormous potential to the electron gun produces the electrons as a source (due to Schottky or field emission). These high-energy electrons are accelerated to their final energies by an anode at a high potential relative to the microscope column kept at ground potential. To get a high-resolution image, this beam of electrons is made to pass through the condenser lens made of electromagnetic lenses. The equipotential surfaces of this electromagnetic lens are used to produce a converging lens, and a non-uniform field is used to create a diverging lens near the sample. The Condenser aperture and condenser stigmata align the optic axis with the aperture and reduce astigmatism from the condenser lenses. The beam passes through the specimen and can fall on the viewing screen.

2.1.5 Dynamic light scattering (DLS)

Classic light scattering assumes that the particles are at fixed positions in space; however, the suspended particles are not stationary. Instead, they move and diffuse in a random fashion which is known as Brownian motion. This motion changes the relative position of particles with time and results in the difference of phase of scattered waves reaching the detector. As the net scattered intensity recorded by the detector is a superposition of

the waves scattered at different times from different scattering volumes, the net power fluctuates with time (Figure 2.4).[7]
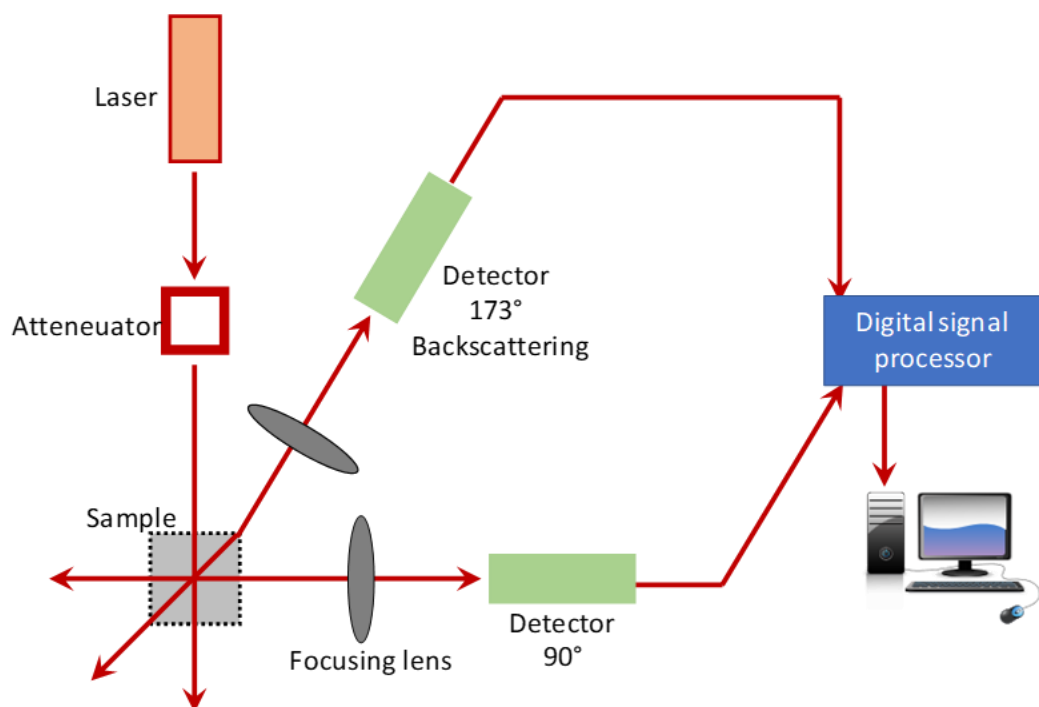
Figure 2.4 *Schematic representation of a DLS instrument.*

The fluctuations (or time dependence) in the net intensity of the scattered waves are the principle of the dynamic light scattering experiment. Appreciating that small particles diffuse in the solution more rapidly than larger particles is essential. This results in a rapid fluctuation in the intensity signal of smaller particles. To obtain the quantitative information from these kinds of fluctuations in the scattered intensity, autocorrelation $g^{(1)}(\tau)$ is used. For a monodispersed suspension of rigid and spherical particles undergoing Brownian motion, the correlation function decays exponentially and is defined as:

$$g^{(1)}(\tau) = \exp(-Dq^2\tau)$$

(2.9)

where D is the translational diffusion coefficient, τ is time, and q is the wave vector. For small, dilute, non-interacting spheres, the hydrodynamic radius R_h obtained from the translational diffusion coefficient using the Stokes-Einstein relationship is

$$R_h = \frac{kT}{6\pi\eta\tau} \qquad\qquad (2.10)$$

where, η is the solvent viscosity, T is the absolute temperature, and k is the Boltzmann constant. If the particle is non-spherical, then R_h is the apparent hydrodynamic radius.

2.1.6 Zeta potential

Zeta potential is a physical property, a charge around the surface of a colloidal particle in a dispersion medium. The nature and magnitude of the zeta potential can give information about the surface charge of the colloidal particle and its stability in the medium. Zeta potential can be used to predict the strength of the sol in a particular medium. Particles with high zeta potential values are electrically stabilized and do not coagulate quickly, whereas colloids with a low zeta potential coagulate easily.[8] The nanoparticles with a net charge have a layer of oppositely charged ions firmly bound to their surface, called the Stern layer. This layer is associated with another layer which is comprised of loosely associated ions. Both layers are termed as an electrical double layer. The Stern layer moves as the particle moves, but the loosely bound layer lags. The electrostatic potential between the dispersion medium and the stationary layer of fluid attached to the dispersed particle is called the zeta potential. It is related to the charge on the nanoparticle's surface. To record the zeta potential, the electric field is applied right angle to that of incident laser light across the sample. Because of the Doppler Effect, the shift in frequency, or phase shift, of the scattered light is measured. According to the Henry equation, this frequency shift is related to the electrophoretic mobility (μ) and the zeta potential (ζ).

$$\mu = \varepsilon \, \zeta / \, 4\pi \, \eta \qquad\qquad (2.11)$$

where ε is the permittivity of the medium, and η is the viscosity of the medium.
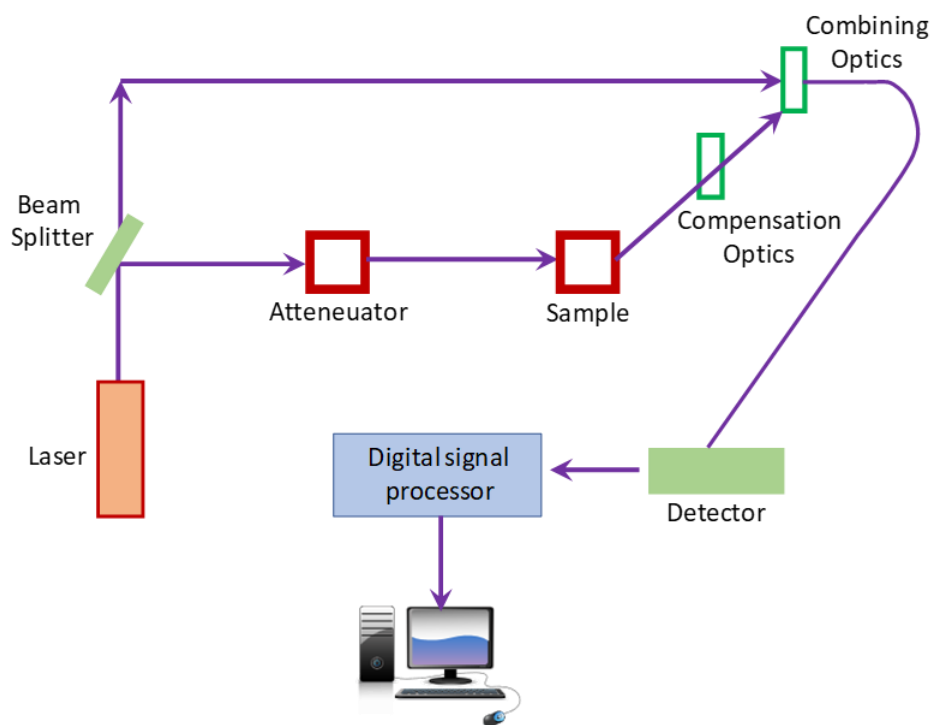
Figure 2.5 *Schematic representation of a Zeta potential instrument.*

2.1.7. Steady state absorption spectroscopy

UV-Vis spectroscopy is an essential and most common technique widely used in analytical chemistry, i.e., in chemical and clinical laboratories. This technique is mainly used for the qualitative analysis and identification of ground-state chromophore (conjugated) organic and inorganic materials, biological macromolecules, etc. When ultraviolet or visible light is allowed to pass through a sample, it can be absorbed if light possesses the same energy as the electronic levels ($\sigma \rightarrow \sigma$ *, $\pi \rightarrow \pi$ *, $n \rightarrow \pi$ *) of the organic/ inorganic compound or sample. Knowing the fraction of light transmitted makes it possible to find the wavelength and absorbance at which the absorption occurred. In

this way, structural elucidation or structural identification can be made. The absorption of light by a species in solution is directly proportional to the sample's concentration and path Beer-Lambert Lambert Law).[9]

The absorbance of the sample must be in the range of 0.1 to 0.9, if one wishes to use it as a quantitative analytical technique.
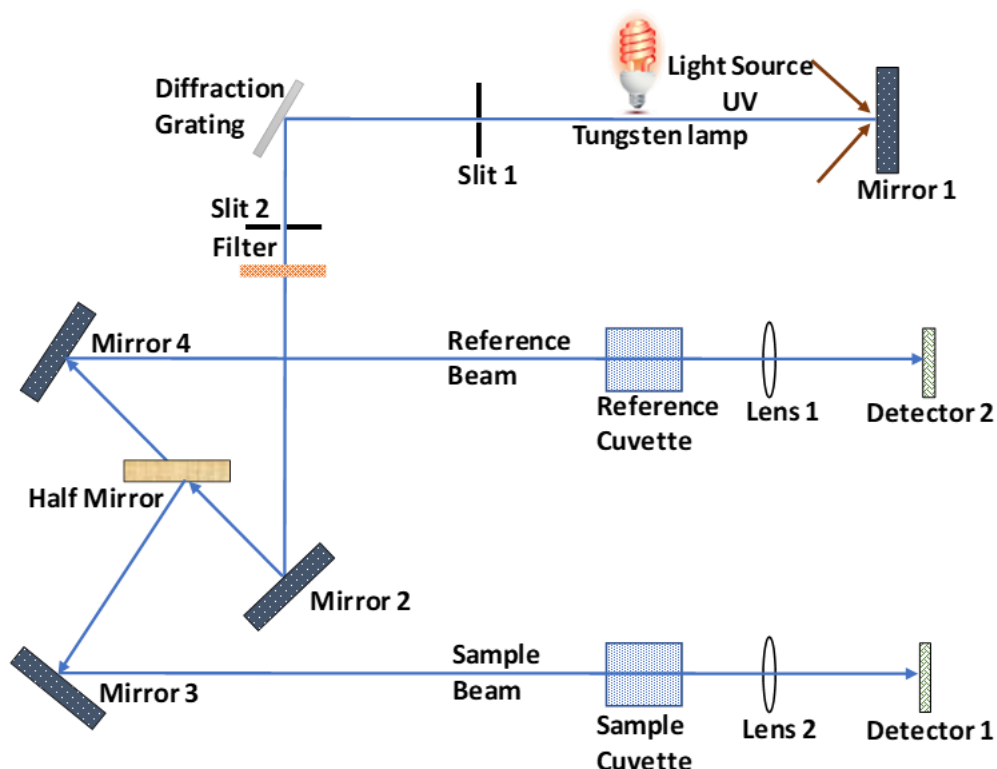
Figure 2.6 Schematic representation of a UV-Vis Instrument.

2.1.8. Steady state emission spectroscopy

Steady-state emission spectroscopy is a very useful technique used in biophysics and biochemistry to investigate the photophysics of molecules in solid and solution phases. Fluorescence occurs when a fluorescent molecule is electronically excited to higher singlet states using an appropriate wavelength of light and returns to the ground electronic state (S=0, V=0) from the lowest vibrational level of the first electronic excited state (S=1, V=0). This causes the emission of photons at a longer wavelength than absorption. Figure

2.7 shows the schematic diagram of a fluorimeter. Such instruments use the most common mercury or xenon lamps as the light source. The excitation monochromator is fixed to a particular wavelength of light for excitation purposes. The emission-monochromator is subjected to scanning through a desired emission wavelength region, and the detector records the fluorescence intensity with respect to the emission wavelength.
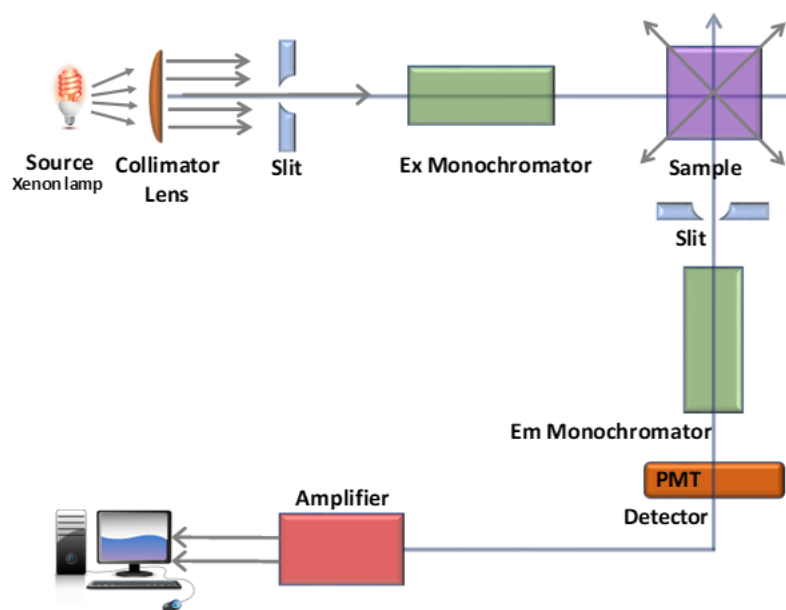
Figure 2.7 *Schematic representation of a Fluorometer Instrument.*

2.1.9 Time-resolved emission spectroscopy.

TCSPC is a conventional technique for measuring fluorescence decay in the time domain and provides information on various excited-state processes in the nanosecond time range. Basically, it measures the time gap between the excitation pulse and the emitted photon. The principle of TCSPC is based on detecting single photons and measuring their arrival times with respect to a reference signal, usually the light source, as shown in **Figure 2.8.** TCSPC is a statistical method requiring a high repetitive light source to accumulate one photon per approximately a hundred-pulse laser.
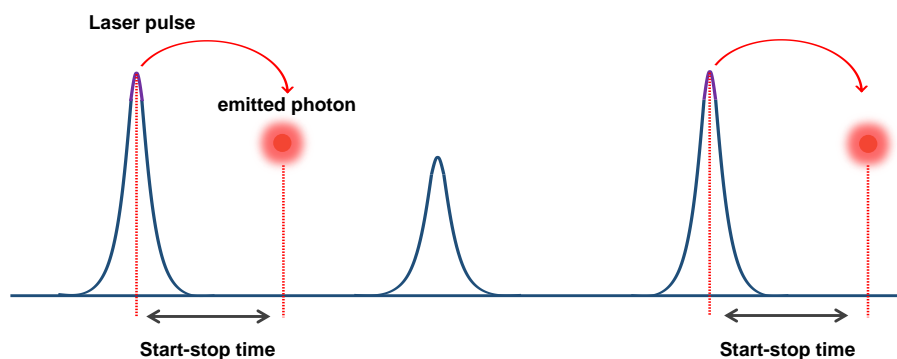
Figure 2.8. *Working principle of time-resolved fluorescence measurement with TCSPC using start-stop method.*

Figure 2.9 displays the main components for signal processing in TCSPC. The key component includes a constant fraction discriminators (CFD), where the start and stop signal are received, electrical delays (DEL), the Time-to-Amplitude Converter (TAC), Amplifier (between the TAC and ADC), an Analogue to Digital Converter (ADC) and a multichannel analyzer (MCA). TCSPC electronics can be compared to a fast stopwatch with two inputs. The clock is started by the START signal pulse and is stopped by the STOP signal. The time for one START-STOP sequence is measured and is represented by an increase in value in a histogram, versus time. There are two different operating modes in TCSPC applications:

1. In Forward Mode, the laser excitation pulse rate from the source is connected to the START input. This rate is substantially higher than the pulses from the detector connected to the STOP input.

2. In Reverse Mode, the signal carrying the pulse rate count from the light source is connected to the STOP input.

The START-STOP process is considered a single event and repeated multiple times to construct a histogram plot with the time delay in the x-axis vs. the number of photons

counts on the y-axis. The resulting histogram data are stored in a multichannel analyzer (MCA), and a fluorescence decay curve is generated.
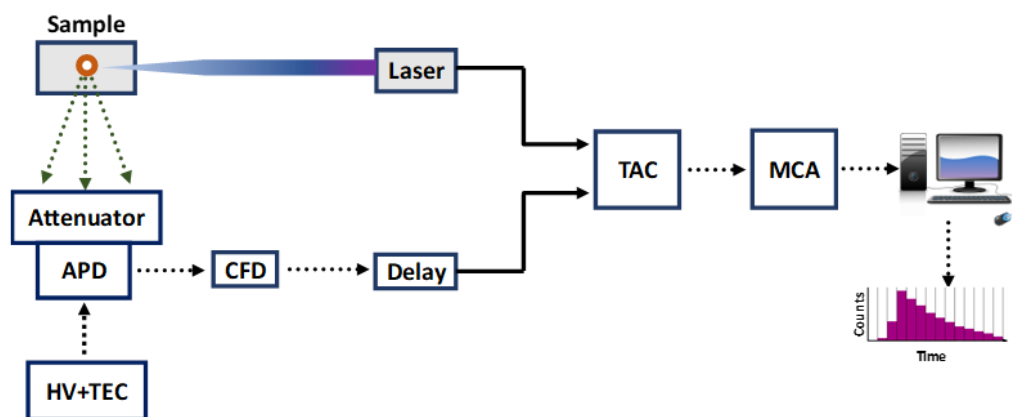
Figure 2.9 *Schematic representation of a Fluorimeter Instrument*

2.1.10 Fluorescence correlation spectroscopy

Fluorescence correlation spectroscopy (FCS) stands as a robust tool for probing molecular dynamics and finds widespread applications in various fields such as biomedicine, biophysics, and chemistry. FCS enables precise measurements of parameters like local concentration, hydrodynamic radius, diffusion coefficient, and interactions among different proteins. The methodology relies on analyzing time correlations in fluorescence fluctuations emitted as fluorescently labeled molecules diffuse into and out of a small observation volume.

FCS is typically conducted in a confocal system, as depicted in Figure 2.10.[10] The objective collects fluorescence emitted by fluorescent molecules within the observation volume, propagating in the opposite direction to the excitation light, which on passing through a long-pass dichroic mirror, is directed through a pinhole onto an avalanche photodiode (APD). The pinhole selectively blocks fluorescence emitted from out-of-focus regions, ensuring it does not reach the detector. As a result, the pinhole confines the

axial extension of the observation volume, significantly enhancing the signal-to-noise ratio and reducing the required measurement time for a correlation curve. The free diffusion of molecules induces intensity fluctuations (F(t)), reflecting their movement into and out of the observation volume.
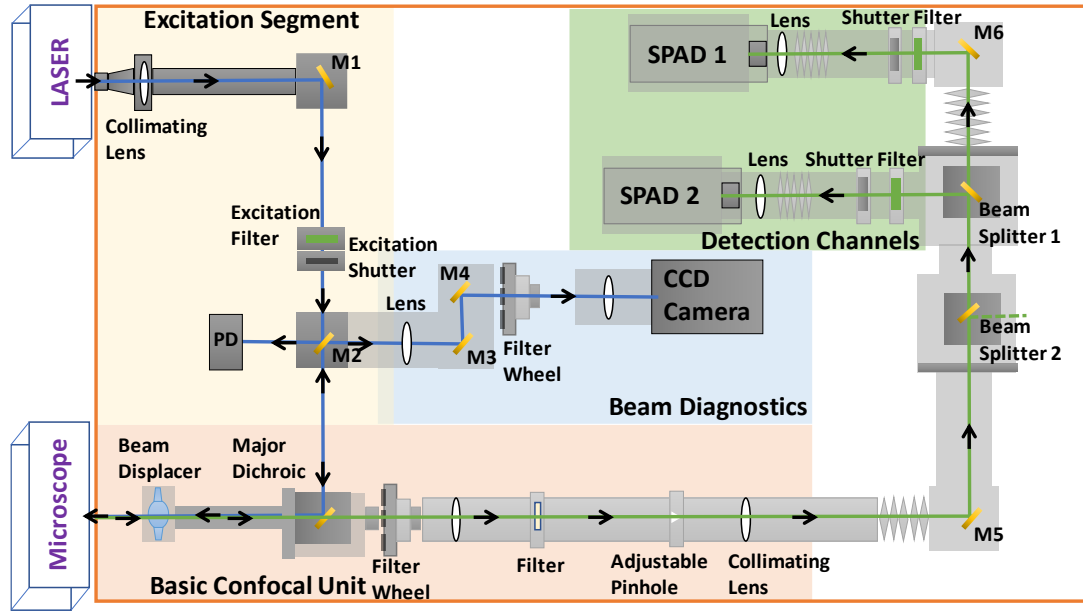
Figure 2.10 *Schematic representation of a FCS Setup*

Subsequently, the autocorrelation of F(t) is determined using the formula:

$$G(\tau) = \frac{< F(t)F(t + \tau) >}{< F(t) >^2}$$

where τ denotes the lag time. G(τ) assesses the self-similarity of a signal over time, indicating the signal's overlap with itself at different lag times τ. Assuming the observation volume approximates a 3D Gaussian profile, G(τ) can be fitted with a 3D diffusion model:

$$G(\tau) = \frac{1}{N}(1 + \frac{\tau}{\tau_D})^{-1}(1 + \frac{\tau}{\tau_D} \cdot \frac{r_0^2}{z_0^2})^{-\frac{1}{2}}$$

where N represents the average molecule number in detection volume, r_0 and z_0 are the lateral and axial radial distances over which the intensity decays by $1/e^2$ in the lateral and axial directions, respectively, and τ_D is the average time for the molecules diffusing through the detection volume. The amplitude of the correlation curve G(0) is inversely proportional to the average number of fluorescent molecules N in the observation volume, *i.e.*, G(0)~1/N.

Furthermore, the width of the correlation curve $\tau_D = r_0^2/(4D)$ represents the average time a molecule diffuses through the waist of the focus laterally. Here D indicates the diffusion coefficient of the molecules. For quantitative analysis, N and τ_D is obtained by fitting $G(\tau)$ with the model in Eq. Then, the diffusion coefficient is calculated. Furthermore, the hydrodynamic radius R_H, is calculated using the following equation:

$R_H = K_B T/6\pi\eta D$

Here, K_B is the Boltzmann constant, T is absolute temperature, and η is solution viscosity at a certain temperature T.
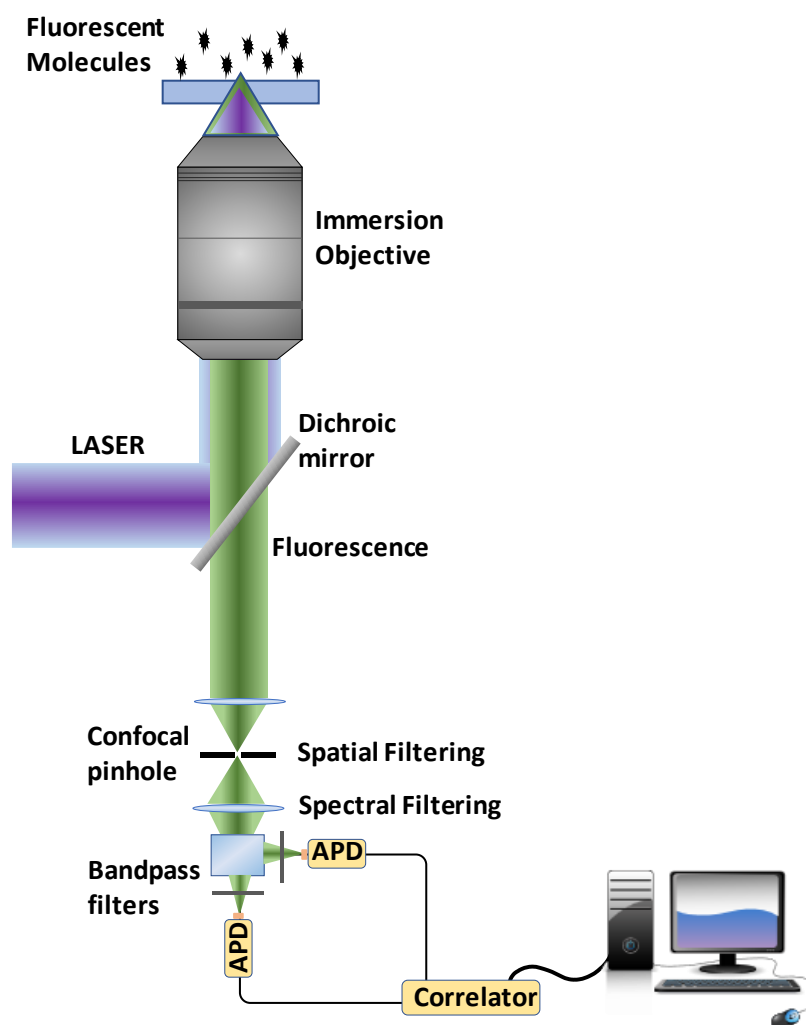
Figure 2.11 *Schematic representation of a FCS confocal setup*

2.1.11 Isothermal titration calorimetry

Isothermal titration calorimetry (ITC) is a physical technique used to determine the thermodynamic parameters of interactions in solution. ITC determines the heat change that occurs upon the binding of two molecules. Heat can be absorbed (endothermic reaction) or released (exothermic reaction).
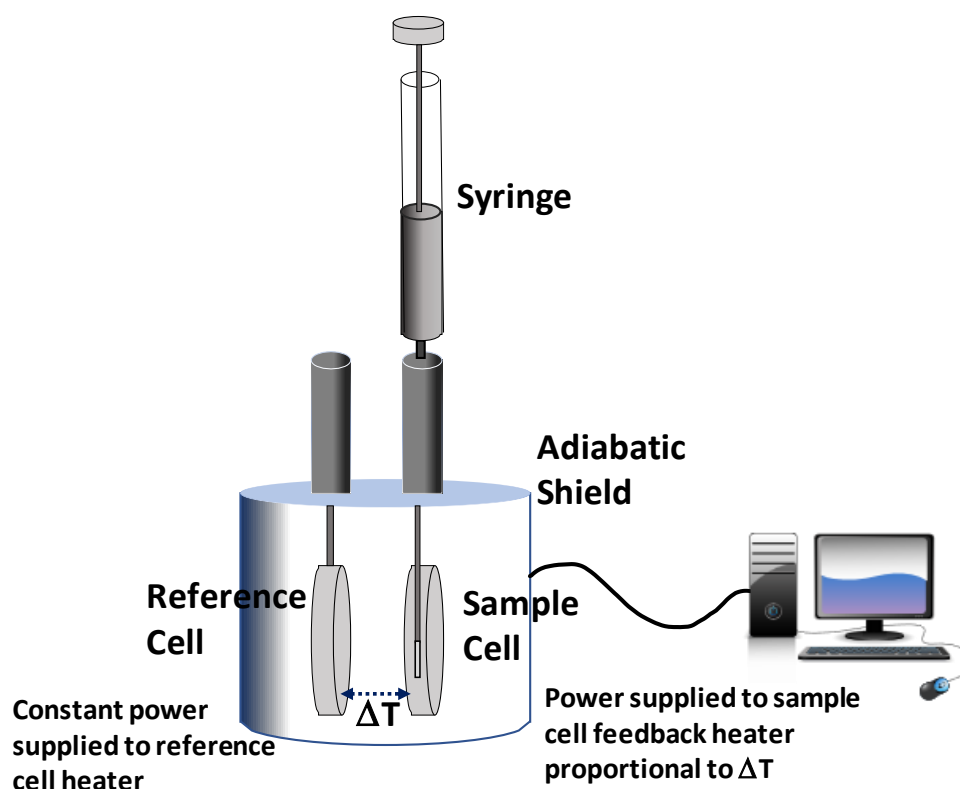
Figure 2.12 *Schematic representation of an ITC Setup*

ITC (Isothermal Titration Calorimetry) monitors heat changes by assessing the differential power delivered by the instrument's heaters to both the reference and sample cells. This adjustment counters any temperature difference between the two cells during the binding reaction, ensuring temperature parity (see Figure 2.12). ITC furnishes crucial insights into the macromolecular interaction, including binding stoichiometry (N), thermodynamic parameters (enthalpy, H, entropy, ΔS, and Gibbs free energy, ΔG), and the strength of the interaction (K_a).[11] Notably, ITC holds two key advantages among methods for characterizing macromolecular interactions: i) biomolecules can move freely in solution, allowing for a direct characterization of the binding event, and ii) ITC is the sole method providing a comprehensive characterization of the binding event, encompassing binding affinity, binding stoichiometry, and thermodynamic parameters.

2.1.12 Circular dichroism spectroscopy

Circular dichroism (CD) spectroscopy stands as a potent tool in structural biology, employed for the analysis of proteins, polypeptides, and peptides. The methodology of CD spectroscopy revolves around the fundamental concept known as the 'Cotton Effect.' It entails the measurement of the disparity in absorption between left and right circularly polarized light in optically active substances..[12]
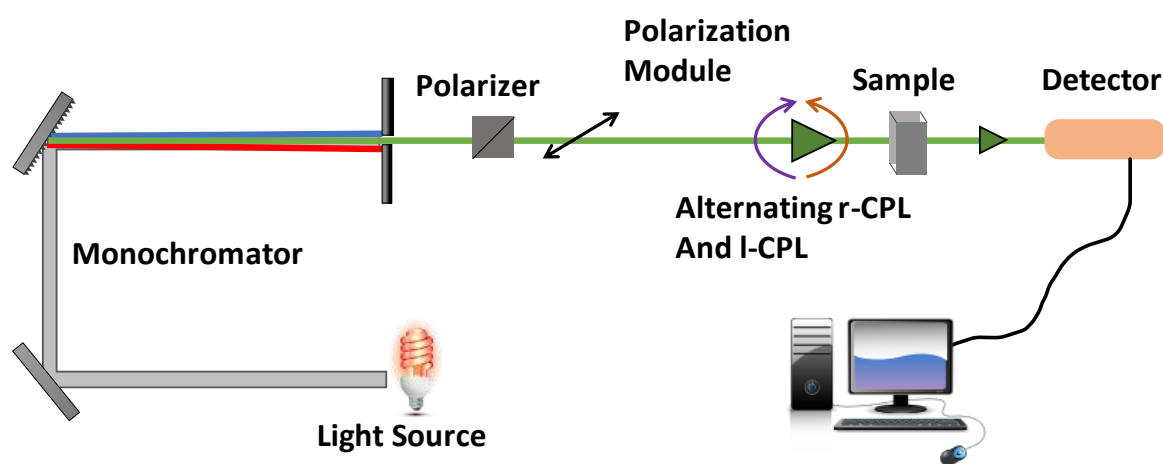
Figure 2.13 *Schematic representation of a CD Setup*

In a CD spectrophotometer, linearly polarized light is converted into circularly polarized light. The xenon arc lamp emits significant UV radiation (Figure 2.13). By purging the monochromator with nitrogen, the mirrors maintain reflectivity and longevity, while reducing oxygen absorption enables the acquisition of sample data further into the far-UV. In the far ultraviolet (UV) regions, the spectra of molecules are characterized by the $n{\rightarrow}\pi^*$ around 190 nm and $\pi{\rightarrow}\pi^*$ between 210-220 nm transitions of amide groups.[12] These spectra are influenced by the geometries of polypeptide backbones, reflecting different types of secondary structures and the associated ϕ, ψ angles. Helical secondary

structures, in particular, yield the most accurate results due to their regularity and well-defined ϕ and ψ angles.

The near-UV CD spectrum (250-320 nm) provides insights into the protein tertiary structure, focusing on the aromatic amino acid side chains. Phenylalanine, tyrosine, and tryptophan residues contribute to fine structure peaks between 255-270 nm, 275-285 nm, and 290-305 nm, respectively.For nucleic acids, CD spectra offer information on the secondary structure based on the stacking orientation of base pairs covalently bound to the backbone chain composed of sugar moieties. The chirality of the sugar groups induces a CD signal in the base pair's π→π* transition, observed in the range of 200-300 nm.

2.2. Computational methodologies

Computational methods are routinely used in chemistry to explain various non-covalent interactions, chemical reactions, and, thermo chemistry of complex reactions to know the thermodynamics of interacted systems. Computational calculations were carried out to support our experimental finding, or the computed data was benchmarked with similar experimental data with some scaling factors.

2.2.1. Geometry optimization

The geometry optimizations of ionic liquids were carried out at B97D/aug-cc-pVDZ level of theory. The B97D method is well known for weak non-covalent interactions.[13] All the geometrical optimizations were done with Turbomole V.6.5[14] and Gaussian 16[15] software package. Frequency calculations were carried out to confirm the minimum energy of optimized structures where no imaginary frequency was observed.

In this study, the electron density of optimized molecular structures was analyzed using Bader's Quantum Theory of Atoms in Molecules (QTAIM) methodology. The wave function calculations were performed using second-order Møller–Plesset perturbation theory (MP2). The molecular graph was generated from the wave function results, representing an accumulative structure by connecting bond paths. The presence of a bond path between two nuclei indicates a covalent or non-covalent bond between them. These bond paths are characterized by bond critical points (BCPs), where the charge density along the bond is at a minimum and the charge density perpendicular to the bond path is at a maximum.

To determine the presence of hydrogen bonds (H-bonds) based on Bader's QTAIM, criteria proposed by Koch and Popelier are followed.[16,17] These criteria are still commonly used to analyze existing BCPs between two noncovalently interacting molecules or molecular subunits.[18] The criteria are as follows:

(i) The interacting atoms must have a BCP between them, and they should be connected through a bond path.

(ii) The charge density ($\rho(r)$) along the bond path should fall within the range of 0.002-0.034 atomic units (a.u.).

(iii) The charge density ($\rho(r)$) perpendicular to the bond path should fall within the range of 0.024-0.139 atomic units (a.u.).

The Noncovalent Interaction (NCI) index is a powerful visualization tool used to analyze intermolecular interactions in molecular systems, relying on the electron density and reduced density gradient (RDG). To visualize these interactions, RDG isosurfaces can be represented either in a real 3D space mapping or on a 2D plot. By examining the sign of

the second eigenvalue of the electron density Hessian matrix ($\lambda2$), attractive and repulsive interactions between atoms or molecules can be distinguished. Specifically, a negative sign of $\lambda2$ indicates an attractive interaction, while a positive sign implies repulsion.To make the visualization more informative, gradient isosurfaces are color-mapped using a bar with two extremes set as 100 times the absolute value of the electron density ($\pm\rho(r)$). In this color scheme, blue represents strong, attractive interactions, while red indicates steric repulsion or strong non-bonded overlap. The data for these plots were generated using the NCIPLOT program, a commonly used software tool for calculating and visualizing the NCI index in molecular systems. With the NCI index and its associated visualizations, researchers can gain valuable insights into the nature of noncovalent interactions, aiding in the understanding of complex molecular structures.

2.2.2 Molecular docking

The molecular docking approach serves as a valuable method for modeling the atomic-level interaction between a small molecule and a protein. This technique enables the characterization of how small molecules behave within the binding site of target proteins, offering insights into essential biochemical processes. For performing the docking studies, we used AutoDock Vina software.[20,21] The structures of ligands were optimized. Using AutoDock Tools, the inputs such as ligands, proteins, and nucleic acids were prepared. The grid size for different systems was varied in x-, y-, and z-direction, fixing the grid space at 1.0 Å. From 15 different conformers produced energetically, the most favored conformer was chosen as the binding mode in each case.

2.2.3 Molecular dynamic simulation

In recent years, the significance of molecular dynamics (MD) simulations in molecular biology has seen a remarkable expansion. The provision of atomic-level structures

through these simulations has proven immensely valuable, offering profound insights into the functioning of biomolecules. Despite the inherent constant motion of atoms within biomolecules, understanding molecular function and intermolecular interactions relies heavily on comprehending the dynamics of these molecules. MD simulations play a crucial role in predicting the movement of every atom within a protein or other molecular system over time, utilizing a general model of the physics governing interatomic interactions.[22] These simulations effectively capture a diverse range of essential biomolecular processes, such as conformational changes, ligand binding, and protein folding. Furthermore, they unveil the precise positions of all atoms at femtosecond temporal resolution. A notable aspect of MD simulations is their ability to forecast how biomolecules respond at the atomic level in the presence of a ligand, enhancing our understanding of molecular interactions.

2.3. REFERENCES

1.   Nakamoto, K., Theory of Normal Vibrations. In Infrared and Raman Spectra of Inorganic and Coordination Compounds, John Wiley and Sons, Inc. 1997.: 2008; pp 1-147.

2.   Nakamoto, K., Applications in Inorganic Chemistry. In Infrared and Raman Spectra of Inorganic and Coordination Compounds, John Wiley and Sons, Inc. 1997.: 2008; pp 149-354.

3.   Pavia, D.; Lampman, G.; Kriz, G.; Vyvyan, J., Introduction to Spectroscopy (4th editio). Belmont, California: Cengage Learning. 2008.

4.   De Hoffmann, E.; Stroobant, V., Mass spectrometry: principles and applications. John Wiley & Sons: 2007.

5.   Zhou, W.; Apkarian, R.; Wang, Z. L.; Joy, D. J. S. M. f. N. T.; Applications, Fundamentals of scanning electron microscopy (SEM). 2007, 1-40.

6.   Carter, C. B.; Williams, D. B., Transmission electron microscopy: Diffraction, imaging, and spectrometry. Springer: 2016.

7.   Schmitz, K. S., Introduction to dynamic light scattering by macromolecules. Elsevier: 2012.

8.   Mendes, B. B.; Conniot, J.; Avital, A.; Yao, D.; Jiang, X.; Zhou, X.; Sharf-Pauker, N.; Xiao, Y.; Adir, O.; Liang, H.; Shi, J.; Schroeder, A.; Conde, J., Nanodelivery of nucleic acids. Nat Rev Methods Primers 2022, 2 (1), 24.

9.   Lakowicz, J. R., Principles of fluorescence spectroscopy. Springer: 2006.

10.   Yu, L.; Lei, Y.; Ma, Y.; Liu, M.; Zheng, J.; Dan, D.; Gao, P., A Comprehensive Review of Fluorescence Correlation Spectroscopy. Front. Phys. 2021, 9.

11.   Bastos, M.; Abian, O.; Johnson, C. M.; Ferreira-da-Silva, F.; Vega, S.; Jimenez-Alesanco, A.; Ortega-Alarcon, D.; Velazquez-Campoy, A., Isothermal titration calorimetry. Nat Rev Methods Primers 2023, 3 (1), 17.

12.   Andrews, S. S.; Tretton, J., Physical Principles of Circular Dichroism. J. Chem. Educ. 2020, 97 (12), 4370-4376.

13.   Grimme, S., Semiempirical GGA-type density functional constructed with a long-range dispersion correction. J. Comput. Chem. 2006, 27 (15), 1787-1799.

14.   TURBOMOLE V6.5 2013, A Development of University of Karlsruhe and Forschungszentrum Karlsruhe GmbH, TURBOMOLE V6.5, University of Karlsruhe and Forschungszentrum Karlsruhe GmbH, 1989-2007.

15.   M. J. Frisch, G. W. T., H. B. Schlegel, G. E. Scuseria, M. A. Robb, J. R. Cheeseman, G. Scalmani, V. Barone, G. A. Petersson, H. Nakatsuji, X. Li, M. Caricato, A. V. Marenich, J. Bloino, B. G. Janesko, R. Gomperts, B. Mennucci, H. P. Hratchian, J. V. Ortiz, A. F. Izmaylov, J. L. Sonnenberg, D. Williams-Young, F. Ding, F. Lipparini, F. Egidi, J. Goings, B. Peng, A. Petrone, T. Henderson, D. Ranasinghe, V. G. Zakrzewski, J. Gao, N. Rega, G. Zheng, W. Liang, M. Hada, M. Ehara, K. Toyota, R. Fukuda, J. Hasegawa, M. Ishida, T. Nakajima, Y. Honda, O. Kitao, H. Nakai, T. Vreven, K. Throssell, J. A. Montgomery, Jr., J. E. Peralta, F. Ogliaro, M. J. Bearpark, J. J. Heyd, E. N. Brothers, K. N. Kudin, V. N. Staroverov, T. A. Keith, R. Kobayashi, J. Normand, K. Raghavachari, A. P. Rendell, J. C. Burant, S. S. Iyengar, J. Tomasi, M. Cossi, J. M. Millam, M. Klene, C. Adamo, R. Cammi, J. W. Ochterski, R. L. Martin, K. Morokuma, O. Farkas, J. B. Foresman, and D. J. Fox Gaussian 16, Revision E.01; Gaussian, Inc.: Wallingford CT, 2016.

16.   Atoms in Molecules, Bader, R. F. W. Acc. Chem. Res. 1985, 18, 9-15.

17.   Characterization of C-H-O Hydrogen Bonds on the Basis of the Charge Density, Koch, U.; Popelier, P. L. A. J. Phys. Chem. A 1995, 99, 9747-9754.

18.   Revealing Noncovalent Interactions, Johnson, E. R.; Keinan, S.; Mori-Sánchez, P.; Contreras-García, J.; Cohen, A. J.; Yang, W. J. Am. Chem. Soc. 2010, 132, 6498-6506.

19.   NCIPLOT: A Program for Plotting Noncovalent Interaction Regions, Contreras; García, J.; Johnson, E. R.; Keinan, S.; Chaudret, R.; Piquemal, J.-P.; Beratan, D. N.; Yang, W. J. Chem. Theory Comput. 2011, 7, 625-632.

20.   Morris, G. M., Huey, R., Lindstrom, W., Sanner, M. F., Belew, R. K., Goodsell, D. S., & Olson, A. J. , AutoDock4 and AutoDockTools4: Automated docking with selective receptor flexibility. J. Comput. Chem. 2009, 30, 2785-2791.

21.   Forli, S.; Huey, R.; Pique, M. E.; Sanner, M. F.; Goodsell, D. S.; Olson, A. J., Computational protein–ligand docking and virtual drug screening with the AutoDock suite. Nat. Protoc. 2016, 11 (5), 905-919.

22.   Roe, D. R.; Cheatham, T. E., PTRAJ and CPPTRAJ: Software for Processing and Analysis of Molecular Dynamics Trajectory Data. J. Chem. Theory Comput. 2013, 9 (7), 3084-3095.

Chapter 3

Storage and Extraction of RNA in Ionic Liquids

3.1 INTRODUCTION

Nucleic acids, particularly RNA, are critical in storing and transmitting genetic information within living organisms. They also serve as essential regulators of gene expression, making them a subject of intense study in various scientific fields. Furthermore, RNA has demonstrated immense potential in medical applications, molecular and cellular biology research, and nano/biotechnology advancements.[1-4] Its involvement in the central dogma of life, acting as a carrier of the DNA blueprint and driving protein synthesis, highlights its significance in the fundamental processes of life.[5-6] RNA possess catalytic properties, enabling them to participate in chemical reactions and providing valuable insights into disease biology.[7] However, one of the primary challenges of studying RNA both in-vivo and in-vitro is to maintain its structural integrity in the solution phase at room temperature.

The molecular architecture of RNA, which includes base pairing, electrostatic interactions, hydration capacity, and the near-environment effect, plays a crucial role in maintaining its stability and integrity. Preserving these characteristics is essential for accurate analysis and experimentation involving RNA.[8] Traditionally, cold storage is the most commonly employed method for RNA storage. Samples are stored at sub-zero temperatures ranging from -20 °C to -80 °C or in liquid nitrogen, slowing down degradation processes.[9] However, these storage methods often require specialized equipment and infrastructure, making them expensive and cumbersome.

In recent years, novel approaches have emerged as potential alternatives for room temperature RNA storage, offering cost-effectiveness and ease of use advantages. One such method involves drying RNA samples and stabilizers and storing them in stainless steel capsules. Fabre et al. demonstrated the effectiveness of this approach, highlighting

that RNA samples could be preserved at room temperature for prolonged periods without significant degradation.[10] Desiccation, the process of removing moisture from the samples, has also proven to be an efficient method for RNA preservation. Seelenfreund et al. reported promising results, indicating that desiccation can prevent RNA degradation even under harsh conditions.[11]

Another notable development in RNA storage technology is the use of silica encapsulation.[12] This method involves embedding RNA molecules within silica gel, creating a protective matrix that shields the RNA from degradation. Silica encapsulation has shown promise in maintaining RNA's structural integrity and stability, even at room temperature. This approach offers the additional advantage of compatibility with various downstream applications, such as gene expression analysis and RNA sequencing.

While these advancements in room-temperature RNA storage hold great promise, it is important to note that they are still relatively new and expensive. Ongoing research is focused on further improving their efficiency and practicality. The challenges associated with maintaining RNA integrity during storage require continued exploration and refinement of existing techniques. Researchers are actively working towards developing cost-effective and user-friendly methods that ensure the long-term stability and integrity of RNA samples without the need for extremely low temperatures or complex storage setups.

RNAs are invaluable biopolymers that carry genetic information and regulators of gene expression. Their significance in various scientific disciplines and medical applications has prompted the development of efficient storage methods. While cold storage has been the conventional approach, recent advancements have offered alternatives for room-temperature RNA storage, such as drying with stabilizers, desiccation, and silica

encapsulation. These methods hold promise regarding cost-effectiveness and ease of use, although further research and optimization are still required. Continued efforts in RNA storage technology will ultimately facilitate breakthroughs in gene therapy, disease biology, and other fields reliant on studying RNA molecules.

On the other hand, Ionic Liquids (ILs) have garnered significant attention in recent years due to their potential as efficient solvents for storing biopolymers, proteins, and enzymes.[13-17] Unlike traditional solvents, ILs are molten salts characterized by low volatility, high ionic conductivity, and non-toxicity, making them environmentally friendly alternatives.[18-23] Their unique properties position them as promising substitutes for organic solvents in various applications, including drug delivery and biochemistry.[24-28]

ILs have demonstrated their suitability for long-term storage and extraction of macromolecules, such as proteins and DNA, as these biomolecules can maintain their functionality in IL environments.[29-36] However, the challenge lies in preserving RNA, which is highly susceptible to temperature, pH, and enzyme degradation. Nevertheless, recent studies suggest that ILs, including Deep Eutectic Solvents (DES) and Room Temperature ILs (RTILs), could offer viable solutions for RNA storage.[37-40]

Several investigations have examined the stability of nucleic acids in IL environments. For instance, researchers have explored the structural stability of nucleic acids in DES and RTILs. The advancement in finding a non-toxic and biocompatible solvent for RNA also demonstrates that ILs could be adequate and effective substitutes. Mamajonav et al. demonstrated the structural stability of nucleic acids in Deep Eutectic Solvents (DES) and Room Temperature ILs (RTILs).[38] Mazid et al. investigated the role of ILs containing choline dihydrogen phosphate in the stability of siRNA in the presence of RNase A.[39]

This was also supported by Fister et al. through their work on the RNA isolation from viruses using imidazolium and ammonium-based ILs.[22] Report by Pedro et al. also illustrates that choline-based ILS are suitable for preservation of recombinant RNAs.[40] Quental et al. successfully used amino acid-based ILs solvents to extract and preserve RNA.[41]

Despite these findings, the underlying mechanisms that make ILs suitable for RNA storage have not been extensively investigated. The researchers aim to bridge this knowledge gap by conducting a meticulous analysis involving spectroscopic measurements and theoretical modeling. Through this comprehensive approach, they hope to unravel the intricate details of how ILs interact with RNA and elucidate the mechanisms contributing to its preservation in IL-based solvents. Such insights could pave the way for developing improved RNA storage techniques using non-toxic and biocompatible ILs.

This study represents a pioneering investigation into the interaction between choline amino acid-based ionic liquids (ChAAILs) and RNA, providing crucial spectroscopic evidence. Unlike DNA, which commonly adopts a B-form conformation, RNA typically exhibits an A-form structure in buffer solutions. The structural conformation of nucleic acids can be perturbed by external factors such as temperature and pressure, highlighting the importance of understanding their interactions with ILs. While RNA is highly susceptible to degradation by enzymes like RNAase, it requires additional precautions during handling compared to other nucleic acids.[42] Notably, in the case of transfer RNA (tRNA), the presence of modified nucleobases plays a significant role in regulating its overall stability.

To gain insights into the interaction between ChAAILs and RNA, the researchers developed an initial hypothesis and employed theoretical modeling techniques, complemented by classical simulations extending up to microsecond timescales. To confirm the RNA-IL interaction, a range of spectroscopic techniques was utilized, including steady-state absorption (UV-Vis and CD) and emission measurements, time-correlated single-photon counting (TCSPC) integrated with femtosecond-fluorescence up-conversion, and fluorescence correlation spectroscopy (FCS). Additionally, isothermal titration calorimetry experiments were conducted to provide thermodynamic information on the binding between RNA and ILs. RNA melting experiments were performed to obtain a comprehensive understanding of the thermal stability of RNA in the presence of ILs.

Combining these experimental and theoretical approaches, the study aims to unravel the atomistic details of the RNA-ChAAIL interaction and shed light on the binding mode between these entities. The spectroscopic evidence obtained will validate the proposed interaction and provide valuable insights into the stability and behavior of RNA in the presence of ChAAILs. Ultimately, this research will contribute to expanding our knowledge of the applications of ILs in RNA storage and open new avenues for developing innovative biocompatible solvents for preserving and manipulating RNA molecules.

3.2 METHODS

3.2.1 Materials

Choline hydroxide, amino acids (Glutamic acid and Aspartic acid), Ribonucleic acid from Torula yeast (Type VI), and the fluorescence probe, 4′,6-Diamidine-2′-phenylindole dihydrochloride (DAPI), were purchased from Sigma and were used directly without any

further purification. Phosphate (200mM, pH 7.4) buffer and Ethidium bromide (EB) fluorescence dye was purchased from G Bioscience. The Ionic liquids were synthesized using neutralization, and 1H and 13C NMR checked their purity.[43] The NMR data of the synthesized ionic liquids are given in Figure 3.1-3.2.
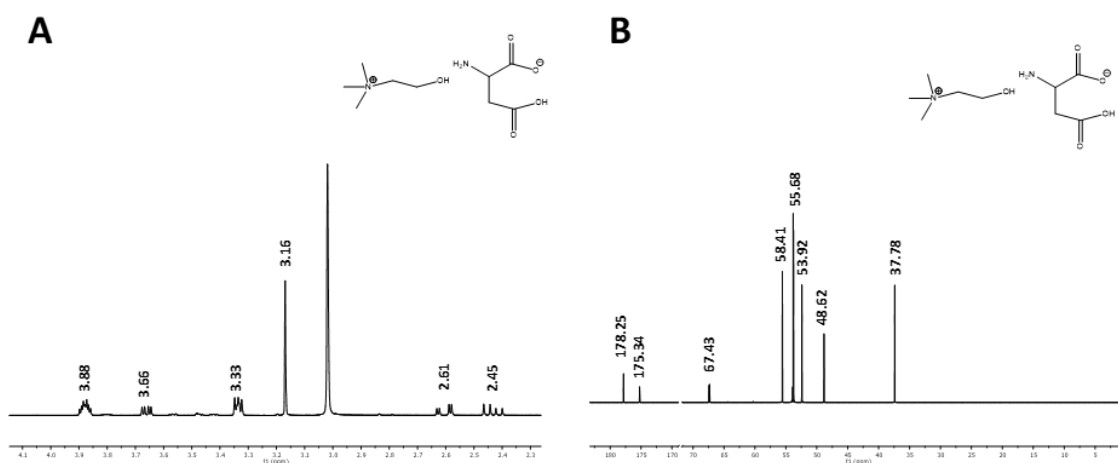
Figure 3.1. ^{1}H and ^{13}C NMR spectrum of [Ch][Glu] IL in D$_2$O.
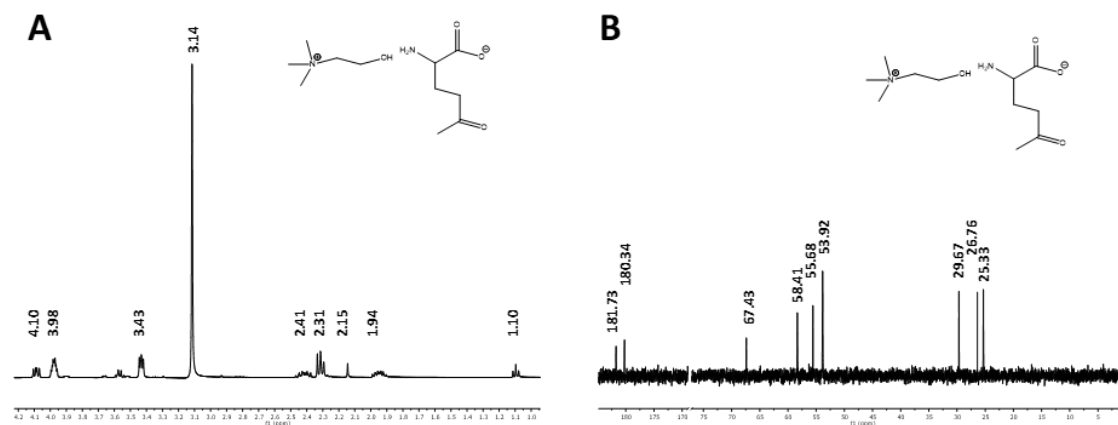
Figure 3.2. ^{1}H and ^{13}C NMR spectrum of [Ch][Asp] IL in D$_2$O.

The molecular structure of the fluorescent probes used are shown in Figure 3.3.
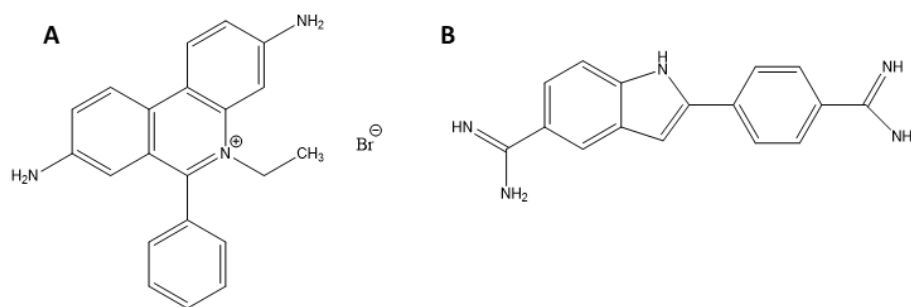
Figure 3.3. Fluorescent probes EB and DAPI.

The purity of RNA was checked by UV-Vis absorption spectroscopy. The absorbances of the RNA stock solution at 260 nm and 280 nm were measured, and their ratio was 1.9. This confirms the absence of any impurity in RNA. Deionized water (Milli Q) was used for all the solution preparation and experiments.

3.2.2 Experimental Section

All sample preparations for recording steady-state absorption, time-resolved emission, and CD are in a 20 mM aqueous phosphate buffer solution of pH 7.4. These measurements are in a quartz cuvette of 10 mm path length. The UV melting measurement uses a fixed wavelength of 260 nm with gradual recording from 20 to 95 ºC. Ti-sapphire laser (Mai Tai, Spectra-Physics) centered at 800 nm (2.9W, 80MHz) is used for time-resolved measurements. 445 nm (repetition rate=993 kHz) photons for sample excitation are generated using a second harmonic generation of 890 nm. For the time-resolved measurements, sample excitation at 445 nm second harmonic (repetition rate=993 kHz) is generated using Ti-sapphire laser (Mai Tai, Spectra-Physics). The output amplified pulses centered at 890 nm typically have an average power of 2.44 W at a repetition rate 80MHz. The obtained IRF is from the Raman scattering of water, which is 250 ps. The decay kinetics are fitted with a multi-exponential kinetic model using IGOR Pro 5 software. The output amplified pulses centered at 890 nm typically have an average power

of 2.44W at a repetition rate 80MHz. The obtained IRF of 250 ps is from the Raman scattering of water.

Isothermal titration calorimetry (ITC) measurement uses a MicroCal ITC-200 calorimeter at 25 ℃. The recordings are with a sample cell containing 200 µL of 350 µM RNA in phosphate buffer and titration against 100 mM injections of choline amino acid-based ionic liquids. 19 injections are used from a 40 µl rotating syringe into the sample cell. In each titration, an injection volume of 2 µl at an interval of 120 s. The heat variation was monitored inside the cell to determine the binding enthalpy of the process (ΔH) and the equilibrium association constant (K). All enthalpy values for binding reactions were exothermic. Control titrations were performed to subtract the heat of dilution and mix for each experiment.

The binding and thermodynamics constants were determined using a single set of sites model. ΔH and ΔS parameters were obtained from the standard Levenberg Marquardt nonlinear regression method in the Origin 7 software. The Gibbs free energy (ΔG) of binding was calculated using Eq. 1, where R is the gas constant ($8.314 \, \mathrm{J \, K^{-1} \, mol^{-1}}$), T is the temperature in Kelvin (T=℃ +273), and K is the association constant at equilibrium.

$$\Delta G^0 = - R.T.\ln K = \Delta H^0 - T.\Delta S^0$$

Fluorescence correlation spectral measurements use a time-resolved confocal microscope from PicoQuant Micro-time 200. The excitation source uses a pulsed diode laser with a wavelength of 403 nm. Laser focus on the sample uses a water immersion object. The experimental recordings use a laser power of 10 µW in a 20 mM phosphate buffer solution containing 150 nM DAPI and 50 µM RNA.

The equation for simple diffusion (Eq 1) along with intersystem crossing (Eq 2) is as follows:

$$G(\tau) = \frac{1}{N}\left(1 + \frac{\tau}{\tau_D}\right)^{-1}\left(1 + \frac{\tau}{\kappa^2 \tau_D}\right)^{-1/2} \qquad \text{Eq}$$

(1)

$$G(\tau) = \frac{1 - T + Te^{-\tau/\tau_{tr}}}{N(1 - T)}\left(1 + \frac{\tau}{\tau_D}\right)^{-1}\left(1 + \frac{\tau}{\kappa^2 \tau_D}\right)^{-1/2} \qquad \text{Eq}$$

(2)

Here, τ_D is the diffusion time, τ is the correlation time, τ_{tr} is the triplet state lifetime, N represents the number of molecules in the observation volume, T is the fraction of molecules in the triplet state, and κ is the structure parameter defined as $\kappa = (\omega_z/\omega_{xy})$ in which ω_z and ω_{xy} are the longitudinal and transverse radii of the observation volume, respectively.[30, 44]

Using the above equation, the τ_D was calculated from the fitted FCS data.

From the diffusion time, the hydrodynamic radius R_H of the molecules is calculated using the following equiation

$$\frac{R_H RNA}{R_H R6G} = \frac{\tau_D RNA}{\tau_D R6G}$$

3.2.3 Computational Section

Starting structure. The molecular basis of stability to RNA structures by ILs remains an open question. To fulfil this knowledge gap, we begin our investigation with computational models to explore the forces contributing to RNA binding and stability. The starting structure of our study is the crystal structure of yeast tRNA resolved at 1.9 Å resolution (PDB Code: 1EHZ).[45] Chemical structures like cationic cholinium ion [Ch], aspartic acid (Asp), and glutamic acid (Glu) and optimized at the B97/Def2-TZVPP level of theory using the Turbomole 6.5 quantum chemistry program.[46] Using the amino acids as the ionic counterpart to Ch, we prepared two separate macromolecular complexes, as

[Ch][Asp]-RNA and [Ch][Glu]-RNA. First, we obtain the Ch (ligand) - RNA (receptor) complex using the Autodock protocol.[47-48] In the next step, we generate a complex between Asp (ligand) - [Ch][RNA] (receptor). Although the docking calculations provide different ligand poses and binding possibilities, further analysis uses the minimum energy conformations. Notably, in Ch-RNA, low-energy complexes are mainly found in the minor groove region. On the other hand, no such specific binding site preference is present for Asp or Glu.

Force-fields. We account for the calculations of three RNA-based systems. Two of the systems are with ILs, viz. [Ch][Asp]-RNA and [Ch][Glu]-RNA. The third system is a control trajectory, focusing only on the RNA dynamics without ionic ILs. The standard force fields for RNA and proteins are from RNA. OL3 and ff14SB parameters from Amber library. For [Ch] molecule, the parameters are from the Generalized Amber force-field (GAFF) method, which includes the partial atomic charges from the RESP method using HF/6-31G* level of theory.[48-49] Additional amber parameters used to describe the modified nucleosides of RNA are from Aduri et al.[50]

Classical simulations. Calculations for molecular dynamics (MD) simulations uses the pmemd module of the Amber18 program. Macromolecular complexes are solvated using an octahedral box. The box sizes a minimum distance of 9 Å between any solute atom and the solvation boundary. Adding Na^+ counter ions to each system helps neutralize the total charge. Preliminary energy minimization of systems is a two-step procedure, each of 10^4 cycles. The first step uses a restraint force of 100 kcal.mol^{-1}.Å^{-2} and is reduced to 10 kcal.mol^{-1}.Å^{-2} in the second step. Following this, gradual heating from 100 K to 300 K under NVT ensemble conditions helps to prepare the system. Temperature controlling is possible with Langevin dynamics with a collision frequency of 1 ps. SHAKE algorithm constrains the hydrogen to its initial position during simulation. The applied integration

time step is 2 fs. The Particle Mesh Ewald (PME) method accounts for long-range electrostatic interactions. A cut-off distance of 8 Å accounts for the non-bonded interactions. Additional system relaxation under NPT condition is for two steps (5 ns each) with a restraint force of 100 and 0.1 kcal.mol^{-1}.Å^{-2}. In every system, trajectory calculations are for 1 μs timescale. CPPTRAJ module[51] of the Amber program and MC-Annotate program[52] utilised to analyze MD simulations.

3.3 RESULTS AND DISCUSSIONS

This study aims to examine the interaction patterns and dynamics between RNA and ILs to better understand their structural insights. Four main aspects are investigated: (i) the preferred binding sites of ILs on the three-dimensional structure of RNA; (ii) the primary forces responsible for stabilizing the complexes, including electrostatic and van der Waals forces; (iii) the physical stability of the RNA-IL complexes; and (iv) the impact of ILs on the dynamic behavior of RNA's structure.

A combination of computational simulations and experimental techniques addresses these objectives. Computational methods allow us to simulate and analyze the interactions between RNA and ILs at the atomic level, providing valuable insights into their binding preferences and the forces involved. Experimental approaches complement these findings by validating the computational results and providing a real-world perspective.

3.3.1 Binding site preference through molecular docking:

In this study, molecular docking was employed to investigate the binding possibilities and site preferences of ChAAILs ([Ch][Glu] and [Ch][Asp]) with RNA, based on energetic evaluations. The preliminary findings indicate that ChAAILs primarily bind to the minor groove of the RNA structure, as depicted in Figures 3.4A and B. However, no discernible

site preferences were observed for the counterion amino acids. The binding energies of the docked complexes were approximately -4 kcal/mol, regardless of whether Glu or Asp was present.
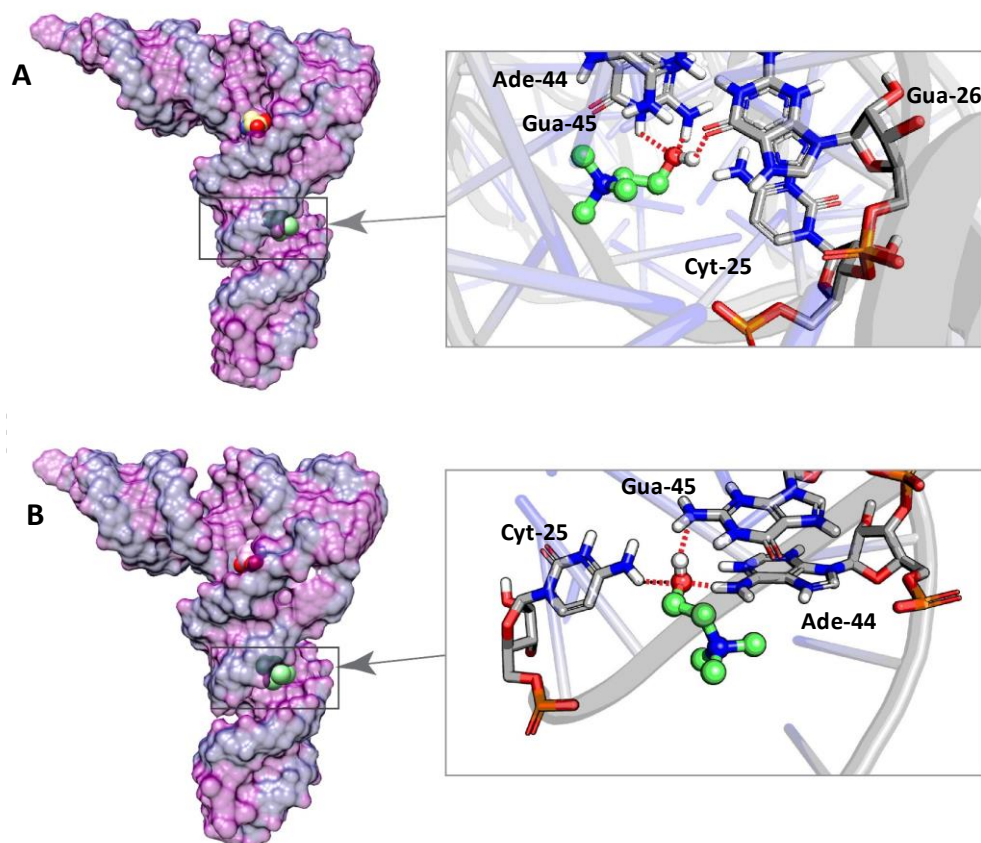
Figure 3.4: Starting structure of RNA complexed with ChAAILs: The zoomed section of IL bound to macromolecule is shown for A) RNA-[Ch][Glu] B) RNA-[Ch][Asp].

The lowest energy conformation of the Ch^+ ion was found to be stabilized through hydrogen bonding, as illustrated in Figure 3.4. Specifically, the O-H group of the ligand formed hydrogen bonds with nucleobases (O-H$\cdots$N). Previous research on DNA has demonstrated that the Lennard-Jones (LJ) parameter between ILs and the macromolecule significantly stabilizes the interaction, with energy contributions ranging from -10 kcal/mol to -23 kcal/mol.[33] However, our results indicate minimal LJ contributions (-1 to -2 kcal/mol), suggesting the absence of hydrophobic interactions between the alkyl group of Ch^+ and the aromatic-π electrons of nucleobases.

Furthermore, to further validate our docking, we performed docking with the ethidium bromide (EB) molecule, which is known to bind preferably at the minor groove of nucleic acid structures, as shown in Figure 3.5. Indeed, the lower energy conformation obtained also shows a preference for the minor-groove location, like Ch$^+$, which further triggered us to verify this experimentally.
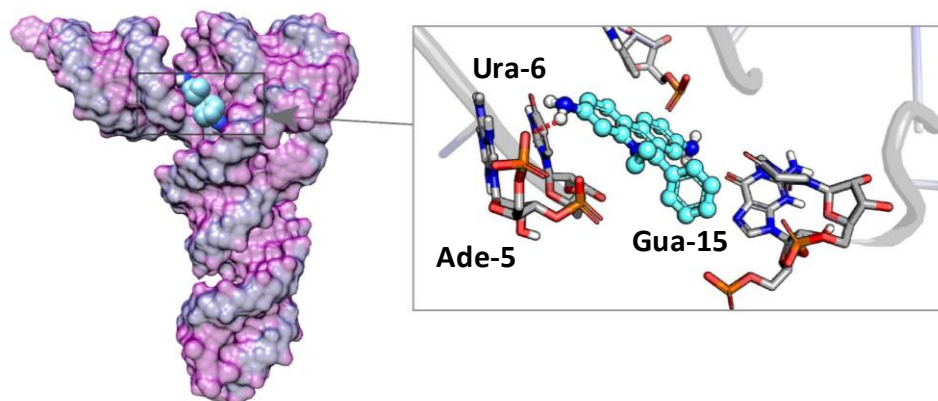
Figure 3.5: Starting structure of RNA complexed with EB: The zoomed section of IL bound to macromolecule is shown for RNA-EB.

3.3.2 Binding mode analysis with steady-state and time-resolved spectroscopy

UV-Vis absorbance measurement is valuable for determining RNA purity and confirming the binding specificity of ILs. Since a small molecule binding to RNA is possible through three modes: intercalation, groove binding, or external binding, the change in absorbance and a shift in absorption maxima (λmax) upon binding are good indicators.[53] A hyperchromic shift of the peak at 260 nm in the UV-Vis spectrum of RNA-[Ch][Glu] confirms the possibility of the presence of interactions between RNA and IL (Figure 3.6A). Similar observations made by Dipak et al. are attributed to multimodal binding in nucleic acids.[33] A similar trend in the absorption spectra for RNA-[Ch][Asp] was also observed (Figure 3.6B). The intercalation mode of EB binding to RNA can be confirmed from the hypochromic and bathochromic shifts (Figure 3.6C), which aligns with the

previous report.[54] The addition of IL to the RNA-EB complex showed hyperchromism at 280 nm, whereas no spectral shift for the peak at 480 nm (corresponding to the EB probe) appeared. No significant change in the spectra of EB on the addition of ILs indicates no binding between them, as shown in Figure 3.6D.
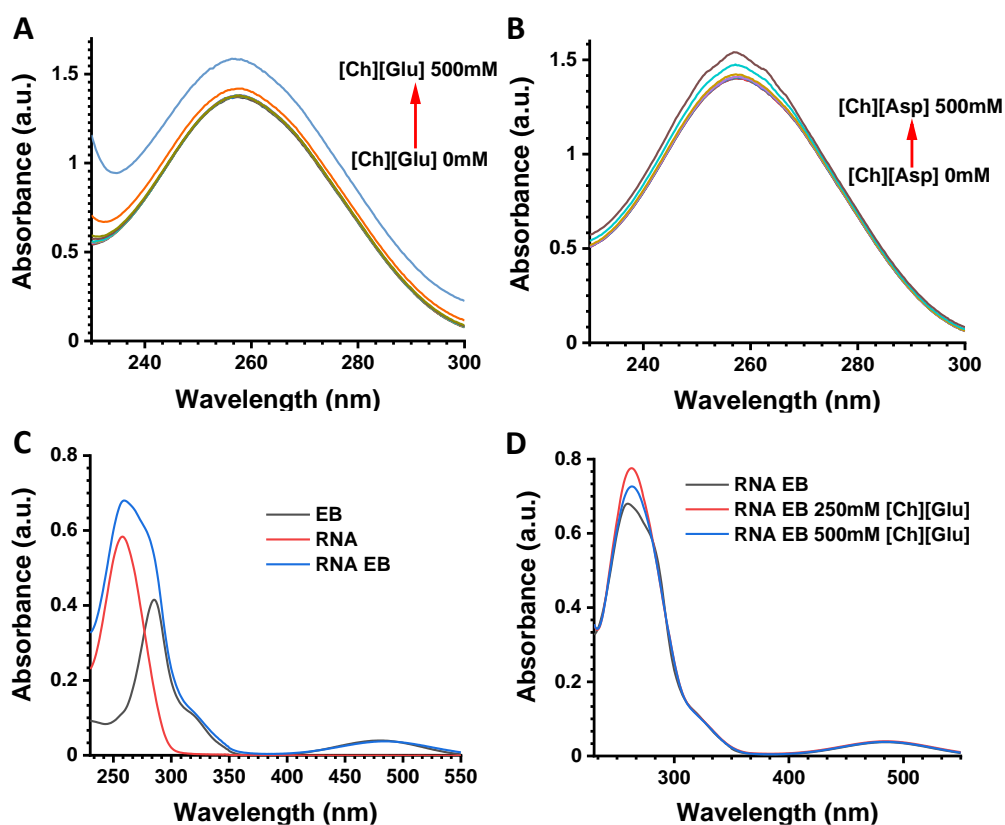
Figure 3.6. Steady-state absorption spectra in phosphate buffer solution (PBS): A) Increasing concentration of [Ch][Asp] in RNA upto 500 mM; B) Increasing concentration of [Ch][Asp] in RNA upto 500 mM; C) RNA, EB, and RNA-EB complex; D) RNA-EB complex in presence of [Ch]Glu] IL upto 500 mM concentration.

As the RNAs have low fluorescence quantum yields, the fluorescence probes such as EB and DAPI are ideal and valuable probes to investigate the structural dynamics of RNA through steady-state and time-resolved fluorescence measurements. Thus, an optimization for the concentration of EB probes to attain maximum binding with RNA was necessary. First, fluorescence emission measurements were carried out by increasing

the concentration of ILs. A gradual increase of both ChAAIL's concentrations resulted in a decrease in the fluorescence intensity of RNA (Figure 3.7 A, B). Here the quenching is attributed to a direct displacement of EB by ILs from the RNA-EB complex. The corresponding Stern-Volmer plots of [Ch][Glu] and [Ch][Asp] give values of 0.00183 and 0.00194 mM-1, respectively (Figure 3.7 C), indicating that the binding strength of both ChAAILs is comparable. Interestingly, this also suggests that the cationic counterpart (Ch) has a significant role in binding, whereas the anionic counterpart only contributes through charge stabilization. A similar observation for the other fluorescent probe (DAPI) that has groove binding with RNA confirms that ChAAILs have both intercalative and groove binding with RNA as ILs displace both the fluorescent probes (Figure 3.7 D-F). These dye displacement results are per previous reports where ILs are found to displace fluorescent probes efficiently.[30, 33]
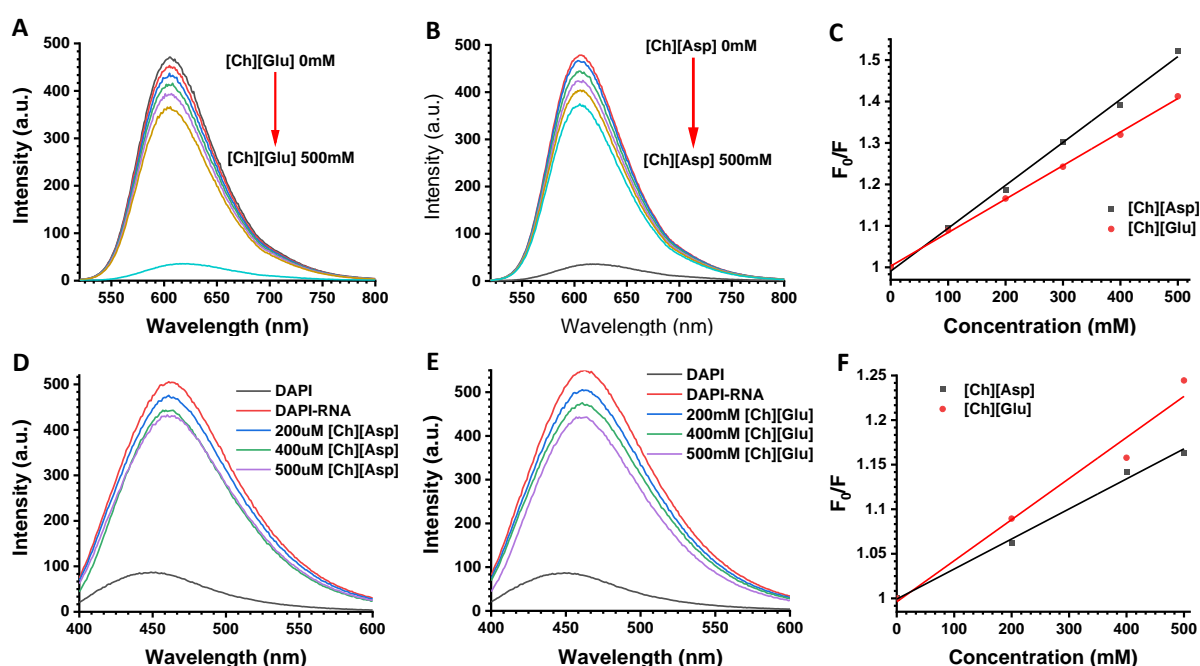
Figure 3.7: Steady-state emission spectra in phosphate buffer solution (PBS): A) Increasing concentration of [Ch][Glu] in RNA-EB complex upto 500 mM; B) Increasing concentration of [Ch][Asp] in RNA-EB complex upto 500 mM; C) Stern-Volmer plot for RNA-EB complex in presence of [Ch][Glu] and [Ch][Asp]; D) Increasing concentration

of [Ch][Glu] in RNA-DAPI complex upto 500 mM; E) Increasing concentration of [Ch][Asp] in RNA-DAPI complex upto 500 mM; F) Stern-Volmer plot for RNA-DAPI complex in presence of [Ch][Glu] and [Ch][Asp].

A. Pabbathi et al. attribute the decrease in fluorescence intensity to the displacement of DAPI by morpholinium-based ILs in DNA and propose that ILs have a multimodal binding with nucleic acids. Dye displacement studies by Dipak et al. also affirm that Ch can preferentially displace EB and DAPI from DNA.

Though the interaction between ChAAILs and RNA happens in a shorter period (ps or ns time scale regime), getting more insights into structural dynamics using the time-resolved fluorescence is critical. Figure 3.8A shows the fluorescence decay profiles for the RNA-EB complex in the presence of [Ch][Glu]. The decay of the EB probe follows a single exponential with a lifetime of 1.77 ns. However, in the presence of RNA, it decays bi-exponentially with a short ($\tau1$) and longer ($\tau2$) component of 1.97 ns and 20 ns, respectively. The corresponding amplitudes of these decays are 0.07 and 0.93 for free EB and RNA-bound EB. These findings agree with the report by Cui et al., which mentions a lifetime of 20.43 ns for RNA-EB complex.[55] Nevertheless, our results confirm the maximum binding of EB to RNA. Upon addition of ILs, the fluorescence decay profiles can be fitted to tri-exponential.
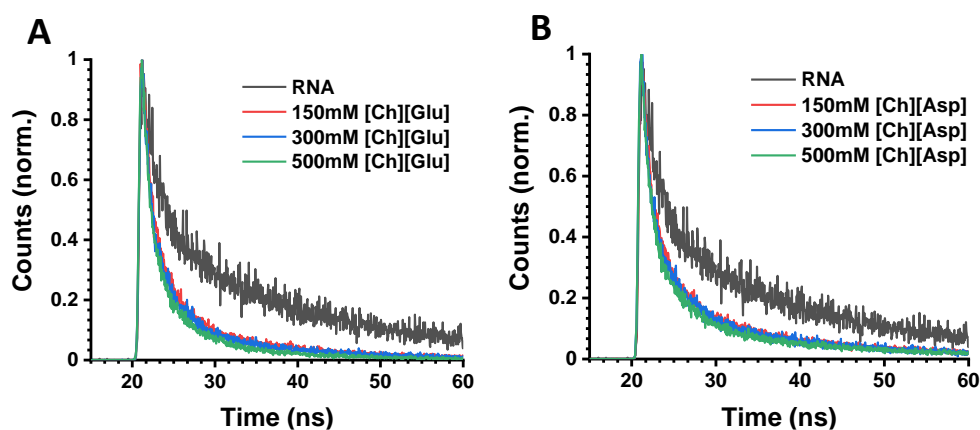
Figure 3.8. Time-resolved emission spectra in phosphate buffer solution (PBS): A) Increasing concentration of [Ch][Glu] in RNA-EB complex upto 500 mM; B) Increasing concentration of [Ch][Asp] in RNA-EB complex upto 500 mM.

The third component confirms the complexation with ILs. τ1 and τ2, in this case, are ca. 1 and 18 ns, respectively, whereas the third component (τ3) is ca. 4 ns. The increase in the concentration of ILs results in a moderate increase in lifetime. Similar observations are made for [Ch][Asp] IL, shown in Figure 3.8B. Thus, the results are consistent among [Ch][Glu] and [Ch][Asp] (Table 3.1).

Table 3.1. Fluorescence decay parameters of free EB, EB-RNA, and EB-RNA complex in the presence of increasing concentrations of ChAAILs.

Sample	IL-1 (mM)	IL-2 (mM)	τ1 (ns)	τ2 (ns)	τ3 (ns)
EB	0	0	1.77(1.00)		
EB+RNA	0	0	1.96(0.07)	18.80(0.93)	
EB+RNA+IL-1	150	-	1.05(0.19)	18.77(0.42)	3.95(0.39)
EB+RNA+IL-1	300	-	1.08(0.23)	18.11(0.35)	4.18(0.42)
EB+RNA+IL-1	500	-	1.06(0.21)	18.69(0.34)	4.23(0.44)
EB+RNA+IL-2	-	150	1.04(0.22)	18.77(0.39)	3.95(0.39)
EB+RNA+IL-2	-	300	1.07(0.23)	18.11(0.37)	4.15(0.40)
EB+RNA+IL-2	-	500	1.06(0.24)	18.69(0.34)	4.20(0.42)

[a] a_i are the pre-exponential factors given in parenthesis represent the fractional contribution of each lifetime component.

3.3.3 Thermodynamic behavior of RNA

The thermodynamic behavior of RNA in the presence of ILs was analysed using ITC. We titrated RNA against EB to determine its binding constant (Kb), 4×10^4 mol^{-1} (Figure 3.9A). The binding affinities of ILs with RNA were calculated by titrating EB against RNA. A higher concentration of ILs is required, owing to their smaller ionic size. The

integrated heat data of RNA in the absence and presence of ILs with a single binding site model fitting ($\chi 2$ = .97) are provided in the Figure 3.9B and C. Table 3.2 shows the thermodynamic parameters, indicating the Kb of [Ch][Glu] and [Ch][Asp] to be 0.4 x 10^3 and 0.6 x 10^3, respectively. The binding affinity for RNA-IL complexes are 100-fold less compared to the binding of EB with RNA. The free energies of binding (ΔG) are ca. -3.57 and -3.91 kcal.mol^{-1} for [Ch][Asp] and [Ch][Glu], respectively, which confirms that both ChAAILs are binding to RNA with equal strength.

Table 3.2. ITC experimental data[a] obtained from fitting of molar heats plotted for RNA against molar ratio of CAAILs.

Sample	N	$K_b x 10^3$ mol^{-1}	ΔG kcal mol^{-1}
EB_RNA	0.97	40	-6.31
RNA_100mM [Ch] [Asp]	1.40	0.4	-3.57
RNA_100mM [Ch] [Glu]	1.53	0.6	-3.91

[a] Binding Stoichiometry (N), Binding Affinity (K_b), D-A distance (ΔG).
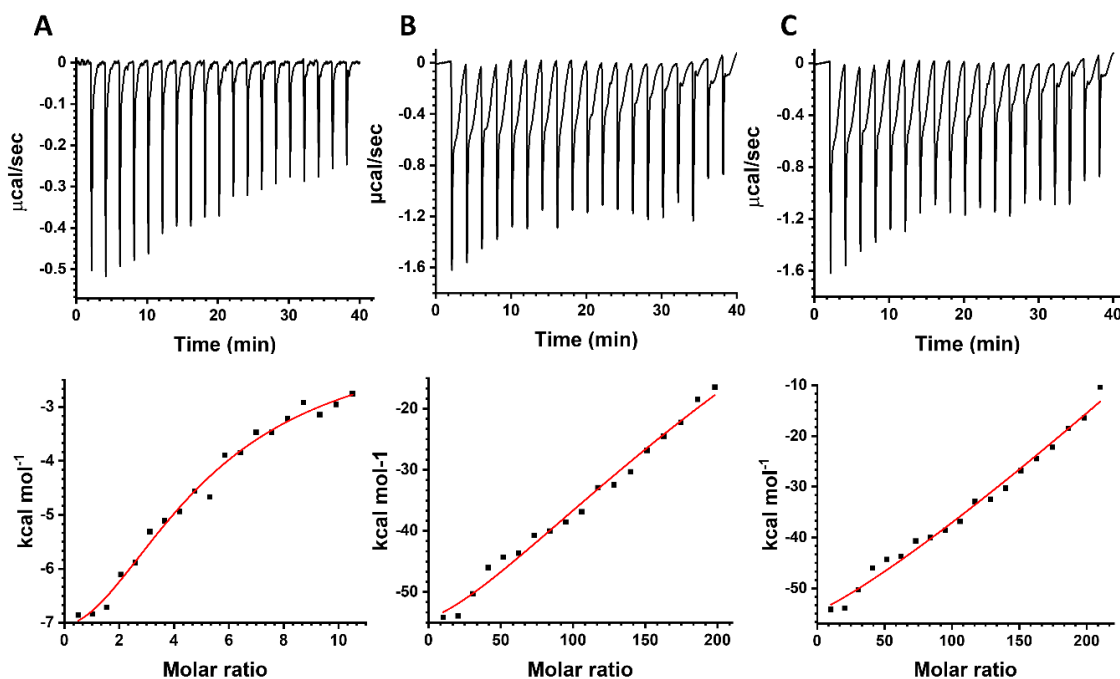
Figure 3.9. *(A) ITC isotherms of RNA binding buffer with EB along with plot obtained by converting the result into molar heats and plotted against the EB to RNA molar ratio (B) ITC isotherms of RNA binding buffer with 100mM [Ch][Glu] IL along with plot obtained by converting the result into molar heats and plotted against the IL to RNA molar ratio (C) ITC isotherms of RNA binding buffer with 100mM [Ch][Asp] IL along with plot obtained by converting the result into molar heats and plotted against the [Ch][Asp] IL to RNA molar ratio.*

3.3.4 Dynamic insights of ChAAIL-RNA interaction up to microsecond regime

In the above section, we recognized the binding mode between ILs and RNA. The predicted binding free energies from the docking calculations are validated using ITC. However, detailed insight is necessary to reveal the dynamic pattern of such interaction, which is possible using molecular dynamic simulations. This analysis uses trajectories of RNA-[Ch][Glu] and RNA-[Ch][Asp] of 1 µs time scale. The corresponding Root Mean-Squared Deviation (RMSD) profiles are shown in Figure 3.10. The conformational dynamicity of RNA achieves states of equilibrium by 0.3 µs timescale. Although RMSD

offers a straight line (deviation <2 Å), it is necessary to compare the dynamic pattern of RNA in the absence of ILs.[56] A control simulation of the only RNA calculation with an equivalent timescale shows that equilibration was achieved <100 ns timescale (Figure 3.10A and B). Furthermore, the deviation in the remaining timescale is comparable to that in the presence of ILs.

The binding preferences of Cholinium cations are primarily in the minor groove region of RNA (Figures 3.10C and D). However, we observed multimodal (heterogeneity) binding. For the natural and modified nucleobase of RNA, we refer the readers to PDB code: 1EHZ. Additionally, to determine the global structural changes among the three simulation systems, RMSDs are taken as a reference to calculate interaction network fidelity (INF) and deformation index (DI).[52] The mentioned parameters help to analyze the structural stability and packing of nucleic acid structures from the simulation snapshots.[57] A strong emphasis on these parameters in the context to three-dimensional RNA structures was discussed earlier by Parisien et al. INF describes the conservation of base-base pairing and the stacking interactions.[56] Identical conservation in successive snapshots scores 1, whereas no conservation scores 0. In this concern, Kührová et al. reported INF as a reliable tool to determine the correct folding of RNA structures than RMSD.[58]
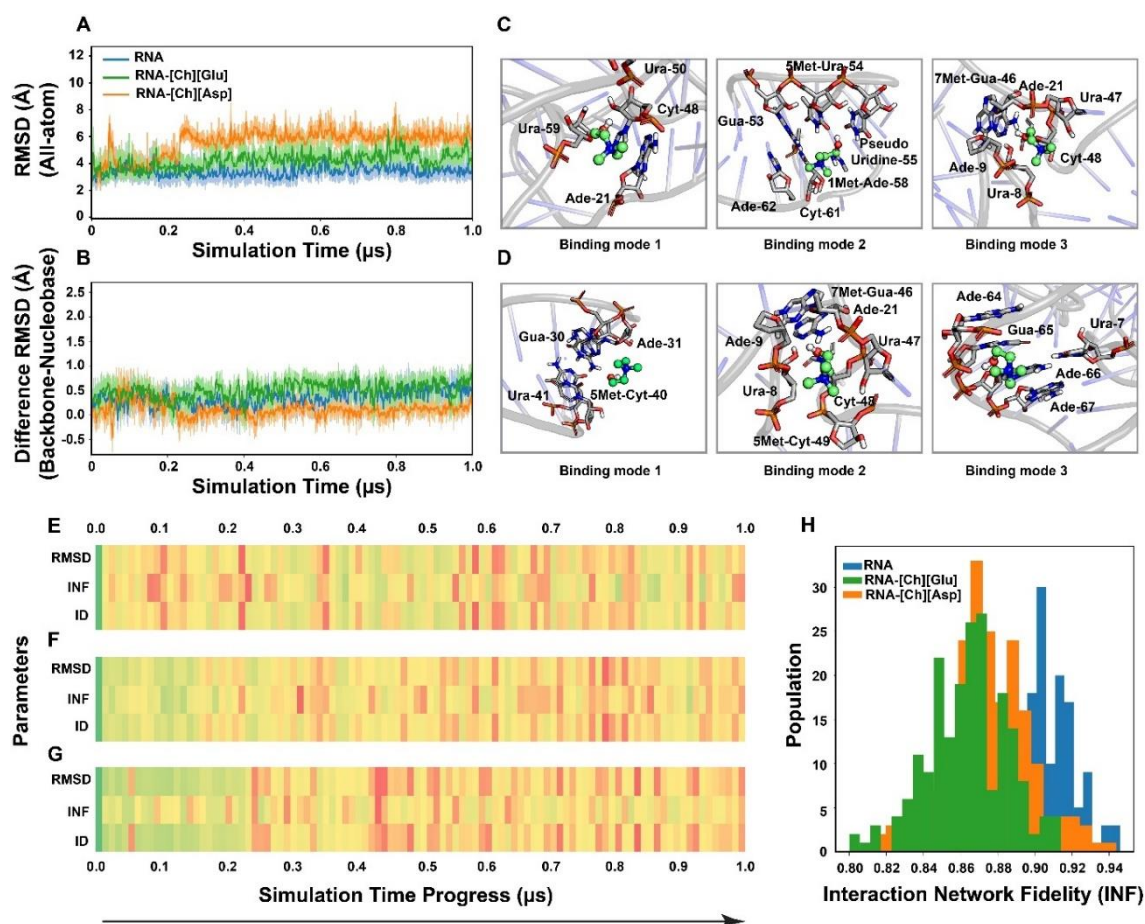
Figure 3.10. A) Time-dependent RMSD analysis of equilibrated structures of RNA. B) Comparison of the backbone with nucleobase dynamics, with difference RMSD. Representation of RNA structure and putative binding of [Ch][Glu] system (among the multimodal binding interaction found in trajectory) for C) [RNA][Ch][Glu] and D). [RNA][Ch][Asp]. Structural analysis of RNA across the simulation progress using the parameters Root-Mean Squared Deviation (RMSD), Interaction Network Fidelity (INF), and Deformation Index (DI), for E) RNA alone, F) RNA-[Ch][Glu], and G) RNA-[Ch][Asp]. The color scheme represents high (green) to low (red) values. H) Histogram plot to show the population of calculated INF values in three systems.

DI parameter accounts for the RMSD and INF to evaluate the ratio between the structural dynamics and base-pair interaction. Figure 3.10 also shows the INF and DI values calculated for snapshots at an interval of 10 ns. A significant deviation in RNA structures occurs when they are with [Ch][Glu] and [Ch][Asp] (Figure 3.10F and G), up to a timescale of 0.25 µs, which is not present in the case of RNA alone (Figure 3.10E).

Nevertheless, the qualitative pattern among both ChAAILs-RNA remains comparable. The INF value for the rest of the timescale remains within 0.8 to 0.9 among the three systems. It also indicates no structural deformation or significant perturbation to the secondary structure of RNA in the presence of ILs.

3.3.5 Conformational stability and regeneration study

Fluorescence correlation spectroscopic (FCS) studies were carried out to investigate the structural integrity of RNA in the presence of IL. FCS provides information about the hydrodynamic radius and diffusion time of the bio-macromolecules. It is known that no significant perturbation tends to occur in DAPI-bound DNA structures in the presence of ILs.[30] In this study, we collected FCS data for DAPI and DAPI-RNA samples (Figure 3.11A). The correlation fluorescence data plots of DAPI−RNA and with ChAAILs are shown in Figure 3.11B, and C.

RNA's hydrodynamic radius (R_H) alone is estimated to be 7 ± 1 nm, which aligns with the reported data.[59-61] The R_H values in the presence of ILs are plotted against the concentrations of ILs (Figure 3.11D). The R_H value does not change significantly with the increased concentration of IL.

Analysis of the thermodynamic stability of RNA-IL binding was undertaken with the UV melting measurements.[62-63] Here, the increase in temperature is responsible for the release of stacking between nucleobases. It results in a strong-hyperchromic shift in absorbance spectra. The melting curves for RNA alone and in the presence of ChAAILs for absorbance at 260 nm are shown in Figure 3.12A. RNA's melting temperature (Tm) is 65 °C, which agrees with the reported literature.[62] Adding ChAAILs leads to an increase in the Tm by 5 °C. The increase in Tm of RNA in the presence of ChAAILs indicates that RNA is more stable in the presence of ILs, which follows the previous reports by Pedro

et al.[40] They showed that Tm of sRNA increases by almost 9 °C in the presence of Ch[DHP] IL, thus providing additional stability to RNA. Similar observations by Quental et al. observed extra stability to RNA by an increase in Tm ca. 14 °C.[41]
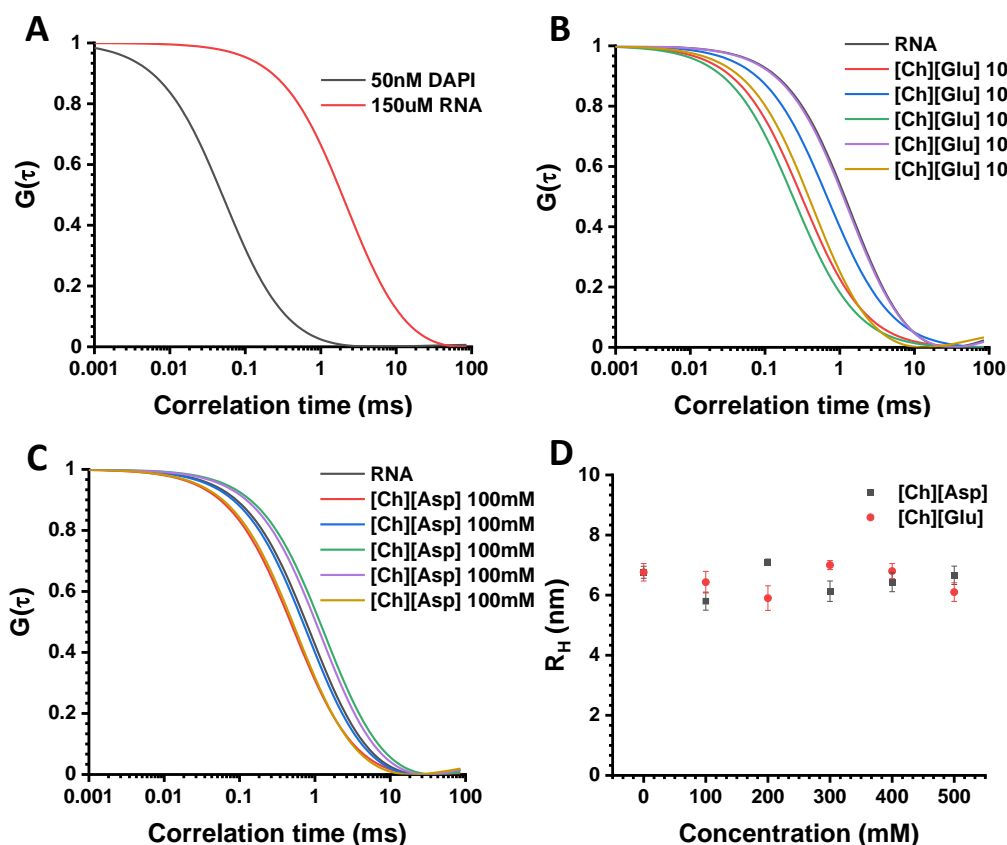
Figure 3.11. A) Normalised autocorrelation function of DAPI and RNA bound DAPI (~50 nM) B) Normalised autocorrelation function of RNA bound DAPI (~50 nM) in increasing concentration of [Ch][Glu] IL C) Normalised autocorrelation function of RNA bound DAPI (~50 nM) in increasing concentration of [Ch][Asp] IL. D) hydrodyna.mic radius (R_H) of RNA as a function of the concentration of [Ch][Glu] and [Ch][Asp] IL

The INF analysis based on snapshots from MD simulations also reveals the differential behavior for RNA in the presence of [Ch][Glu] and [Ch][Asp] compared to RNA alone (Figure 3.10H). Such confirmation for the long-term stability of nucleic acid structures in the presence of Ch and imidazolium ILs binding with DNA is also reported based on MD simulations.[64] This increment in Tm is attributed to the fact that ILs add stability to the

secondary structure of RNA. However, it also indicates the possibility of multimodal binding because a single preference for groove binding cannot increase stabilization. Such observations align with DNA's properties in the presence of ILs.[33]
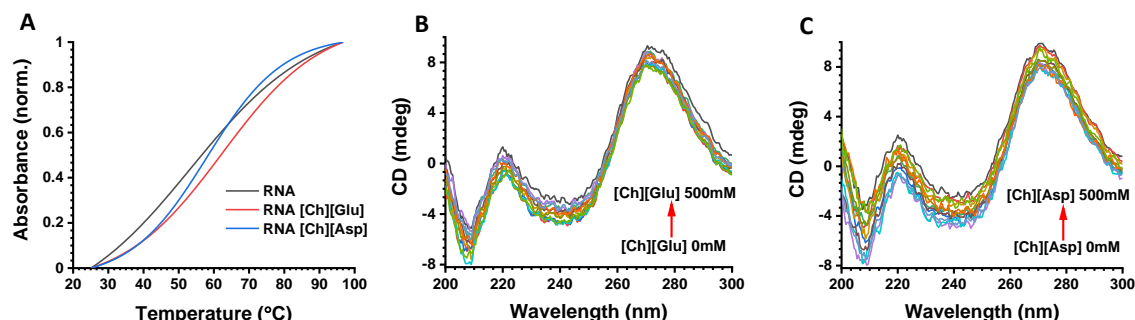
Figure 3.12. Structural stability and conformational analysis of RNA in the presence of ILs: (A) Hydrodynamic radius (R_H) of RNA as a function of the concentration of [Ch][Glu] and [Ch][Asp] IL (B) Melting curves of RNA and RNA in 50mM [Ch][Glu] IL and [Ch][Asp] IL (C) CD spectra of RNA with increasing concentration of [Ch][Glu] up to 100mM (D) CD spectra of RNA with increasing concentration of [Ch][Asp] up to 100mM (E) CD spectra of preserved RNA samples in ChAAILs (F) Absorption spectra of preserved and extracted RNA samples from ChAAILs.

The assessment of dynamic insights and structural perturbations is possible using CD spectroscopy. It is a well-known fact that the secondary structure of RNA has A-type double-stranded helices.[65] It gives a characteristic positive peak at 270 nm with a molar ellipticity of 9 mdeg and two negative peaks at 241 and 210 nm with corresponding molar ellipticity of -2.5 and -5 mdeg, respectively. CD measurements of our sample with an increasing concentration of ChAAILs are in Figures 3.12B and C. No substantial changes occur in both positive and negative peaks of RNA upon binding to ILs. It remains constant even after adding 500 mM IL, which provides additional validity that RNA structures retain their structural stability in ChAAILs. The minimal change in CD spectra in the presence of ILs is as per the previous reports,[33, 40] where it is observed that ILs do not alter the conformation of nucleic acids. We further compare the CD spectra of stored and

extracted RNA from IL solution (after 3 weeks) using the same method. Figure 3.13 A shows no change in the confirmation of extracted RNA.

The absorption spectra of the RNA sample extracted from the IL solution are shown in Figure 3.13 B. The ratio between the absorbance at 260 and 280nm confirms the stable conformation of the stored sample. These observations prove that no structural degradation or significant perturbation to the three-dimensional structure of the RNA happens in the solution containing ILs. Furthermore, this is also in good agreement with the observations made from the MD trajectories, where no significant difference in RNA structures (RMSD and INF analysis – Figure 3.10) with and without ILs.
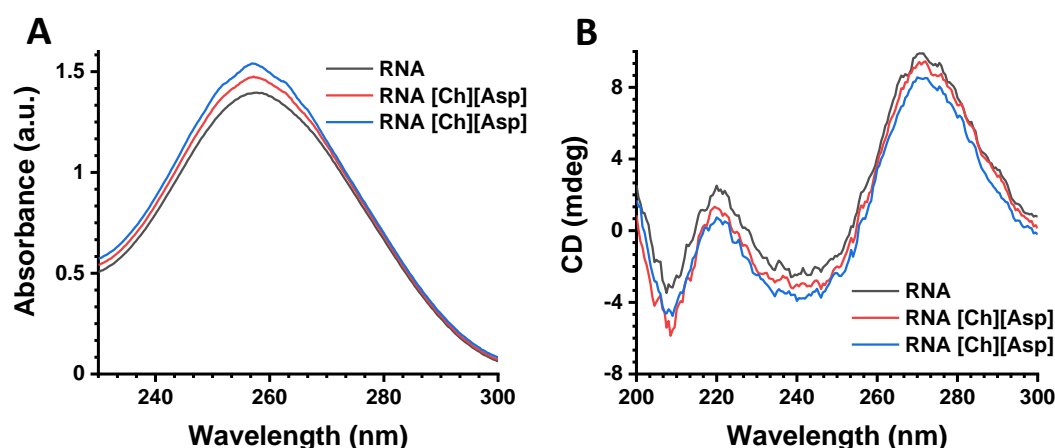
Figure 3.13. A) Absorption spectra of preserved and extracted RNA samples from ChAAILs. B) CD spectra of preserved and extracted RNA samples from ChAAILs.

3.3.6 RNA-IL binding is driven by electrostatic interaction

For additional insights into structural dynamics, we turned to the calculated trajectories. No evidence is available from the RMSD and base-stacking RNA analysis to indicate any significant structural perturbations. The analyzed binding modes of Ch determine the proximal distance (min) between any atom of RNA and ligand (Figure 3.14), where min < 0.4 nm represents a very close interaction between Ch and RNA. However, the

fluctuation in the min distance denotes that ILs interact in several instances in the simulation.
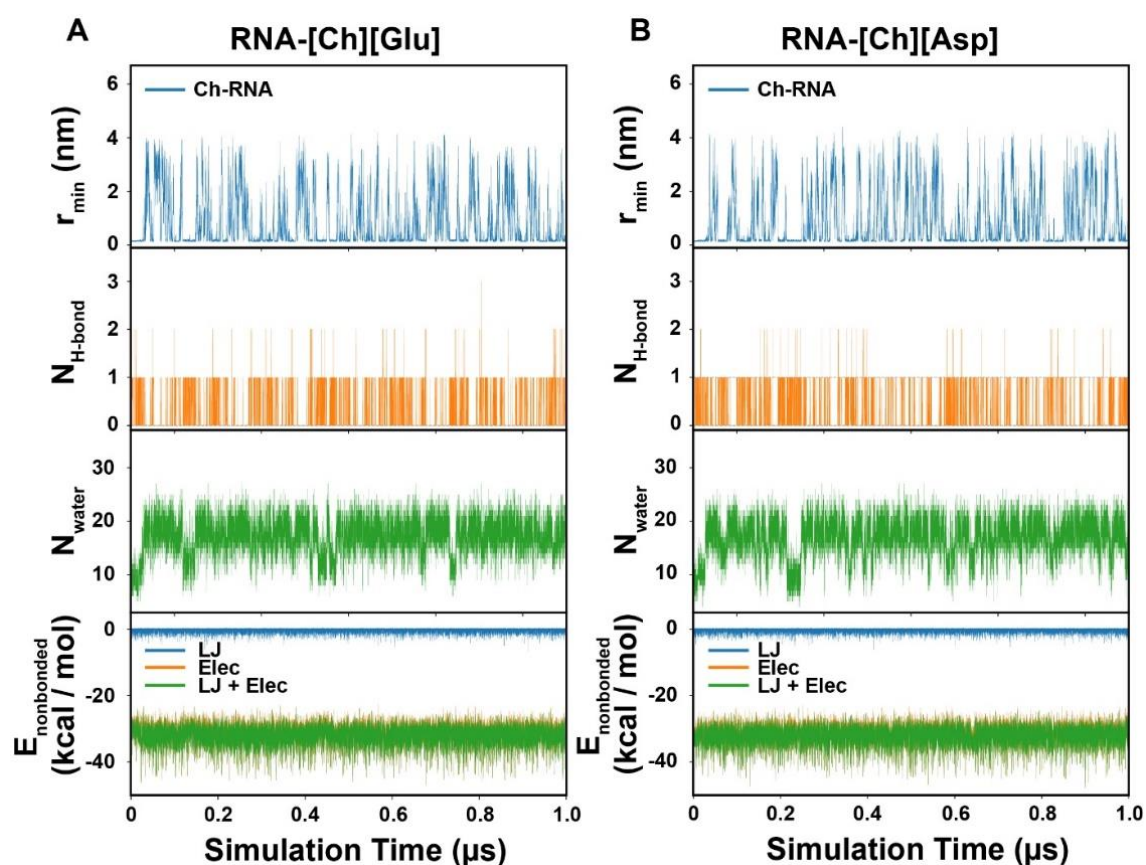
Figure 3.14. Dynamic insights from ChAAILs interaction with RNA: (A) RNA-[Ch][Glu] and (B) RNA-[Ch][Asp]. rmin denotes the proximal distance (nm units) between Ch and RNA, NH-bond¬ represents the number of hydrogen bonds between RNA and Ch molecule, and Nwater indicates the number of water molecules in the near shell of Ch molecule (0.3 nm). The energetics of interaction between Ch and the rest of the system is shown in terms of individual contribution (kcal/mol units) from Lennard-Jones (LJ) and Electrostatic (Elec).

More evidence of binding between Ch and RNA is available through the number of hydrogen bonds. These hydrogen bonds mostly form between the positively charged Ch and the negatively charged phosphate group. These data also indicate that a lower min value in simulation time is because of one or more H-bonds. The water molecules present in the close shell of Ch also mediate the multimodal binding with RNA. These

observations are in good agreement with the experimental measurements. Further, we compared these data with the behavior of IL binding to DNA. We found that in the case of RNA, the binding is comparatively weak, as indicated by the binding free energy, H-bonds, and the r-min distance.

The energetic contribution analysis focuses on the non-bonded interaction between Ch and the rest of the system (RNA, water molecules, and counterions). The hydrophobic contribution (Lennard-Jones) in the Ch dynamics is negligible and appears as ca. -3 kcal.mol^{-1}. However, the driving force in these simulations is the electrostatic interaction. Such energetic contribution accounts for ca. -35 kcal.mol^{-1}. This is obvious because the Ch binding is mainly through the H-bonding. Thus, we conclude that IL binding with RNA is mediated not by the surface-bound state but by the groove-bound state. At the same time, the critical stabilization force is not through the hydrophobic and van der Waals forces. Our simulation results also confirm that the amino acid counterpart imparts no significant difference in the overall behavior. These observations agree with the spectral features from UV-Vis, fluorescence, and CD spectroscopy.

3.3.7 ILs-RNA interaction for potential application

ILs are valuable alternatives to organic solvents because of their superior physiochemical properties, like low toxicity, low chemical reactivity, high thermal stability, low inflammability, and high conductivity. [Ch] has been recognized as central to ILs due to the fact they are less cytotoxic, biodegradable, and easily synthesizable based on green chemistry.[66] On the other hand, a wide variety of anionic counterparts of ILs with [Ch] has been reported in conjunction with nucleic acids, including chlorides, acesulfamates, and bis(trifluoromethylsulfonyl)imides[67]; imidazolium-based[68]; morpholinium-based[30]; pyridinium-based[69]; glycolate and pyruvate-based[31]; and glycolateacetate and dihydrogen

phosphate[70]. Though all of these anionic counterparts have reported multimodal binding, they are either not acceptable for routine use of ILs due to expensive chemical routes of synthesis, differential chemical stability, and non-biodegradability. Furthermore, the level of cytotoxicity is different, which otherwise is higher compared to AAILs.[71]

Long-term RNA storage with marked extract efficacy is challenging and an evolving research field. Other than biochemical use, RNA also has potential pharmaceutical applications. For example, RNA robed with ammonium-based ILs are useful prodrugs for dermatological treatment.[72] Likewise, in another study, it is evidenced that topical delivery of RNA using ammonium-based ILs has remarkable therapeutic efficacy.[73] Hence, ILs can also be useful drug delivery agents for RNA. Since ILs facilitate additional RNA stability, they also have the potential to trigger new direction for their use in pharmaceutical and biotechnology.

Since ILs are salts with organic cations or anions, having irregular structures to delocalize their charges. The chemical shape of these molecules and low charges allow these molecules to (i) avoid tight packing during crystallization and (ii) acquire the property of low melting points. Considering the amino acid-based ILs (AAILs), polarity is the important factor determining their efficacy. This property determines the solubility of solute, miscibility with other solvents, and its reaction efficiency as a solvent, the polarizability of AAILs must be compared for their usefulness in specific applications. According to the Kamlet-Taft parameters for a series of AAILs the polarizability ranges from a minimum 1.04 [Val] to maximum 1.13 [Asp] and [Glu].[74] Thus, we hypothesized that AAILs, irrespective of the amino acid counterpart, could display identical behaviour when used as a solvent medium for RNA.

3.4 CONCLUSIONS

Herein, we elucidate the molecular-level understanding of the structural perturbation of RNA induced through choline amino acid-based ILs. The initial hypothesis for structural factors driving the interaction between ILs and RNA is obtained using computational modeling. The experimental validation of these findings is possible with suitable techniques such as steady-state fluorescence, UV-Vis absorbance, circular dichroism spectroscopy, and isothermal titration calorimetry (ITC). Fluorescence co-relation spectroscopy confirms that there is no change in the hydrodynamic radius of RNA in the presence of ILs, revealing the structural integrity of the biomolecule in the IL environment, which is further confirmed by circular dichroism analysis. UV-Vis spectra analysis indicates multimodal binding of CAAILs with RNA, whereas dye displacement studies through fluorescence emission confirm IL molecules' intrusion into the minor groove of RNA.

Interestingly, we found that increases in IL concentration do not affect structural instability. From isothermal titration calorimetry and molecular docking study, the binding energy of ILs with RNA is ≈ -4 kcal/mol, which indicates weaker binding of ILs to RNA. Our results demonstrate that ILs preserves the structural integrity of RNA and hence are helpful as non-toxic and biocompatible solvent. The lower binding energy of ILs with RNA further accounts for RNA extraction from the IL media. The significance of this study lies in the spectroscopic and theoretical evidence that non-cytotoxic and eco-friendly CAAILs are helpful for the extraction and safe storage of RNA. The molecular-level information obtained from the present results can be valuable guidance for designing suitable ILs for the in-vivo application of RNA.

Long-term storage of RNA with higher extraction efficacy is challenging and an evolving research field. Zakrewsky et al. have recently shown that RNA robed with ammonium-based ILs are used as a prodrug for treating skin diseases. They have also added that the robed RNA properties are independent of RNA sequence, which opens up the possibility of yeast RNA in ChAAILs to act as a prodrug. Further, Dharamdasani et al. provide evidence of topical delivery of RNA using ammonium-based ILs as an efficient therapeutic strategy. They have shown binary ILs as potential drug delivery agents for RNA while maintaining the drug's efficacy. They reported the contribution of each component of ILs in drug delivery and silencing, which is due to the presence of interactions between RNA and ILs. Thus, the non-covalent interactions present between ILs and RNA that stabilize the structural conformation of the biomolecule trigger to look into the direction of RNA handling and drug delivery. This study also opens up new RNA preservation and extraction routes, which could be useful in storing and preserving other biomolecules.

3.5 REFERENCES

1.   Haque, F.; Pi, F.; Zhao, Z.; Gu, S.; Hu, H.; Yu, H.; Guo, P., RNA versatility, flexibility, and thermostability for practice in RNA nanotechnology and biomedical applications. *WIREs RNA* **2018,** *9* (1), e1452.

2.   Hu, X.-P.; Dourado, H.; Schubert, P.; Lercher, M. J., The protein translation machinery is expressed for maximal efficiency in Escherichia coli. *Nat. Commun.* **2020,** *11* (1), 5260-5269.

3.   Di Giorgio, S.; Martignano, F.; Torcia, M. G.; Mattiuz, G.; Conticello, S. G., Evidence for host-dependent RNA editing in the transcriptome of SARS-CoV-2. *Sci. Adv.* **2020,** *6* (25), eabb5813.

4.   Guo, P., The emerging field of RNA nanotechnology. *Nat. Nanotechnol.* **2010,** *5* (12), 833-842.

5.   Attila Reményi, H. R. S. M. W., Combinatorial control of gene expression. *Nat. Struct. Mol. Biol.* **2004,** *11*, 812-815.

6.   Chandramouly, G.; Zhao, J.; McDevitt, S.; Rusanov, T.; Hoang, T.; Borisonnik, N.; Treddinick, T.; Lopezcolorado, F. W.; Kent, T.; Siddique, L. A.; Mallon, J.; Huhn, J.; Shoda, Z.; Kashkina, E.; Brambati, A.; Stark, J. M.; Chen, X. S.; Pomerantz, R. T., Polθ reverse transcribes RNA and promotes RNA-templated DNA repair. *Sci. Adv.* **2021,** *7* (24), eabf1771.

7.   Mandal, A.; Kumbhojkar, N.; Reilly, C.; Dharamdasani, V.; Ukidve, A.; Ingber, D. E.; Mitragotri, S., Treatment of psoriasis with NFKBIZ siRNA using topical ionic liquid formulations. *Sci. Adv.* **2020,** *6* (30), eabb6049.

8.   Levy, M.; Miller, S. L., The stability of the RNA bases: Implications for the origin of life. *PNAS* **1998,** *95* (14), 7933-7938.

9.   S. Ma, Y. H., R.B. van Huystee, Improved plant RNA stability in storage. *Anal. Biochem.* **2004,** *326* (1), 122-124.

10.   Fabre, A.-L.; Colotte, M.; Luis, A.; Tuffet, S.; Bonnet, J., An efficient method for long-term room temperature storage of RNA. *Eur. J. Hum.* **2014,** *22* (3), 379-385.

11.   Seelenfreund, E.; Robinson, W. A.; Amato, C. M.; Tan, A.-C.; Kim, J.; Robinson, S. E., Long Term Storage of Dry versus Frozen RNA for Next Generation Molecular Studies. *PLoS One* **2014,** *9* (11), e111827.

12.   Puddu, M.; Stark, W. J.; Grass, R. N., Silica Microcapsules for Long-Term, Robust, and Reliable Room Temperature RNA Preservation. *Adv. Healthc. Mater.* **2015,** *4* (9), 1332-1338.

13.   Tateishi-Karimata, H.; Sugimoto, N., Biological and nanotechnological applications using interactions between ionic liquids and nucleic acids. *Biophys. Rev.* **2018,** *10* (3), 931-940.

14.   Introduction: Ionic Liquids. *Chem. Rev.* **2017,** *117* (10), 6633-6635.

15.   Greaves, T. L.; Drummond, C. J., Protic Ionic Liquids: Properties and Applications. *Chem. Rev.* **2008,** *108* (1), 206-237.

16.   Thoppil, A. A.; Chennuri, B. K.; Gardas, R. L., Insights into the structural changes of bovine serum albumin in ethanolammonium laurate based surface active ionic liquids. *J. Mol. Liq.* **2019,** *290*, 111229.

17.   Swatloski, R. P.; Spear, S. K.; Holbrey, J. D.; Rogers, R. D., Dissolution of Cellose with Ionic Liquids. *J. Am. Chem. Soc.* **2002,** *124* (18), 4974-4975.

18.   Sahoo, D. K.; Mundlapati, V. R.; Gagrai, A. A.; Biswal, H. S., Efficient SO2 Capture through Multiple Chalcogen Bonds, Sulfur-Centered Hydrogen Bonds and S••π Interactions: A Computational Study. *ChemistrySelect* **2016,** *1* (8), 1688-1694.

19.   Sahoo, D. K.; Chand, A.; Jena, S.; Biswal, H. S., Hydrogen-bond-driven thiouracil dissolution in aqueous ionic liquid: A combined microscopic, spectroscopic and molecular dynamics study. *J. Mol. Liq.* **2020,** *319*, 114275.

20.   Choi, Y. H.; Verpoorte, R., Green solvents for the extraction of bioactive compounds from natural products using ionic liquids and deep eutectic solvents. *Curr. Opin. Food Sci.* **2019,** *26*, 87-93.

21.   Clark, K. D.; Trujillo-Rodríguez, M. J.; Anderson, J. L., Advances in the analysis of biological samples using ionic liquids. *Anal. Bioanal. Chem.* **2018,** *410* (19), 4567-4573.

22.   Fister, S.; Fuchs, S.; Mester, P.; Kilpeläinen, I.; Wagner, M.; Rossmanith, P., The use of ionic liquids for cracking viruses for isolation of nucleic acids. *Sep. Purif. Technol.* **2015,** *155*, 38-44.

23.   Naushad, M.; Alothman, Z. A.; Khan, A. B.; Ali, M., Effect of ionic liquid on activity, stability, and structure of enzymes: A review. *Int. J. Biol. Macromol.* **2012,** *51* (4), 555-560.

24.   Sahoo, D. K.; Jena, S.; Tulsiyan, K. D.; Dutta, J.; Chakrabarty, S.; Biswal, H. S., Amino-Acid-Based Ionic Liquids for the Improvement in Stability and Activity of Cytochrome c: A Combined Experimental and Molecular Dynamics Study. *J. Phys. Chem. B* **2019,** *123* (47), 10100-10109.

25.   Kumar Sahoo, D.; Devi Tulsiyan, K.; Jena, S.; Biswal, H. S., Implication of Threonine-Based Ionic Liquids on the Structural Stability, Binding and Activity of Cytochrome c. *ChemPhysChem.* **2020,** *21* (23), 2525-2535.

26.   Lin, Y.; Zhao, A.; Tao, Y.; Ren, J.; Qu, X., Ionic Liquid as an Efficient Modulator on Artificial Enzyme System: Toward the Realization of High-Temperature Catalytic Reactions. *J. Am. Chem. Soc.* **2013,** *135* (11), 4207-4210.

27.   Singh, S. K.; Savoy, A. W., Ionic liquids synthesis and applications: An overview. *J. Mol. Liq.* **2020,** *297*, 112038.

28.   Ventura, S. P. M.; e Silva, F. A.; Quental, M. V.; Mondal, D.; Freire, M. G.; Coutinho, J. A. P., Ionic-Liquid-Mediated Extraction and Separation Processes for Bioactive Compounds: Past, Present, and Future Trends. *Chem. Rev.* **2017,** *117* (10), 6984-7052.

29.   Lee, C. K.; Shin, S. R.; Lee, S. H.; Jeon, J.-H.; So, I.; Kang, T. M.; Kim, S. I.; Mun, J. Y.; Han, S.-S.; Spinks, G. M.; Wallace, G. G.; Kim, S. J., DNA Hydrogel Fiber with Self-Entanglement Prepared by Using an Ionic Liquid. *Angew. Chem. Int. Ed.* **2008,** *47* (13), 2470-2474.

30.   Pabbathi, A.; Samanta, A., Spectroscopic and Molecular Docking Study of the Interaction of DNA with a Morpholinium Ionic Liquid. *J. Phys. Chem. B* **2015,** *119* (34), 11099-11105.

31.   Sharma, M.; Mondal, D.; Singh, N.; Trivedi, N.; Bhatt, J.; Prasad, K., High concentration DNA solubility in bio-ionic liquids with long-lasting chemical and structural stability at room temperature. *RSC Adv.* **2015,** *5* (51), 40546-40551.

32.   Zhao, H., DNA stability in ionic liquids and deep eutectic solvents. *J. Chem. Technol. Biotechnol.* **2015,** *90* (1), 19-25.

33.   Sahoo, D. K.; Jena, S.; Dutta, J.; Chakrabarty, S.; Biswal, H. S., Critical Assessment of the Interaction between DNA and Choline Amino Acid Ionic Liquids: Evidences of Multimodal Binding and Stability Enhancement. *ACS Cent. Sci.* **2018,** *4* (12), 1642-1651.

34.   Egorova, K. S.; Posvyatenko, A. V.; Larin, S. S.; Ananikov, Valentine P., Ionic liquids: prospects for nucleic acid handling and delivery. *Nucleic Acids Res* **2021,** *49* (3), 1201-1234.

35.   Pabbathi, A.; Samanta, A., On the Stability and Conformational Dynamics of Cytochrome c in Ammonium Ionic Liquids. *J. Phys. Chem. B* **2020,** *124* (37), 8132-8140.

36.   Ghoshdastidar, D.; Senapati, S., Dehydrated DNA in B-form: ionic liquids in rescue. *Nucleic Acids Res* **2018,** *46* (9), 4344-4353.

37.   Brisco, M. J.; Morley, A. A., Quantification of RNA integrity and its use for measurement of transcript number. *Nucleic Acids Res* **2012,** *40* (18), e144-e144.

38.   Mamajanov, I.; Engelhart, A. E.; Bean, H. D.; Hud, N. V., DNA and RNA in Anhydrous Media: Duplex, Triplex, and G-Quadruplex Secondary Structures in a Deep Eutectic Solvent. *Angew. Chem. Int. Ed.* **2010,** *49* (36), 6310-6314.

39.   Mazid, R. R.; Divisekera, U.; Yang, W.; Ranganathan, V.; MacFarlane, D. R.; Cortez-Jugo, C.; Cheng, W., Biological stability and activity of siRNA in ionic liquids. *Chem. Commun.* **2014,** *50* (88), 13457-13460.

40.   Pedro, A. Q.; Pereira, P.; Quental, M. J.; Carvalho, A. P.; Santos, S. M.; Queiroz, J. A.; Sousa, F.; Freire, M. G., Cholinium-Based Good's Buffers Ionic Liquids as Remarkable Stabilizers and Recyclable Preservation Media for Recombinant Small RNAs. *ACS Sustain. Chem. Eng.* **2018,** *6* (12), 16645-16656.

41.   Quental, M. V.; Pedro, A. Q.; Pereira, P.; Sharma, M.; Queiroz, J. A.; Coutinho, J. A. P.; Sousa, F.; Freire, M. G., Integrated Extraction-Preservation Strategies for RNA Using Biobased Ionic Liquids. *ACS Sustain. Chem. Eng.* **2019,** *7* (10), 9439-9448.

42.   Boo, S. H.; Kim, Y. K., The emerging role of RNA modifications in the regulation of mRNA stability. *Exp. Mol. Med.* **2020,** *52* (3), 400-408.

43.   Liu, Q.-P.; Hou, X.-D.; Li, N.; Zong, M.-H., Ionic liquids from renewable biomaterials: synthesis, characterization and application in the pretreatment of biomass. *Green Chem.* **2012,** *14* (2), 304-307.

44.   Lakowicz, J. R., *Principles of fluorescence spectroscopy*. Springer science & business media: 2013.

45.   Lehmann, J.; Jossinet, F.; Gautheret, D., A universal RNA structural motif docking the elbow of tRNA in the ribosome, RNAse P and T-box leaders. *Nucleic Acids Res* **2013,** *41* (10), 5494-5502.

46.   Balasubramani, S. G.; Chen, G. P.; Coriani, S.; Diedenhofen, M.; Frank, M. S.; Franzke, Y. J.; Furche, F.; Grotjahn, R.; Harding, M. E.; Hättig, C.; Hellweg, A.; Helmich-Paris, B.; Holzer, C.; Huniar, U.; Kaupp, M.; Marefat Khah, A.; Karbalaei Khani, S.; Müller, T.; Mack, F.; Nguyen, B. D.; Parker, S. M.; Perlt, E.; Rappoport, D.; Reiter, K.; Roy, S.; Rückert, M.; Schmitz, G.; Sierka, M.; Tapavicza, E.; Tew, D. P.; van Wüllen, C.; Voora, V. K.; Weigend, F.; Wodyński, A.; Yu, J. M., TURBOMOLE: Modular program suite for <i>ab initio</i> quantum-chemical and condensed-matter simulations. *J. Chem. Phys.* **2020**.

47.   Morris, G. M., Huey, R., Lindstrom, W., Sanner, M. F., Belew, R. K., Goodsell, D. S., & Olson, A. J. , AutoDock4 and AutoDockTools4: Automated docking with selective receptor flexibility. *J. Comput. Chem.* **2009,** *30*, 2785-2791.

48.   Forli, S.; Huey, R.; Pique, M. E.; Sanner, M. F.; Goodsell, D. S.; Olson, A. J., Computational protein–ligand docking and virtual drug screening with the AutoDock suite. *Nat. Protoc.* **2016,** *11* (5), 905-919.

49.   Cieplak, P.; Cornell, W. D.; Bayly, C.; Kollman, P. A., Application of the multimolecule and multiconformational RESP methodology to biopolymers: Charge derivation for DNA, RNA, and proteins. *J. Comput. Chem.* **1995,** *16* (11), 1357-1377.

50.   Aduri, R.; Psciuk, B. T.; Saro, P.; Taniga, H.; Schlegel, H. B.; SantaLucia, J., AMBER Force Field Parameters for the Naturally Occurring Modified Nucleosides in RNA. *J. Chem. Theory Comput.* **2007,** *3* (4), 1464-1475.

51.   Roe, D. R.; Cheatham, T. E., PTRAJ and CPPTRAJ: Software for Processing and Analysis of Molecular Dynamics Trajectory Data. *J. Chem. Theory Comput.* **2013,** *9* (7), 3084-3095.

52.   Gendron, P.; Lemieux, S.; Major, F., Quantitative analysis of nucleic acid three-dimensional structures11Edited by I. Tinoco. *J. Mol. Biol.* **2001,** *308* (5), 919-936.

53.   Biver, T., Use of UV-Vis Spectrometry to Gain Information on the Mode of Binding of Small Molecules to DNAs and RNAs. *Appl. Spectrosc. Rev.* **2012,** *47* (4), 272-325.

54.   Gatti, C., Houssier, C., & Fredericq, E. , Binding of ethidium bromide to ribosomal RNA. Absorption, fluorescence, circular and electric dichroism study. *Biochim. Biophys. Acta* **1975,** *, 407* (3), 308–319.

55.   Cui, H. H.; Valdez, J. G.; Steinkamp, J. A.; Crissman, H. A., Fluorescence lifetime-based discrimination and quantification of cellular DNA and RNA with phase-sensitive flow cytometry. *Cytometry A* **2003,** *52A* (1), 46-55.

56.   Šponer, J.; Bussi, G.; Krepl, M.; Banáš, P.; Bottaro, S.; Cunha, R. A.; Gil-Ley, A.; Pinamonti, G.; Poblete, S.; Jurečka, P.; Walter, N. G.; Otyepka, M., RNA Structural Dynamics As Captured by Molecular Simulations: A Comprehensive Overview. *Chem. Rev.* **2018,** *118* (8), 4177-4338.

57.   Bottaro, S.; Di Palma, F.; Bussi, G., The role of nucleobase interactions in RNA structure and dynamics. *Nucleic Acids Res* **2014,** *42* (21), 13306-13314.

58.   Kührová, P.; Banáš, P.; Best, R. B.; Šponer, J.; Otyepka, M., Computer Folding of RNA Tetraloops? Are We There Yet? *J. Chem. Theory Comput.* **2013,** *9* (4), 2115-2125.

59.   Bernacchi, S., Dynamic Light Scattering Analysis on RNA Associated to Proteins. In *RNA Spectroscopy: Methods and Protocols*, Arluison, V.; Wien, F., Eds. Springer US: New York, NY, 2020; pp 31-39.

60.   Borodavka, A.; Singaram, S. W.; Stockley, P. G.; Gelbart, W. M.; Ben-Shaul, A.; Tuma, R., Sizes of Long RNA Molecules Are Determined by the Branching Patterns of Their Secondary Structures. *Biophys J* **2016,** *111* (10), 2077-2085.

61.   Harvey, J. D., Diffusion coefficients and hydrodynamic radii of three spherical RNA viruses by laser light scattering. *Virol.* **1973,** *56* (1), 365-368.

62.   Wu, P.; Nakano, S.-i.; Sugimoto, N., Temperature dependence of thermodynamic properties for DNA/DNA and RNA/DNA duplex formation. *Eur. J. Biochem.* **2002,** *269* (12), 2821-2830.

63.   Puglisi, J. D.; Tinoco, I., Absorbance melting curves of RNA. In *Meth. Enzymol.*, Academic Press: 1989; Vol. 180, pp 304-325.

64.   Chandran, A.; Ghoshdastidar, D.; Senapati, S., Groove Binding Mechanism of Ionic Liquids: A Key Factor in Long-Term Stability of DNA in Hydrated Ionic Liquids? *J. Am. Chem. Soc.* **2012,** *134* (50), 20330-20339.

65.   Moore, D. S.; Wagner, T. E., Origins of the differences between the circular dichroism of DNA and RNA: Theoretical calculations. *Biopolymers* **1973,** *12* (1), 201-221.

66.   Petkovic, M.; Ferguson, J. L.; Gunaratne, H. Q. N.; Ferreira, R.; Leitão, M. C.; Seddon, K. R.; Rebelo, L. P. N.; Pereira, C. S., Novel biocompatible cholinium-based ionic liquids—toxicity and biodegradability. *Green Chem.* **2010,** *12* (4), 643-649.

67.   Pernak, J.; Syguda, A.; Mirska, I.; Pernak, A.; Nawrot, J.; Prądzyńska, A.; Griffin, S. T.; Rogers, R. D., Choline-Derivative-Based Ionic Liquids. *Eur. J. Chem.* **2007,** *13* (24), 6817-6827.

68.   Mishra, A.; Ekka, M. K.; Maiti, S., Influence of Ionic Liquids on Thermodynamics of Small Molecule–DNA Interaction: The Binding of Ethidium Bromide to Calf Thymus DNA. *J. Phys. Chem. B* **2016,** *120* (10), 2691-2700.

69.   Docherty, K. M.; Kulpa, J. C. F., Toxicity and antimicrobial activity of imidazolium and pyridinium ionic liquids. *Green Chem.* **2005,** *7* (4), 185-189.

70.   Bisht, M.; Venkatesu, P., Influence of cholinium-based ionic liquids on the structural stability and activity of α-chymotrypsin. *New J. Chem.* **2017,** *41* (22), 13902-13911.

71.   Cho, C.-W.; Pham, T. P. T.; Zhao, Y.; Stolte, S.; Yun, Y.-S., Review of the toxic effects of ionic liquids. *Sci. Total Environ.* **2021,** *786*, 147309.

72.   Zakrewsky, M.; Mitragotri, S., Therapeutic RNAi robed with ionic liquid moieties as a simple, scalable prodrug platform for treating skin disease. *J. Control. Release* **2016,** *242*, 80-88.

73.   Dharamdasani, V.; Mandal, A.; Qi, Q. M.; Suzuki, I.; Bentley, M. V. L. B.; Mitragotri, S., Topical delivery of siRNA into skin using ionic liquids. *J. Control. Release* **2020,** *323*, 475-482.

74.   Ohno, H.; Fukumoto, K., Amino Acid Ionic Liquids. *Acc. Chem. Res.* **2007,** *40* (11), 1122-1129.

Chapter 4

Effect of Choline Amino Acid Ionic Liquids (CAAILs) on Haemoglobin

4.1. INTRODUCTION

Developing techniques to enhance the solubility, activity, and stability of biomolecules in ILs is an active area of research. However, the toxicity of the solvent plays a crucial role in maintaining protein stability. Recent investigations have focused on the cytotoxicity and microbial toxicity of ILs, leading to the discovery that non-toxic ILs can be generated by altering the combination of ions.[1-4] It is widely accepted that the head group of the cation plays a crucial role in determining toxicity, with longer side chains exerting more severe effects on living cells.[3, 5] The morpholinium head group has been identified as the least toxic, making it an ideal candidate for designing inherently safe ILs combined with short polar side chains and non-toxic anions.[6-7] Choline amino acid-based ILs (ChAAILs) have emerged as promising biocompatible ILs, particularly for applications involving the storage and stability of proteins and biomolecules.[8-14] ChAAILs are environmentally friendly, as their constituent ingredients are non-toxic. Recent studies have explored the cytotoxicity and skin permeation properties of ChAAILs for their potential application as drug delivery agents. [12-13]

While most tested ILs show no significant toxicological effects regarding their anions, hydrophobic and fluorinated species are generally unsuitable for non-toxic IL applications.[15] Therefore, the biocompatibility of ILs needs to be defined based on their specific target applications. It has also been observed that certain ILs exhibit environmental sensitivity and demonstrate specificity in terms of protein stability.[16-17] Some ILs can stabilize one protein while destabilizing others, highlighting the importance of studying the toxicity and stability of the same IL in different proteins.

ChAAILs are already well established to have large applications in biomolecules. It is an environmentally benign solvent for proteins and nucleic acids and provides structural

stability to them. The strong affinity between ChAAILs with various motifs of biomolecules such as lipid bilayer, cytochrome-c, lysozyme, and nucleic acids such as DNA, RNA, and G-quadruplex is found to be the major factor contributing to their stability.[6, 18] ChAAILs have also successfully applied in the fields of biosensors and proton conduction.[19-20] However, we did not find any reports on the effect of ChAAILs on haemoglobin (Hb).

This article aims to provide insights into the effect of ChAAILs on hemoglobin (Hb) protein, an iron-containing oxygen transporter found exclusively in red blood cells.[21] Hb is a tetrameric protein consisting of four heme prosthetic groups and four polypeptide chains (two α chains and two β chains).[22-23] Due to its significance in biology, chemistry, medicine, and pharmaceuticals, extensive research has been conducted on Hb.[24-25] The native state of Hb is highly stable due to various interactions, including hydrogen bonding, electrostatic forces, and hydrophobic interactions. However, changes in physiological conditions such as temperature, pressure, pH, and solvents can disrupt the native structure of Hb.[26] Under altered conditions, some proteins exist in a partially unfolded state known as the molten globule or hemichrome intermediate. In this state, proteins retain their native-like secondary structures but lose certain tertiary interactions, leading to exposure of hydrophobic residues. Understanding the molten globular state of proteins and elucidating structure-function relationships has garnered significant interest in the scientific community. Recent studies have characterized the unfolding pathways in Hb, quantitatively analyzing the native state, partially unfolded hemichrome intermediate, and free dissociated hemin state.[27] Such investigations provide insights into the pathophysiology of hemoglobinopathies and other conditions associated with unstable globins.

ILs have gained considerable attention as designer solvents due to their versatile properties. They offer numerous advantages, such as low vapor pressure, high thermal stability, and biocompatibility, making them suitable for various applications. ChAAILs, particularly, have shown promise in biomolecules, exhibiting stability-enhancing properties. However, the effects of ILs, including ChAAILs, on specific proteins like Hb require further exploration. Hb, as a well-studied protein with crucial biological implications, can serve as a model for investigating the impact of ILs on protein stability and function. Understanding the behavior of ILs in different proteins and physiological conditions will contribute to their effective and safe utilization in various biotechnological and biomedical applications.

A limited number of studies have investigated the effect of ILs on Hb, considering their significance as an essential component of human blood. Venkatesu et al. conducted fluorescence and CD spectroscopy studies to examine the structural stability of myoglobin (Mb) and Hb in ammonium-based ILs.[14] Vashishat et al. explored the interaction between Hb and Surface-Active Ionic Liquids (SAILs), such as [C_{12}mim][Cl] and [C_6mim][SDS], in an aqueous medium and found that the process is driven by enthalpy.[28] Singh et al. utilized an IL as a co-solvent to investigate the interaction between Hb and triazolium-based ILs.[29] They reported that Hb maintains structural stability at lower concentrations of triazolium-based ILs, while denaturation occurs at higher concentrations. These studies revealed that the structural stability of Hb can be influenced by different ILs, with the protein demonstrating both stable and unstable behavior depending on the specific IL used.

Given the extensive in vitro studies on the application of ChAAILs in drug delivery, it becomes essential to investigate the stability of Hb in the presence of ChAAILs in an in vivo setting. Therefore, this study aims to examine the effect of two different ChAAILs

on the structural conformation of Hb using various spectroscopic techniques, including UV-Vis spectroscopy, fluorescence spectroscopy, circular dichroism (CD) spectroscopy, Time-Correlated Single Photon Counting (TCSPC), and molecular docking. Additionally, thermodynamic parameters are monitored using isothermal titration calorimetry (ITC). The choice of two different ILs is based on the alkyl chain length of the anion, as the length of the alkyl chain can impact the conformation of a protein. Glycinate and methionate anions are selected to gain insights into the role of alkyl chain length in anions on the native state of the protein. Furthermore, the unfolding of the protein is compared with the key stages of Hb unfolding in the presence of guanidinium hydrochloride ([GuHCl]).

By conducting a comprehensive analysis using various spectroscopic techniques and thermodynamic measurements, this study aims to elucidate the impact of ChAAILs on the structural stability of Hb. Molecular docking studies will provide insights into the binding interactions between ChAAILs and Hb. Comparisons with the unfolding stages induced by [GuHCl] will further enhance the understanding of how ChAAILs influence the stability of Hb. The findings from this study will contribute to the knowledge of IL-protein interactions and provide valuable information for the design and development of IL-based systems for drug delivery and other biomedical applications.

4.2. METHODS

4.2.1. Materials

Hemoglobin (Hb) porcine from Sigma Aldrich was utilized in its as-received form without any additional purification steps. The concentration of Hb was determined by spectrophotometry at a wavelength of 405 nm, utilizing an extinction coefficient (ε) of

approximately 167 mM^{-1}.cm^{-1}.[30] This measurement was performed in a 20 mM sodium phosphate buffer at pH 7.4.

Choline hydroxide (46 wt% in water), glycine (>99%, HPLC), and methionine (>99.5%, HPLC) were procured from Sigma-Aldrich. Guanidine hydrochloride (>99%, molecular biology grade) was obtained from Merck chemicals. Autoclaved Milli-Q water was used for all solution preparations throughout the experimental procedures.

The stock solution of Hb was prepared by dissolving powdered Hb in a 20 mM phosphate buffer with stirring in a 3D shaker, and it was stored at -20°C for future use. The concentration of the Hb solution was determined using UV-Vis absorption spectroscopy, with a molar absorption coefficient (ε) value of 167 mM^{-1}·cm^{-1} at an absorbance of 405 nm. The synthesis of the ionic liquids [Ch][Gly] and [Ch][Met] was carried out through acid-base neutralization reactions according to the prescribed method[31], and the products were characterized using 1H and 13C NMR spectroscopy. The synthesized ILs were stored in a vacuum oven at room temperature to prevent moisture and air contact. The purity of the ILs was confirmed using NMR spectroscopy, as depicted in Figures 4.1 and 4.2.
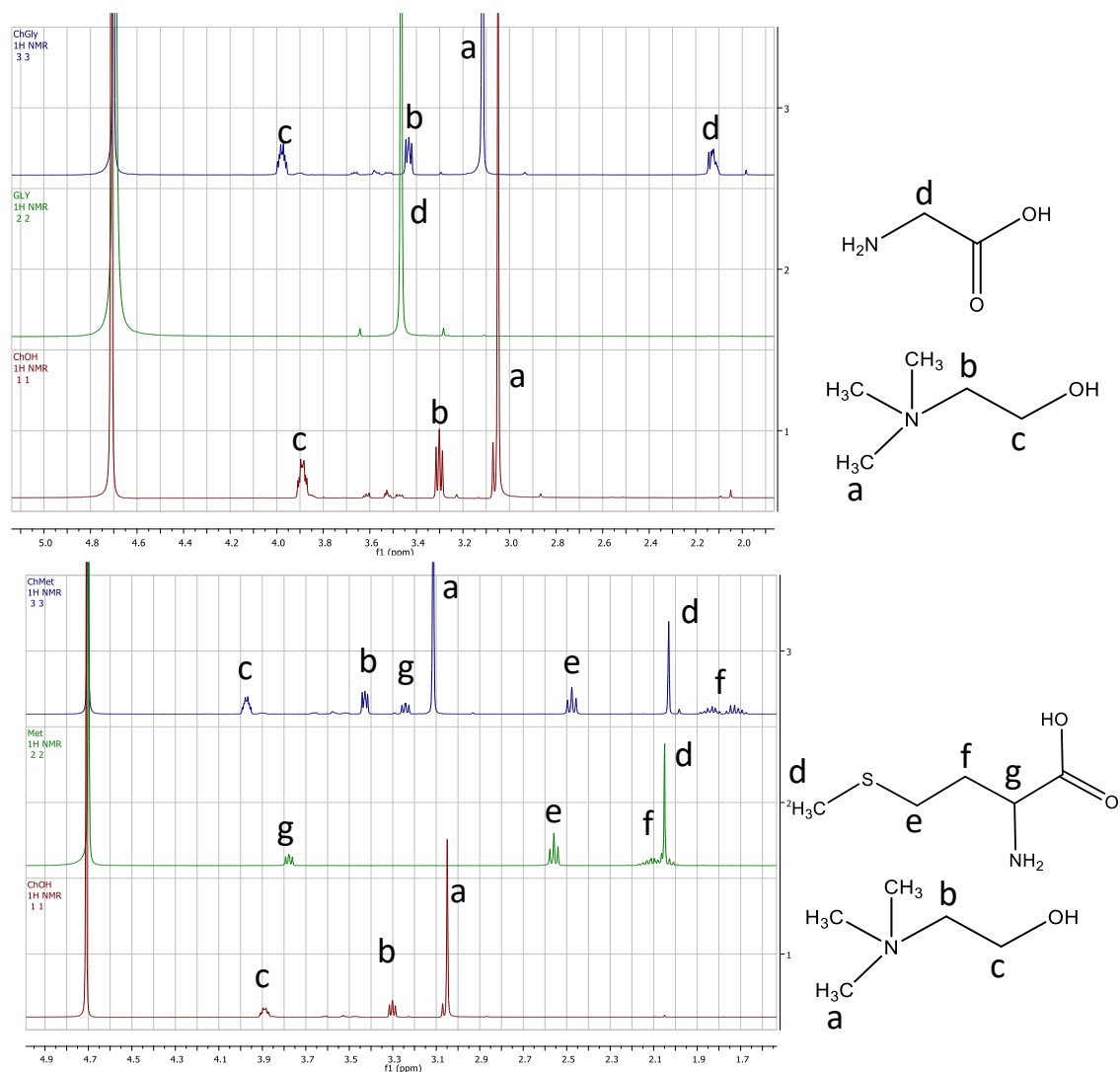
Figure 4.1. ^1H and spectrum of [Ch][Gly] and [Ch][Met] IL in D_2O.
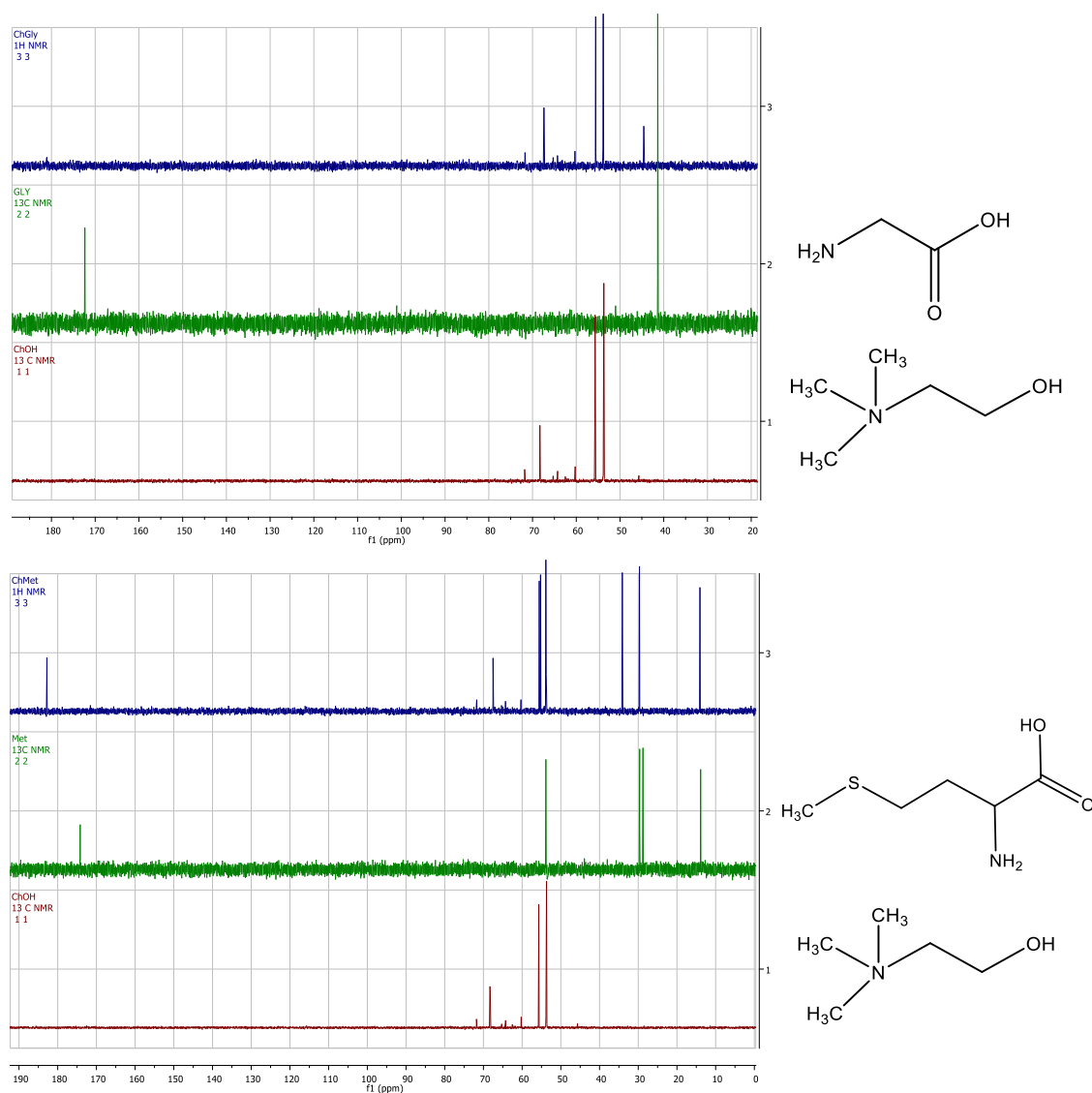
Figure 4.2. ^{13}C *NMR spectrum of [Ch][Asp] and [Ch][Met] IL in D₂O.*

4.2.2. Experimental Section

For the circular dichroism (CD) measurements of Hb, a JASCO J-1500 instrument equipped with a Peltier-type temperature controller (PTC-100) was used. CD spectra of Hb were recorded at 25°C and pH 7.4, both in the far-UV and near-UV/Soret regions. The measurements in the far-UV region used a cuvette with a 0.1 cm path length, while a cuvette with a 1 cm path length was used for the near-UV and Soret regions. The CD spectra were recorded by averaging three scans to improve the signal-to-noise ratio, with

a scanning speed of 100 nm/min and a bandwidth of 1 nm. A 20 mM phosphate buffer baseline was used, and a constant nitrogen flow was maintained throughout the experiment.

UV-Vis absorption measurements were conducted using an Agilent Cary spectrophotometer to obtain the absorption spectra of native Hb, ChAAILs, and Hb in the presence of different concentrations of ChAAILs. A 20 mM phosphate buffer baseline was used, and the measurements were performed in a quartz cuvette with a 1 cm optical path length.

Fluorescence measurements were carried out using an Edinburgh-made fluorimeter equipped with a Peltier element. A quartz cuvette with a 1 cm path length was used, and the fluorescence emission spectra were recorded between 310 nm and 500 nm with an excitation wavelength of 280 nm. The concentration of Hb in the cuvette was 10 µM, and the excitation and emission slits were set to 3 nm. The measurements were performed at a constant temperature of 25°C maintained by the Peltier element.

Isothermal titration microcalorimetry (ITC) was employed to measure the thermodynamic parameters of ChAAILs binding to Hb. A MicroCal iTC-200 calorimeter with a sample cell and 200 µL volume capacity reference cells were used. An adiabatic shield insulated the cells, and the sample cell was filled with a fixed concentration of Hb prepared in phosphate buffer. Titrations were performed by injecting ChAAILs from a 40 µL rotating syringe into the sample cell. The IL and Hb concentrations were set at 10 mM and 10 µM, respectively, with 25 injections performed for each titration. Each injection had a volume of 1.5 µL and an interval of 120 s.

4.2.3. Computational Section

Molecular docking studies were conducted using AutoDock Vina software.[32] The 3D crystal structure of a well-characterized Hb protein with a resolution of 1.5 Å (PDB ID: 1QPW)[21] was downloaded from the protein data bank. The ligand structures (ChAAILs) were optimized at the B3LYP/6-31G** level using Gaussian 16 software package.[33] Hb and ligands were prepared using AutoDock Tools, and different grid sizes were used for various systems in the x, y, and z directions while maintaining a constant grid spacing of 1.0 Å. The docking results were analyzed, and the binding mode with the lowest energy was selected. At least 15 different conformers were observed for each case.
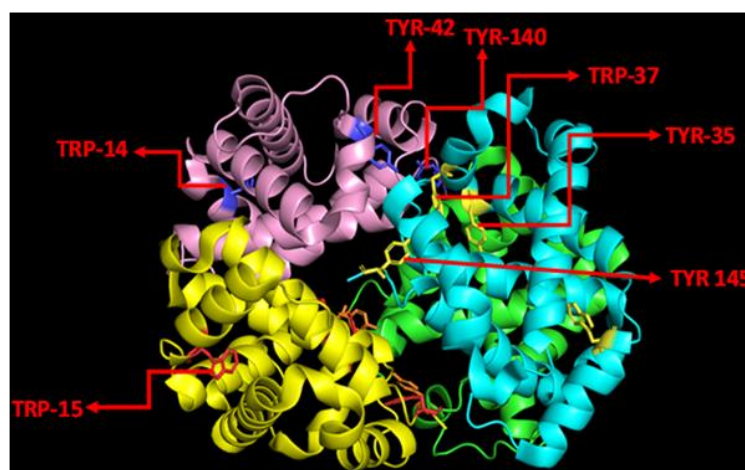
Figure 4.3. Cartoon representation of Hemoglobin (PDB: 1QPW)

In the computational methods, it was not feasible to perform quantum mechanical calculations due to the large size of the Hb PDB file. Therefore, only the (i-1)th, ith, and (i+1)th residues involved in the Hb•IL interaction were considered. The (i-1)th and (i+1)th residues were removed, and the N-terminal and C-terminal of the ith residue were capped with an acetyl group (CH_3CO) and a methylamine (CH_3NH) group, respectively. The positions of hydrogen atoms in the model compounds were optimized while keeping all other atoms fixed using the B3LYP/6-31G** level of theory in the Gaussian 16

software package. The wave functions of the complexes were calculated at the B3LYP/6-31G** level, and the molecular graph and bond critical points were generated using Bader's quantum theory of atoms in molecules (QTAIM)[34] with the Multiwfn software.[35] The plots of the noncovalent interaction index (NCI index) were produced by plotting the reduced density gradient data using the NCIPLOT program[36] in VMD 1.9.3.[37]

4.3. RESULTS AND DISCUSSIONS

Ionic liquids (ILs) have been known to impact the surrounding protein environment through various noncovalent interactions with amino acid residues. These interactions have been investigated using spectroscopic techniques such as circular dichroism (CD), steady-state absorption, and emission spectroscopy. The strength of these interactions has been determined using isothermal titration calorimetry (ITC) and is further supported by molecular docking and quantum mechanical studies.

4.3.1. Structural conformation of Hemoglobin

In the case of the structural stability of hemoglobin (Hb) in the presence of ILs, circular dichroism spectroscopy was employed to monitor the structural perturbations. CD spectra were recorded in the far-UV (200-250 nm), near-UV (250-300 nm), and visible (350-450 nm) regions to examine the secondary, tertiary, and Soret band regions of Hb, respectively. In the far-UV CD spectra of Hb in buffer, characteristic peaks were observed at 222 nm (n-π* transition) and 208 nm (π-π* transition), corresponding to the α-helix region of the protein.[38-39] The near-UV region exhibited CD bands at 260 and 285 nm, attributed to the π-π* transition of the C=O group of tryptophan (TRP) residues.[40] The Soret band region displayed a positive peak at 405 nm, corresponding to the four heme groups of Hb.

The CD spectra in the far-UV range showed no significant perturbation when Hb was exposed to a low concentration (500 μM) of ChAAILs, indicating that the protein remained structurally stable at low IL concentrations. However, upon further addition of ChAAILs, an increase in the HT (heat transfer) voltage was observed, leading to abrupt data. This behavior has been previously reported and attributed to the presence of a multi-component system.[41]

The near-UV region, which monitors the tertiary structure of Hb, exhibited minimal changes in the CD bands at 260 nm and 285 nm in the presence of ChAAILs. However, the intensity of these bands decreased as the concentration of ChAAILs increased (Figure 4.4A, B)). The decrease in intensity was more pronounced in the presence of the glycinate anion than in the methionate anion. Analysis of the Soret band region revealed a decrease in the Soret peak when ChAAILs were present, with the methionate anion causing a more significant decrease (Figure 4.4C, D). The reduction in the Soret peak indicates partial unfolding of the protein in the IL environment.[40] These observations confirm that both ChAAILs induce partial unfolding of Hb, with the glycinate anion primarily perturbing the tertiary region and the methionate anion affecting the heme region.
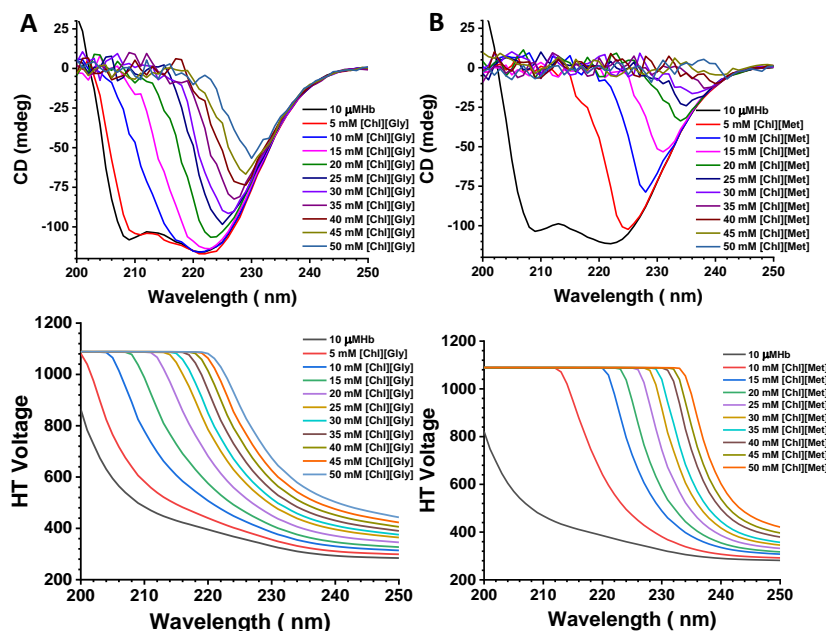
Figure 4.4. CD spectra analysis along with the HT voltage data plots of secondary region Hb in the presence of (A) [Chl][Gly] (B) [Chl][Met]
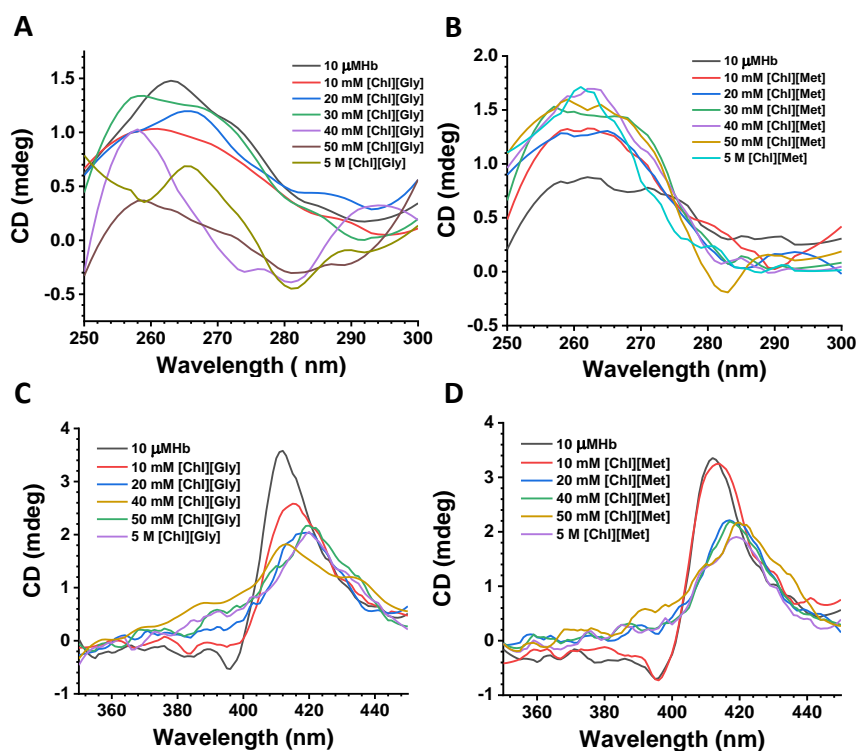
Figure 4.5. CD spectra analysis of Hb in the presence of [Chl][Gly] (A) in the tertiary region CD) in the soret region. CD spectra analysis of Hb in the presence of [Chl][Met] (B) in the tertiary region (D) in the soret region

A comparison was made to assess the protein unfolding induced by the ChAAILs with a well-known denaturant, guanidinium hydrochloride ([GuHCl]). The effect of [GuHCl] on the secondary region of the protein was observed in Figure 4.6A, where a decrease in the intensity of the characteristic peaks at 222 and 208 nm indicated protein unfolding. However, a direct comparison of these data was impossible due to the increase in HT voltage resulting in noisy spectra in the presence of ChAAILs. Nonetheless, when monitoring the tertiary region of the protein, the denaturant [GuHCl] caused a decrease in the intensity of the 260 and 285 nm bands, which eventually disappeared at higher [GuHCl] concentrations (Figure 4.6B). In contrast, the 260 and 285 nm bands did not completely vanish in the presence of ChAAILs, suggesting that partial unfolding of the protein occurred in the presence of ILs. This inference was further supported by the decrease in the intensity of the Soret peak observed in the presence of [GuHCl] (Figure 4.6C). The disappearance of the Soret peak at higher [GuHCl] concentrations is a characteristic feature of heme protein denaturation. However, the moderate change observed in the Soret band of Hb in the presence of ChAAILs can be attributed to the partial unfolding of Hb.
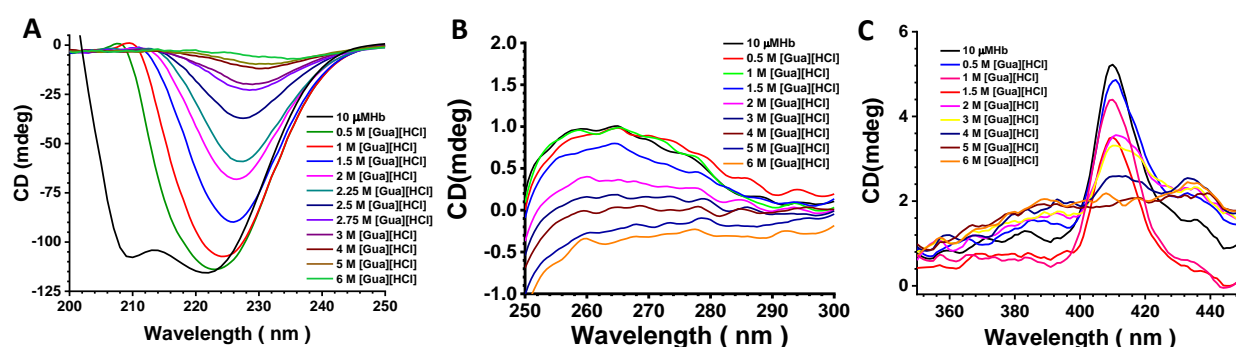
Figure 4.6. CD spectra analysis of Hb in the presence of GuHCl (A) in the secondary region (B) in the tertiary region (C) in the soret region

4.3.2. Binding mode analysis through spectroscopic techniques for Hemoglobin

Steady-state absorption spectroscopy is one of the techniques used to investigate the structural changes in proteins and deduce binding insights in the protein-ligand system.[42-43] The absorption spectrum of Hb exhibits three peaks at 210, 270 and 406 nm. The peak at 270 nm corresponds to the π-π* transitions of the carbonyl (C=O) groups of tyrosine (TYR), tryptophan (TRP), and phenylalanine (PHE) amino acid residues. The sharp peak at 406 nm is the Soret band of porphyrin moiety in the heme group of Hb.[44] Absorption spectra of Hb were recorded with the gradual addition of ChAAILs to investigate the interaction of ILs with Hb. As shown in Figure 4.7A, B, an increase in absorption intensity at 270 nm peak of Hb was observed on successive addition of ChAAILs. However, the Soret band at 406 nm, which corresponds to the four heme groups, showed a decrease in intensity with increasing concentration of ChAAILs. The results indicate that the ChAAILs bind with the protein and heme parts of Hb which further leads to protein unfolding. The percentage of unfolding was calculated for both the ChAAILs by monitoring the absorbance of 406 nm. It was found that irrespective of the different alkyl chain lengths of the anion, the [Chl][Gly] and [Chl][Met] unfold the Hb in a similar manner (Figure 4.7D).
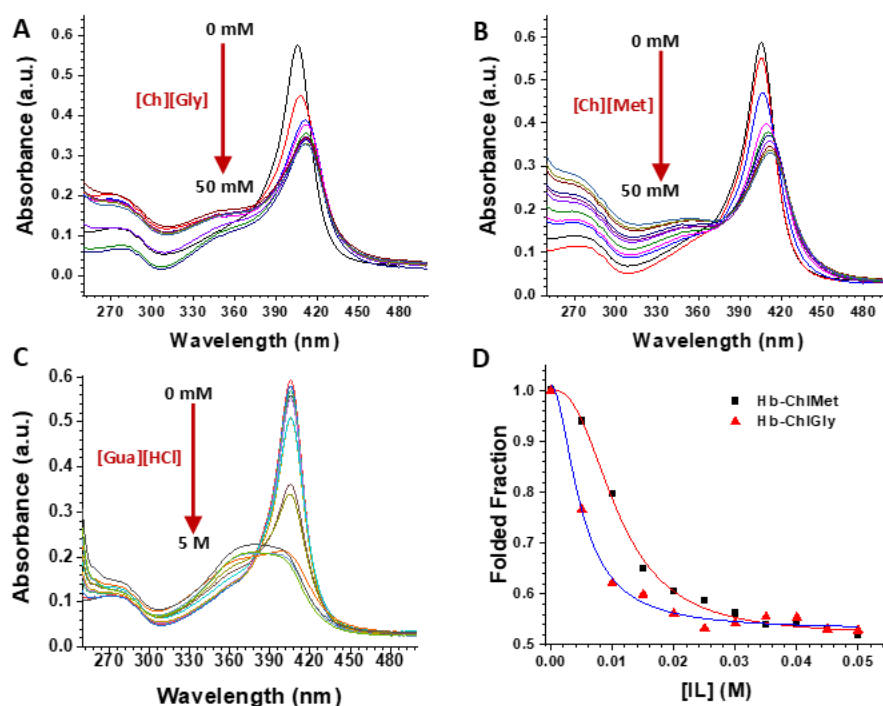
Figure 4.7. (A) Absorbance spectra of Hb with the increasing concentration of [Chl][Gly] up to 5 M (B) Absorbance spectra of Hb with the increasing concentration of [Chl][Met] up to 5 M (C) Absorbance spectra of Hb with the increasing concentration of [Gua][HCl] up to 6 M (D) Folding fraction profiles of Hb as a function of [Chl][Gly] and [Chl][Met] concentration.

These changes in the heme peaks indicate major conformational alterations in the heme pocket. Carter et al. associated this decrease in the Soret band with a loss in contact between the heme group and the proximal histidine, subsequently converting the heme into a four-coordinated low-spin species.[45] Apart from this, the shift in the Soret band is attributed to the conversion of metHb to hemichrome in the presence of ChAAILs by Rajni et al.[28] However, the hemichrome is stabilized in the presence of ILs as no frother alteration in the band is observed on addition of ILs. On the other hand, the key stages of the unfolding of Hb are characterized by the decrease in the Soret band in the presence of [GuHCl] by Samuel et al.[27] There exists an hemichrome intermediate in between the native and unfolded state of Hb.[46-47] This is attributed to the strong perturbations of the heme pocket and is achieved on addition of 1.6 M concentration of [GuHCl] to Hb (Figure

4.7C). This is similar to the spectra when compared to the CHAAILs, which strongly indicates that the Hb is in its intermediate state in the presence of both the ILs.

There are several tryptophan residues in human Hb. Among them, TRP-37 is the most dominant fluorophore as it induce motion of distal HIS-64 in the heme binding pocket.[48] We used fluorescence spectroscopy to monitor the interactions of Hb with [Chl][Gly] and [Chl][Met] ILs. The emission spectrum of native Hb has a peak at 330 nm. [Chl][Gly] and [Chl][Met] ILs were added to the solution of native Hb, and the subsequent changes in the spectra were recorded. The increasing concentration of the ILs led to a significant 3-fold increase in the fluorescence intensity of the protein with a remarkable red shift of 50 nm in the peak position (Figure 4.8A, B).
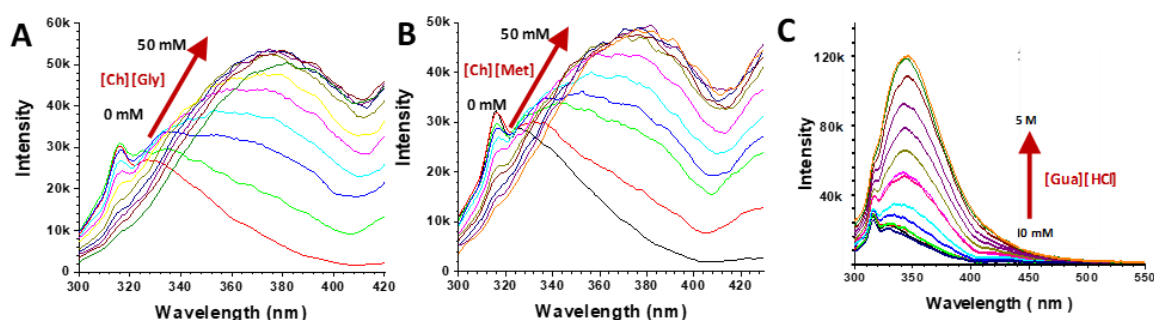
Figure 4.8. (A) Fluorescence emission spectra of Hb on increasing concentration of [Chl][Gly] (B) Fluorescence emission spectra of Hb on the increasing concentration of [Chl][Met]. (C) Fluorescence emission spectra of Hb on increasing concentration of GuHCl upto 5M

The TRP buried in the hydrophobic region of hemoglobin gets exposed with the addition of ILs.[49] The increase in the emission intensity can be attributed to the unfolding of Hb in the presence of the ILs. The red shift in the peak position corresponds to the fluorescence of the TRP in the polar environment of the [Chl][Gly] and [Chl][Met] ILs.[49] On the contrary, the presence of [GuHCl] in the Hb protein leads to a 6-fold increase in the intensity of the tryptophan emission spectrum (Figure 4.8C). This suggests that

[Chl][Gly] and [Chl][Met] ILs lead to the hemichrome intermediate state of Hb, while [GuHCl] completely denatures it.

The interaction between a biological macromolecule, such as a protein, and a ligand or drug can occur through various forces, including hydrophobic interactions, hydrogen bonding, van der Waals forces, and electrostatic interactions. Understanding the thermodynamic parameters, such as enthalpy (ΔH) and entropy (ΔS), of these interactions provides insights into the nature of the protein-ligand interactions. Isothermal titration calorimetry (ITC) is useful for measuring these thermodynamic parameters. In the case of hemoglobin (Hb) and ionic liquids (ILs), ITC was employed to study their interactions.

The enthalpy values were directly obtained using ITC, and the change in entropy was calculated using the standard equation $\Delta G = \Delta H - T\Delta S$, where ΔG represents the change in Gibbs free energy.[50] The enthalpogram for the titration of an IL ([Ch][Gly]) with Hb is shown in Figure 7A. The upper panel displays the heat flow for each injection as a function of time, while the lower panel shows the integrated heat in each injection after subtracting the heat of dilution. The thermodynamic parameters, including the number of binding sites, binding affinity, enthalpy, entropy, and Gibbs free energy, are presented in the lower panel of Figure 4.9.
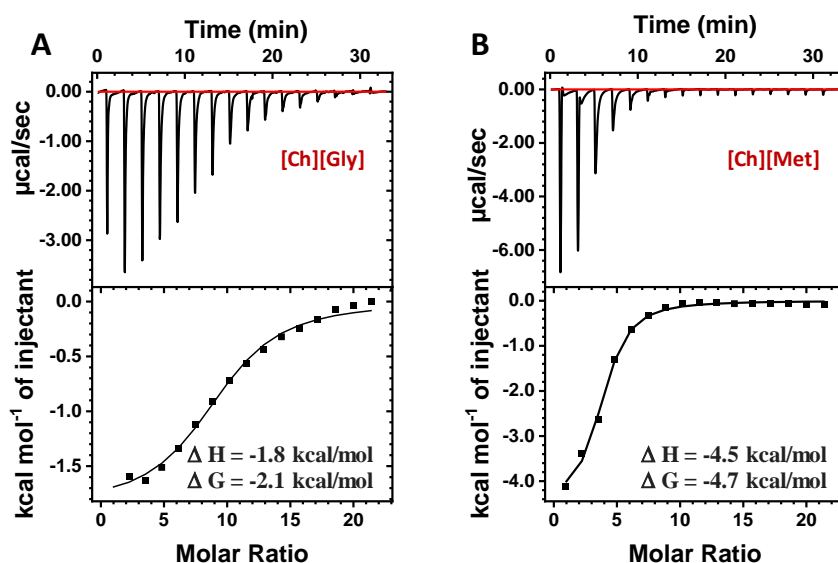
Figure 4.9. (A) ITC isotherm of the interaction of Hb and [Chl][Gly] (B) ITC isotherm of the Hb and [Chl][Met] binding interaction. The top panel shows heat flow for each injection (μcal/s) as a function of time (min). the lower panel shows integrated heats in each injection as a function of the molar ratio of the IL along with the thermodynamic parameters (ΔH, ΔG) for the interaction of [Chl][Gly] and [Chl][Met] ILs with Hb.

The interaction between [Ch][Gly] IL and Hb was found to be a spontaneous reaction, with a negative change in Gibbs free energy (-2.1 kcal/mol). The negative enthalpy and positive entropy indicate that the process is both enthalpically and entropically favorable. The endothermic heat changes observed during the titration can be attributed to the binding of ILs to Hb through weak electrostatic and hydrophobic interactions.[28] Similarly, the titration of [Ch][Met] IL with Hb (Figure 7B) resulted in a change in Gibbs free energy of -4.7 kcal/mol. The higher value of Gibbs free energy for the methionate anion can be attributed to its larger alkyl chain length and interaction with the heme region of Hb.

4.3.3. Binding mode analysis through molecular docking

Molecular docking studies were also conducted to model the atomic-level interactions between ILs and Hb.[32, 51] The docking results confirmed hydrogen bonding is the primary noncovalent interaction between the ILs and Hb. Specific amino acid residues of Hb were

involved in hydrogen bonding interactions with the ILs. The [Ch]$^+$ cation forms strong H-bonding interactions with ALA142, TYR145, and HIS146 residue. A total of 3 interactions were found for glycinate anion, one with ASP126 and two with SER102 and SER133 (Figure 4.10).

The methionate anion forms H-bonds with ASP 126 and TYR35 residues of Hb (Figure 4.11). The binding site of the anions is close to the heme site of the Hb, resulting in the intermediate state. The binding energies obtained from molecular docking were consistent with the ITC results, with [Ch][Gly] and [Ch][Met] exhibiting binding energies of -7.2 and -8.7 kcal/mol, respectively. The weak binding of ILs to Hb may result from dynamic binding or unbinding, leading to the formation of the hemichrome intermediate state.
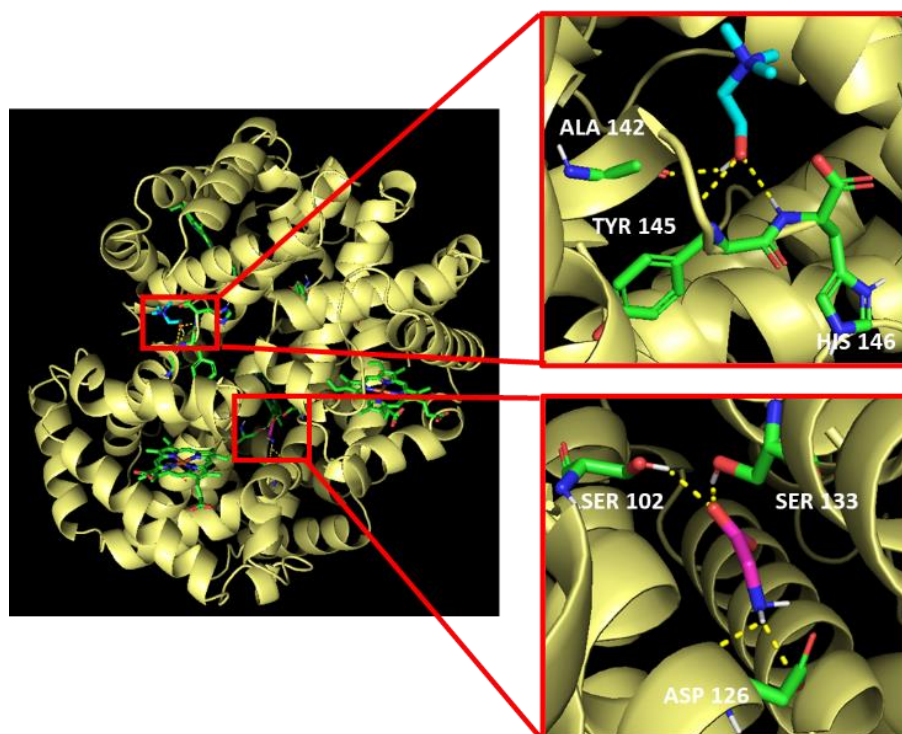
Figure 4.10. Cartoon view of the energetically most favored docked model of Hb interacting with cation and anion of [Chl][Gly] IL
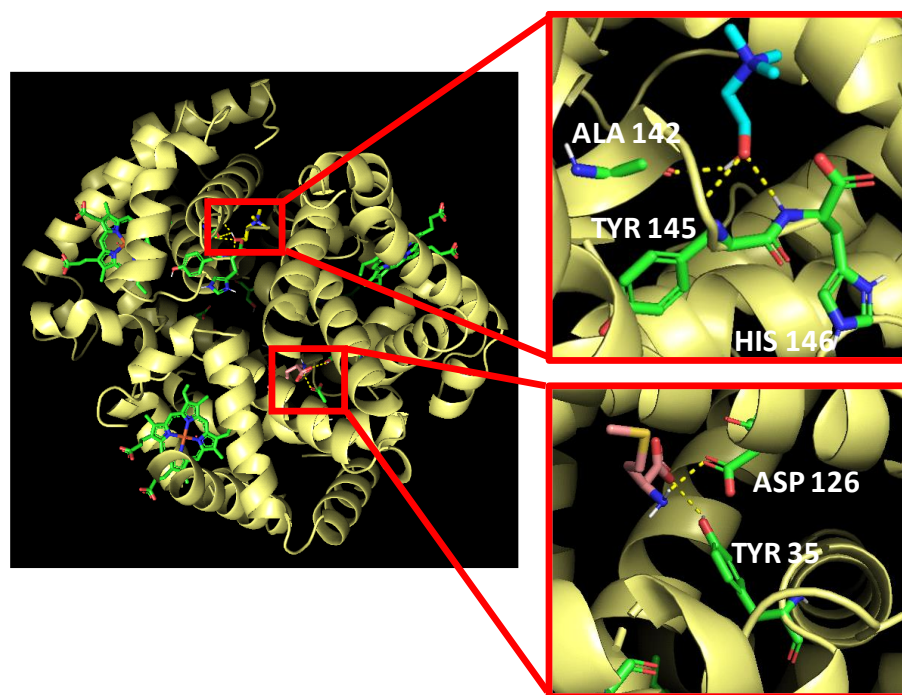
Figure 4.11. Cartoon view of the energetically most favored docked model of Hb interacting with cation and anion of [Chl][Met] IL

4.3.4. DFT analysis

Quantum mechanical calculations and electron density analyses were performed to confirm the interactions further. The presence of bond critical points (BCPs) between the ILs and Hb and the analysis of electron density and noncovalent interaction (NCI) indices supported the presence of hydrogen bonding and other interactions between the ILs and specific amino acid residues of Hb.

We optimized the positions of the hydrogen atoms of the amino acid residues interacting with the ILs obtained from the docking at B97D/6-31G* level of theory using the Gaussian 16 program. The geometrical parameters and the interaction energies suggest the possibility of H-bonding between the ILs and the Hb. For further confirmation, we performed electron density analyses. The atoms in molecules (AIM) analysis shows a bond critical point (BCP) between two ILs and Hb.[34] The electron density ($\rho(r)$) and the

Laplacian of electron density ($\nabla^2\rho(r)$) at BCP range from 0.002-0.034 a.u. and 0.024-0.139 a.u., respectively. The molecular graphs for [Chl] and [Gly] with the interacting amino acid residues of Hb are shown in Figures 4.12A and B, respectively.
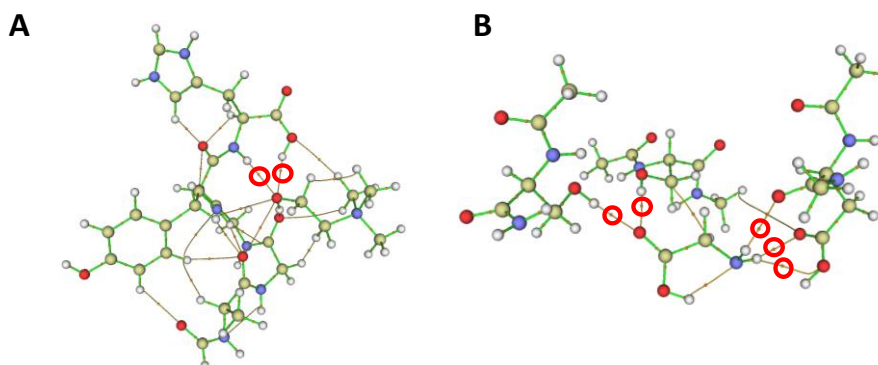
Figure 4.12. (A) Molecular graphs of the [Chl] with the amino acid residues of Hb (B) Molecular graphs of the [Gly] with the amino acid residues of Hb. The BCPs are encircled in red.

We also performed the non-covalent interaction (NCI) index analysis. Reduced density gradient (RDG) isosurfaces (isosurface value = 0.5) for [Chl] and [Gly] with interacting amino acid residues of Hb are shown in Figures 4.13A, B. The blue isosurface indicates strong and attractive interactions, whereas green indicates weak interactions. All of these analyses support the presence of O···H-N and O···H-O H-bond between [Chl][Gly] and Hb.
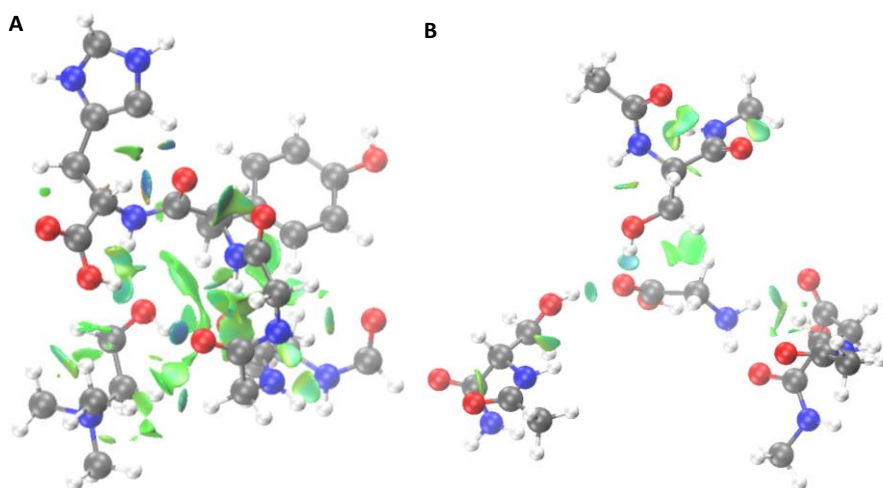
Figure 4.13. Reduced density gradient (RDG) isosurface in real 2D-space of amino acids of Hb with (A) Choline cation (B) Glycinate anion

The molecular graphs for [Chl] and [Met] with the interacting amino acid residues of Hb are shown in Figures 4.14A and B, respectively. We observed the presence of S···O chalcogen bond along with N···H-C, O···H-N, and O···H-O H-bond between [Chl][Met] and Hb.
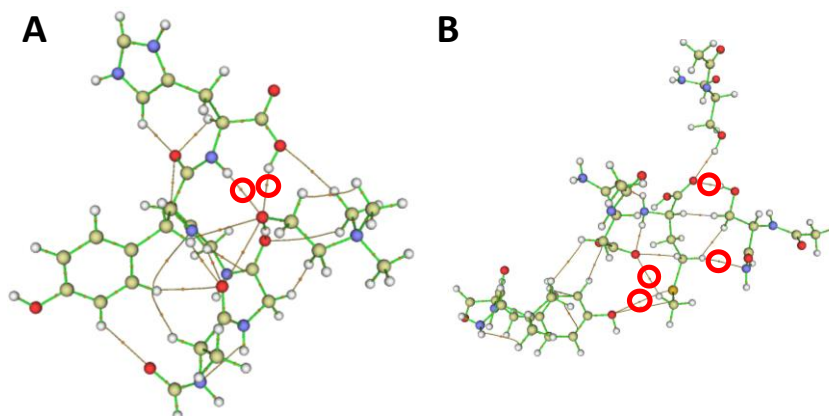
Figure 4.14. (B) Molecular graphs of the [Chl] with the amino acid residues of Hb (C) Molecular graphs of the [Met] with the amino acid residues of Hb. The BCPs are encircled in red.

The RDG isosurface indicates the strong and attractive interaction between [Chl][Met] and Hb (Figures 4.15).
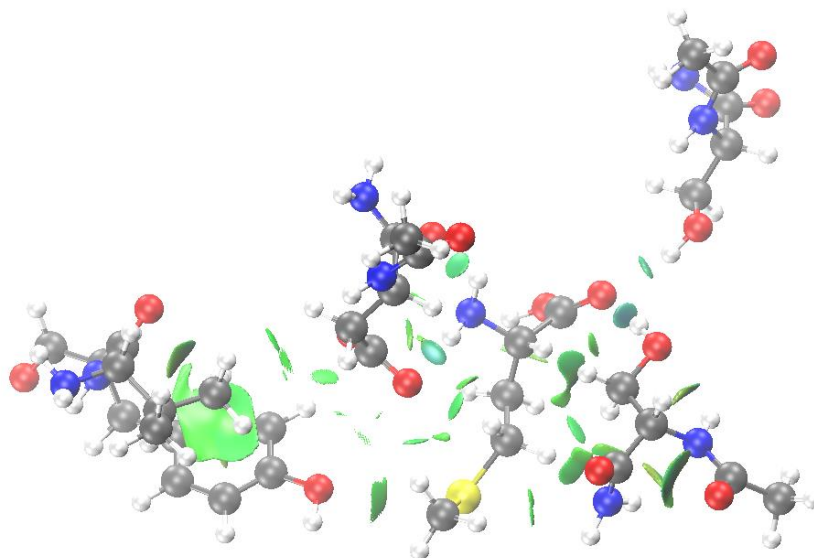
Figure 4.15. Reduced density gradient (RDG) isosurface in real 2D-space of amino acids of Hb with methionate anion

4.4. CONCLUSIONS

Ionic liquids (ILs) are known for their use as alternative solvents for storing and stabilizing nucleobases and proteins. Different ILs can have varying effects on the native structure of proteins, with some ILs allowing the protein to retain its native conformation and others causing a complete loss of structure. In the case of choline amino acid-based ILs (ChAAILs), this study demonstrates that they alter the native structure of hemoglobin.

The intermediate state of hemoglobin (Hb) is of great interest, and finding suitable ligands or ILs to study this state is a significant challenge. The fluorescence and circular dichroism (CD) measurements indicate that ChAAILs induce partial protein unfolding. Although [Ch][Met] strongly binds to Hb with a binding energy of -4.7 kcal/mol, neither ChAAILs completely denature the protein. The interactions between ILs and Hb

primarily involve hydrogen bonding. This suggests that ChAAILs have the potential as external ligands for exploring the hemichrome intermediate state of hemoglobin.

These findings have implications in medicinal chemistry, as ILs exhibit strong binding with Hb. The ability of ChAAILs to modulate the structure of hemoglobin opens up avenues for further research and applications. By understanding the interactions between ILs and Hb, it may be possible to design novel ligands or therapeutic agents targeting specific hemoglobin states or functions. Therefore, this study contributes to the broader understanding of protein-IL interactions and their potential in medicinal chemistry.

4.5. REFERENCES

1. Kebaili, H.; Pérez de los Ríos, A.; Salar-García, M. J.; Ortiz-Martínez, V. M.; Kameche, M.; Hernández-Fernández, J.; Hernández-Fernández, F. J., Evaluating the Toxicity of Ionic Liquids on Shewanella sp. for Designing Sustainable Bioprocesses. *Front. Mater.* **2020,** *7*.

2. Flieger, J.; Flieger, M., Ionic Liquids Toxicity—Benefits and Threats. *Int. J. Mol. Sci.* **2020,** *21* (17), 6267.

3. Biczak, R.; Pawłowska, B.; Bałczewski, P.; Rychter, P., The role of the anion in the toxicity of imidazolium ionic liquids. *J. Hazard. Mater.* **2014,** *274*, 181-190.

4. Thuy Pham, T. P.; Cho, C.-W.; Yun, Y.-S., Environmental fate and toxicity of ionic liquids: A review. *Wat. Res.* **2010,** *44* (2), 352-372.

5. Kumar, R. A.; Papaïconomou, N.; Lee, J.-M.; Salminen, J.; Clark, D. S.; Prausnitz, J. M., In vitro cytotoxicities of ionic liquids: Effect of cation rings, functional groups, and anions. *Environ. Toxicol.* **2009,** *24* (4), 388-395.

6. Yan, F.; Xia, S.; Wang, Q.; Ma, P., Predicting Toxicity of Ionic Liquids in Acetylcholinesterase Enzyme by the Quantitative Structure–Activity Relationship Method Using Topological Indexes. *J. Chem. Eng. Data* **2012,** *57* (8), 2252-2257.

7. Pernak, J.; Borucka, N.; Walkiewicz, F.; Markiewicz, B.; Fochtman, P.; Stolte, S.; Steudte, S.; Stepnowski, P., Synthesis, toxicity, biodegradability and physicochemical properties of 4-benzyl-4-methylmorpholinium-based ionic liquids. *Green Chem.* **2011,** *13* (10), 2901-2910.

8. Sahoo, D. K.; Chand, A.; Jena, S.; Biswal, H. S., Hydrogen-bond-driven thiouracil dissolution in aqueous ionic liquid: A combined microscopic, spectroscopic and molecular dynamics study. *J. Mol. Liq.* **2020,** *319*, 114275.

9. Kumar Sahoo, D.; Devi Tulsiyan, K.; Jena, S.; Biswal, H. S., Implication of Threonine-Based Ionic Liquids on the Structural Stability, Binding and Activity of Cytochrome c. *ChemPhysChem* **2020,** *21* (23), 2525-2535.

10. Sahoo, D. K.; Jena, S.; Tulsiyan, K. D.; Dutta, J.; Chakrabarty, S.; Biswal, H. S., Amino-Acid-Based Ionic Liquids for the Improvement in Stability and Activity of Cytochrome c: A Combined Experimental and Molecular Dynamics Study. *J. Phys. Chem. B* **2019,** *123* (47), 10100-10109.

11. Sahoo, D. K.; Jena, S.; Dutta, J.; Chakrabarty, S.; Biswal, H. S., Critical Assessment of the Interaction between DNA and Choline Amino Acid Ionic Liquids:

Evidences of Multimodal Binding and Stability Enhancement. *ACS Cent. Sci.* **2018,** *4* (12), 1642-1651.

12.   Li, X.; Ma, N.; Zhang, L.; Ling, G.; Zhang, P., Applications of choline-based ionic liquids in drug delivery. *Int. J. Pharm.* **2022,** *612*, 121366.

13.   Tanner, E. E. L.; Ibsen, K. N.; Mitragotri, S., Transdermal insulin delivery using choline-based ionic liquids (CAGE). *J Control Release* **2018,** *286*, 137-144.

14.   Kumar, P. K.; Bisht, M.; Venkatesu, P.; Bahadur, I.; Ebenso, E. E., Exploring the Effect of Choline-Based Ionic Liquids on the Stability and Activity of Stem Bromelain. *J. Phys. Chem. B* **2018,** *122* (46), 10435-10444.

15.   Vieira, N. S. M.; Stolte, S.; Araújo, J. M. M.; Rebelo, L. P. N.; Pereiro, A. B.; Markiewicz, M., Acute Aquatic Toxicity and Biodegradability of Fluorinated Ionic Liquids. *ACS Sustainable Chem. Eng.* **2019,** *7* (4), 3733-3741.

16.   Singh, O.; Lee, P.-Y.; Matysiak, S.; Bermudez, H., Dual mechanism of ionic liquid-induced protein unfolding. *Phys. Chem. Chem. Phys.* **2020,** *22* (35), 19779-19786.

17.   Constatinescu, D.; Herrmann, C.; Weingärtner, H., Patterns of protein unfolding and protein aggregation in ionic liquids. *Phys. Chem. Chem. Phys.* **2010,** *12* (8), 1756-1763.

18.   Tulsiyan, K. D.; Jena, S.; González-Viegas, M.; Kar, R. K.; Biswal, H. S., Structural Dynamics of RNA in the Presence of Choline Amino Acid Based Ionic Liquid: A Spectroscopic and Computational Outlook. *ACS Cent. Sci.* **2021,** *7* (10), 1688-1697.

19.   Zappi, D.; Caminiti, R.; Ingo, G. M.; Sadun, C.; Tortolini, C.; Antonelli, M. L., Biologically friendly room temperature ionic liquids and nanomaterials for the development of innovative enzymatic biosensors. *Talanta* **2017,** *175*, 566-572.

20.   Campetella, M.; Montagna, M.; Gontrani, L.; Scarpellini, E.; Bodo, E., Unexpected proton mobility in the bulk phase of cholinium-based ionic liquids: new insights from theoretical calculations. *Phys. Chem. Chem. Phys.* **2017,** *19* (19), 11869-11880.

21.   Katz, D. S.; White, S. P.; Huang, W.; Kumar, R.; Christianson, D. W., Structure Determination of Aquomet Porcine Hemoglobin at 2.8 Å Resolution. *J. Mol. Biol.* **1994,** *244* (5), 541-553.

22.   Ahmed, M. H.; Ghatge, M. S.; Safo, M. K., Hemoglobin: Structure, Function and Allostery. In *Vertebrate and Invertebrate Respiratory Proteins, Lipoproteins and other*

Body Fluid Proteins, Hoeger, U.; Harris, J. R., Eds. Springer International Publishing: Cham., 2020; pp 345-382.

23.   Safo, M. K.; Ahmed, M. H.; Ghatge, M. S.; Boyiri, T., Hemoglobin–ligand binding: Understanding Hb function and allostery on atomic level. *Biochim. Biophys. Acta - Proteins Proteom.* **2011,** *1814* (6), 797-809.

24.   Schechter, A. N., Hemoglobin research and the origins of molecular medicine. *Blood* **2008,** *112* (10), 3927-3938.

25.   Vibhudutta, A., Pharmaceutical Aspects of Hemoglobin-Based Oxygen Carriers. *Curr Drug Deliv.* **2005,** *2*, 133-142.

26.   Ken A. Dill, D. S., Denatured states of proteins. *Annu. Rev. Biochem.* **1991,** *90*, 795-825.

27.   Samuel, P. P.; White, M. A.; Ou, W. C.; Case, D. A.; Phillips, G. N.; Olson, J. S., The Interplay between Molten Globules and Heme Disassociation Defines Human Hemoglobin Disassembly. *Biophys. J.* **2020,** *118* (6), 1381-1400.

28.   Vashishat, R.; Chabba, S.; Mahajan, R. K., Surface active ionic liquid induced conformational transition in aqueous medium of hemoglobin. *RSC Adv.* **2017,** *7* (22), 13041-13052.

29.   Singh, D.; Panigrahi, S. K.; Sharma, G.; Gardas, R. L., Scrutinizing the stability of haemoglobin in 1,2,4-triazolium based ionic liquid. *J. Mol. Liq.* **2022,** *349*, 118213.

30.   Meng, F.; Alayash, A. I., Determination of extinction coefficients of human hemoglobin in various redox states. *Analytical biochemistry* **2017,** *521*, 11-19.

31.   De Santis, S.; Masci, G.; Casciotta, F.; Caminiti, R.; Scarpellini, E.; Campetella, M.; Gontrani, L., Cholinium-amino acid based ionic liquids: a new method of synthesis and physico-chemical characterization. *Phys. Chem. Chem. Phys.* **2015,** *17* (32), 20687-20698.

32.   Morris, G. M.; Huey, R.; Lindstrom, W.; Sanner, M. F.; Belew, R. K.; Goodsell, D. S.; Olson, A. J., AutoDock4 and AutoDockTools4: Automated docking with selective receptor flexibility. *J Comput. Chem.* **2009,** *30* (16), 2785-2791.

33.   Frisch, M. J.; Trucks, G. W.; Schlegel, H. B.; Scuseria, G. E.; Robb, M. A.; Cheeseman, J. R.; Scalmani, G.; Barone, V.; Petersson, G. A.; Nakatsuji, H.; Li, X.; Caricato, M.; Marenich, A. V.; Bloino, J.; Janesko, B. G.; Gomperts, R.; Mennucci, B.; Hratchian, H. P.; Ortiz, J. V.; Izmaylov, A. F.; Sonnenberg, J. L.; Williams; Ding, F.; Lipparini, F.; Egidi, F.; Goings, J.; Peng, B.; Petrone, A.; Henderson, T.; Ranasinghe, D.;

Zakrzewski, V. G.; Gao, J.; Rega, N.; Zheng, G.; Liang, W.; Hada, M.; Ehara, M.; Toyota, K.; Fukuda, R.; Hasegawa, J.; Ishida, M.; Nakajima, T.; Honda, Y.; Kitao, O.; Nakai, H.; Vreven, T.; Throssell, K.; Montgomery Jr., J. A.; Peralta, J. E.; Ogliaro, F.; Bearpark, M. J.; Heyd, J. J.; Brothers, E. N.; Kudin, K. N.; Staroverov, V. N.; Keith, T. A.; Kobayashi, R.; Normand, J.; Raghavachari, K.; Rendell, A. P.; Burant, J. C.; Iyengar, S. S.; Tomasi, J.; Cossi, M.; Millam, J. M.; Klene, M.; Adamo, C.; Cammi, R.; Ochterski, J. W.; Martin, R. L.; Morokuma, K.; Farkas, O.; Foresman, J. B.; Fox, D. J. *Gaussian 16 Rev. C.01*, Wallingford, CT, 2016.

34. Bader, R. F. W., Atoms in molecules. *Acc. Chem. Res.* **1985,** *18* (1), 9-15.

35. Lu, T.; Chen, F., Multiwfn: A multifunctional wavefunction analyzer. *J. Comput. Chem.* **2012,** *33* (5), 580-592.

36. Contreras-García, J.; Johnson, E. R.; Keinan, S.; Chaudret, R.; Piquemal, J. P.; Beratan, D. N.; Yang, W., NCIPLOT: a program for plotting non-covalent interaction regions. *J Chem Theory Comput.* **2011,** *7* (3), 625-632.

37. Humphrey, W.; Dalke, A.; Schulten, K., VMD: Visual molecular dynamics. *J. Mol. Graph.* **1996,** *14* (1), 33-38.

38. Samuni, U.; Dantsker, D.; Juszczak, L. J.; Bettati, S.; Ronda, L.; Mozzarelli, A.; Friedman, J. M. J. B., Spectroscopic and functional characterization of T state hemoglobin conformations encapsulated in silica gels. *Biochemistry* **2004,** *43* (43), 13674-13682.

39. Ueda, Y.; Shiga, T.; Tyuma, I. J.; Communications, B. R., Circular dichroism spectra of human adult hemoglobin and its subunits. *Biochem. Biophys. Res. Commun.* **1969,** *35* (1), 1-5.

40. Kristinsson, H. G., Acid-Induced Unfolding of Flounder Hemoglobin: Evidence for a Molten Globular State with Enhanced Pro-oxidative Activity. *J. Agric. Food Chem.* **2002,** *50* (26), 7669-7676.

41. Jha, I.; Attri, P.; Venkatesu, P., Unexpected effects of the alteration of structure and stability of myoglobin and hemoglobin in ammonium-based ionic liquids. *Phys. Chem. Chem. Phys.* **2014,** *16* (12), 5514-5526.

42. Mahato, M.; Pal, P.; Kamilya, T.; Sarkar, R.; Chaudhuri, A.; Talapatra, G. B., Hemoglobin−Silver Interaction and Bioconjugate Formation: A Spectroscopic Study. *J. Phys. Chem. B* **2010,** *114* (20), 7062-7070.

43.   Wang, Y.; Guo, R.; Xi, J., Comparative studies of interactions of hemoglobin with single-chain and with gemini surfactants. *J. Colloid Interface Sci.* **2009,** *331* (2), 470-475.

44.   Tajima, H.; Ikeda, S.; Matsuda, M.; Hanasaki, N.; Oh, J.-W.; Akiyama, H., A light-emitting diode fabricated from horse-heart cytochrome c. *Solid State Commun.* **2003,** *126* (10), 579-581.

45.   Carter, P., Spectrophotometric determination of serum iron at the submicrogram level with a new reagent (ferrozine). *Anal. Biochem.* **1971,** *40* (2), 450-458.

46.   Riccio, A.; Vitagliano, L.; di Prisco, G.; Zagari, A.; Mazzarella, L., The crystal structure of a tetrameric hemoglobin in a partial hemichrome state. *Proc. Natl. Acad. Sci. U.S.A.* **2002,** *99* (15), 9801-9806.

47.   Balasco, N.; Alba, J.; D'Abramo, M.; Vitagliano, L., Quaternary Structure Transitions of Human Hemoglobin: An Atomic-Level View of the Functional Intermediate States. *J. Chem. Inf. Model.* **2021,** *61* (8), 3988-3999.

48.   Ioannou, A.; Varotsis, C., Probing hemoglobin glyco-products by fluorescence spectroscopy. *RSC Adv.* **2019,** *9* (64), 37614-37619.

49.   Gryczynski, Z.; Lubkowski, J.; Bucci, E., Heme-Protein Interactions in Horse Heart Myoglobin at Neutral pH and Exposed to Acid Investigated by Time-resolved Fluorescence in the Pico- to Nanosecond Time Range. *J. Biol. Chem.* **1995,** *270* (33), 19232-19237.

50.   Duff MR Jr, G. J., Howell EE, Isothermal titration calorimetry for measuring macromolecule-ligand affinity. *J Vis Exp.* **2011,** *55*, 2796.

51.   Meng Xuan-Yu, Z. H.-X., Mezei Mihaly and Cui Meng, , Molecular Docking: A Powerful Approach for Structure-Based Drug Discovery, . *Curr. Comput.-Aided Drug Des.* **2011,** *7*.

Chapter 5

Compaction of DNA in Magnetic Ionic Liquids

5.1. INTRODUCTION

The compaction of deoxyribose nucleic acid (DNA) has been fascinating over the years[1-5], not only because of its widespread applications in gene therapy but also because the basic physics and chemistry involved in the compaction process are still elusive. DNA is one of the essential biological polymers with highly negative charges in solution. Perturbation on the effective negative charges leads to structural changes in DNA; sometimes, DNA compaction happens during this process. In simpler words, the transition of DNA from its double helical structure to a compact and coiled form is known as the compaction of DNA.[6] The reverse compaction process is termed decompaction, wherein the DNA retains its double helical structure. The compaction and decompaction of DNA have potential applications in nanomaterial templating[7], stress protection, gene regulation[8], photocontrol of gene expression, and DNA integrity protection[9]. Hence, enormous efforts have been put forth in the past decade to discover and explore several compacting and decompacting agents.[10] Owing to its negative charge, DNA can be compacted using a variety of cationic agents such as polyamines, polymers, nanoparticles, vesicles, and surfactants. Some compacting agents include light, divalent and trivalent ions such as Co^{3+}, Fe^{2+}, Fe^{3+}, etc., and small polyamines like spermine.[11-14] On the contrary, monovalent ions such as Na^+ or divalent cations such as Mg^{2+} act as decompacting agents.[15-17] Thus, the multivalent salts act as compacting or decompacting agents. The enhancement of compaction in DNA in the presence of negatively charged nanoparticles has also been reported. However, these multivalent ions and nanoparticles pose toxic effects on DNA, which encourages to explore the ionic liquids (ILs) as alternative compacting agents for DNA.

Low cytotoxicities and biodegradability of ILs render them a more promising solvent for storing and extracting biomolecules.[18] Several exciting research on the interaction of various imidazolium and ammonium-based ILs with nucleic acids have been reported.[19-20] However, very few reports on magnetic ILs (MILs) have attracted the scientific communities to look into the favorable interactions between ILs and nucleic acids.[21-22] Anderson and coworkers efficiently extracted DNA from aqueous solutions using phosphonium-based MILs.[23-25] They also reported that ammonium and phosphorous-based MILs enhance DNA stability at room temperature. Recently, Kumar and coworkers explored the stability of DNA in phosphonium-based MILs and its efficacy in acting as a contrast agent for MRI applications.[26-27]

In addition, the past decade has witnessed bio-ILs, namely choline-based ILs (ChILs), as promising ILs based on the principles of green chemistry.[28] Recently, Biswal and coworkers have provided spectroscopic evidence on long-term storage and extraction of DNA and RNA by using choline amino acid-based ionic liquids (ChAAILs).[29-30] They proposed that cations of ILs play an essential role in the stability of biomolecules. Further, Frade *et al.* studied the toxicity of choline-based magnetic ILs (ChMILs) in two human cell lines. They reported $[FeCl_4]^-$ and $[MnCl_4]^{2-}$ as the most and least suitable magnetic anions.[31] However, on the contrary, Sintra *et al.* found $[MnCl_4]^{2-}$ to be less toxic to marine bacteria.[32] In this regard, we aimed to understand the DNA-ChMIL interaction using various spectroscopic techniques such as steady-state absorption and emission, time-resolved emission, circular dichroism (CD), scanning electron microscopy (SEM), and fluorescence correlation spectroscopy (FCS). Thermodynamic parameters involved in DNA-ChMIL interaction and the binding mode were evaluated with the isothermal titration calorimetry (ITC) experiment and molecular docking studies, respectively. A deliberate study of the interactions between ILs and DNA has also been put together from

the perspective of molecular dynamic simulations. We have also tried to show that counter-anions play a vital role in binding with biomolecules. We observed that the solution turns turbid on adding ChMIL to DNA. However, the transparency is resumed when NaCl is added to the precipitate (**Figure 5.1**). This is the very first indication of the compaction of DNA by and decompaction by NaCl which needs a carful investigation. Herein we have tried to uravel the interactions between DNA and ChMILs by using several spectroscopic techniques and molecular dynamics (MD) simulation studies.
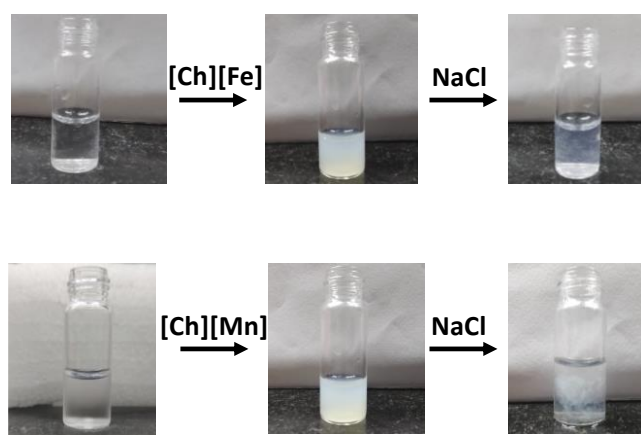
*Figure 5.1. Top panel: Compaction of ct-DNA in the presence of 5 mM [Ch][Fe] IL and decompaction in the presence of 5 mM NaCl **Bottom panel:** Compaction of ct-DNA in the presence of 5 mM [Ch]2[Mn] IL and decompaction in the presence of 5 mM NaCl.*

5.2. METHODS

5.2.1. Materials

Chemicals like Choline chloride, metal salts ($FeCl_3$, $MnCl_2$), DNA from calf thymus and the fluorescence probe - DAPI, are from Sigma and used without further purification. Phosphate buffer (1M, pH 7.4) and the fluorescence dye - Ethidium bromide (EB) is from G Bioscience. Synthesis of ionic liquids (ILs) are according to the previous report. The purity analysis of synthesized molecules were characterized using NMR (1H and 13C) and EPR (see Apendix A1-A5) spectroscopy. UV/Vis absorbance measurement at 260

and 280 nm gives a ratio of 1.8, which confirms the purity of DNA. All the sample preparation and experimental measurement use deionized Milli Q water.

5.2.2. Computational methods:

Methodology:

In this work, the AMBER99SB[33] force field was used to mimic the interatomic interactions of $[Chl]^+$ ions. For $[MnCl_4]^{2-}$ and $[FeCl_4]^-$, the Panteva and York fine-tuned divalent cation parameters[34] and the universal force field (UFF) described by Rappe *et al.*[35] were used, respectively. Appendix A6 provides all force field parameters employed in this study. Simulations were performed for two systems, namely (i) DNA-[Ch][Fe] IL in water and (ii) DNA-$[Ch]_2[Mn]$ in water.

Simulations details:

For the molecular dynamic simulation of DNA in magnetic ionic liquids (ILs), we used the Gromacs 2021 package[36]. Once the topology was generated based on the above-mentioned force field parameters, the DNA molecule was kept in a cubic simulation box with a minimum of 10 nm distance from its surface and filled with the simple point charge (SPC) water molecules[37]. Consistent with the experimental composition, the ratio of DNA to [Ch][Fe] or $[Ch]_2[Mn]$ in the box was set at 1:30. Requisite counterions were added to make every system electrically neutral. Having accomplished energy minimization with the steepest descent integrator for 5000 steps under a force convergence of < 1000 kcal. mol^{-1}. nm^{-1}, we ran MD simulations.

First, the canonical (NVT) and isothermal-isobaric (NPT) ensembles were used to equilibrate each system for 5 ns. We employed the Parrinello-Rahman pressure and Berendsen temperature controllers during equilibration to maintain 1 bar pressure and

300 K temperature, respectively. With a Fourier grid spacing of 0.12 nm, the long-range Coulomb interactions were treated using the particle mesh Ewald (PME) technique[38]. The short-range van der Waals interaction was modeled by the Lennard-Jones potential function with a cut-off distance of 1 nm. The linear constraint solver (LINCS)[39] method was used to limit all bond vibrations.

After equilibration, two systems were subjected to 1 μs production runs, with the system's coordinates being stored at an interval of 10 ps. As in previous studies[40-41], post-MD analyses, including root-mean-square-deviation (RMSD), solvent accessible surface area (SASA), principal component analysis (PCA), radial distribution function (RDF), and H-bonds, were performed using MD trajectories. Applying the the MM-PBSA method[42], binding free energies for the two systems were computed.

5.3. RESULTS AND DISCUSSIONS

5.3.1. MIL-Induced Conformational Changes in ct-DNA

CD spectroscopy is a valuable technique to monitor the structural stability of nucleic acids and proteins.[43]CD spectra display characteristic peaks for different types of DNA structures. The A-form of DNA exhibits a dominant positive band at 260 nm and a negative band at 210 nm. On the other hand, the B-form of DNA (B-DNA) displays a positive band at 276 nm due to π-π base stacking and a negative band at 246 nm due to helicity. Lastly, the Z-form of DNA demonstrates a negative band at 290 nm, a positive band around 260 nm, and another characteristic negative band at around 205 nm.[44]

Figure 5.2A illustrates the CD spectra of ct-DNA at increasing concentrations of [Ch][Fe] IL. Up to 2 mM, minimal conformational changes were observed in both the positive and negative bands of B-DNA. However, with further addition of ILs, a significant change

occurred, leading to the disappearance of the bands in the CD spectra by adding 3 mM of [Ch][Fe] IL. Additionally, the solution turned turbid. To examine the effect of anions on ct-DNA, CD spectra of ct-DNA with increased concentrations of $[Ch]_2[Mn]$ IL were recorded (Figure 5.2B). Similar to [Ch][Fe] IL, no significant change was noticed up to 2 mM concentration of $[Ch]_2[Mn]$ IL. Nonetheless, upon further addition of IL, the solution turned turbid, and the band disappeared. These unaltered CD spectra indicate that the DNA remains stable in ChMILs at low concentrations, while compaction of DNA occurs at higher concentrations, as evident from the changes in CD spectra. These findings align with previous reports that chelation at high concentrations of Fe and Mn results in the compaction of DNA.[12, 45] Apart from this, there is a deviation from the well-established concept that cations play an essential role in maintaining the structural stability and integrity of DNA as [Ch] cation is previously known to maintain the structural integrity of DNA.[30]
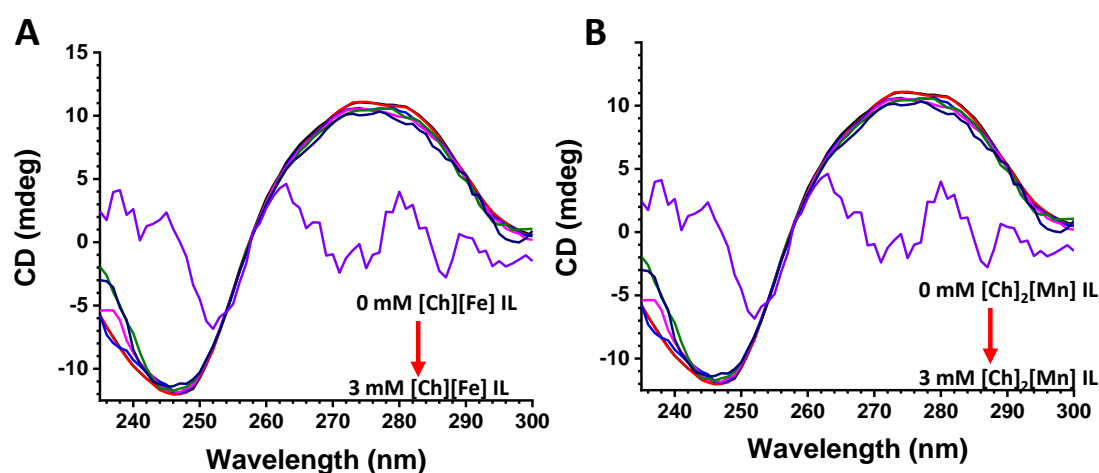
Figure 5.2. Circular dichroism spectra of ct-DNA in phosphate buffer and with increasing concentration of (A) [Ch][Fe], and (B)[Ch][Mn] up to 3 mM

Figure 5.3A presents the zeta potential measurements exploring the effect of [Ch][Fe] IL concentrations on the surface of ct-DNA. Initially, ct-DNA exhibits a ζ value of -40 mV due to the presence of phosphate groups on its surface, conferring a negative charge. Upon

adding 2 mM [Ch][Fe] IL, the negative value of ζ decreases significantly to -13 mV, indicating a substantial interaction of choline cations with ct-DNA. This interaction is attributed to the neutralization of the overall negative surface of ct-DNA by the positive counterion of ChMIL at lower concentrations.[27] However, at higher concentrations (5 mM), the negative counterions of [Ch][Fe] IL also interact with the exposed surface charge of ct-DNA, resulting in only a minor 3 mV change in the ζ value. Similarly, Figure 5.3B shows the zeta potentials of ct-DNA in the presence of [Ch]₂[Mn] IL. Upon adding 2 mM [Ch]₂[Mn] IL, the ζ value is reduced to -9 mV due to the higher interaction of choline cations with the phosphate groups of ct-DNA. As observed previously, minimal change in the ζ value at higher concentrations of [Ch]₂[Mn] IL suggests the interaction between the anionic counterpart and ct-DNA. The zeta potential measurements indicate that both [Ch][Fe] IL and [Ch]₂[Mn] IL interact significantly with the surface charge of ct-DNA, affecting its effective surface charge. At lower concentrations, choline cations neutralize the negative surface charge of ct-DNA, whereas at higher concentrations, both positive and negative counterions of ChMILs contribute to the interaction with ct-DNA.
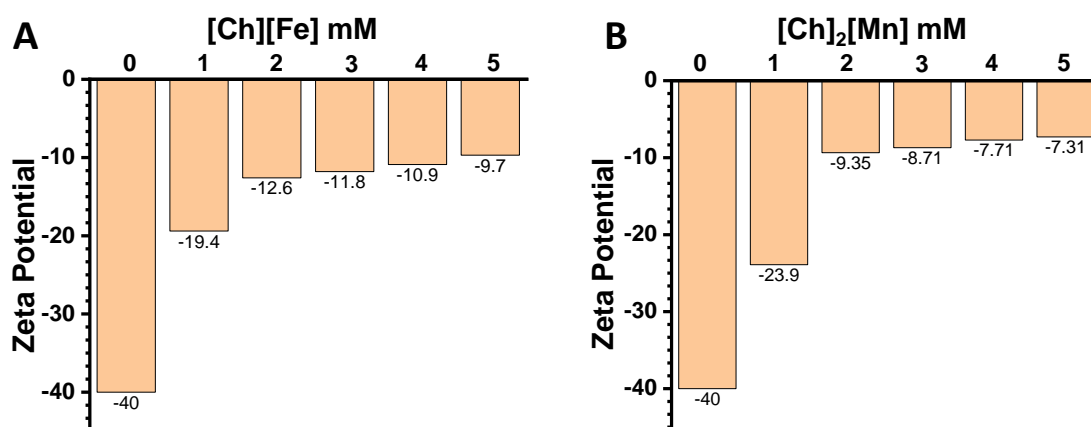
Figure 5.3. Zeta potential of ct-DNA in the absence and presence of the varying amount of A) [Ch][Fe] IL B) [Ch]₂[Mn] IL

5.3.2. Spectroscopic Insight on Interaction between MIL and ct-DNA

To investigate the nature of the binding mode between ChMILs and ct-DNA, researchers utilized steady-state absorption and emission measurements. These measurements are useful for detecting shifts in the absorption maxima, which can indicate interactions between ct-DNA and ChMILs. Additionally, a dye displacement study was conducted to further characterize these interactions. Upon monitoring the absorbance at 260 nm for ct-DNA, the addition of [Ch][Fe] IL resulted in a hyperchromic shift (Figure 5.4A). This shift signifies an increase in absorbance intensity, indicating binding interactions between [Ch][Fe] IL and ct-DNA. Furthermore, as the concentration of [Ch][Fe] IL increased, a broadening of the 260 nm peak was observed, providing additional evidence for the binding interaction between the positive and negative counterions of the ILs and ct-DNA. Similar binding was observed in [Ch]2[Mn] (Figure 5.4B). The steady-state absorption and emission measurements, along with the dye displacement study, provide valuable insights into the binding mode of ChMILs with ct-DNA, revealing specific interactions between the ILs and the DNA structure.
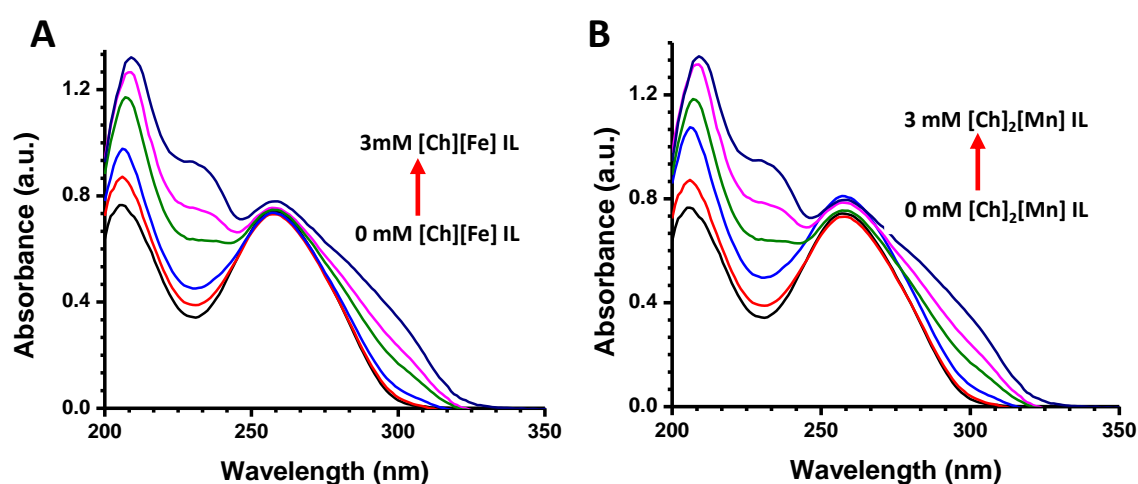
Figure 5.4. Absorption spectra of ct-DNA in absence and presence of the variable amount of A) [Ch][Fe] IL B) [Ch]2[Mn] ILs

These findings contribute to a deeper understanding of the molecular interactions occurring in the system under investigation. Steady-state fluorescence studies were carried out using the well-known ct-DNA binding probes, ethidium bromide (EB). EB binds to the intercalating sites[46-47] of the ct-DNA[48], resulting in an increase in the fluorescence intensity of the ct-DNA-EB complex. Figure 5.5A demonstrates a quenching of the fluorescence intensity upon the addition of [Ch][Fe] IL to the ct-DNA-EB complex. This quenching effect provides strong evidence for the displacement of ethidium bromide (EB) from the ct-DNA-EB complex and the subsequent binding of [Ch][Fe] IL at the intercalating sites of ct-DNA. The fluorescence quenching indicates that the [Ch][Fe] IL competes with EB for binding to the ct-DNA, resulting in the displacement of EB molecules from the DNA-EB complex. This suggests that the [Ch][Fe] IL is able to intercalate into the DNA structure, occupying the same sites previously occupied by EB. The observed quenching in fluorescence intensity confirms the specific and competitive binding of [Ch][Fe] IL at the intercalating sites of ct-DNA, further supporting the findings from the previous steady-state absorption and emission measurements.
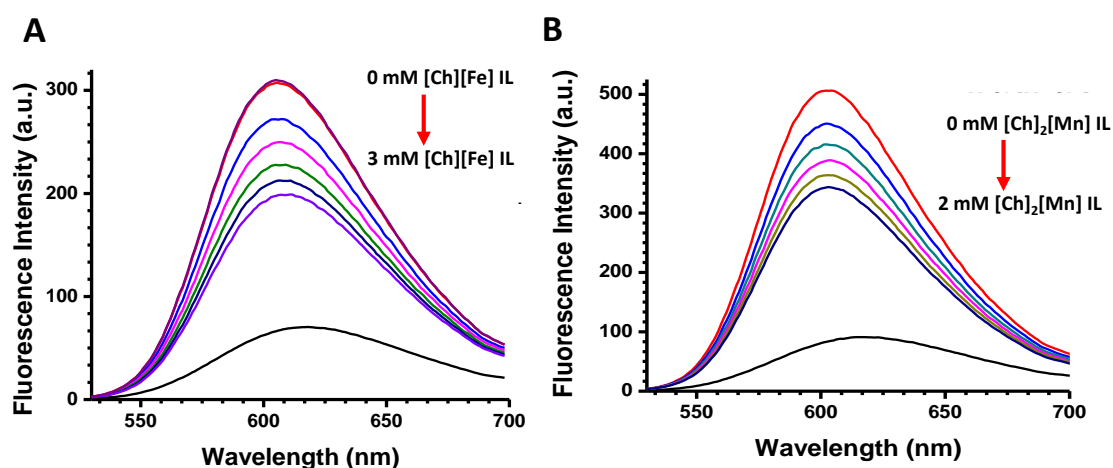
Figure 5.5. Emission spectra of 10 μM EB, ct-DNA-EB complex and on varying the amount of A) [Ch][Fe] , and B) [Ch]₂[Mn] ILs

The binding of choline cation to the intercalating site of DNA through electrostatic interactions has previously been reported by Khan *et al.* [49] and Sahoo *et al.*[30] Figure 5.5B illustrates the results of steady-state absorption and dye displacement studies for [Ch]$_2$[Mn] IL with ct-DNA. In the presence of [Ch]$_2$[Mn] IL, fluorescence quenching was observed for the ct-DNA-EB complex. Importantly, the quenching rate was found to be higher in [Ch]$_2$[Mn] IL compared to [Ch][Fe] IL. This enhanced quenching rate can be attributed to the stronger interaction of the choline cation of [Ch]$_2$[Mn] IL with ct-DNA, as validated by the zeta potential studies. The increased fluorescence quenching in the presence of [Ch]$_2$[Mn] IL indicates that the choline cation from [Ch]$_2$[Mn] IL exhibits a higher affinity for binding to ct-DNA compared to [Ch][Fe] IL. This stronger interaction enables [Ch]$_2$[Mn] IL to more effectively displace the ethidium bromide (EB) molecules from the ct-DNA-EB complex. The findings from the steady-state absorption and dye displacement studies, along with the zeta potential studies, collectively highlight the robust binding interaction between [Ch]$_2$[Mn] IL and ct-DNA, with the choline cation playing a crucial role in this process.

Time-resolved fluorescence was utilized to investigate the mode of interactions between ChMILs and ct-DNA. The excited state lifetimes were determined by fitting the decay profiles using a biexponential equation as shown below:

$$I(t) = a_1 \exp(-t/\tau 1) + a_2 \exp(-t/\tau 2),$$

where τ_1, and τ_2 are individual lifetime components and a_1, and a_2 are the associated amplitudes.

The excited state lifetime of ethidium bromide (EB) alone was found to follow a single exponential decay with a lifetime of 1.62 ns. However, upon forming a complex with ct-DNA, the decay profile exhibited a biexponential decay. The excited state lifetimes for

the ct-DNA-EB complex were observed as follows: a shorter component with a lifetime of 1.59 ns and a longer component with a lifetime of 18.73 ns. The corresponding amplitudes for EB and the ct-DNA-EB complex were 0.07 and 0.93, respectively. These findings are consistent with the reported binding interactions by Hellar et al.[50] The biexponential decay profile of the ct-DNA-EB complex, with a longer lifetime component and higher amplitude, suggests a more stable and prolonged interaction between ethidium bromide and ct-DNA in the presence of ChMILs. This time-resolved fluorescence analysis provides valuable insights into the binding dynamics and stability of the ChMILs and ct-DNA complex, confirming their specific and significant interactions.

Figure 5.6A and Figure 5.6B display the lifetime decay profiles of the ct-DNA-EB complex upon gradual addition of [Ch][Fe] IL and [Ch]$_2$[Mn] IL, respectively. In both cases, the lifetime decay profiles continue to exhibit a biexponential decay in the presence of ChMILs. However, there are noticeable changes in the amplitude of the two components as the IL concentration increases.
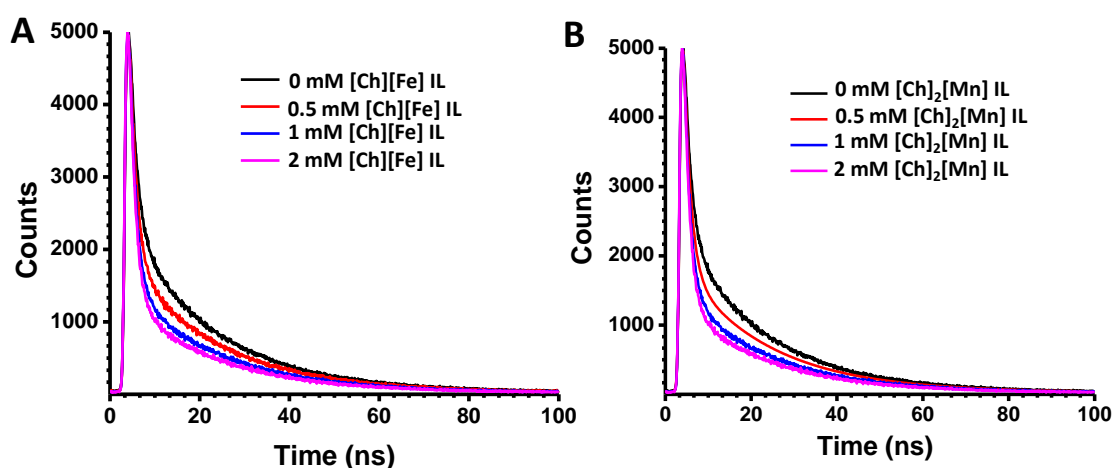
Figure 5.6. Fluorescence decay profiles of EB-DNA in buffer and EB-DNA system in presence of A) [Ch][Fe], and B)[Ch]$_2$[Mn] ILs

Specifically, the amplitude of the shorter component increases from 7% to 33% with the addition of [Ch][Fe] IL, and from 7% to 35% with [Ch]$_2$[Mn] IL. Simultaneously, the amplitude of the longer component decreases from 93% to 67% for [Ch][Fe] IL and from 93% to 65% for [Ch]$_2$[Mn] IL. These observations align with the dye displacement study, where the increase in the shorter component's amplitude suggests the release of ethidium bromide (EB) from the ct-DNA-EB complex upon the gradual addition of ILs. This implies that the ChMILs compete with EB for binding to ct-DNA, leading to the displacement of EB from the DNA complex. Additionally, the increase in the shorter component's amplitude also corresponds to the higher quenching effect observed in [Ch]$_2$[Mn] IL, indicating a more significant interaction between [Ch]$_2$[Mn] IL and ct-DNA compared to [Ch][Fe] IL.

A comprehensive fluorescence decay parameters of the ct-DNA-EB complex in the presence of MILs is provided in Table 5.1. These findings provide valuable insights into the dynamic interactions between ChMILs and ct-DNA and confirm the competitive binding of ILs with ct-DNA-EB complexes, leading to the release of EB and altering the fluorescence decay profiles.

Table 5.1. Fluorescence decay parameters (lifetimes in ns) of free EB, EB-DNA in buffer and EB-DNA system in the presence of [Ch][Fe] and [Ch]$_2$[Mn] IL.

Sample	$\tau_1(a_1)$	$\tau_2(a_2)$	χ^2
EB	1.62 (1.00)		1.15
EB_DNA	1.59 (0.07)	18.73 (0.93)	1.19
EB_DNA_0.5 mM [Ch][Fe]	1.42 (0.21)	19.60 (0.79)	1.05
EB_DNA_1 mM [Ch][Fe]	1.34 (0.28)	19.42 (0.72)	1.15
EB_DNA_2 mM [Ch][Fe]	1.12 (0.33)	19.46 (0.67)	1.07
EB_DNA_0.5 mM [Ch][Mn]	1.47 (0.26)	19.49 (0.74)	1.19
EB_DNA_1 mM [Ch][Mn]	1.43 (0.30)	19.52 (0.70)	1.21
EB_DNA_2 mM [Ch][Mn]	1.40 (0.35)	19.45 (0.45)	1.12

The thermal stability of ct-DNA was derived from the UV melting study. This revealed hyperchromism at 260 nm, which indicates the release of stacking interactions among the nucleobases. During the heating process in the UV melting study, the DNA double helix starts to unwind, leading to the separation of the base pairs. As the temperature increases, the stacking interactions between adjacent nucleobases are disrupted, resulting in the exposure of the nucleobases to the solvent. This causes an increase in the absorbance at 260 nm. The hyperchromic effect is a characteristic feature observed in UV melting studies and is used to study the thermal stability and denaturation of DNA molecules. By monitoring the changes in absorbance at 260 nm as a function of temperature, valuable information about the DNA's melting temperature (Tm) and its thermal stability is obtained.[51] The UV melting plots of ct-DNA were analyzed by taking the first derivative of the absorbance with respect to temperature and plotting it against temperature, as depicted in Figure 5.7. In the absence of ChMILs, the melting temperature (Tm) of ct-DNA was determined to be 75°C. Remarkably, in the presence of ChMILs, the Tm increased by approximately 3-4°C with [Ch][Fe] IL and 4-5°C with [Ch]2[Mn] IL.
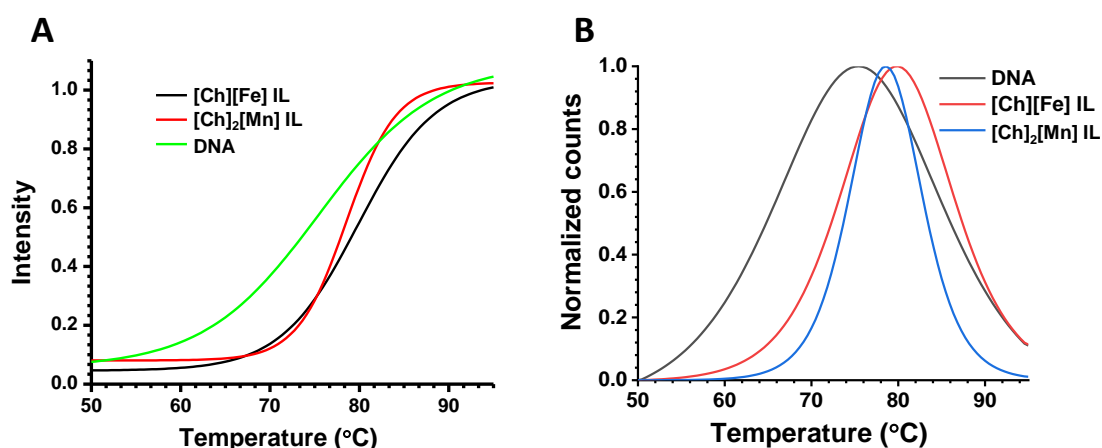
Figure 5.7. A) Melting curves of DNA in buffer, [Ch][Fe] IL, and [Ch]2[Mn] IL.B) First derivative of melting curves of ct-DNA in buffer, [Ch][Fe] IL, and [Ch]2[Mn] IL.

This notable increase in Tm demonstrates that the presence of ChMILs enhances the thermal stability of ct-DNA. It is important to note that this increase in melting temperature cannot be attributed to thermal instability.

On the contrary, the results suggest that the low concentration of ChMILs contributes to an increase in ct-DNA's thermal stability. This enhancement in Tm implies that ChMILs likely engage in non-covalent binding modes other than groove binding to ct-DNA. The findings indicate that ChMILs form specific non-covalent interactions with ct-DNA, leading to increased thermal stability. This suggests that ChMILs may act as stabilizing agents for DNA, potentially influencing various applications involving DNA interactions with ionic liquids. These observations are further supported by a recent simulation study conducted by Garai et al., which revealed a significant increase in the persistence length and stretch modulus of DNA in the presence of higher concentrations of ILs. This simulation study aligns with our findings and corroborates the role of ChMILs in augmenting ct-DNA's thermal stability.[52] The increased rigidity of ct-DNA would result in a higher melting point, as observed here.

5.3.3. Thermodynamics of Interaction between Ionic Liquid and ct-DNA System

Isothermal titration calorimetry (ITC) is a technique that provides information on the thermodynamics of the ligands binding to the protein or nucleic acids. Thermodynamic parameters such as binding affinity (k_A), enthalpy (ΔH), entropy (ΔS), Gibbs free energy (ΔG), and stoichiometry (n), were evaluated based on the heat change due to ligand-DNA interactions.[53] Figure 5.8 shows the ITC profile for the ct-DNA-EB complex, where each injection is represented by individual peaks. By integrating the heat change during each injection, the binding interactions were quantified. The thermodynamic analysis yielded a negative ΔH (enthalpy change) and a positive ΔS (entropy change) value, indicating

that the binding process is both enthalpy and entropy-driven. This suggests that the interaction between ct-DNA and EB involves both favorable enthalpy and entropy contributions.
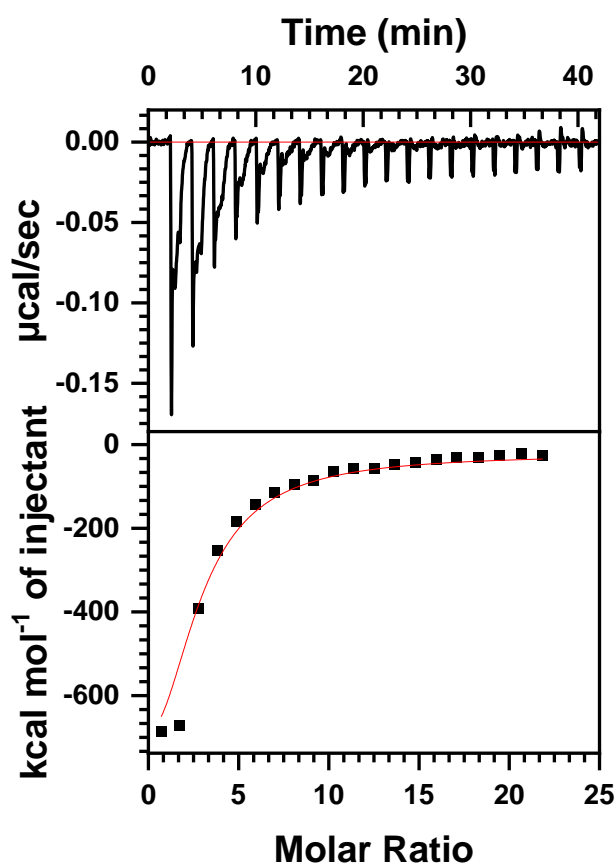
Figure 5.8. ITC isotherms of EB-DNA binding. Top part of both panels are obtained by converting the results into molar heats and plotted against the ligand to DNA molar ratio. Bottom part of both left and right panels are integrated data.

To investigate the binding of [Ch][Fe] IL with ct-DNA, an ITC enthalpogram was generated, and the integrated heat data is presented in Figure 5.9A. The thermodynamic parameters revealed positive ΔH and TΔS (temperature multiplied by entropy change) values, indicating that the binding process is entropically driven. As supported by literature, groove binding of ligands often leads to an increase in the system's entropy, making the binding entropically driven. Similarly, the ITC profiles for [Ch]$_2$[Mn] IL are shown in Figure 5.9B, and the thermodynamic parameters once again confirm that the

process is entropically driven. The expected cause for these effects is that the anions of the ionic liquids induce the aggregation of cations through electrostatic interactions. This cation aggregation likely promotes the compaction of ct-DNA, resulting in the observed entropically driven binding processes.
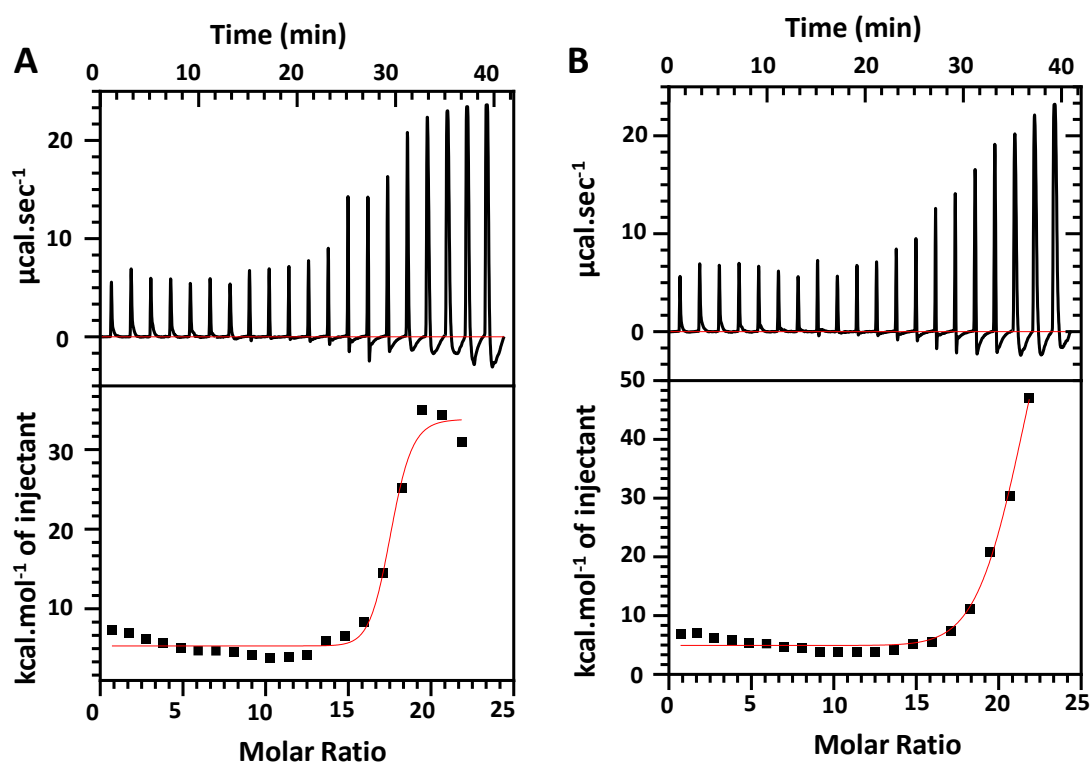
Figure 5.9. A) ITC isotherms of [Ch]₂[Fe]-DNA binding in buffer B) ITC isotherms of [Ch]₂[Mn]-DNA binding in buffer. Top part of both panels are obtained by converting the results into molar heats and plotted against the ligand to DNA molar ratio. Bottom part of both left and right panels are integrated data.

The ITC studies reveal valuable insights into the thermodynamics of the interactions between ct-DNA, EB, and ChMILs. The results indicate that the binding processes involve enthalpy and entropy contributions and suggest that electrostatic interactions between the anions and cations in the ionic liquids play a crucial role in promoting ct-DNA compaction.

5.3.4. Compaction of ct-DNA

Field emission scanning electron microscopy (FESEM) provides insight into the morphology of the ct-DNA.[54] As depicted in Figure 5.10A, ct-DNA assumes a coiled structure of approximately 50 nm in size when observed in the buffer solution. However, in the presence of [Ch][Fe] IL (see Figure 5.10B), ct-DNA undergoes compaction, forming a globular structure with a size of around 5 μm. Similarly, [Ch]2[Mn] IL also induces compaction of ct-DNA, as shown in Figure 5.10C, resulting in a globular form with a size of approximately 7 μm.
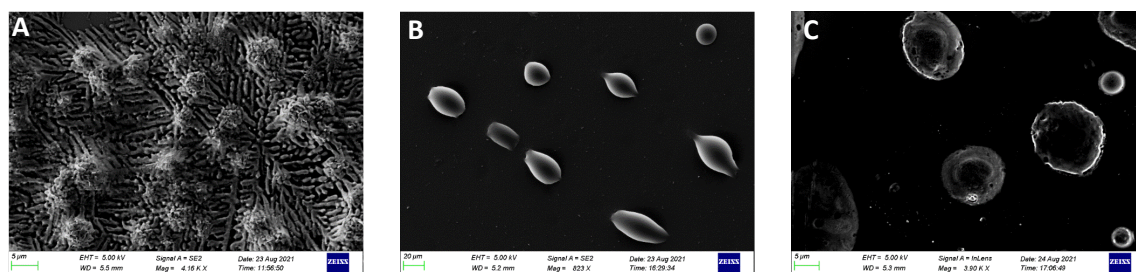
Figure 5.10. A) FESEM image of ct-DNA, B) FESEM image of ct-DNA in the presence of 5 mM [Ch][Fe] IL C) FESEM image of ct-DNA in the presence of 5 mM [Ch]2[Mn] IL

The FESEM (Field Emission Scanning Electron Microscopy) images provide visual evidence of the compaction process induced by the MILs. The globular morphology of ct-DNA in the presence of MILs is in good agreement with previous literature findings.[63] It is important to note that FESEM imaging is conducted under dried conditions, which may lead to increased probabilities of aggregation, potentially explaining the larger globule sizes observed in our case. The FESEM images corroborate the compaction of ct-DNA upon the addition of ChMILs, resulting in globular structures of varying sizes. These observations provide valuable visual evidence of the morphological changes

induced by the MILs, which align with the existing literature on ct-DNA globule formation.[54]

Further, fluorescence correlation spectroscopic (FCS) measurements were carried out using the well-known DNA binding probe 4',6-diamidino-2-phenylindole (DAPI).[55] DAPI is known to bind at the minor groove region of the DNA.[56] In Figure 5.11A, it can be observed that with an increase in the concentration of [Ch][Fe] IL in the ct-DNA-DAPI complex, the $G(\tau)$ value at zero time delay (represented as $G(0)$) decreases. The $G(0)$ value is related to the effective number of molecules (N) in the observation volume, with the relationship $G(0) = 1 / N(1 + A)$, where A is the ratio of the number of molecules (ct-DNA-DAPI complex) present in the native state. The decrease in the $G(0)$ value suggests an increase in the effective number of molecules in the observation volume that are undergoing intensity fluctuation.
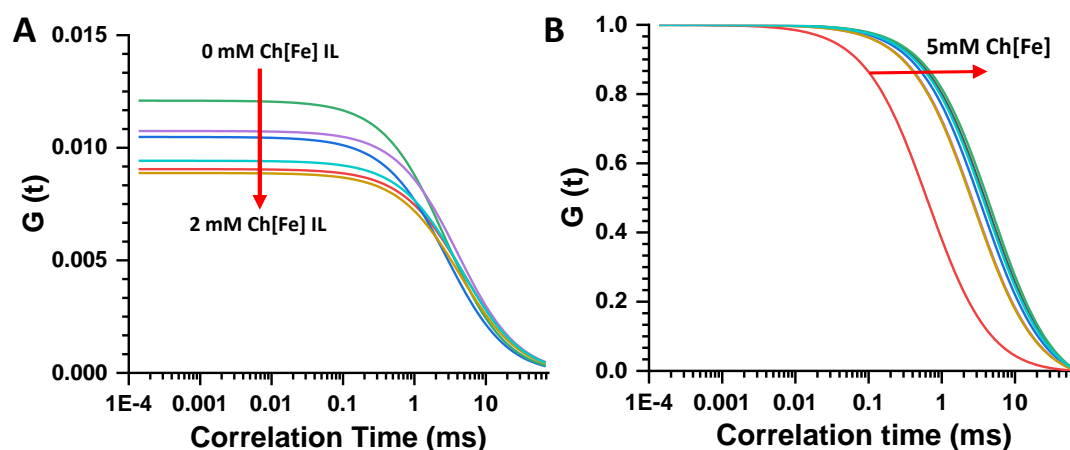
Figure 5.11. A) FCS data of DNA-DAPI complex in absence and presence of varying amount of [Ch][Fe] IL B) Normalised FCS data of DNA-DAPI complex in absence and presence of varying amount of [Ch][Fe] IL

Simultaneously, upon normalizing the $G(\tau)$ function, it is observed that the diffusion coefficient increases with the increasing concentration of [Ch][Fe] IL (Figure 5.11B). Similar observations were made for [Ch]$_2$[Mn] IL, as shown in Figure 5.12A and 5.12B.
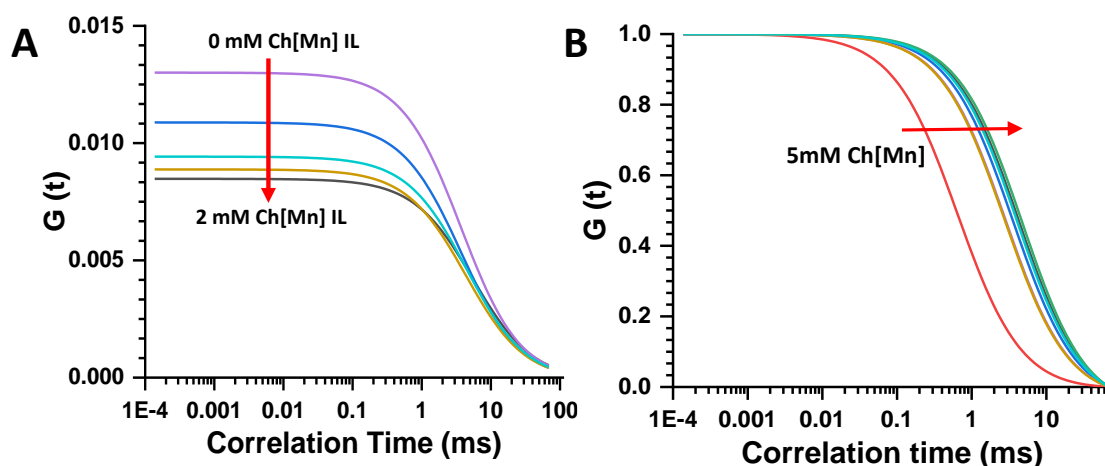
Figure 5.12. A) FCS data of DNA-DAPI complex in absence and presence of varying amount of [Ch]₂[Mn] IL B) Normalised FCS data of DNA-DAPI complex in absence and presence of varying amount of [Ch]₂[Mn] IL

Furthermore, the Fluorescence Correlation Spectroscopy (FCS) technique provides valuable information about the hydrodynamic radius (RH) of biomolecules. In this study, the RH of the ct-DNA-DAPI complex was found to be approximately 15-20 nm. However, with the addition of ChMILs, the R_H increases significantly and is estimated to be in the range of 115-130 nm. This increase in R_H can be attributed to the compaction of ct-DNA in the presence of ChMILs. Overall, the FCS technique provides insightful data on the dynamics and hydrodynamic properties of the ct-DNA-DAPI complex and how they are affected by the presence of ChMILs. The observed increase in the effective number of molecules and the diffusion coefficient, as well as the significant increase in the hydrodynamic radius, indicate the compaction of ct-DNA induced by ChMILs. These findings contribute to a deeper understanding of the structural changes and interactions occurring in the ct-DNA-DAPI-ChMIL system.

5.3.5. Decompaction of ct-DNA:

Monovalent anions and cations have been observed to act as decompacting agents for ct-DNA. In our experiments, we investigated the effect of common salt NaCl on the

compacted ct-DNA structure. The addition of excess NaCl (5mM) to the compacted ct-DNA solution led to the conversion of the condensed ct-DNA into a soluble form, likely facilitated by an efficient ion exchange process. The decompaction of ct-DNA was verified using UV-Vis spectroscopy (Figure 5.13A) and CD spectroscopy (Figure 5.13B). These analyses revealed the reappearance of the same characteristic bands as native ct-DNA, indicating the restoration of the original DNA structure without any degradation. The presence of the characteristic positive peak at 274 nm and negative peak at 245 nm in the CD spectra further confirmed the secondary structural stability of ct-DNA after decompaction. Additionally, we assessed the purity of ct-DNA by calculating the absorbance ratio at 260 nm and 280 nm, which was found to be 1.8. This ratio provides further evidence of the high purity of the ct-DNA sample.
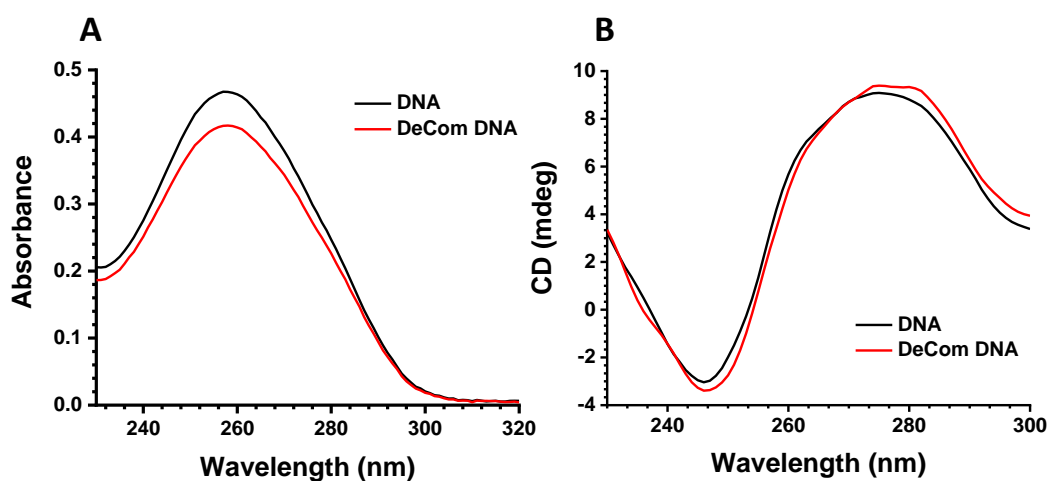
Figure 5.13. A) Absorption spectra of DNA in its purest form and the decompacted DNA B) CD data of DNA in its purest form and the decompacted DNA.

Thus, the addition of excess NaCl efficiently decompacts the ct-DNA structure, leading to the restoration of its original form without degradation. These findings emphasize the role of monovalent anions and cations, such as NaCl, as effective decompacting agents for ct-DNA, and they provide valuable insights into the structural dynamics of ct-DNA in the presence of different ionic environments.

The experimental results are aided by molecular docking and molecular dynamics simulations.

5.3.6. Molecular dynamics (MD) simulations and post-MD parameters

An initial idea on binding ChMILs to ct-DNA was obtained using molecular docking. [57], [58] MD simulations were conducted to gain a detailed understanding of the interactions between ct-DNA and ChMILs over time. Classical MD allows exploration of the physical processes and conformational space of the system over a large span. Various post-MD parameters, such as root-mean-square deviation (RMSD), solvent-accessible surface area (SASA), principal component analysis (PCA), and radial distribution function (RDF), were used to characterize the time evolution of the systems using MD trajectories. RMSD serves as a crucial parameter to assess conformational stability. A significant variation in RMSD indicates a large instability and weak interaction between DNA and an IL. The simulations revealed that DNA-[Ch]$_2$[Mn] exhibited a lower RMSD for DNA compared to DNA-[Ch][Fe], indicating greater stability or stronger interaction between DNA and [Ch]$_2$[Mn] IL (see Figure 5.14A). SASA analysis of DNA showed a similar trend between [Ch]$_2$[Mn] and [Ch][Fe]. Regardless of the ILs present, the SASA in Figure 5.14B demonstrated a steady decrease during the simulation, suggesting that ILs had closer contact with the DNA surface than water.
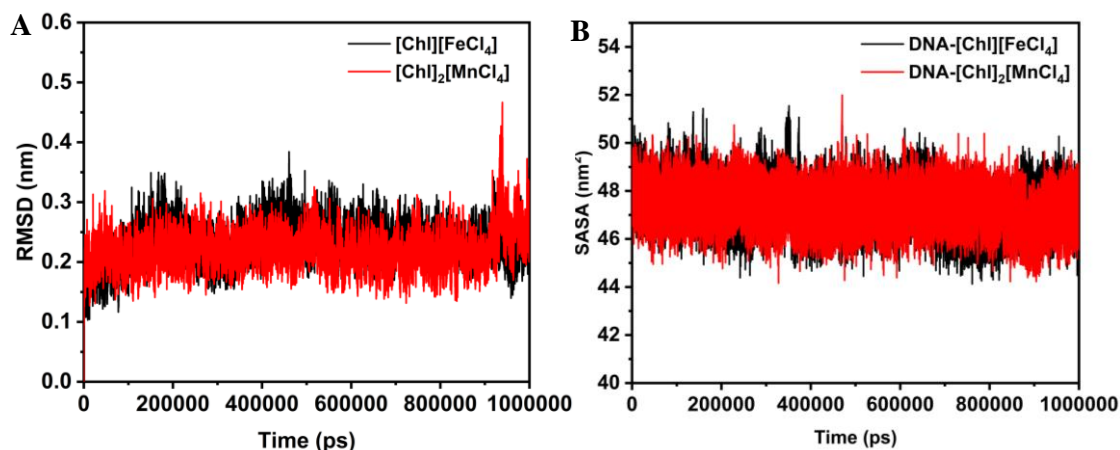
Figure 5.14. (A) RMSD plots of DNA, and (B) SASA plots of DNA and [Ch][Fe] or[Ch]$_2$[Mn] ILs.

To further elucidate the structural organization among DNA, $[Ch]^+$, $[FeCl_4]^-$, $[MnCl_4]^{2-}$, and water, we computed the radial distribution function (RDF) for both systems (Figure 5.15). Notably, the $[Ch]^+$ ions were found to be closer to DNA in both systems, with the maximum likelihood peak at around 0.5 nm. Conversely, water, $[FeCl_4]^-$, and $[MnCl_4]^{2-}$ ions were farther from DNA.
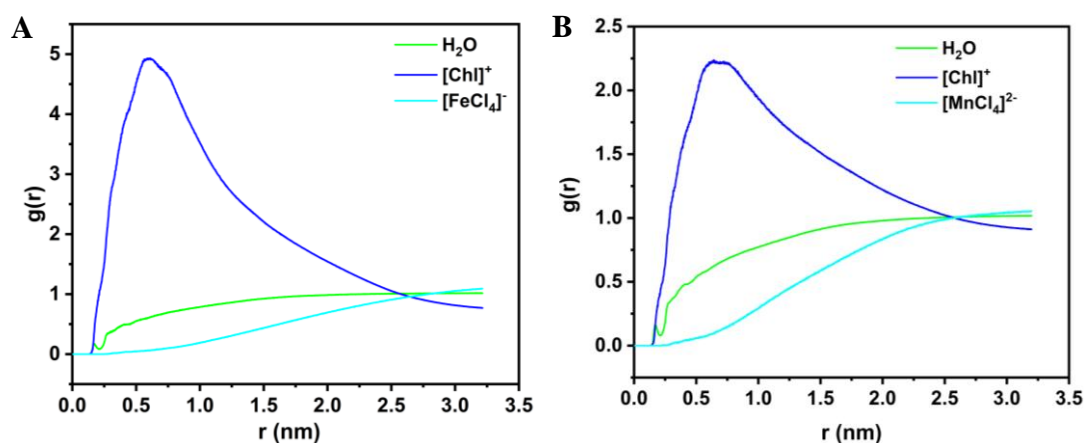
Figure 5.15. RDF plots of H2O, $[Ch]^+$, and [FeCl4]$^-$ or [MnCl4]$^{2-}$ with respect to DNA in (A) DNA-[Ch][Fe] and (B) DNA-[Ch]$_2$[Mn] systems.

The close proximity of $[Ch]^+$ ions to DNA, specifically with its phosphate groups, indicates a charge-neutralizing combination, which aligns with the observed Zeta

potential value. The decrease in ζ value from -40 mV to -13 mV in [Ch][Fe] IL or to -9 mV in [Ch]$_2$[Mn] IL is thus justified by this charge neutralization between [Ch]$^+$ and DNA. Furthermore, as evident in Figure 5.16, [Ch]$_2$[Mn] establishes a greater number of hydrogen bond interactions with DNA compared to [Ch][Fe].
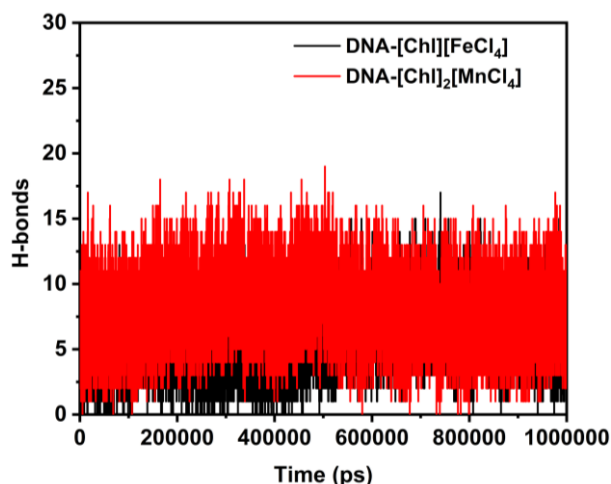
Figure 5.16. A) Number of H-bonds between DNA and [Ch][Fe] or [Ch]$_2$[Mn].

Consequently, [Ch]$_2$[Mn] is expected to exert a much stronger attraction to DNA than [Ch][Fe]. The MD simulations and analysis of post-MD parameters provide valuable insights into the dynamics and interactions between ct-DNA and ChMILs. The observed RMSD, SASA, RDF, and hydrogen bond interactions highlight the different behavior and binding characteristics of [Ch]$_2$[Mn] and [Ch][Fe] with DNA, shedding light on their respective roles in influencing ct-DNA's stability and structural organization.

During the MD simulation, the ct-DNA structure in [Ch][Fe] IL undergoes gradual changes due to its interaction with [Ch]$^+$ and the ionic liquid. Over time, the DNA molecule begins to bend and dilate in diameter, resulting in alterations to both the major and minor grooves. An unsuccessful overlay of DNA structures between 0 ns and 1000 ns in Figure 5.17 illustrates the extent of structural deformation. At 1000 ns, one of the DNA terminals is conspicuously bent.
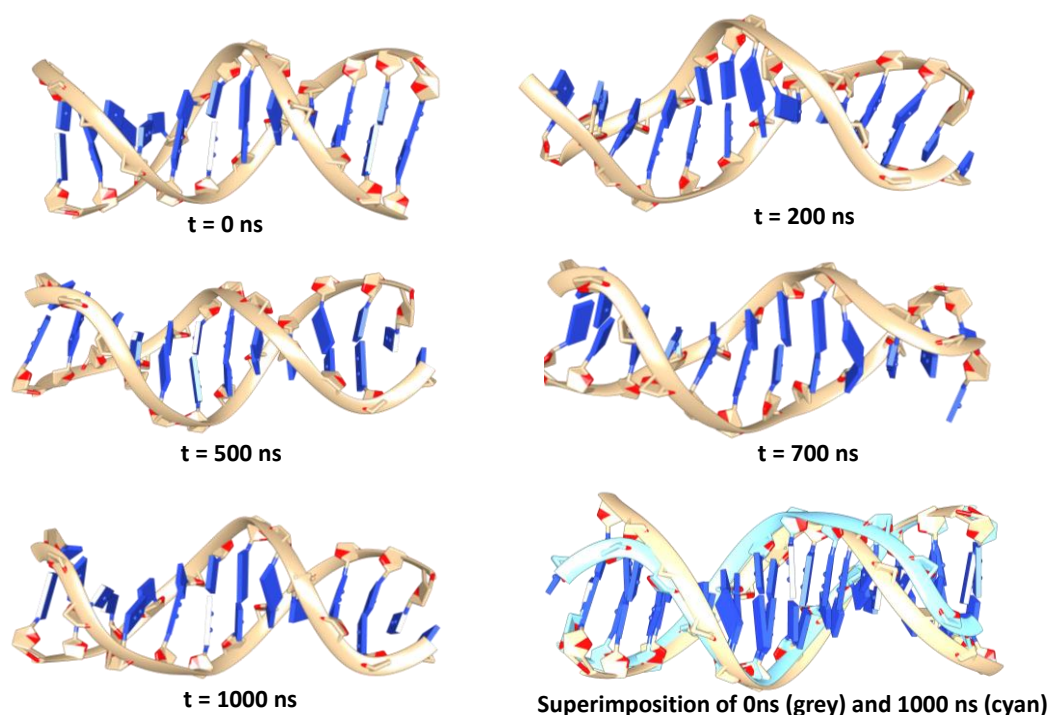
Figure 5.17. DNA conformations at different time instants (0, 200, 500, 700, and 1000 ns) and superimposition of structures at 0 ns and 1000 ns in [Ch][Fe] IL.

Similarly, $[Ch]_2[Mn]$ IL also distorts the DNA structure, as depicted in Figure 5.18. In this case, the DNA loses one primary and one minor groove. The $[Ch]^+$ ions in the IL exert strong Coulombic and hydrogen bonding forces, which cause the DNA helices/strands to be pulled apart. As a result, the length of the DNA is markedly reduced, while its diameter increases, leading to DNA compaction.
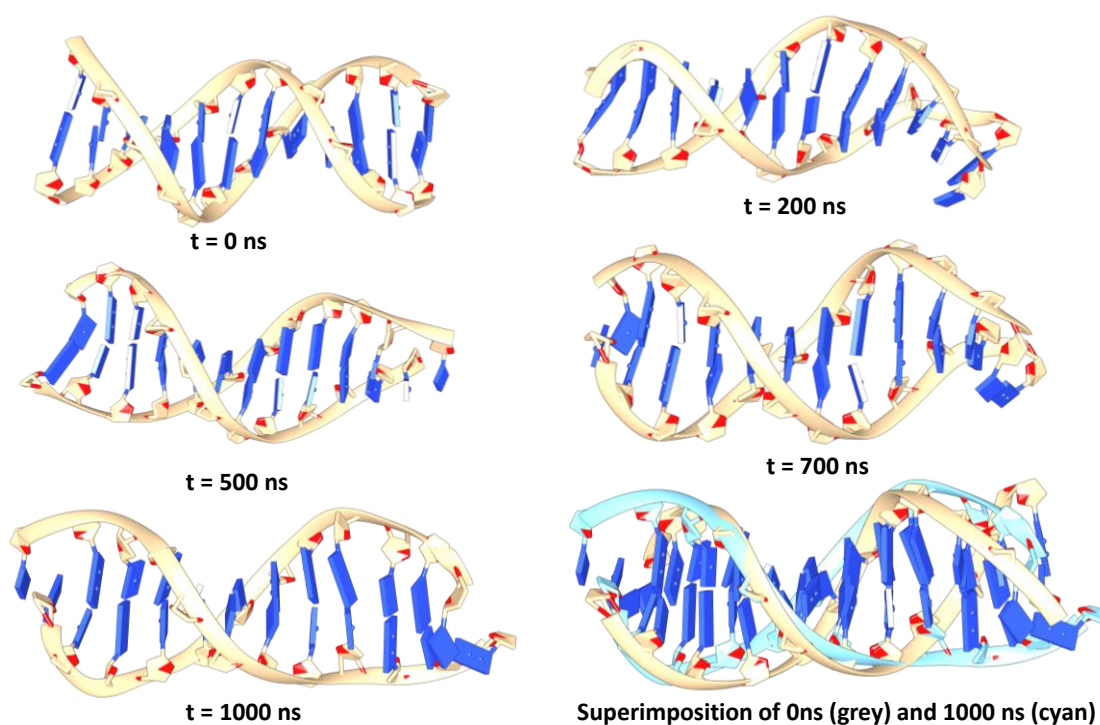
Figure 5.18. DNA conformations at different time instants (0, 200, 500, 700, and 1000 ns) and superimposition of structures at 0 ns and 1000 ns in [Ch]$_2$[Mn] IL.

To monitor these changes in DNA structure, the lengths and diameters of DNA at different time points are provided in Tables 5.2 and 5.3, respectively.

Table 5.2. The length and diameter of DNA in the [Ch][Fe] ionic liquid at different instants: 0, 200, 500, 700, and 1000 ns.

Time instant (ns)	Length (Å)	Diameter (Å)
0	43.6	27.2
200	41.9	34.2
500	40.5	38.7
700	45.9	30.8
1000	38.5	33.6

Table 5.3. The length and diameter of DNA in the [Ch]$_2$[Mn] ionic liquid at different instants: 0, 200, 500, 700, and 1000 ns.

Time instants (ns)	Length (Å)	Diameter (Å)
0	44.5	26.9
200	47.5	26.2
500	40.8	32.9
700	39.5	32.9
1000	39.6	35.3

Additionally, 3D elliptical images in Figures 5.19 and 5.20 effectively illustrate the change in DNA volume during the simulation, supporting the FESEM data. In these images, the major and minor axes of the ellipses represent DNA length and diameter, respectively. The transformation from an elliptical to a spherical shape (decrease in major axis and increase in minor axis) over time signifies the substantial compaction of DNA in ILs, particularly more pronounced in $[Ch]_2[Mn]$ IL.
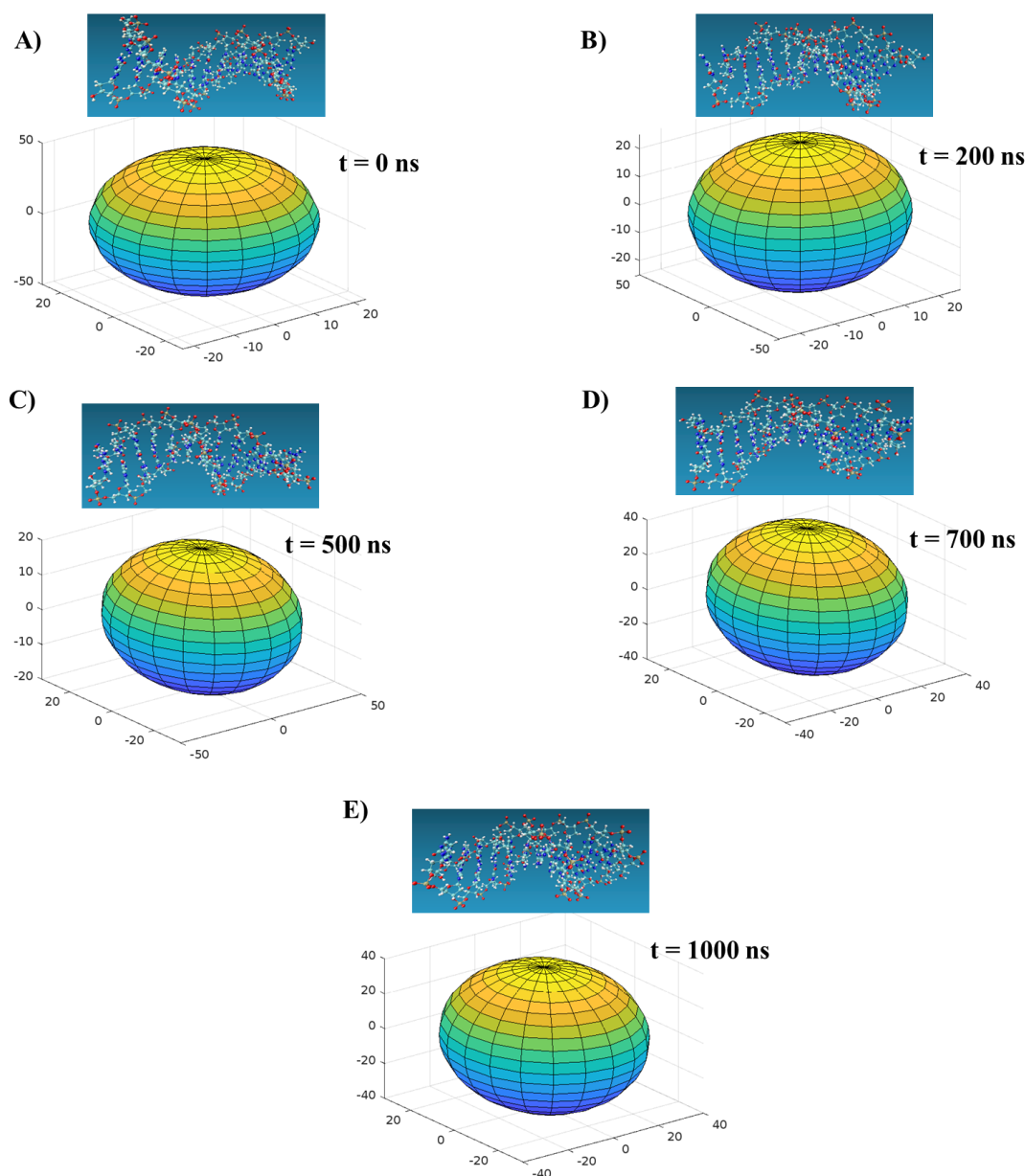
Figure 5.19. Illustrates the DNA volume as a 3D elliptical image for the DNA-[Ch][Fe] system at different time instants: 0 ns, 200 ns, 500 ns, 700 ns, and 1000 ns.

A)

t = 0 ns

B)

t = 200 ns

C)

t = 500 ns

D)

t = 700 ns

E)
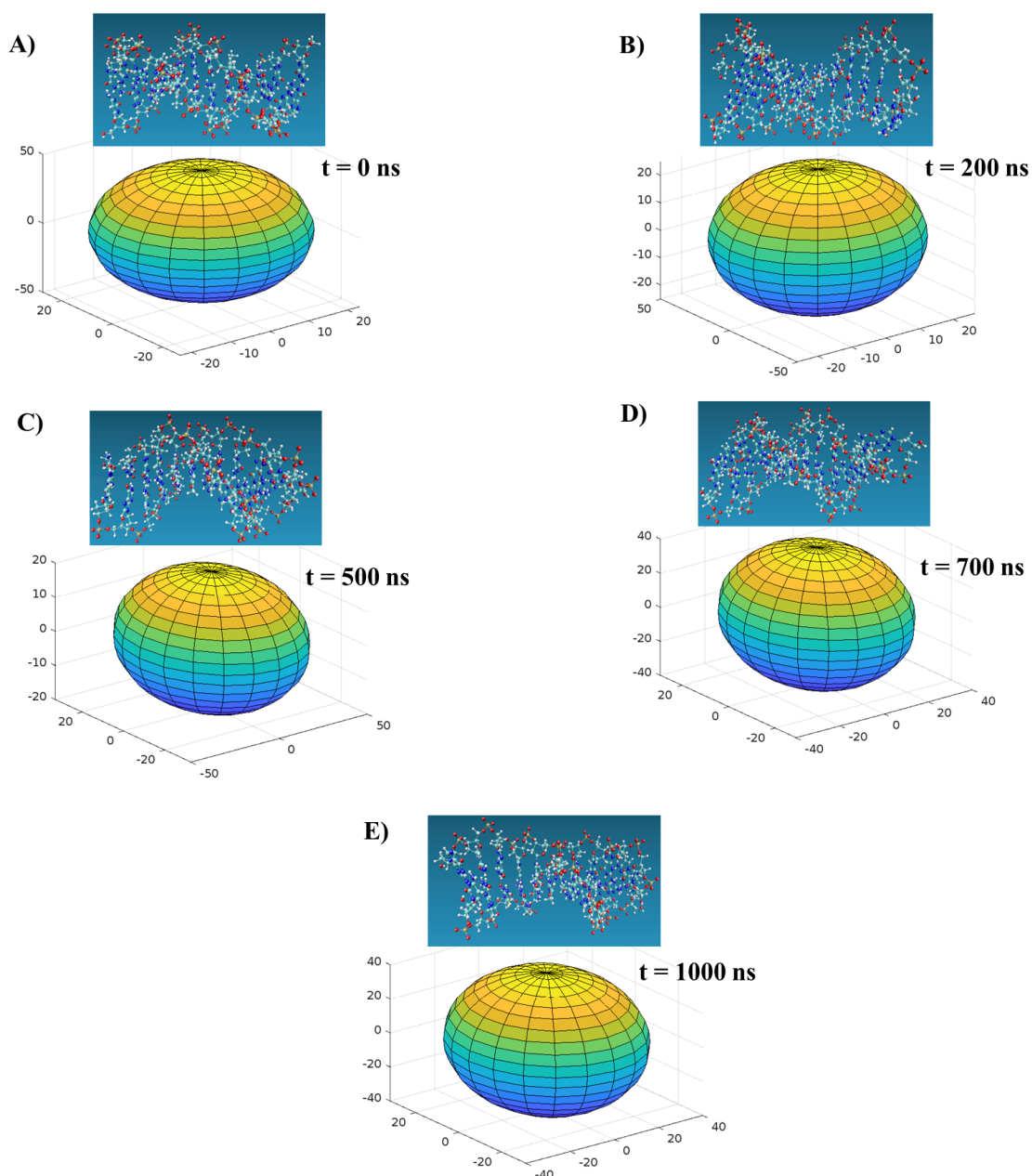
t = 1000 ns

Figure 5.20. Illustrates the DNA volume as a 3D elliptical image for the DNA-[Ch]$_2$[Mn] system at different time instants: 0 ns, 200 ns, 500 ns, 700 ns, and 1000 ns.

To quantify the affinity and binding strength between DNA and the ILs, we calculated the binding free energy (ΔG_{bind}) using the final 10 ns of MD trajectories. Figure 5.21 shows the computed ΔG_{bind} values along with their respective error bars and contributory interactions for both systems.
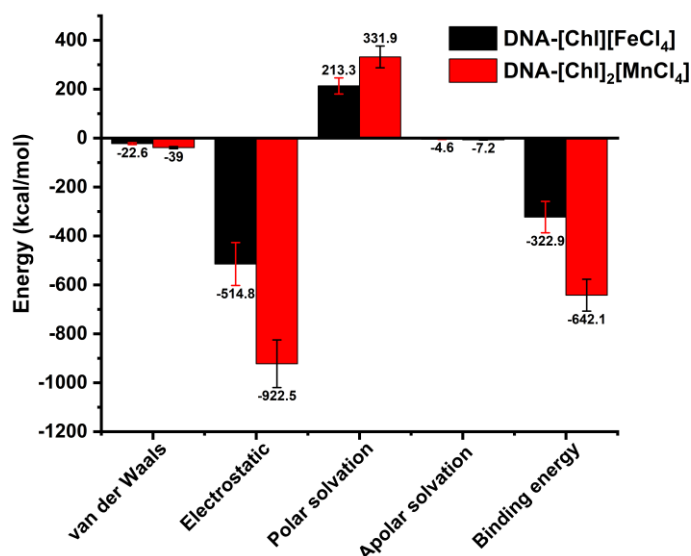
Figure 5.21. Binding free energies for DNA-[Ch][Fe] and DNA-[Ch]$_2$[Mn], including van der Waals, electrostatic, polar solvation, and apolar solvation components. Respective error bars are also shown.

For the DNA-[Ch][Fe] system, ΔG_{bind} is comprised of van der Waals, electrostatic, polar, and apolar solvation energy components, with values of -322.9, -22.6, -514.8, 213.3, and -4.6 kcal/mol, respectively. Similarly, in the DNA-[Ch]$_2$[Mn] system, the respective values are -642.1, -39, -922.5, 331.9, and -7.2 kcal/mol. It is evident that the electrostatic component contributes most to the interaction between DNA and the ILs, and it is greater by -407.7 kcal/mol in [Ch]$_2$[Mn] IL. Consequently, [Ch]$_2$[Mn] IL exhibits a stronger affinity for DNA, approximately twice that of [Ch][Fe] IL, which is consistent with the earlier post-MD parameters. This analysis also agrees qualitatively with the ITC Gibbs free energy changes of approximately -6 kcal/mol in [Ch][Fe] IL and approximately -9 kcal/mol in [Ch]$_2$[Mn] IL.

To gain further insights, the entire MD trajectories were subjected to Principal Component (PC) analysis. Considering the first two PCs, Figure 5.22 illustrates the conformational space of DNA in both systems during the last 10 ns of the MD trajectories. A comparison between the two systems shows that DNA in [Ch]$_2$[Mn] IL occupies a

smaller subspace compared to that in [Ch][Fe] IL. A smaller subspace indicates a more

pronounced interaction between DNA and [Ch]$_2$[Mn] IL.
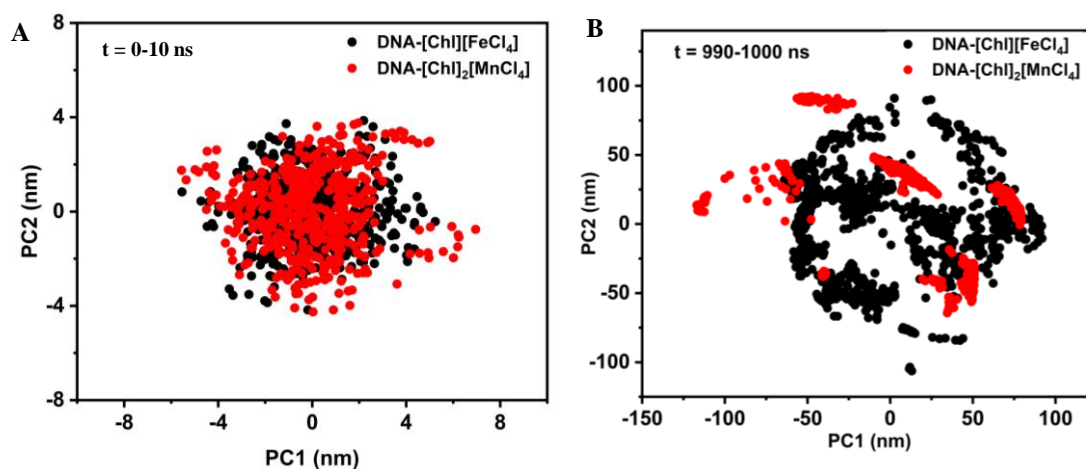
Figure 5.22. Principal component analysis of the DNA-[Ch][Fe] (black) and DNA-[Ch]$_2$[Mn] (red) simulation trajectories for the (A) first 10 ns (0-10 ns) and (B) last 10 ns (990-1000 ns).

Additionally, the residues' correlation contact map generated from the final 10 ns MD

trajectories for both systems provides more evidence. Figure 5.23 reveals that [Ch]$_2$[Mn]

IL has more contacts with DNA base pairs than [Ch][Fe] during the simulation period.

The MD analysis of the binding free energy, PC analysis, and contact maps further

supports the experimental findings, including the higher quenching rate and melting

temperature of DNA in [Ch]$_2$[Mn] IL. These provide valuable insights into the

interactions between ct-DNA and the ILs at the molecular level, helping to understand

the factors influencing DNA stability and behavior in different ionic liquid environments.
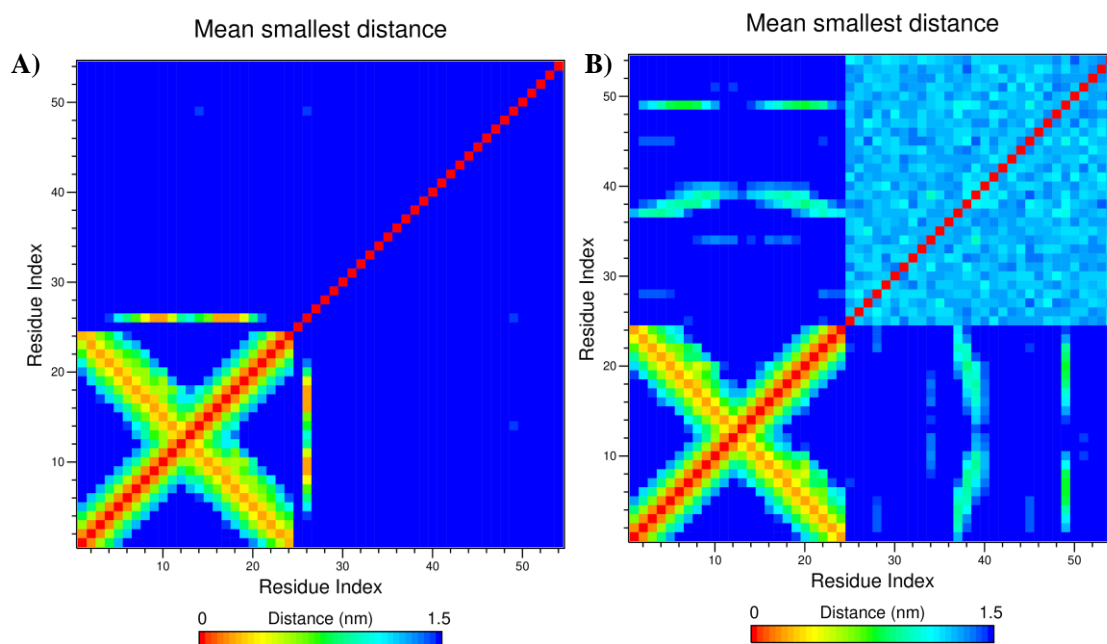
Figure 5.23. Residue co-relation contact maps for (A) DNA-[Ch][Fe] and (B) DNA-[Ch]₂[Mn]. In both systems, DNA is represented by 1-24 base pairs, whereas [Ch][Fe]/[Ch]₂[Mn] is represented by 25-54 residue indexes.

5.4. CONCLUSIONS

The binding characteristics and molecular mechanisms of ChMILs with ct-DNA were extensively investigated using a combination of experimental techniques and molecular docking. The observed turbidity in ct-DNA with increasing concentrations of ChMILs provided strong evidence of DNA compaction. SEM and FCS analyses further validated the compaction of ct-DNA in the presence of ChMILs. The molecular interactions between ILs and ct-DNA were revealed through various experimental methods. UV-Vis spectra, fluorescence dye displacement study, zeta potential, and molecular docking all pointed to the involvement of electrostatic, hydrogen bonding, and hydrophobic interactions in the binding process. Notably, these interactions were primarily mediated by the choline cation present in the ILs, independent of the specific anions used in the study. MD simulations provided crucial insights into the dynamic interactions between

ct-DNA and ChMILs. The simulations revealed a strong interaction between $[Ch]_2[Mn]$ and DNA, resulting in a more significant conformational shift of DNA compared to $[Ch][Fe]$. During the simulation, the surface of DNA exposed to solvent steadily decreased in both complexes, with the DNA structure bending or becoming more spherical due to the interactions with the two magnetic ionic liquids. The observed DNA compaction was found to be more prominent in the presence of $[Ch]_2[Mn]$, corroborating the earlier experimental findings. Based on the estimated binding free energy, $\Delta G = -642$ kcal/mol, it was conclusively confirmed that $[Ch]_2[Mn]$ exhibited a stronger affinity for DNA compared to $[Ch][Fe]$. This result aligned perfectly with the overall experimental and theoretical evidence, further supporting the conclusion that MILs can effectively bind ct-DNA through their choline cation, regardless of the anions involved. The comprehensive investigation using experimental techniques, molecular docking, and MD simulations provided a comprehensive understanding of the interactions between ChMILs and ct-DNA. The study unequivocally demonstrated the strong affinity and binding capacity of $[Ch]_2[Mn]$ with ct-DNA, highlighting its potential as a promising agent for DNA-related applications and providing valuable insights for future research in this field.

5.5. REFERENCES

1.   Gonzalez-Perez, A.; Dias, R. S., Different strategies for controlling DNA conformation: compaction and decompaction. *Front. Biosci.* **2009,** *1* (1), 228-241.

2.   Li, X.; Sun, D.; Chen, Y.; Wang, K.; He, Q.; Wang, G., Studying compaction-decompaction of DNA molecules induced by surfactants. *Biochem. Biophys. Res. Commun.* **2018,** *495* (4), 2559-2565.

3.   Xiong, Q.; Lee, O.-S.; Mirkin, C. A.; Schatz, G., Ethanol-Induced Condensation and Decondensation in DNA-Linked Nanoparticles: A Nucleosome-like Model for the Condensed State. *J. Am. Chem. Soc.* **2023,** *145* (1), 706-716.

4.   Saraswathi, S. K.; Karunakaran, V.; Maiti, K. K.; Joseph, J., DNA Condensation Triggered by the Synergistic Self-Assembly of Tetraphenylethylene-Viologen Aggregates and CT-DNA. *Front. Chem.* **2021,** *9.*

5.   Nakazawa, K.; El Fakih, F.; Jallet, V.; Rossi-Gendron, C.; Mariconti, M.; Chocron, L.; Hishida, M.; Saito, K.; Morel, M.; Rudiuk, S.; Baigl, D., Reversible Supra-Folding of User-Programmed Functional DNA Nanostructures on Fuzzy Cationic Substrates. *Angew. Chem. Int. Ed.* **2021,** *60* (28), 15214-15219.

6.   Estévez-Torres, A.; Baigl, D., DNA compaction: fundamentals and applications. *Soft Matter* **2011,** *7* (15), 6746-6756.

7.   Becerril, H. A.; Woolley, A. T., DNA-templated nanofabrication. *Chem. Soc. Rev.* **2009,** *38* (2), 329-337.

8.   Demeneix, B.; Hassani, Z.; Behr, J.-P., Towards Multifunctional Synthetic Vectors. *Curr Gene Ther,* **2004,** *4* (4), 445-455.

9.   You, Y.-Z.; Yu, Z.-Q.; Cui, M.-M.; Hong, C.-Y., Preparation of Photoluminescent Nanorings with Controllable Bioreducibility and Stimuli-Responsiveness. *Angew. Chem. Int. Ed.* **2010,** *49* (6), 1099-1102.

10.   González-Pérez, A.; Carlstedt, J.; Dias, R. S.; Lindman, B., Cyclodextrins in DNA decompaction. *Colloids Surf. B: Biointerfaces* **2010,** *76* (1), 20-27.

11.   Zinchenko, A. A.; Sergeyev, V. G.; Yamabe, K.; Murata, S.; Yoshikawa, K., DNA Compaction by Divalent Cations: Structural Specificity Revealed by the Potentiality of Designed Quaternary Diammonium Salts. *ChemBioChem* **2004,** *5* (3), 360-368.

12.   Gawęda, S.; Morán, M. C.; Pais, A. A. C. C.; Dias, R. S.; Schillén, K.; Lindman, B.; Miguel, M. G., Cationic agents for DNA compaction. *J. Colloid Interface Sci.* **2008,** *323* (1), 75-83.

13.   Kikuchi, T.; Sato, S.; Fujita, D.; Fujita, M., Stepwise DNA condensation by a histone-mimic peptide-coated M12L24 spherical complex. *Chem. Sci.* **2014,** *5* (8), 3257-3260.

14.   Deiana, M.; Pokladek, Z.; Matczyszyn, K.; Mlynarz, P.; Buckle, M.; Samoc, M., Effective control of the intrinsic DNA morphology by photosensitive polyamines. *J. Mater. Chem. B* **2017,** *5* (5), 1028-1038.

15.   Dias, R. S.; Lindman, B.; Miguel, M. G., Compaction and Decompaction of DNA in the Presence of Catanionic Amphiphile Mixtures. *J. Phys. Chem. B* **2002,** *106* (48), 12608-12612.

16.   Grueso, E.; Cerrillos, C.; Hidalgo, J.; Lopez-Cornejo, P., Compaction and Decompaction of DNA Induced by the Cationic Surfactant CTAB. *Langmuir* **2012,** *28* (30), 10968-10979.

17.   Guo, X.; Cui, B.; Li, Y.; Ding, J., Effects of salt and temperature on single-chained cationic surfactant/oligodeoxynucleotide vesicle formation. *J. Polym. Sci. A Polym. Chem.* **2012,** *50* (9), 1740-1745.

18.   Sivapragasam, M.; Moniruzzaman, M.; Goto, M., Recent advances in exploiting ionic liquids for biomolecules: Solubility, stability and applications. *Biotechnology Journal* **2016,** *11* (8), 1000-1013.

19.   Benedetto, A.; Ballone, P., Room Temperature Ionic Liquids Meet Biomolecules: A Microscopic View of Structure and Dynamics. *ACS Sustainable Chem. Eng.* **2016,** *4* (2), 392-412.

20.   Shukla, S. K.; Mikkola, J.-P., Use of Ionic Liquids in Protein and DNA Chemistry. *Phys. Chem. Chem. Phys.* **2020,** *8* (1219).

21.   Ding, X.; Clark, K. D.; Varona, M.; Emaus, M. N.; Anderson, J. L., Magnetic ionic liquid-enhanced isothermal nucleic acid amplification and its application to rapid visual DNA analysis. *Anal. Chim. Acta* **2019,** *1045*, 132-140.

22.   Emaus, M. N.; Clark, K. D.; Hinners, P.; Anderson, J. L., Preconcentration of DNA using magnetic ionic liquids that are compatible with real-time PCR for rapid nucleic acid quantification. *Anal. Bioanal. Chem.* **2018,** *410* (17), 4135-4144.

23.   Bowers, A. N.; Trujillo-Rodríguez, M. J.; Farooq, M. Q.; Anderson, J. L., Extraction of DNA with magnetic ionic liquids using in situ dispersive liquid–liquid microextraction. *Anal. Bioanal. Chem.* **2019,** *411* (28), 7375-7385.

24.   Clark, K. D.; Yamsek, M. M.; Nacham, O.; Anderson, J. L., Magnetic ionic liquids as PCR-compatible solvents for DNA extraction from biological samples. *Chem. Commun.* **2015,** *51* (94), 16771-16773.

25.   Clark, K. D.; Nacham, O.; Yu, H.; Li, T.; Yamsek, M. M.; Ronning, D. R.; Anderson, J. L., Extraction of DNA by Magnetic Ionic Liquids: Tunable Solvents for Rapid and Selective DNA Analysis. *Anal. Chem.* **2015,** *87* (3), 1552-1559.

26.   Gehlot, P. S.; Gupta, H.; Kumar, A., Paramagnetic Surface Active Ionic Liquids: Interaction with DNA and MRI Application. *Colloids Interface Sci. Commun.* **2018,** *26*, 14-23.

27.   Gehlot, P. S.; Gupta, H.; Rathore, M. S.; Khatri, K.; Kumar, A., Intrinsic MRI contrast from amino acid-based paramagnetic ionic liquids. *Mater. Adv.* **2020,** *1* (6), 1980-1987.

28.   Caparica, R.; Júlio, A.; Baby, A. R.; Araújo, M. E. M.; Fernandes, A. S.; Costa, J. G.; Santos de Almeida, T., Choline-Amino Acid Ionic Liquids as Green Functional Excipients to Enhance Drug Solubility. *Pharmaceutics* **2018,** *10* (4), 288.

29.   Tulsiyan, K. D.; Jena, S.; González-Viegas, M.; Kar, R. K.; Biswal, H. S., Structural Dynamics of RNA in the Presence of Choline Amino Acid Based Ionic Liquid: A Spectroscopic and Computational Outlook. *ACS Cent. Sci.* **2021,** *7* (10), 1688-1697.

30.   Sahoo, D. K.; Jena, S.; Dutta, J.; Chakrabarty, S.; Biswal, H. S., Critical Assessment of the Interaction between DNA and Choline Amino Acid Ionic Liquids: Evidences of Multimodal Binding and Stability Enhancement. *ACS Cent. Sci.* **2018,** *4* (12), 1642-1651.

31.   Frade, R. F. M.; Simeonov, S.; Rosatella, A. A.; Siopa, F.; Afonso, C. A. M., Toxicological evaluation of magnetic ionic liquids in human cell lines. *Chemosphere* **2013,** *92* (1), 100-105.

32.   Sintra, T. E.; Nasirpour, M.; Siopa, F.; Rosatella, A. A.; Gonçalves, F.; Coutinho, J. A. P.; Afonso, C. A. M.; Ventura, S. P. M., Ecotoxicological evaluation of magnetic ionic liquids. *Ecotoxicol. Environ. Saf.* **2017,** *143*, 315-321.

33.   Hornak, V.; Abel, R.; Okur, A.; Strockbine, B.; Roitberg, A.; Simmerling, C., Comparison of multiple Amber force fields and development of improved protein backbone parameters. *Proteins: Structure, Function, and Bioinformatics* **2006,** *65* (3), 712-725.

34.   Panteva, M. T.; Giambaşu, G. M.; York, D. M., Force Field for Mg2+, Mn2+, Zn2+, and Cd2+ Ions That Have Balanced Interactions with Nucleic Acids. *The Journal of Physical Chemistry B* **2015,** *119* (50), 15460-15470.

35.   Rappe, A. K.; Casewit, C. J.; Colwell, K. S.; Goddard, W. A., III; Skiff, W. M., UFF, a full periodic table force field for molecular mechanics and molecular dynamics simulations. *Journal of the American Chemical Society* **1992,** *114* (25), 10024-10035.

36.   Spoel., L. A. H. v. d., GROMACS 2021 Source Code. Zenodo. **January 22, 2021**.

37.   Berendsen, H. J. C.; Postma, J. P. M.; van Gunsteren, W. F.; Hermans, J., Interaction Models for Water in Relation to Protein Hydration. In *Intermolecular Forces: Proceedings of the Fourteenth Jerusalem Symposium on Quantum Chemistry and Biochemistry Held in Jerusalem, Israel, April 13–16, 1981*, Pullman, B., Ed. Springer Netherlands: Dordrecht, 1981; pp 331-342.

38.   Essmann, U.; Perera, L.; Berkowitz, M. L.; Darden, T.; Lee, H.; Pedersen, L. G., A smooth particle mesh Ewald method. *The Journal of Chemical Physics* **1995,** *103* (19), 8577-8593.

39.   Hess, B.; Bekker, H.; Berendsen, H. J. C.; Fraaije, J. G. E. M., LINCS: A linear constraint solver for molecular simulations. *Journal of Computational Chemistry* **1997,** *18* (12), 1463-1472.

40.   Panda, S. K.; Sen Gupta, P. S.; Biswal, S.; Ray, A. K.; Rana, M. K., ACE-2-Derived Biomimetic Peptides for the Inhibition of Spike Protein of SARS-CoV-2. *Journal of Proteome Research* **2021,** *20* (2), 1296-1303.

41.   Panda, S. K.; Saxena, S.; Gupta, P. S. S.; Rana, M. K., Inhibitors of Plasmepsin X Plasmodium falciparum: Structure-based pharmacophore generation and molecular dynamics simulation. *Journal of Molecular Liquids* **2021,** *340*, 116851.

42.   Miller, B. R., III; McGee, T. D., Jr.; Swails, J. M.; Homeyer, N.; Gohlke, H.; Roitberg, A. E., MMPBSA.py: An Efficient Program for End-State Free Energy Calculations. *Journal of Chemical Theory and Computation* **2012,** *8* (9), 3314-3321.

43.   Webb, R. L., Circular Dichroism and the Conformational Analysis of Biomolecules Edited by Gerald D. Fasman. Plenum Press, New York and London. 1996. ix + 738 pp. 17 × 25.5 cm. ISBN 0-306-45152-5. $125.00. *J. Med. Chem.* **1996,** *39* (26), 5285-5286.

44.   Kypr, J.; Kejnovská, I.; Renčiuk, D.; Vorlíčková, M., Circular dichroism and conformational polymorphism of DNA. *Nucleic Acids Res.* **2009,** *37* (6), 1713-1725.

45.   Roncarati, D.; Pelliciari, S.; Doniselli, N.; Maggi, S.; Vannini, A.; Valzania, L.; Mazzei, L.; Zambelli, B.; Rivetti, C.; Danielli, A., Metal-responsive promoter DNA compaction by the ferric uptake regulator. *Nat Commun* **2016,** *7* (1), 12593.

46.   Tsai, C. C.; Jain, S. C.; Sobell, H. M., X-ray crystallographic visualization of drug-nucleic acid intercalative binding: structure of an ethidium-dinucleoside monophosphate crystalline complex, Ethidium: 5-iodouridylyl (3'-5') adenosine. *Proc. Natl. Acad. Sci.* **1975,** *72* (2), 628-632.

47.   Galindo-Murillo, R.; Cheatham, T. E., III, Ethidium bromide interactions with DNA: an exploration of a classic DNA–ligand complex with unbiased molecular dynamics simulations. *Nucleic Acids Res.* **2021,** *49* (7), 3735-3747.

48.   Kapuscinski, J., DAPI: a DNA-Specific Fluorescent Probe. *Biotech. Histochem.* **1995,** *70* (5), 220-233.

49.   Haque, A.; Khan, I.; Hassan, S. I.; Khan, M. S., Interaction studies of cholinium-based ionic liquids with calf thymus DNA: Spectrophotometric and computational methods. *J. Mol. Liq.* **2017,** *237*, 201-207.

50.   Heller, D. P.; Greenstock, C. L., Fluorescence lifetime analysis of DNA intercalated ethidium bromide and quenching by free dye. *Biophys. Chem.* **1994,** *50* (3), 305-312.

51.   Rehman, S. U.; Sarwar, T.; Husain, M. A.; Ishqi, H. M.; Tabish, M. J. A. o. b.; biophysics, Studying non-covalent drug–DNA interactions. *Arch. Biochem.* **2015,** *576*, 49-60.

52.   Garai, A.; Ghoshdastidar, D.; Senapati, S.; Maiti, P. K., Ionic liquids make DNA rigid. *J. Chem. Phys.* **2018,** *149* (4).

53.   Freyer, M. W.; Lewis, E. A., Isothermal Titration Calorimetry: Experimental Design, Data Analysis, and Probing Macromolecule/Ligand Binding and Kinetic Interactions. In *Methods in Cell Biology*, Academic Press: 2008; Vol. 84, pp 79-113.

54.   Satpathi, S.; Sengupta, A.; Hridya, V. M.; Gavvala, K.; Koninti, R. K.; Roy, B.; Hazra, P., A Green Solvent Induced DNA Package. *Sci Rep* **2015,** *5* (1), 9137.

55.   Yu, L.; Lei, Y.; Ma, Y.; Liu, M.; Zheng, J.; Dan, D.; Gao, P., A Comprehensive Review of Fluorescence Correlation Spectroscopy. *Front. Phys.* **2021,** *9*.

56.   Pabbathi, A.; Samanta, A., Spectroscopic and Molecular Docking Study of the Interaction of DNA with a Morpholinium Ionic Liquid. *J. Phys. Chem. B* **2015,** *119* (34), 11099-11105.

57.   Mati, S. S.; Roy, S. S.; Chall, S.; Bhattacharya, S.; Bhattacharya, S. C., Unveiling the Groove Binding Mechanism of a Biocompatible Naphthalimide-Based Organoselenocyanate with Calf Thymus DNA: An "Ex Vivo" Fluorescence Imaging Application Appended by Biophysical Experiments and Molecular Docking Simulations. *J. Phys. Chem. B* **2013,** *117* (47), 14655-14665.

58.   Eberhardt, J.; Santos-Martins, D.; Tillack, A. F.; Forli, S., AutoDock Vina 1.2.0: New Docking Methods, Expanded Force Field, and Python Bindings. *J. Chem. Inf. Model.* **2021,** *61* (8), 3891-3898.

Chapter 6

Peroxidase Activity of Cytochrome-c in Magnetic Ionic Liquids

6.1. INTRODUCTION

Cytochrome c (Cyt-c) is a crucial protein in mitochondria that plays a vital role in electron transport and ATP synthesis. Apart from its primary function, Cyt-c also exhibits significant peroxidase activity, which is involved in apoptosis and cell signaling. Enhancing the peroxidase activity of Cyt-c is of great importance. Native Cyt-c has a six-coordinated heme group, with a distal coordination site occupied by Met80. However, in the presence of hydrogen peroxide (H_2O_2), Cyt-c undergoes self-oxidation, breaking the Fe-Met80 bond and increasing peroxidase activity.[1-5] This activity is attributed to the 40-57 Ω-loop dynamics and the Met80 amino acid in the heme region (Figure 6.1).[6-7]
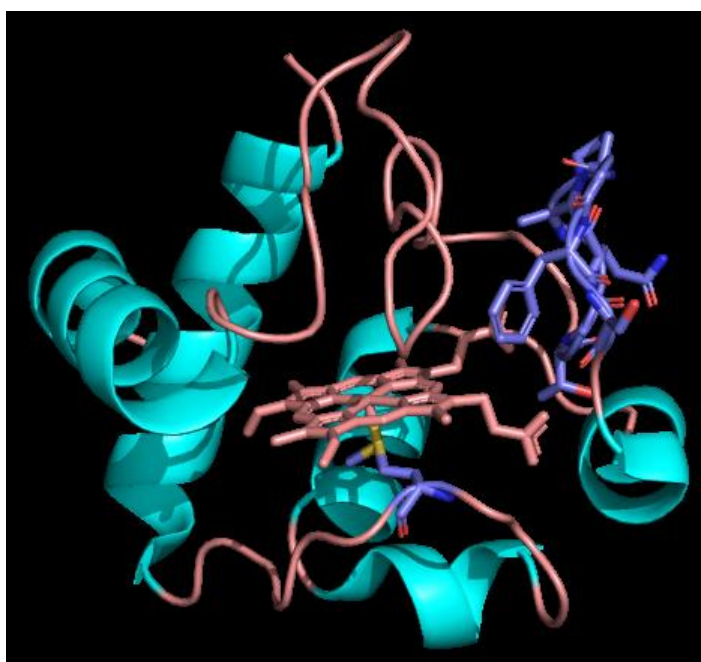
Figure 6.1. Cartoon representation of cytochrome-c PDB : 2B4Z

The structural stability and activity of a protein are influenced by various factors such as temperature, pressure, pH, and the cellular environment. The solvent environment also plays a crucial role in maintaining protein conformation. Organic solvents can denature proteins and reduce their activity.[8] Therefore, finding effective solvent environments that provide stability and enhance enzymatic activity is an active area of research.

For this, Ionic liquids (ILs) have recently emerged as green solvents for proteins. These molten salts have melting points below 100°C and possess high thermal stability, low toxicity, low vapor pressure, and biodegradability.[9-12] The physicochemical properties of ILs can be tailored by choosing specific cations and anions, making them "designer solvents." ILs have been used for preserving, extracting, and stabilizing proteins and biomolecules.[13-16] They have shown effectiveness in storing, stabilizing, and extracting proteins and nucleic acids.[17-19] ILs are classified into different categories based on their properties and applications, such as room-temperature ILs (RTILs), task-specific ILs (TSILs), supported IL membranes (SILMs), and magnetic ILs (MILs)[20-27]. MILs, in particular, have garnered interest in various fields due to their strong response to external magnetic fields.

Some studies have demonstrated the potential of MILs as solvents for the storage and extraction of biomolecules and nucleic acids. For example, MILs have been employed for efficient extraction of DNA from bacterial cell lysate and salmon testes. MILs have also been used in sequencing-specific DNA extraction and as contrasting agents for MRI applications.[21, 24, 27] However, the effect of MILs on the activity of Cyt-c has not been investigated.

Previous research has explored the storage and stability of Cyt-c in imidazolium and ammonium-based ILs, but no significant changes in peroxidase activity were observed.[28-29] However, a study reported a twofold enhancement in the activity of Cyt-c at higher temperatures in the presence of ILs.[30] Another study showed increased peroxidase activity of Cyt-c when exposed to Mn-doped quantum dots and choline-based ILs.[31] Nevertheless, there are no reports on the impact of MILs on the activity of Cyt-c.

In this study, we aim to investigate the effect of MILs on the peroxidase activity of Cyt-c. We selected two MILs based on Fe and Mn due to their magnetic and biological activity. Various spectroscopic techniques, including absorption, emission, time-resolved emission, and circular dichroism (CD), were employed to study the interactions between MILs and Cyt-c. The thermodynamic parameters involved in protein-ligand interactions were evaluated using isothermal titration calorimetry (ITC).[32] Molecular docking and molecular dynamics simulations were performed to gain insights into the binding mode at the molecular level.

This study focuses on understanding the influence of MILs on the peroxidase activity of Cyt-c. By investigating the interactions between MILs and Cyt-c using a range of spectroscopic techniques, thermodynamic analysis, and computational simulations, we aim to shed light on the potential of MILs as solvents to enhance the enzymatic activity of Cyt-c. The findings of this study can contribute to developing strategies to improve the stability and activity of proteins in biomedical and biotechnological applications.

6.2. METHODS

6.2.1. Materials

Cytochrome c from bovine heart from Sigma Aldrich was used without further purification. The concentration of oxidized cyt c was determined spectrophotometrically at 409 nm ($\varepsilon \approx 106100$ $M^{-1}.cm^{-1}$) at pH 7.4 in 20 mM sodium phosphate buffer.[33] Choline chloride, ferric chloride, and manganese chloride were purchased from Sigma-Aldrich. Hydrogen peroxide (30%) was purchased from Merck chemicals, whereas guaiacol (2-Methoxy phenol) was purchased from Spectrochem chemicals Pvt. Ltd. Throughout the experiments Milli-Q water was used for solution preparation. Preparation of stock solution, synthesis, and characterization of ILs are provided.[34] Detailed experimental

methods such as circular dichroism measurements, absorbance measurements, lifetime measurements, transmission electron microscopy (TEM), peroxidase activity of Cyt-c, isothermal titration calorimetry (ITC), and computational methods (Molecular Docking and MD simulations) are provided. All the measurements are taken as an average of 3 scans. All the experiments are performed thrice to confirm their reproducibility. The experimental error percentage was less than 10% for each set of experiments.

6.2.2. Stock solution

Cyt-c stock solution was prepared by dissolving powdered Cyt-c in 20mM phosphate buffer with stirring in a 3D shaker, and the stock solution was stored at -20°C for further use. Cyt-c solution concentration was calculated experimentally using molar absorbance coefficient (ε) values of 106100 $M^{-1}.cm^{-1}$ at 409 nm in UV-vis absorption spectroscopy. The ionic liquids [Ch][Fe] and [Ch]$_2$[Mn] were synthesized according to the prescribed method via simple acid-base neutralization reactions. 1H, 13C NMR, and EPR spectroscopy characterized the products formed. The synthesized ionic liquids were kept in a vacuum oven at room temperature to avoid moisture and air contact for further use.

6.2.3. Experimental methods

CD measurements for Cyt-c were performed on JASCO J-1500, equipped with a Peltier-type temperature controller (PTC-100). CD spectra of Cyt-c were taken with, and without MILs at 25 °C and pH 7.4. For CD measurements of the far-UV region, a cuvette with a path length of 0.1 cm was used, while a cuvette with a path length of 1 cm was used for CD measurements of near-UV and Soret regions. An average of three scans were recorded to improve the signal-to-noise ratio at a scanning speed of 100 nm/min with a bandwidth of 1 nm. CD spectrum of 10μM Cyt-c in phosphate buffer was performed with 20mM phosphate buffer as a baseline. On gradual addition of MILs to Cyt-c, the CD spectra

were recorded to know the effect of MIL on Cyt-c stability. During the experiment, a constant nitrogen flow was maintained.

The absorption spectra of native Cyt-c, MILs, Cyt-c in the presence of different concentrations of MILs were recorded with an Agilent Cary spectrophotometer. 20 mM phosphate buffer was taken as a baseline for measuring all sample spectra. All measurements were carried out in a quartz cuvette with an optical path length of 1 cm.

Fluorescence measurements were performed by using a quartz cuvette of path-length 1 cm in an Einberg-made fluorimeter equipped with a Peltier element. Fluorescence emission spectra were measured between 310 nm and 450 nm with 280 nm excitation wavelength in the presence and absence of MILs. The concentration of cyt c in a cuvette was 10 μM. Excitation and emission slits of 3 nm width were used for measurements of fluorescence spectra. All measurements were performed at 25 °C, kept constant by Peltier element.

Edinberg made a time-correlated single photon counting (TCSPC) spectrometer (F700) to calculate fluorescence lifetimes from time-resolved fluorescence intensity decays. The excitation source was a pulsed nanosecond LED laser (λexc = 280 nm) and the detector used was MCP photomultiplier. Ludox (colloidal silica) was used to measure lamp profiles at the excitation wavelength and the fluorescence lifetime data were measured to 5000 counts in the peak. The instrumental response function was recorded sequentially using a scattering solution and a 1024 ps/channel time calibration. The emission wavelength was set to 340 nm, and lifetimes were obtained by tri-exponential fit. Chi-squared ($\chi2$) value and weighted residuals were used for the acceptable fit.

The peroxidase activity of the Cyt-c (2 μM) with and without the presence of ChMILs was investigated using guaiacol as substrate and H_2O_2 as oxygen donor. In a typical

experiment, 100 µL of Cyt-c was taken in a vial with the addition of 800 µL of 20mM phosphate buffer +100 µL guaiacol (20mM), +100 µL H_2O_2 (50mM). Different concentrations of ChMILs were added before H_2O_2 to get activity in the presence of ILs. H_2O_2 was added at the end to avoid oxidation of the enzyme. The activity was measured from the absorbance of the UV-vis absorption spectrometer at 470 nm. The absorbance was obtained from the oxidation of guaiacol to tetra guaiacol catalysed by Cyt-c. The oxidation reaction can be known qualitatively from the appearance of the orange color. The formation rate of tetra guaiacol can be measured using molar absorption coefficients of 26,678 mM^{-1} cm^{-1}. Similarly, activity at different temperatures (30, 50, and 70 °C) was measured by UV-vis spectrophotometer at 470 nm using a Peltier system.

The binding of ChMILs to Cyt-c was measured using isothermal titration calorimetry with a MicroCal iTC-200 calorimeter at 25 °C. The volume capacity of the sample and reference cells are 200 µL and 100 µL, respectively, and an adiabatic shield insulates both cells. The sample cell was filled with a fixed concentration of Cyt-c prepared in phosphate buffer, and the titration was carried out by injecting IL from a 40 µL rotating syringe into the sample cell. The concentration of IL and Cyt-c were taken as 10mM and 10µM respectively, to carry out the titrations for getting the thermodynamics of the IL-Cyt-c system. 25 injections were chosen for each titration, and each injection was of 1.5 µL volume with an interval of 120 s.

6.2.4. Computational methods

The 3D crystal structure of well-characterized Cyt-c protein with 1.5 Å resolutions was downloaded from a protein data bank with PDB ID 2B4Z[35] and chosen as the model protein for both docking and MD simulations. The molecular docking studies were carried out using AutoDock Vina software.[36] The ligand structures (ChMILs) were optimized at

B97D/def2TZVPP level using S6 Turbomole V6.5.3.[37] Cyt-c and ligands were prepared using Auto Dock Tools. The grid sizes were varied for different systems in x, y, and z directions keeping constant grid spacing of 1.0 Å. The one with the lowest energy docked conformer was selected as the binding mode out of the 15 different conformers in each case.

The X-ray crystal structure of Cytochrome C protein (PDB: 2B4Z) was retrieved from the RCSB database for preparing the starting structure of MD simulation studies. We used the CHARMM-GUI[38] Solution builder tool to generate the input simulation parameter files. Both protein and ions were modeled using an all-atom CHARMM36m force field[39-41], while water molecules were modeled using the TIP3P[42] water model.

The Choline [Ch] cation parameters were obtained from the Cgenff server integrated into the CHARMM-GUI server. For anions $[FeCl_4]^-$ and $[MnCl_4]^{2-}$, the CHARMM36 compatible parameters were generated by performing ab-initio quantum mechanics (QM) calculation. Towards this end, the initial geometries for these ligands were first built using Avogadro software. Geometry optimization of these initial geometries was performed using Density Functional Theory (DFT)[43] calculations using the Gaussian-16 suite program[44]. Calculations were performed using local meta-General Gradient Approximate (GGA) exchange-correlation functional M06L[45] with 6-31G (d,p)**[46] and SDD(ESP)[47] as the basis set for transition metal atoms. Charges from electrostatic potentials using grid-based methods were employed to calculate the ESP charges. The gaussian-16 generated log and fchk files generated the forcefield parameters for $[FeCl_4]^-$ and $[MnCl_4]^{2-}$ anions. QM-acquired geometric and vibrational harmonic frequencies generated the equilibrium values and force constants for bond and angle terms using a modified Seminaro approach[48] with a scaling factor of 1.0. The Lennard-Jones parameters for Fe^{3+} ion was obtained from the existing CHARMM36 FF database. For Mn^{2+} ion, these LJ

parameters were obtained from the Force field calculations done by Won and co-workers[49].

We performed an independent set of MD simulations for (i) Cyt-C with [Ch][Fe] system and (ii) Cyt-c with [Ch]₂[Mn] system. The molar ratio of protein to ionic Liquid (IL) was maintained at 1:100 for both systems. The whole system was then solvated by adding 5721 water particles in the case of the $[FeCl_4]$ system and 4,972 water molecules in the case $[MnCl_4]^{2-}$ system. The overall charge of the system was neutralized, and salt concentration was maintained by adding 21 Na^+ and 27 Cl^- ions. The total size of the system was 21531 particles for $[FeCl_4]$ system and 21384 particles for $[MnCl_4]^{2-}$ system. The cubic box with dimensions 6.1 x 6.1 x 6.1 nm^3 was used for both systems. The system was minimized using the steepest-descent algorithm and then further equilibrated using an NVT ensemble under position restraints. The system's average temperature was set to 298.15 K (25 °C), and a Nose-Hoover thermostat[50] was used. Initial random velocities were assigned to each atom according to the Boltzmann distribution of velocities at that temperature.

Finally, all simulations were performed in an NPT ensemble using the leap-frog integrator with a 2-fs time step. The Verlet cut-off scheme was employed throughout the simulation, with the Lenard Jones interaction extending to 1.2 nm with dispersion corrections. The electrostatic interactions were implemented with a short-range electrostatic cut-off at 1.2 nm, and long-range interactions were treated by Particle Mesh Ewald summation with cubic interpolation and in a Fourier-grid space of 0.16 nm. The neighbor lists were updated every 20 steps. All bond lengths involving hydrogen atoms of the lipids and the ligands were constrained using the LINCS algorithm, and water molecules were kept rigid using the SETTLE approach. The average temperature is maintained at 298.15 K by coupling solute and solvent separately to the Nose-Hoover thermostat[13] with a relaxation

constant of 1.0 ps. The pressure was controlled at 1 bar by Parrinello-Rahman barostat with a time constant of 5 ps and compressibility of 4.5*10-5 bar with isotropic coupling. The system was periodic in all three directions. Finally, all simulations were performed in an NPT ensemble using the leap-frog integrator with a 2-fs time step. The Verlet cut-off scheme[51] was employed throughout the simulation with the Lenard Jones interaction extending to 1.2 nm with dispersion corrections. The electrostatic interactions were implemented with a short-range electrostatic cut-off at 1.2 nm, and long-range interactions were treated by Particle Mesh Ewald[52] summation with cubic interpolation and in a Fourier-grid space of 0.16 nm. The neighbour lists were updated every 20 steps. All bond lengths involving hydrogen atoms of the lipids and the ligands were constrained using the LINCS algorithm[53] and water molecules were kept rigid using the SETTLE approach[54]. The average temperature is maintained at 298.15 K by coupling solute and solvent separately to the Nose-Hoover thermostat with a relaxation constant of 1.0 ps. The pressure was controlled at 1 bar by Parrinello-Rahman barostat[55] with a time constant of 5 ps and compressibility of 4.5*10-5 bar with isotropic coupling. The system was periodic in all three directions. We performed a total 2 copies of atomistic simulations for both $[FeCl_4]^-$ and $[MnCl_4]^{2-}$ systems, each of them was of 200 ns in duration. All the simulations are carried out using GROMACS 2019 version[56] and trajectory was saved at every 100 ps for the analysis.

6.3. RESULTS AND DISCUSSIONS

6.3.1. Peroxidase Activity of Cyt-c:

To investigate the effect of MILs on the peroxidase activity of Cyt-c, we conducted experiments using guaiacol oxidation in the presence of H_2O_2 at pH 7.4. The progress of

the reaction was monitored using UV-Vis absorption spectroscopy, specifically observing

the absorption maxima of tetraguaiacol at 474 nm (Figure 6.2).[5]
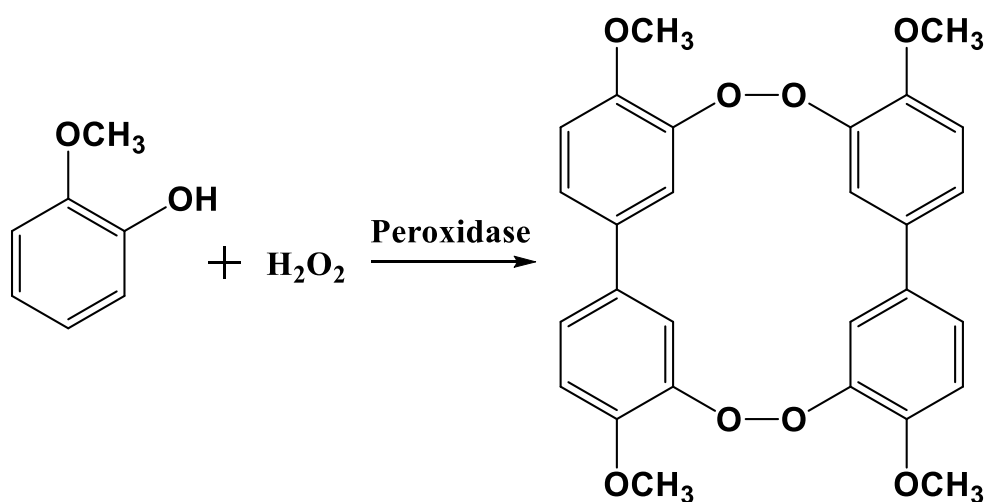
Figure 6.2. Oxidation of guaiacol to tetraguaiacol, with peroxidase (Cyt-c) B

First, we examined the impact of [Ch][Fe] MIL on the activity of Cyt-c. Gradually adding

[Ch][Fe] MIL revealed that the activity of Cyt-c remained unaffected at lower

concentrations. However, as the concentration of [Ch][Fe] MIL increased, we observed

an enhancement in the activity of Cyt-c (Figure 6.3A). In fact, upon the addition of 5 mM

[Ch][Fe] MIL, the activity of Cyt-c increased two-fold. Further addition of [Ch][Fe] MIL

did not result in significant changes in activity. To rule out the possibility that the

increased activity was due to unreacted $FeCl_3$, control experiments were conducted by

adding $FeCl_3$ alone, which did not affect the activity of Cyt-c. Similarly, we investigated

the impact of $[Ch]_2[Mn]$ MIL on the activity of Cyt-c (Figure 6.3B). However, $[Ch]_2[Mn]$

MIL had minimal influence on the activity of Cyt-c, with only a 20% increase observed

upon adding 5 mM $[Ch]_2[Mn]$ MIL.
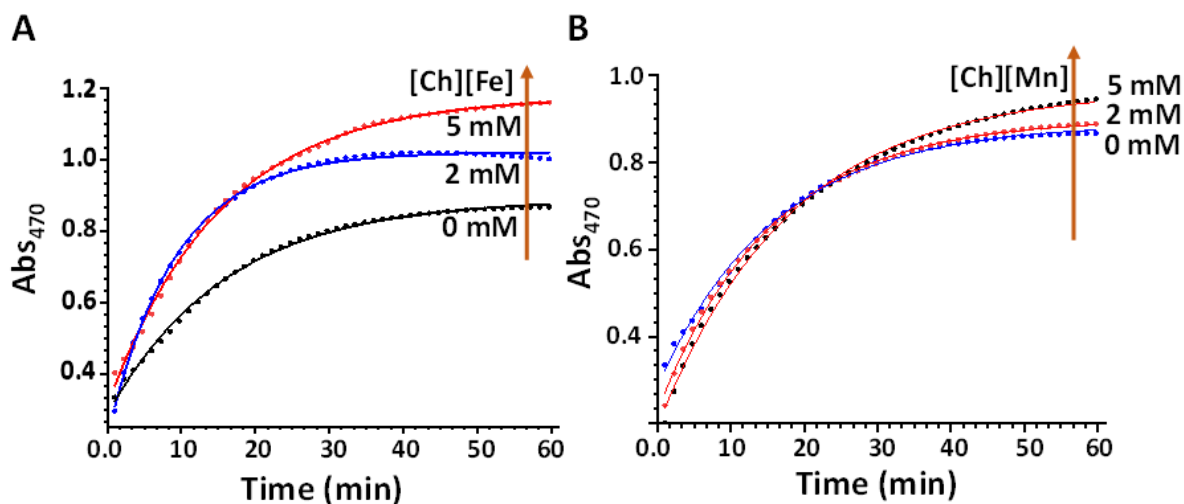
Figure 6.3. A) Peroxidase activity of Cyt-c (20 µM) in the presence of [Ch][Fe] B) Peroxidase activity of Cyt-c (20 µM) in the presence of [Ch]2[Mn].

It is important to note that the peroxidase activity of Cyt-c in its native state requires activation through H_2O -induced covalent modifications. Previous studies have reported a 7-fold increase in the activity of a mutated form of Cyt-c, attributed to increased dynamics in the 40-57 Ω-loop and Met80.

Table 6.1. Rate constants, k ($x10^{-3}$), for peroxidase activity of Cyt-c in the presence of different concentrations of MILs obtained by exponential growth fitting

MILs	0mM	2mM	5mM
	k (x 10^{-3} s^{-1})	k (x 10^{-3} s^{-1})	k (x 10^{-3} s^{-1})
[Ch][Fe]	5.8	8.6	9.2
[Ch][Mn]	5.8	5.5	5.6

Additionally, it has been proposed that the increased peroxidase activity of Cyt-c in the presence of denaturants like urea is due to the destabilization of foldons and an increase in the dynamic equilibrium between different coordination states of Cyt-c.

To gain further insights into the enhanced peroxidase activity of Cyt-c in MILs, we employed various spectroscopic methods and molecular docking. These techniques were utilized to elucidate the underlying mechanisms behind the observed enhancement in activity.

6.3.2. Conformational insights

The structural modifications of Cyt-c induced by the addition of MILs were monitored using CD spectroscopy. The far-UV region (200-250 nm) provided information about changes in the secondary structure, while the near-UV region (250-300 nm) allowed analysis of the tertiary structure. The soret band region (375-450 nm) was used to observe alterations in the conformational environment of the heme group.

In the far-UV region, Cyt-c exhibited a typical negative CD spectrum, indicating its native conformation. The addition of [Ch][Fe] IL at increasing concentrations did not cause significant changes in the negative CD spectra, suggesting minimal impact on the secondary structure (Figure 6.4A). However, with the addition of [Ch]$_2$[Mn] IL, a decrease in the negative CD spectra was observed, indicating alterations in the secondary structure (Figure 6.4B), specifically a decrease in the percentage of α-helix (Table 6.2).
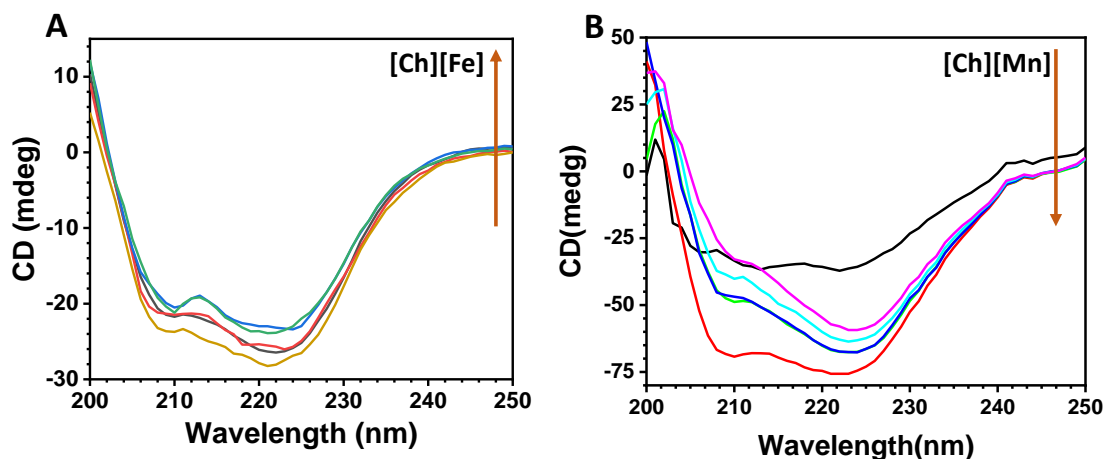
Figure 6.4. Far-UV CD spectra of native Cyt-c (20 × 10^{-6} M) and Cyt-c with different concen-trations of A) [Ch][Fe]] and B) [Ch]₂[Mn]

Table 6.2. % α-Helical Content of Cyt-c with and without MILs Obtained from Far-UV CD Data at $\Theta_{222\ nm}$

System	0 mM	1 mM	2 mM	5 mM
Cyt C-FeIL	40.2	39.8	39.4	38.7
Cyt C-MnIL	40.1	37.5	36.8	33.7

The near-UV region CD spectra, which are sensitive to the tertiary structural packing of tryptophan residues, showed two fingerprint minima at 282 and 289 nm. The addition of [Ch][Fe] IL up to 10 mM concentration resulted in changes in the CD spectra (Figure 6.5A), indicating modifications in the tertiary structure of Cyt-c. On the other hand, minimal changes were observed upon the addition of [Ch]₂[Mn] IL, suggesting that it had a lesser impact on the tertiary structure compared to the secondary structure (Figure 6.5B).
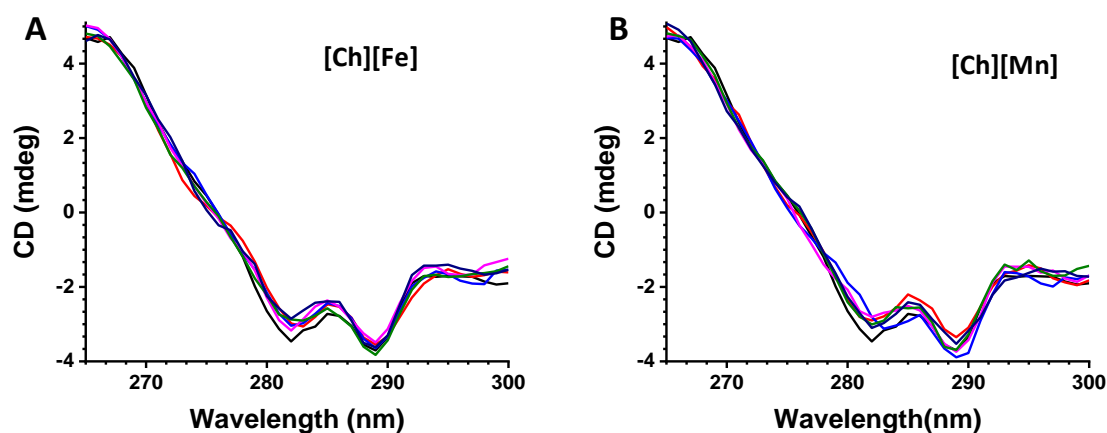
Figure 6.5. Near-UV CD spectra of native Cyt-c (20 × 10⁻⁶ M) and Cyt-c with different concen-trations of A) [Ch][Fe]] and B) [Ch]₂[Mn]

Examining the soret band region during CD measurements provided insights into the heme-polypeptide interactions and spin state of heme-Fe. With the gradual addition of [Ch][Fe] IL (Figure 6.6A), the 417 nm peak representing Met80-Fe and Phe82-heme interaction disappeared, while the 406 nm positive peak, corresponding to heme-globin interaction and the spin state of heme-Fe, increased. In contrast, no significant change in the soret band region was observed in the presence of [Ch]₂[Mn] IL, indicating that heme-polypeptide interaction and the spin state of heme-Fe were retained (Figure 6.6B).
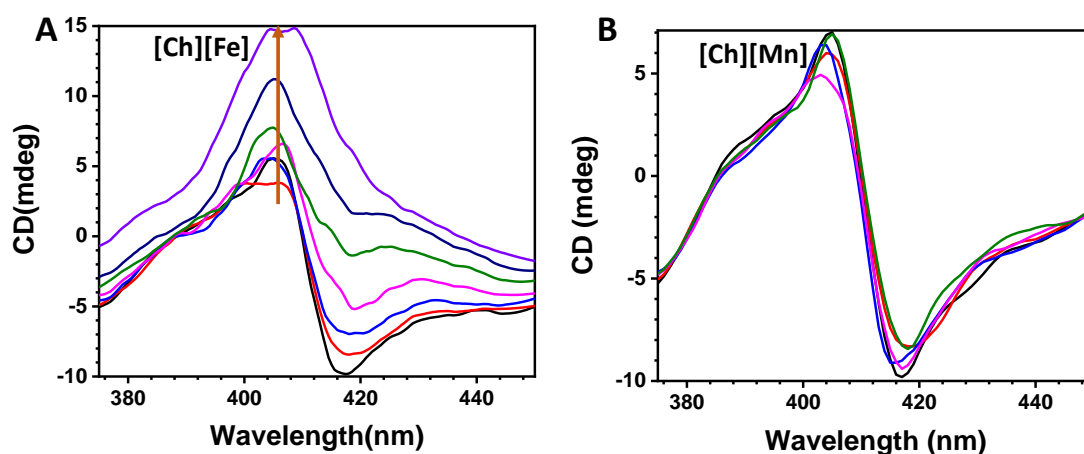
Figure 6.6. . Soret band region of native Cyt-c (20 × 10⁻⁶ M) and Cyt-c with different concen-trations of A) [Ch][Fe]] and B) [Ch]₂[Mn]

6.3.3. Steady-state Absorption Analysis:

The absorption spectroscopic investigation confirmed the structural changes in Cyt-c induced by MILs. The characteristic peak at 409 nm, attributed to the native conformation of Cyt-c, was blue-shifted upon the addition of [Ch][Fe] IL (Figure 6.7A), indicating conformational alterations in the heme region. The Q-band, associated with the reduced form of heme, disappeared, suggesting modifications in the heme-binding site of Cyt-c. In contrast, minimal changes were observed in the characteristic peak of Cyt-c upon the addition of [Ch]$_2$[Mn] IL (Figure 6.7B).
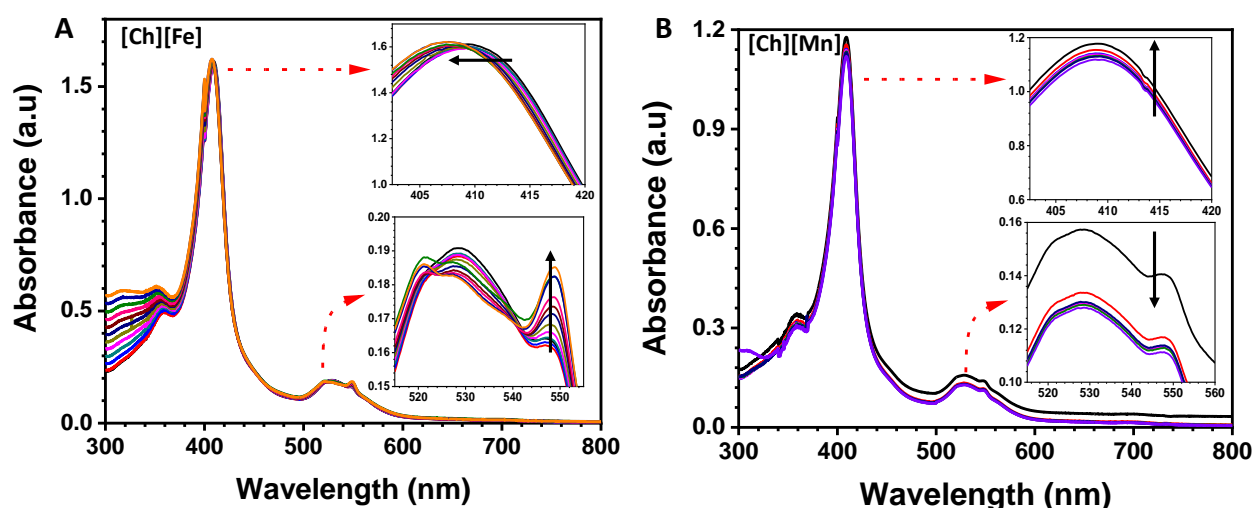
Figure 6.7. UV−vis spectra of Cyt-c (20 μM) at different concentrations of A) [Ch][Fe] and B) [Ch]$_2$[Mn]. Insets provide the zoomed region of Soret region and Q bands.

6.3.4. Steady-emission Absorption Analysis:

The fluorescence study focused on the tryptophan residue, which is located close to the heme and experiences strong quenching in its native state. The appearance of tryptophan fluorescence upon increasing the concentration of [Ch][Fe] IL indicated structural perturbation in the heme region (Figure 6.8A). However, no enhancement in tryptophan

fluorescence was observed in the presence of $[Ch]_2[Mn]$ IL, suggesting no perturbation in the heme region (Figure 6.8B).
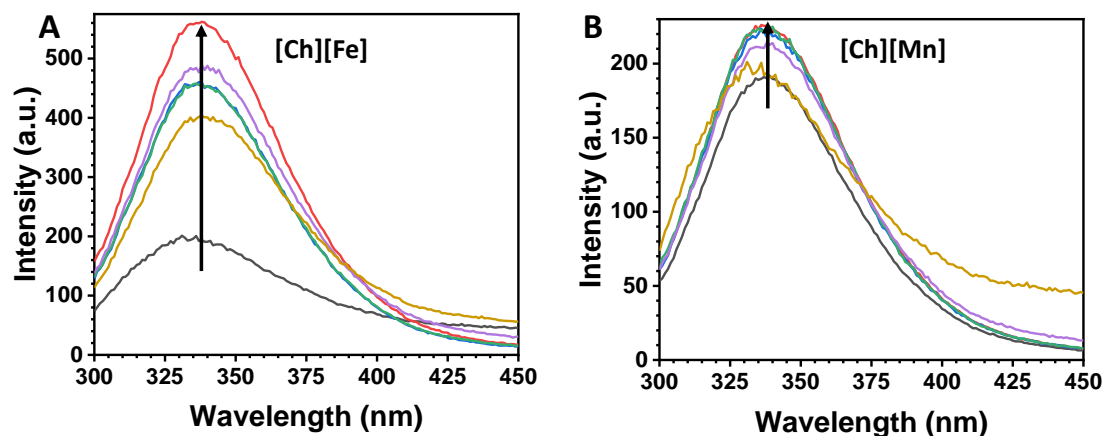
Figure 6.8. Emission spectra of Cyt-c (20 μM) at different concentrations of A) [Ch][Fe] and B) [Ch]₂[Mn]

Fluorescence lifetime measurements provided insights into the dynamics of molecular interactions. The fluorescence decay of tryptophan in Cyt-c exhibited two lifetime components (Table 6.3).

Table 6.3. Fluorescence decay parameters (ns) of Cyt-c in presence of different concentrations of MIL obtained by bi-exponential growth fitting.

System	τ_1 (a_1)	τ_2 (a_2)	χ^2
Cyt C	2.9	6.2	1.02
Cyt C-1mM FeIL	2.8	5.9	1.1
Cyt C-2mM FeIL	2.8	5.1	1.05
Cyt C-5mM FeIL	2.8	4.5	1.15
Cyt C-1mM MnIL	2.9	6.0	1.07
Cyt C-2mM MnIL	2.9	5.8	1.03
Cyt C-5mM MnIL	2.9	5.7	1.11

The longer lifetime component decreased upon gradual addition of [Ch][Fe] IL, indicating conformational changes near the Trp59 region. However, the presence of [Ch]$_2$[Mn] IL did not affect the tryptophan lifetime of Cyt-c.

6.3.5. Isothermal Titration Calorimetry Analysis:

Additionally, isothermal titration calorimetry (ITC) was used to determine the thermodynamic parameters of the Cyt-c-IL interaction. The interaction of Cyt-c with [Ch][Fe] IL was found to be spontaneous, as indicated by the negative Gibbs free energy (Figure 6.9A). The enthalpy was negative, and the entropy was positive, supporting the favorable enthalpic and entropic contributions to the process. The interaction of Cyt-c with [Ch]$_2$[Mn] IL was also spontaneous, with a negative Gibbs free energy, but the process was primarily entropy-driven (Figure 6.9B and Table 6.4).

Table 6.4. Thermodynamic parameters were calculated from the ITC fitting using a one-site binding fitting model. (% error = ±10%)

System	ΔH (cal/mol)	ΔS (cal/mol)	ΔG (kJ/mol)
Cyt C-FeIL	-96.20	16.7	-21.5
Cyt C-MnIL	-332.3	8.59	-9.314
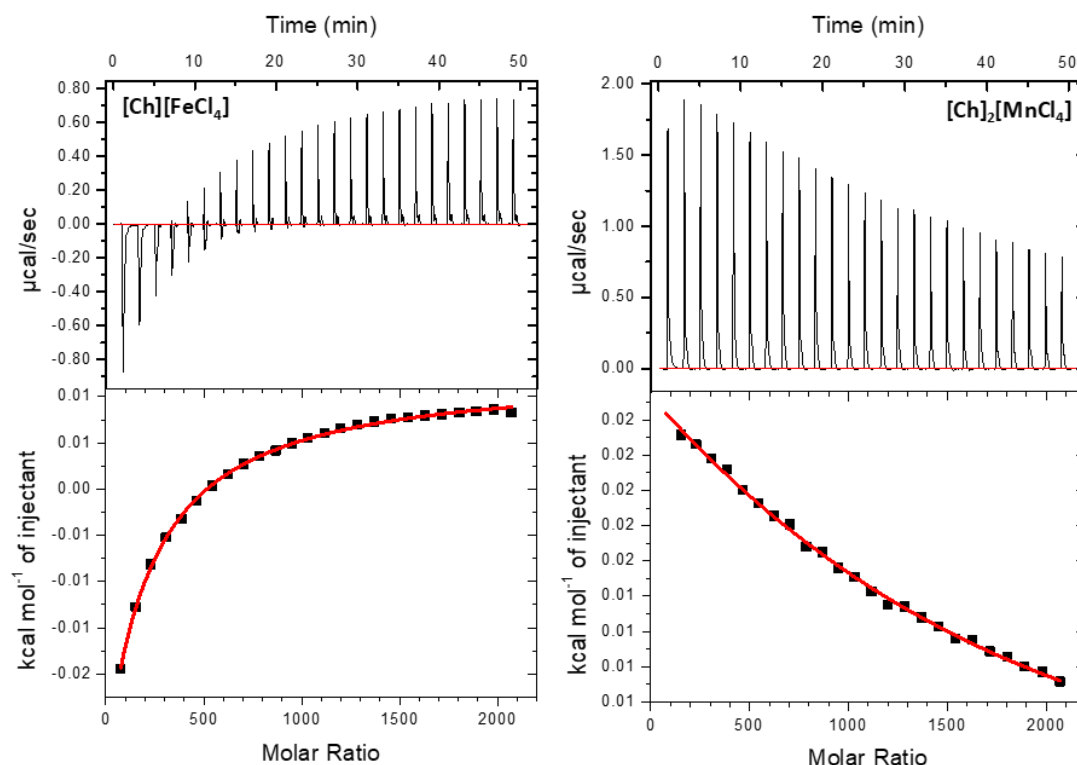
Figure 6.8. A) ITC isotherms of interaction of Cyt-c and [Ch][Fe] binding B) ITC isotherms of interaction of Cyt-c and [Ch]₂[Mn] binding.

Overall, CD spectroscopy provided insights into the perturbations in the secondary and tertiary structure of Cyt-c induced by MILs. Absorption and fluorescence spectroscopy corroborated the structural changes in the heme region. Thermodynamic analysis further characterized the interactions between Cyt-c and MILs, highlighting the spontaneous nature of the interactions and the differences between [Ch][Fe] IL and [Ch]₂[Mn] IL in their impact on Cyt-c structure and activity.

Tomaskova et al. investigated the enhancement of peroxidase-like activity in cytochrome c (Cyt-c) by replacing the dynamics of the sixth coordination bond of methionine-80 without significant conformational changes. The researchers employed molecular docking to understand the interactions between Cyt-c and the cationic and anionic components of metal-organic ionic liquids (MILs).

6.3.6. Molecular Dynamics Simulations

The authors identified specific binding sites for MILs on Cyt-c in their study. Figure 6.9 illustrates the energetically favorable conformation of Cyt-c in the presence of [Ch][Fe] IL, where the choline cation interacts with amino acid residues within the binding pocket of Cyt-c. This interaction primarily relies on weak hydrophobic and van der Waals forces. On the other hand, the $[FeCl_4]^-$ anion binds through van der Waals and hydrophobic interactions, surrounded by a tertiary loop region of amino acid residues. The calculated binding energies for both the cations and anions of MILs ranged from -15 to -24 kJ/mol.

In contrast, the binding energy between Cyt-c and $[Ch]_2[Mn]$ IL was found to be lower, ranging from -8 to -16 kJ/mol. This lower binding energy correlates with the previously observed lower peroxidase activity. The docking results align with the findings from isothermal titration calorimetry analysis, further supporting the notion of weaker interactions between Cyt-c and $[Ch]_2[Mn]$ IL.
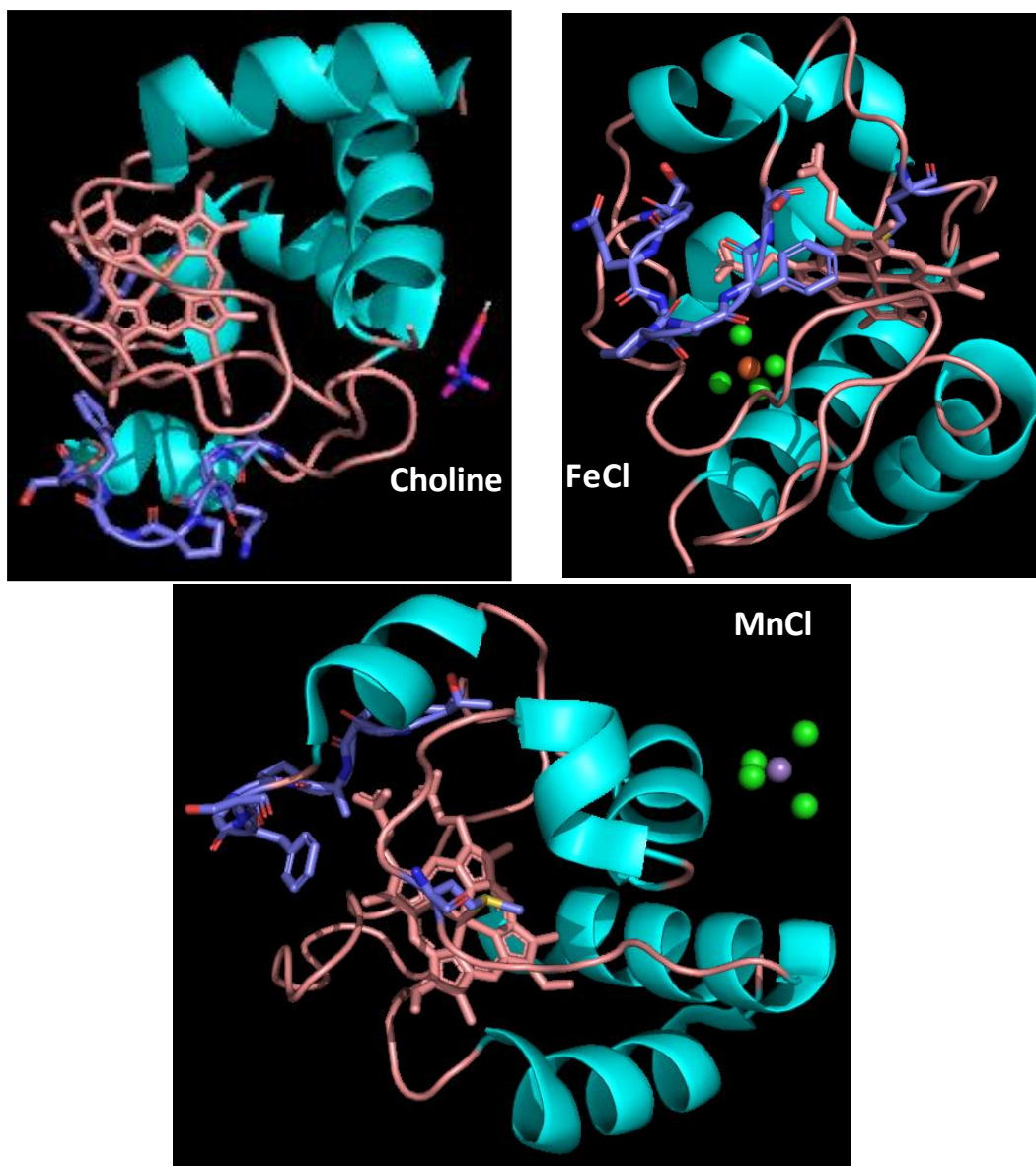
Figure 6.8. artoon representation of energetically favoured docked site of cyt-c showing the separate interaction of cation and anion of MILs

Overall, molecular docking revealed the binding modes and energies of MILs with Cyt-c. The interactions involved hydrophobic and van der Waals forces, with [Ch][Fe] IL exhibiting higher binding affinity and [Ch]$_2$[Mn] IL displaying lower binding affinity, consistent with their respective peroxidase activities.

This comprehensive study provides compelling evidence for the influence of MILs on the structure and peroxidase activity of Cyt-c. The interaction between Cyt-c and MILs was

extensively investigated using a combination of experimental and computational approaches, elucidating the underlying thermodynamics involved.
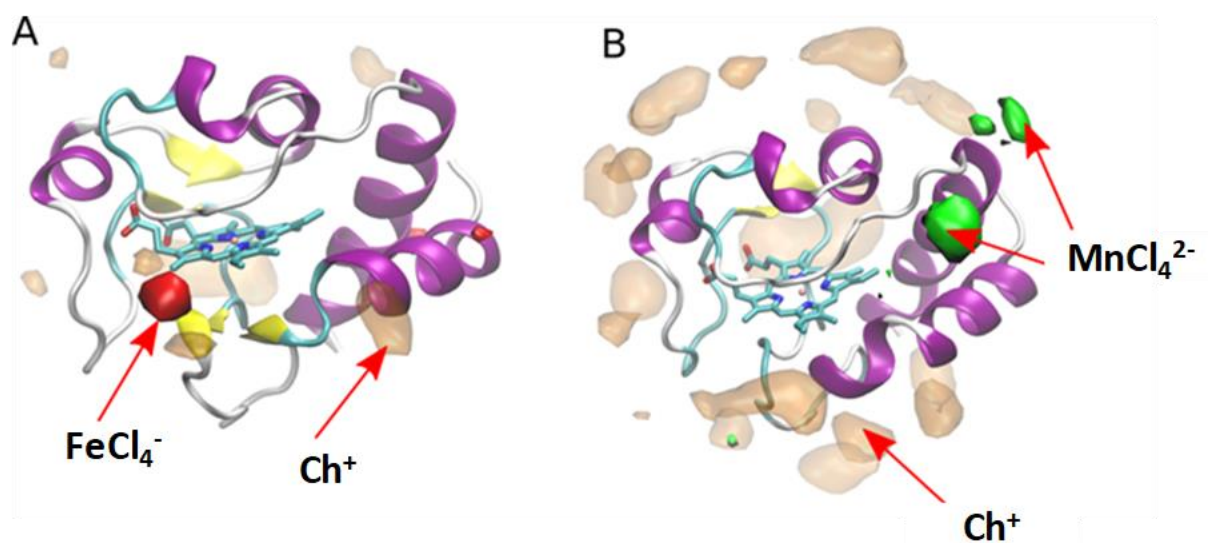
Figure 6.9. Comparison of Spatial density profile of (A) [FeCl₄]⁻ anion (red) and (B) [MnCl₄]²⁻ anion (green). The [Ch]⁺ cation density is shown in orange.

In the presence of [Ch][Fe] IL, Cyt-c exhibited a notable twofold increase in peroxidase activity. Conversely, [Ch]₂[Mn] IL resulted in a more modest 20% increase in peroxidase activity. Analysis of circular dichroism (CD) spectra revealed perturbations in the tertiary structures and heme region of Cyt-c upon exposure to [Ch][Fe] IL. On the other hand, [Ch]₂[Mn] IL specifically induced modifications in the secondary structure of Cyt-c. Consistent with these findings, UV-Vis absorption and fluorescence spectra also indicated alterations in the heme region of Cyt-c.
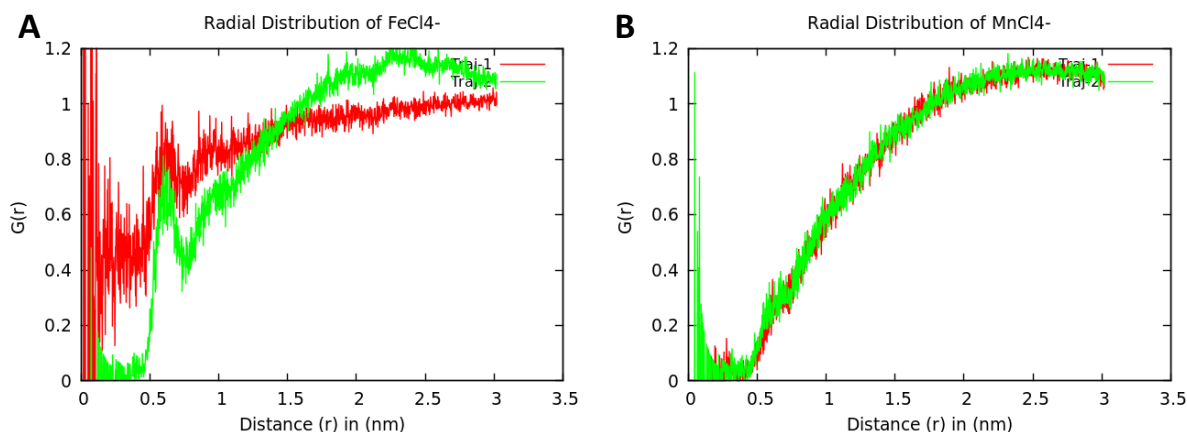
Figure 6.10. Radial distribution (RDF) of anions nearby 40–57 Ω-loop and the Met80 region (A) [FeCl₄]⁻ anion and (B) [MnCl₄]²⁻ anion

In summary, this study provides a comprehensive understanding of the impact of MILs on Cyt-c, revealing the thermodynamic and structural changes underlying the modulation of its peroxidase activity. The combination of experimental and computational techniques employed in this investigation contributes to thoroughly characterizing the Cyt-c-MILs interaction.

6.4. CONCLUSIONS

This study presents compelling evidence regarding the impact of MILs (ionic liquids) on the structure and peroxidase activity of Cyt-c. The thermodynamics underlying the interaction between Cyt-c and MILs were comprehensively investigated using a combination of experimental and computational methods.

In the presence of [Ch][Fe] IL, Cyt-c exhibited a significant twofold increase in peroxidase activity, whereas the presence of [Ch]₂[Mn] IL led to a 20% increase in peroxidase activity. Analysis of circular dichroism (CD) spectra revealed perturbations in the tertiary structures and heme region of Cyt-c when exposed to [Ch][Fe] IL. Conversely, [Ch]₂[Mn] IL primarily induced modifications in the secondary structure of Cyt-c.

Consistent with these findings, UV-Vis absorption and fluorescence spectra analysis corroborated the perturbation in the heme region of Cyt-c.

The binding enthalpy between Cyt-c and MILs, determined through isothermal titration calorimetry (ITC) measurements, was estimated to be -21 kJ/mol, indicating multiple binding sites. Molecular docking studies further supported these findings.

Overall, our results suggest that the dynamic equilibrium of the native sixth coordination bond of methionine-80 plays a pivotal role in the enhanced peroxidase-like activity of Cyt-c. By elucidating the intricate thermodynamic aspects of Cyt-c-MILs interactions, this study provides valuable insights into the underlying mechanisms driving the observed effects on Cyt-c structure and peroxidase activity.

6.5. REFERENCES

1.   Bertini, I.; Cavallaro, G.; Rosato, A., Cytochrome c: Occurrence and Functions. *Chem. Rev.* **2006,** *106* (1), 90-115.

2.   Eleftheriadis, T.; Pissas, G.; Liakopoulos, V.; Stefanidis, I., Cytochrome c as a Potentially Clinical Useful Marker of Mitochondrial and Cellular Damage. *Front. Immunol.* **2016,** *7*.

3.   Ow, Y.-L. P.; Green, D. R.; Hao, Z.; Mak, T. W., Cytochrome c: functions beyond respiration. *Nat Rev Mol Cell Biol* **2008,** *9* (7), 532-542.

4.   Santucci, R.; Sinibaldi, F.; Cozza, P.; Polticelli, F.; Fiorucci, L., Cytochrome c: An extreme multifunctional protein with a key role in cell fate. *Int. J. Biol. Macromol.* **2019,** *136*, 1237-1246.

5.   Yin, V.; Shaw, G. S.; Konermann, L., Cytochrome c as a Peroxidase: Activation of the Precatalytic Native State by H2O2-Induced Covalent Modifications. *J. Am. Chem. Soc.* **2017,** *139* (44), 15701-15709.

6.   Laszlo, J. A.; Compton, D. L., Comparison of peroxidase activities of hemin, cytochrome c and microperoxidase-11 in molecular solvents and imidazolium-based ionic liquids. *J. Mol. Catal.* **2002,** *18* (1), 109-120.

7.   Tomášková, N.; Varhač, R.; Lysáková, V.; Musatov, A.; Sedlák, E., Peroxidase activity of cytochrome c in its compact state depends on dynamics of the heme region. *BBA-PROTEINS PROTEOM* **2018,** *1866* (11), 1073-1083.

8.   Kaminsky, L. S.; Davison, A. J., Effect of organic solvents on the spectrum of cytochrome c. *Biochemistry* **1969,** *8* (11), 4631-4637.

9.   Zhigang Lei, B. C., Yoon-Mo Koo, and Douglas R. MacFarlane, Introduction: Ionic Liquids. *Chem. Rev.* **2017,** *117* (10), 6633-6635.

10.   Rogers, R. D.; Seddon, K. R., Ionic Liquids--Solvents of the Future? *Science* **2003,** *302* (5646), 792-793.

11.   Benedetto, A.; Ballone, P., Room Temperature Ionic Liquids Meet Biomolecules: A Microscopic View of Structure and Dynamics. *ACS Sustainable Chem. Eng.* **2016,** *4* (2), 392-412.

12.   Singh, S. K.; Savoy, A. W., Ionic liquids synthesis and applications: An overview. *J. Mol. Liq.* **2020,** *297*, 112038.

13.   Saha, D.; Mukherjee, A., Effect of water and ionic liquids on biomolecules. *Biophys Rev* **2018,** *10* (3), 795-808.

14.   Naushad, M.; Alothman, Z. A.; Khan, A. B.; Ali, M., Effect of ionic liquid on activity, stability, and structure of enzymes: A review. *Int. J. Biol. Macromol.* **2012,** *51* (4), 555-560.

15.   Bharmoria, P.; Trivedi, T. J.; Pabbathi, A.; Samanta, A.; Kumar, A., Ionic liquid-induced all-α to α + β conformational transition in cytochrome c with improved peroxidase activity in aqueous medium. *Phys. Chem. Chem. Phys.* **2015,** *17* (15), 10189-10199.

16.   Pabbathi, A.; Samanta, A., On the Stability and Conformational Dynamics of Cytochrome c in Ammonium Ionic Liquids. *J. Phys. Chem. B* **2020,** *124* (37), 8132-8140.

17.   Kumar Sahoo, D.; Devi Tulsiyan, K.; Jena, S.; Biswal, H. S., Implication of Threonine-Based Ionic Liquids on the Structural Stability, Binding and Activity of Cytochrome c. *ChemPhysChem* **2020,** *21* (23), 2525-2535.

18.   Sahoo, D. K.; Jena, S.; Dutta, J.; Chakrabarty, S.; Biswal, H. S., Critical Assessment of the Interaction between DNA and Choline Amino Acid Ionic Liquids: Evidences of Multimodal Binding and Stability Enhancement. *ACS Cent. Sci.* **2018,** *4* (12), 1642-1651.

19.   Sahoo, D. K.; Jena, S.; Tulsiyan, K. D.; Dutta, J.; Chakrabarty, S.; Biswal, H. S., Amino-Acid-Based Ionic Liquids for the Improvement in Stability and Activity of Cytochrome c: A Combined Experimental and Molecular Dynamics Study. *J. Phys. Chem. B* **2019,** *123* (47), 10100-10109.

20.   Santos, E.; Albo, J.; Irabien, A., Magnetic ionic liquids: synthesis, properties and applications. *RSC Adv.* **2014,** *4* (75), 40008-40018.

21.   Alves, M. S.; Neto, L. C. F.; Scheid, C.; Merib, J., An overview of magnetic ionic liquids: From synthetic strategies to applications in microextraction techniques. *J Sep Sci.* **2022,** *45* (1), 258-281.

22.   Emaus, M. N.; Anderson, J. L., Magnetic ionic liquids as microRNA extraction solvents and additives for the exponential amplification reaction. *Anal. Chim. Acta* **2021,** *1181*, 338900.

23.   Zhu, C.; Varona, M.; Anderson, J. L., Magnetic Ionic Liquids as Solvents for RNA Extraction and Preservation. *ACS Omega* **2020,** *5* (19), 11151-11159.

24.   Clark, K. D.; Yamsek, M. M.; Nacham, O.; Anderson, J. L., Magnetic ionic liquids as PCR-compatible solvents for DNA extraction from biological samples. *Chem. Commun.* **2015,** *51* (94), 16771-16773.

25.   Trujillo-Rodríguez, M. J.; Anderson, J. L., In situ formation of hydrophobic magnetic ionic liquids for dispersive liquid-liquid microextraction. *J. Chromatogr. A* **2019,** *1588*, 8-16.

26.   Emaus, M. N.; Anderson, J. L., Simultaneous cell lysis and DNA extraction from whole blood using magnetic ionic liquids. *Anal Bioanal Chem* **2020,** *412* (29), 8039-8049.

27.   Gehlot, P. S.; Gupta, H.; Rathore, M. S.; Khatri, K.; Kumar, A., Intrinsic MRI contrast from amino acid-based paramagnetic ionic liquids. *Mater. Adv.* **2020,** *1* (6), 1980-1987.

28.   Laszlo, J. A.; Compton, D. L., Comparison of peroxidase activities of hemin, cytochrome c and microperoxidase-11 in molecular solvents and imidazolium-based ionic liquids. *J. Mol. Catal. B: Enzymatic* **2002,** *18* (1), 109-120.

29.   Bisht, M.; Mondal, D.; Pereira, M. M.; Freire, M. G.; Venkatesu, P.; Coutinho, J. A. P., Long-term protein packaging in cholinium-based ionic liquids: improved catalytic activity and enhanced stability of cytochrome c against multiple stresses. *Green Chem.* **2017,** *19* (20), 4900-4911.

30.   Bharmoria, P.; Kumar, A., Unusually high thermal stability and peroxidase activity of cytochrome c in ionic liquid colloidal formulation. *Chem. Commun.* **2016,** *52* (3), 497-500.

31.   Deacon, O. M.; White, R. W.; Moore, G. R.; Wilson, M. T.; Worrall, J. A. R., Comparison of the structural dynamic and mitochondrial electron-transfer properties of the proapoptotic human cytochrome c variants, G41S, Y48H and A51V. *J. Inorg. Biochem.* **2020,** *203*, 110924.

32.   Bastos, M.; Abian, O.; Johnson, C. M.; Ferreira-da-Silva, F.; Vega, S.; Jimenez-Alesanco, A.; Ortega-Alarcon, D.; Velazquez-Campoy, A., Isothermal titration calorimetry. *Nat Rev Methods Primers* **2023,** *3* (1), 17.

33.   Appaix, F.; Minatchy, M.-N.; Riva-Lavieille, C.; Olivares, J.; Antonsson, B.; Saks, V. A., Rapid spectrophotometric method for quantitation of cytochrome c release from isolated mitochondria or permeabilized cells revisited. *Biochim. Biophys. Acta - Bioenergetics* **2000,** *1457* (3), 175-181.

34.   de Pedro, I.; García-Saiz, A.; González, J.; Ruiz de Larramendi, I.; Rojo, T.; Afonso, C. A. M.; Simeonov, S. P.; Waerenborgh, J. C.; Blanco, J. A.; Ramajo, B.; Fernández, J. R., Magnetic ionic plastic crystal: choline[FeCl4]. *Phys. Chem. Chem. Phys.* **2013,** *15* (30), 12724-12733.

35.   Mirkin, N.; Jaconcic, J.; Stojanoff, V.; Moreno, A., High resolution X-ray crystallographic structure of bovine heart cytochrome c and its application to the design of an electron transfer biosensor. *Proteins: Structure, Function, and Bioinformatics* **2008,** *70* (1), 83-92.

36.   Eberhardt, J.; Santos-Martins, D.; Tillack, A. F.; Forli, S., AutoDock Vina 1.2.0: New Docking Methods, Expanded Force Field, and Python Bindings. *J. Chem. Inf. Model.* **2021,** *61* (8), 3891-3898.

37.   Franzke, Y. J.; Holzer, C.; Andersen, J. H.; Begušić, T.; Bruder, F.; Coriani, S.; Della Sala, F.; Fabiano, E.; Fedotov, D. A.; Fürst, S.; Gillhuber, S.; Grotjahn, R.; Kaupp, M.; Kehry, M.; Krstić, M.; Mack, F.; Majumdar, S.; Nguyen, B. D.; Parker, S. M.; Pauly, F.; Pausch, A.; Perlt, E.; Phun, G. S.; Rajabi, A.; Rappoport, D.; Samal, B.; Schrader, T.; Sharma, M.; Tapavicza, E.; Treß, R. S.; Voora, V.; Wodyński, A.; Yu, J. M.; Zerulla, B.; Furche, F.; Hättig, C.; Sierka, M.; Tew, D. P.; Weigend, F., TURBOMOLE: Today and Tomorrow. *J. Chem. Theory Comput.* **2023**.

38.   Jo, S.; Kim, T.; Iyer, V. G.; Im, W., CHARMM-GUI: A web-based graphical user interface for CHARMM. *J. Comput. Chem.* **2008,** *29* (11), 1859-1865.

39.   Brooks, B. R.; Brooks Iii, C. L.; Mackerell Jr, A. D.; Nilsson, L.; Petrella, R. J.; Roux, B.; Won, Y.; Archontis, G.; Bartels, C.; Boresch, S.; Caflisch, A.; Caves, L.; Cui, Q.; Dinner, A. R.; Feig, M.; Fischer, S.; Gao, J.; Hodoscek, M.; Im, W.; Kuczera, K.; Lazaridis, T.; Ma, J.; Ovchinnikov, V.; Paci, E.; Pastor, R. W.; Post, C. B.; Pu, J. Z.; Schaefer, M.; Tidor, B.; Venable, R. M.; Woodcock, H. L.; Wu, X.; Yang, W.; York, D. M.; Karplus, M., CHARMM: The biomolecular simulation program. *J. Comput. Chem.* **2009,** *30* (10), 1545-1614.

40.   Klauda, J. B.; Venable, R. M.; Freites, J. A.; O'Connor, J. W.; Tobias, D. J.; Mondragon-Ramirez, C.; Vorobyov, I.; MacKerell, A. D., Jr.; Pastor, R. W., Update of the CHARMM All-Atom Additive Force Field for Lipids: Validation on Six Lipid Types. *J. Phys. Chem. B* **2010,** *114* (23), 7830-7843.

41.   Huang, J.; Rauscher, S.; Nawrocki, G.; Ran, T.; Feig, M.; de Groot, B. L.; Grubmüller, H.; MacKerell, A. D., CHARMM36m: an improved force field for folded and intrinsically disordered proteins. *Nat Methods* **2017,** *14* (1), 71-73.

42.   Jorgensen, W. L.; Chandrasekhar, J.; Madura, J. D.; Impey, R. W.; Klein, M. L., Comparison of simple potential functions for simulating liquid water. *J. Chem. Phys.* **1983,** *79* (2), 926-935.

43.   van Mourik, T.; Bühl, M.; Gaigeot, M. P., Density functional theory across chemistry, physics and biology. *Philosophical transactions. Series A, Mathematical, physical, and engineering sciences* **2014,** *372* (2011), 20120488.

44.   Frisch, M. J.; Trucks, G. W.; Schlegel, H. B.; Scuseria, G. E.; Robb, M. A.; Cheeseman, J. R.; Scalmani, G.; Barone, V.; Petersson, G. A.; Nakatsuji, H.; Li, X.; Caricato, M.; Marenich, A. V.; Bloino, J.; Janesko, B. G.; Gomperts, R.; Mennucci, B.; Hratchian, H. P.; Ortiz, J. V.; Izmaylov, A. F.; Sonnenberg, J. L.; Williams; Ding, F.; Lipparini, F.; Egidi, F.; Goings, J.; Peng, B.; Petrone, A.; Henderson, T.; Ranasinghe, D.; Zakrzewski, V. G.; Gao, J.; Rega, N.; Zheng, G.; Liang, W.; Hada, M.; Ehara, M.; Toyota, K.; Fukuda, R.; Hasegawa, J.; Ishida, M.; Nakajima, T.; Honda, Y.; Kitao, O.; Nakai, H.; Vreven, T.; Throssell, K.; Montgomery Jr., J. A.; Peralta, J. E.; Ogliaro, F.; Bearpark, M. J.; Heyd, J. J.; Brothers, E. N.; Kudin, K. N.; Staroverov, V. N.; Keith, T. A.; Kobayashi, R.; Normand, J.; Raghavachari, K.; Rendell, A. P.; Burant, J. C.; Iyengar, S. S.; Tomasi, J.; Cossi, M.; Millam, J. M.; Klene, M.; Adamo, C.; Cammi, R.; Ochterski, J. W.; Martin, R. L.; Morokuma, K.; Farkas, O.; Foresman, J. B.; Fox, D. J. *Gaussian 16 Rev. C.01*, Wallingford, CT, 2016.

45.   Zhao, Y.; Truhlar, D. G., A new local density functional for main-group thermochemistry, transition metal bonding, thermochemical kinetics, and noncovalent interactions. *J. Chem. Phys.* **2006,** *125* (19), 194101.

46.   Hehre, W. J.; Ditchfield, R.; Pople, J. A., Self—Consistent Molecular Orbital Methods. XII. Further Extensions of Gaussian—Type Basis Sets for Use in Molecular Orbital Studies of Organic Molecules. *J. Chem. Phys.* **2003,** *56* (5), 2257-2261.

47.   Breneman, C. M.; Wiberg, K. B., Determining atom-centered monopoles from molecular electrostatic potentials. The need for high sampling density in formamide conformational analysis. *J. Comput. Chem.* **1990,** *11* (3), 361-373.

48.   Allen, A. E. A.; Payne, M. C.; Cole, D. J., Harmonic Force Constants for Molecular Mechanics Force Fields via Hessian Matrix Projection. *J. Chem. Theory Comput.* **2018,** *14* (1), 274-281.

49.   Won, Y., Force Field for Monovalent, Divalent, and Trivalent Cations Developed under the Solvent Boundary Potential. *J. Phys. Chem. A* **2012,** *116* (47), 11763-11767.

50.   Evans, D. J.; Holian, B. L., The Nose–Hoover thermostat. *J. Chem. Phys.* **1985,** *83* (8), 4069-4074.

51.   Páll, S.; Hess, B., A flexible algorithm for calculating pair interactions on SIMD architectures. *Comput. Phys. Commun.* **2013,** *184* (12), 2641-2650.

52.   Darden, T.; York, D.; Pedersen, L., Particle mesh Ewald: An N·log(N) method for Ewald sums in large systems. . *J. Chem. Phys.* **1993,** *98* (12), 10089-10092.

53.   Hess, B.; Bekker, H.; Berendsen, H. J. C.; Fraaije, J. G. E. M., LINCS: A linear constraint solver for molecular simulations. *J. Comput. Chem.* **1997,** *18* (12), 1463-1472.

54.   Miyamoto, S.; Kollman, P. A., Settle: An analytical version of the SHAKE and RATTLE algorithm for rigid water models. *J. Comput. Chem.* **1992,** *13* (8), 952-962.

55.   Parrinello, M.; Rahman, A., Polymorphic transitions in single crystals: A new molecular dynamics method. *J. Appl. Phys.* **1981,** *52* (12), 7182-7190.

56.   Abraham, M. J.; Murtola, T.; Schulz, R.; Páll, S.; Smith, J. C.; Hess, B.; Lindahl, E., GROMACS: High performance molecular simulations through multi-level parallelism from laptops to supercomputers. *SoftwareX* **2015,** *1-2*, 19-25.

SUMMARY AND FUTURE PERSPECTIVE

7.1. Summary

This thesis explores the emerging potential of ionic liquids (ILs) as an environmentally friendly alternative to volatile organic compounds. By capitalizing on their non-toxic, biocompatible, and biodegradable nature, novel non-toxic ILs are synthesized and their interactions with biomolecules are examined. The study addresses crucial concerns related to biomolecules, such as enhancing long-term storage, stability, and activity of proteins and nucleic acids at room temperature. This thesis primarily centers on exploring choline-based ILs while addressing their interactions with proteins, and nucleic acids. It is further divided into two subdivisions. Chapters 3 and 4 specifically focus on choline amino acid-based ILs (CAAILs) with amino acids as the anionic counterpart. On the other hand, chapters 5 and 6 delve into the study of choline magnetic ionic liquids (ChMILs) with paramagnetic ferric chloride and manganese chloride as their anionic counterparts. The key discoveries made in this thesis are outlined below:

Chapter 1 presents a concise overview of the history and current applications of ILs and biomolecules. It also highlights recent advancements in the field of biological applications of biomolecules and identifies the gaps and motivations that drive this thesis's research direction. It focuses on the potential of ILs to revolutionize biomolecular studies and applications is revealed, offering promising avenues for sustainable and effective solutions in various biotechnological and biomedical domains.

Chapter 2 delves into the comprehensive explanation of the experimental and computational methodologies utilized throughout this thesis. These methodologies have been have been useful in obtaining valuable insights into the characterization of Ionic ILs and the intricate binding interactions between ILs and proteins, as well as nucleic acids. The combination of experimental and computational techniques has provided a robust

framework for understanding the fundamental properties of ILs and their behavior in conjunction with biomolecules. By elucidating these interactions, this chapter lays the foundation on the spectroscopic and computational techniques that provides a deeper understanding of the potential applications and implications of ILs in various biomolecular processes, offering a pathway for advancing research and practical implementation in this exciting field.

In Chapter 3, a detailed molecular-level investigation is conducted to understand the structural changes induced in RNA when interacting with CAAILs. The study begins with a computational modeling approach to hypothesize the structural factors driving the interaction between ILs and RNA. To validate these hypotheses experimentally, various techniques such as steady-state fluorescence, UV-Vis absorbance, circular dichroism (CD) spectroscopy, and isothermal titration calorimetry (ITC) are employed. The results of fluorescence correlation spectroscopy reveal that RNA's hydrodynamic radius remains unchanged in the presence of ILs, indicating the preservation of the biomolecule's structural integrity in the IL environment, which is further confirmed through CD analysis. UV-Vis spectra analysis indicates multimodal binding of CAAILs with RNA, while fluorescence emission studies demonstrate that IL molecules enter the minor groove of RNA. Interestingly, it is observed that increasing ILs concentration does not lead to structural instability. ITC and molecular docking studies reveal that the binding energy of ILs with RNA is approximately -4 kcal/mol, indicating a weaker binding affinity. This finding suggests that RNA can be efficiently extracted from the IL media due to the lower binding energy of ILs. The significance of this study lies in the spectroscopic and theoretical evidence showing that non-cytotoxic and eco-friendly CAAILs can be effectively used for the extraction and safe storage of RNA. The molecular-level insights

gained from these results serve as valuable guidance for designing suitable ILs for in-vivo applications of RNA, offering a promising avenue for advancing biotechnological and biomedical research. Ultimately, the findings underscore the potential of ILs as non-toxic and biocompatible solvents, contributing to the sustainable advancement of RNA-related applications in various fields.

In Chapter 4, the focus shifts to exploring how different ILs can impact the native structure of proteins, leading to varying effects. Some ILs enable proteins to retain their native conformation, while others cause a complete loss of structure. Specifically, the investigation centers on ChAAILs and their influence on hemoglobin (Hb), a protein of great interest due to its intermediate state. Through fluorescence and CD measurements, the study reveals that ChAAILs induce partial unfolding of Hb without completely denaturing the protein. Notably, [Ch][Met] strongly binds to Hb with a binding energy of -4.7 kcal/mol, suggesting hydrogen bonding plays a vital role in the interactions between ILs and Hb. This intriguing finding indicates that ChAAILs hold promise as external ligands for investigating the hemichrome intermediate state of Hb. The implications of these discoveries extend to medicinal chemistry, as ILs exhibit strong binding Hb, this research opens new avenues for further exploration and potential applications. It may pave the way for designing novel ligands or therapeutic agents targeting specific Hb states or functions. Consequently, this study contributes to a deeper understanding of protein-IL interactions and their potential in medicinal chemistry, offering valuable insights for advancing research and development in this field.

Chapter 5 extensively investigates the binding characteristics and molecular mechanisms of ChMILs with ct-DNA. The experimental observations of increased turbidity in ct-DNA with rising concentrations of ChMILs provide strong evidence of DNA compaction.

SUMMARY AND FUTURE PERSPECTIVE

Additional validation is achieved through SEM and FCS analyses, further confirming ct-DNA compaction in the presence of ChMILs Various experimental methods, including UV-Vis spectra, fluorescence dye displacement study, zeta potential, and molecular docking, reveal that electrostatic, hydrogen bonding, and hydrophobic interactions are involved in the binding process. Molecular dynamics (MD) simulations offer crucial insights into the dynamic interactions between ct-DNA and ChMILs. The simulations demonstrate a robust interaction between [Ch]$_2$[Mn] and DNA, leading to a more significant conformational shift of DNA compared to [Ch][Fe]. The surface of DNA exposed to solvent steadily decreases in both complexes during the simulation, resulting in DNA bending or adopting a more spherical structure due to interactions with the two magnetic ionic liquids. Notably, the DNA compaction is more pronounced in the presence of [Ch]$_2$[Mn], consistent with earlier experimental findings. The estimated binding free energy, $\Delta G = -642$ kcal/mol, conclusively confirms the stronger affinity of [Ch]$_2$[Mn] for DNA in comparison to [Ch][Fe]. This result aligns perfectly with the overall experimental and theoretical evidence, reinforcing the notion that MILs can effectively bind ct-DNA through their choline cation, regardless of the anions involved. The comprehensive investigation, incorporating experimental techniques, molecular docking, and MD simulations, yields a profound understanding of the interactions between ChMILs and ct-DNA. The study demonstrates the strong affinity and binding capacity of [Ch]$_2$[Mn] with ct-DNA, showcasing its potential as a promising agent for DNA-related applications. These findings provide valuable insights for future research in this exciting and promising field.

Chapter 6 presents compelling evidence concerning the influence of Ionic Liquids (ILs) on the structure and peroxidase activity of Cyt-c (cytochrome c). Through a combination

of experimental and computational methods, the thermodynamics underlying the interaction between Cyt-c and MILs are thoroughly investigated. In the presence of [Ch][Fe] IL, Cyt-c exhibits a substantial twofold increase in peroxidase activity, while [Ch]$_2$[Mn] IL leads to a 20% increase in peroxidase activity. Analysis of (CD) spectra reveals perturbations in the tertiary structures and heme region of Cyt-c when exposed to [Ch][Fe] IL. Conversely, [Ch]$_2$[Mn] IL primarily induces modifications in the secondary structure of Cyt-c. These findings are further supported by UV-Vis absorption and fluorescence spectra analysis, which confirm the perturbation in the heme region of Cyt-c. The binding enthalpy between Cyt-c and MILs, as determined through ITC measurements, is estimated to be -21 kJ/mol, suggesting the presence of multiple binding sites. Molecular docking studies further validate these observations. Overall, the results indicate that the dynamic equilibrium of the native sixth coordination bond of methionine-80 plays a crucial role in the enhanced peroxidase-like activity of Cyt-c. By elucidating the intricate thermodynamic aspects of Cyt-c-MILs interactions, this study provides valuable insights into the underlying mechanisms driving the observed effects on Cyt-c structure and peroxidase activity. These findings contribute to a deeper understanding of the interplay between ILs and biomolecules, paving the way for potential applications and advancements in the field of biocatalysis and enzyme modulation.

7.2. Future Perspective

Indeed, Ionic Liquids (ILs) have emerged as leading contenders for green solvents, and choline-based ILs, in particular, show great promise in the drug processing of antibiotics. However, to fully harness their potential in biotechnology and pharmaceutics, a deeper understanding of the sustainable nature of choline-based ILs is essential, especially in preserving the natural identity of proteins.

SUMMARY AND FUTURE PERSPECTIVE

This thesis has laid the groundwork by establishing guidelines for future investigations, which can aid in overcoming some of the major limitations encountered in the development of protein-IL formulations. It paves the way for further exploration of choline-based ILs as solvents in protein preservation, overcoming major limitations in the development of protein-IL formulations. By advancing our understanding of the interactions between proteins and ILs, researchers can unlock new possibilities in the efficient and eco-friendly processing of pharmaceutical drugs. With these guidelines, researchers can embark on further studies to optimize the use of ammonium-based ILs as green solvents in biotechnology and pharmaceutics. This has the potential to revolutionize drug processing and enhance the preservation of protein structures, ultimately contributing to more sustainable and environmentally friendly approaches in the pharmaceutical industry.

APPENDIX
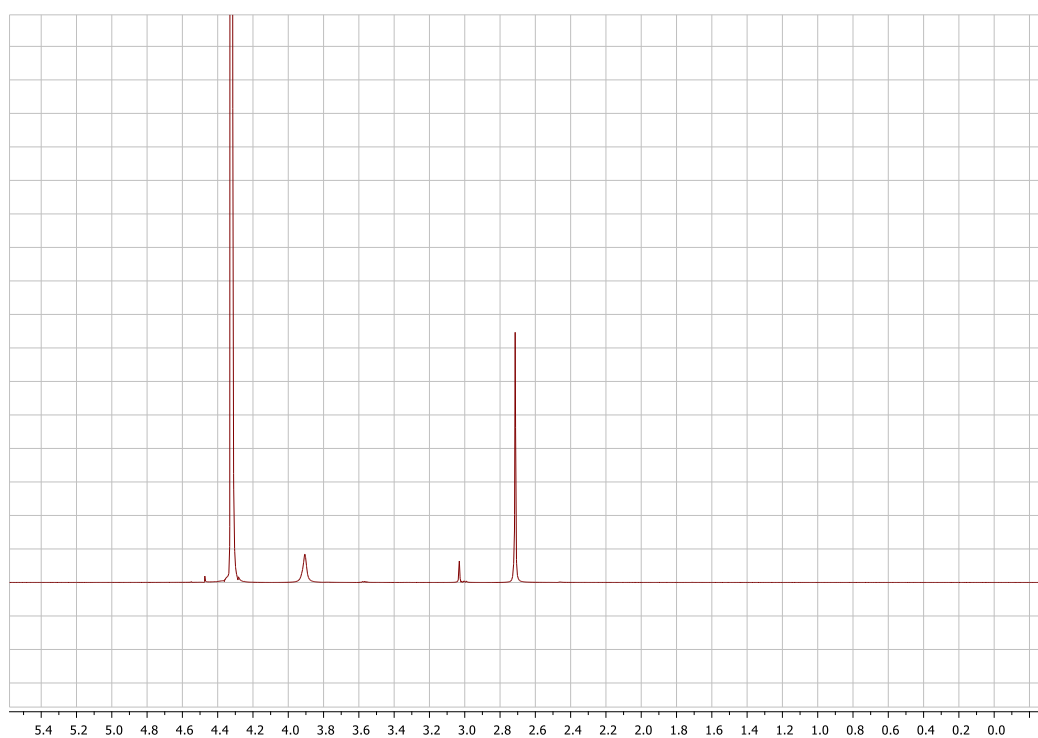
Figure A1. ^{1}H NMR spectra of [Ch][Fe] IL
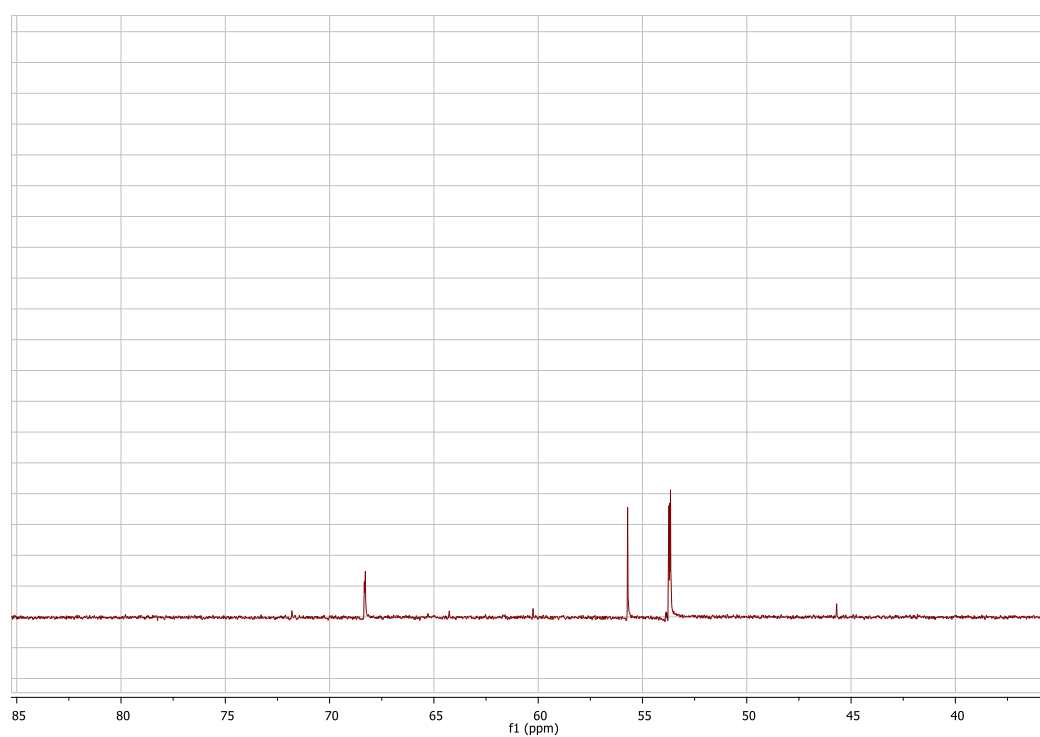
Figure A2. ^{13}C NMR spectra of [Ch][Fe] IL
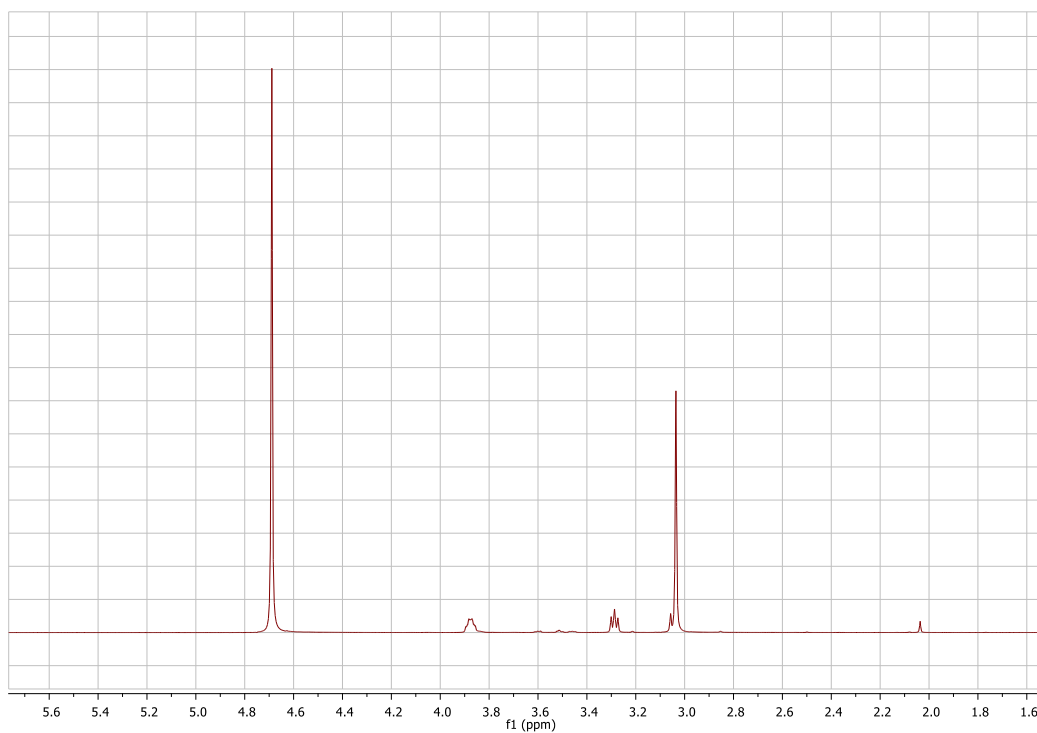
Figure A3. ^{1}H NMR spectra of [Ch]$_2$[Mn] IL
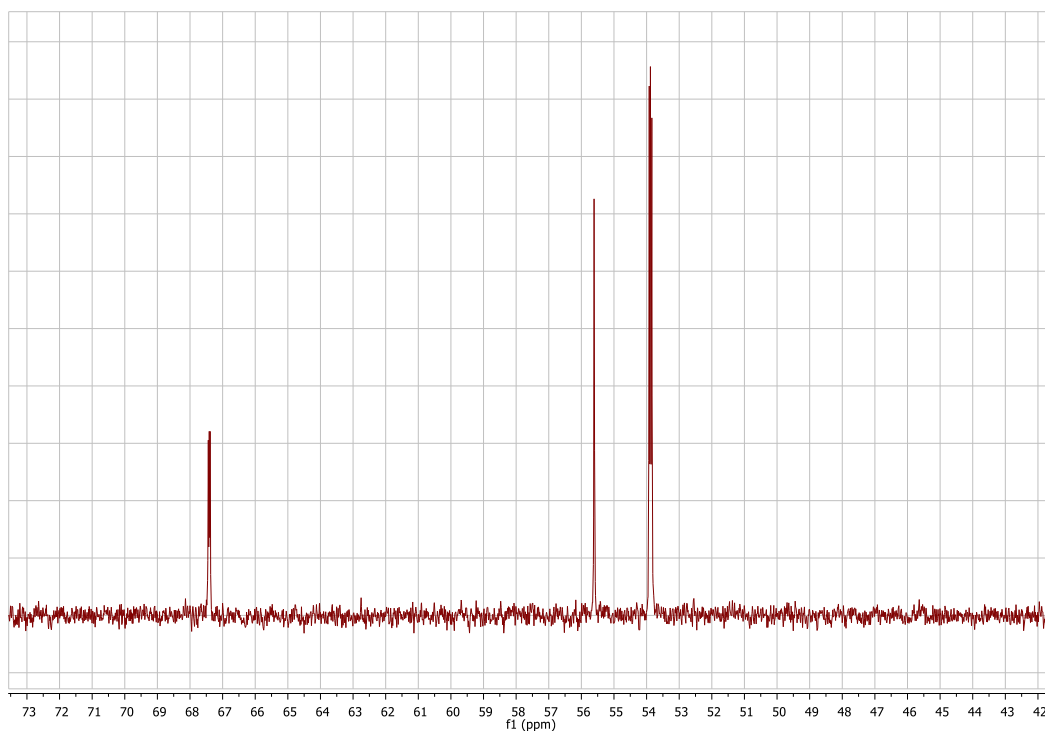
Figure A4. ^{13}C NMR spectra of [Ch]$_2$[Mn] IL
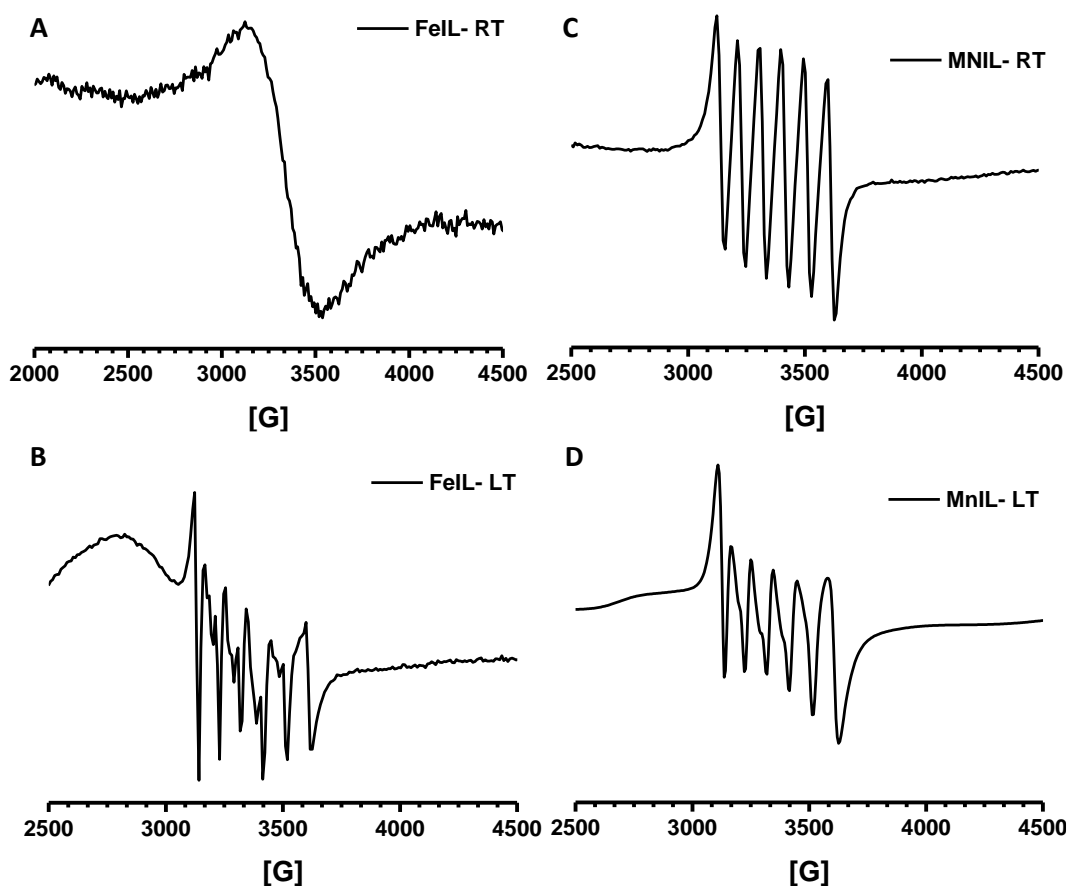
Figure A5. A) X-band EPR spectrum of [Ch][Fe] IL at room temperature in CH_3OH, B) X-band EPR spectrum of [Ch][Fe] IL at 100 K in CH_3OH, C) X-band EPR spectrum of [Ch]$_2$[Mn] IL at room temperature in CH_3OH, D) X-band EPR spectrum of [Ch]$_2$[Mn] IL at 100 K in CH_3OH.

Table A6.. Force field parameters for $[Ch]^+$, $[FeCl4]^-$ and $[MnCl_4]^{2-}$ ions used in this work.

[Ch]$^+$		
Force field: AMBER99SB		
Atoms	**σ (nm)**	**ε (kJ/mol)**
N4	2.49951E-01	1.62122e+0
C3	3.39771E-01	4.51035E-01
OH	3.24287E-01	3.89112E-01
HO	5.37925E-02	1.96648E-02
HX	1.88746E-01	8.70272E-02
H1	2.42200E-01	8.70272E-02

[FeCl₄]⁻		
Force field: Universal Force Field (UFF)		
Fe	2.08000E-01	0.560656
Cl	3.47000E-01	1.10876
[MnCl₄]²⁻		
Force Field: Panteva and York's fine-tuned divalent cation parameters		
Mn	3.01123E-01	0.058576
Cl	3.47000E-01	1.10876

Bond parameters

[Ch]⁺

Atom	Atom	r_{eq} (nm)	K_b (kJ/mol.nm²)
1	2	1.5110E-01	1.8627E+05
1	3	1.5110E-01	1.8627E+05
1	4	1.5110E-01	1.8627E+05
1	5	1.5110E-01	1.8627E+05
2	16	1.0910E-01	3.2342E+05
2	17	1.0910E-01	3.2342E+05
2	18	1.0910E-01	3.2342E+05
3	13	1.0910E-01	3.2342E+05
3	14	1.0910E-01	3.2342E+05
3	15	1.0910E-01	3.2342E+05
4	19	1.0910E-01	3.2342E+05
4	20	1.0910E-01	3.2342E+05
4	21	1.0910E-01	3.2342E+05
5	6	1.5380E-01	1.9456E+05
5	9	1.0910E-01	3.2342E+05
5	10	1.0910E-01	3.2342E+05

6	7	1.4230E-01	2.4552E+05
6	11	1.0970E-01	3.1455E+05
6	12	1.0970E-01	3.1455E+05
7	8	9.7300E-02	4.7154E+05
1	2	1.5110E-01	1.8627E+05
1	3	1.5110E-01	1.8627E+05
1	4	1.5110E-01	1.8627E+05
1	5	1.5110E-01	1.8627E+05
2	16	1.0910E-01	3.2342E+05
2	17	1.0910E-01	3.2342E+05
2	18	1.0910E-01	3.2342E+05

<table>
<tr><td colspan="4" align="center">

$[FeCl_4]^-$

</td></tr>
<tr><td>Fe</td><td>Cl</td><td>0.22600</td><td>328.27664</td></tr>
<tr><td colspan="4" align="center">

$[MnCl_4]^{2-}$

</td></tr>
<tr><td>Mn</td><td>Cl</td><td>0.238974</td><td>328.27664</td></tr>
<tr><td colspan="4" align="center">

Angle parameters

</td></tr>
<tr><td colspan="4" align="center">

$[Ch]^+$

</td></tr>
</table>

Atom	Atom	Atom	θ (deg)	K_θ (kJ.mol^{-1}.rad^{-2})
1	2	1	1.08E+02	5.03E+02
1	2	1	1.08E+02	5.03E+02
1	2	1	1.08E+02	5.03E+02
1	3	1	1.08E+02	5.03E+02
1	3	1	1.08E+02	5.03E+02
1	3	1	1.08E+02	5.03E+02
1	4	1	1.08E+02	5.03E+02
1	4	1	1.08E+02	5.03E+02
1	4	1	1.08E+02	5.03E+02
1	5	1	1.14E+02	6.78E+02
1	5	1	1.08E+02	5.03E+02
1	5	1	1.08E+02	5.03E+02
2	1	1	1.10E+02	5.40E+02
2	1	1	1.10E+02	5.40E+02
2	1	1	1.10E+02	5.40E+02
3	1	1	1.10E+02	5.40E+02
3	1	1	1.10E+02	5.40E+02

4	1	1	1.10E+02	5.40E+02
5	6	1	1.10E+02	7.08E+02
5	6	1	1.10E+02	3.92E+02
5	6	1	1.10E+02	3.92E+02
6	5	1	1.11E+02	3.91E+02
6	5	1	1.11E+02	3.91E+02
6	7	1	1.07E+02	4.10E+02
7	6	1	1.10E+02	5.23E+02
7	6	1	1.10E+02	5.23E+02
9	5	1	1.10E+02	3.25E+02
11	6	1	1.08E+02	3.25E+02
13	3	1	1.10E+02	3.25E+02
13	3	1	1.10E+02	3.25E+02
14	3	1	1.10E+02	3.25E+02
16	2	1	1.10E+02	3.25E+02
16	2	1	1.10E+02	3.25E+02
17	2	1	1.10E+02	3.25E+02
19	4	1	1.10E+02	3.25E+02
19	4	1	1.10E+02	3.25E+02
20	4	1	1.10E+02	3.25E+02
22	23	1	1.08E+02	5.03E+02
22	23	1	1.08E+02	5.03E+02
22	23	1	1.08E+02	5.03E+02
22	24	1	1.08E+02	5.03E+02
22	24	1	1.08E+02	5.03E+02
22	24	1	1.08E+02	5.03E+02
22	25	1	1.08E+02	5.03E+02
22	25	1	1.08E+02	5.03E+02
22	25	1	1.08E+02	5.03E+02
22	26	1	1.14E+02	6.78E+02
22	26	1	1.08E+02	5.03E+02
22	26	1	1.08E+02	5.03E+02
23	22	1	1.10E+02	5.40E+02
23	22	1	1.10E+02	5.40E+02
23	22	1	1.10E+02	5.40E+02
24	22	1	1.10E+02	5.40E+02
24	22	1	1.10E+02	5.40E+02
25	22	1	1.10E+02	5.40E+02
26	27	1	1.10E+02	7.08E+02
26	27	1	1.10E+02	3.92E+02
26	27	1	1.10E+02	3.92E+02
27	26	1	1.11E+02	3.91E+02
27	26	1	1.11E+02	3.91E+02
27	28	1	1.07E+02	4.10E+02
28	27	1	1.10E+02	5.23E+02
28	27	1	1.10E+02	5.23E+02
30	26	1	1.10E+02	3.25E+02
32	27	1	1.08E+02	3.25E+02
34	24	1	1.10E+02	3.25E+02

34	24	1	1.10E+02	3.25E+02
35	24	1	1.10E+02	3.25E+02
37	23	1	1.10E+02	3.25E+02
37	23	1	1.10E+02	3.25E+02
38	23	1	1.10E+02	3.25E+02
40	25	1	1.10E+02	3.25E+02
40	25	1	1.10E+02	3.25E+02
41	25	1	1.10E+02	3.25E+02
43	44	1	1.09E+02	9.74E+02
43	44	1	1.09E+02	9.74E+02
43	44	1	1.09E+02	9.74E+02
45	44	1	1.09E+02	9.74E+02
46	44	1	1.09E+02	9.74E+02
45	44	1	1.09E+02	9.74E+02
34	24	1	1.10E+02	3.25E+02
35	24	1	1.10E+02	3.25E+02
37	23	1	1.10E+02	3.25E+02
37	23	1	1.10E+02	3.25E+02
$[FeCl_4]^-$				
22	24	23	1.09E+02	9.74E+02
22	24	25	1.09E+02	9.74E+02
22	24	26	1.09E+02	9.74E+02
23	24	25	1.09E+02	9.74E+02
25	24	26	1.09E+02	9.74E+02
23	24	26	1.09E+02	9.74E+02
$[MnCl_4]^{2-}$				
43	44	45	1.09E+02	9.74E+02
43	44	46	1.09E+02	9.74E+02
43	44	47	1.09E+02	9.74E+02
45	44	46	1.09E+02	9.74E+02
46	44	47	1.09E+02	9.74E+02
45	44	47	1.09E+02	9.74E+02